

# **Analysis of Particle Deformation during Impact Deposition**

### Saba Saifoori

Submitted in accordance with the requirements for the degree of

## **Doctor of Philosophy**

The University of Leeds

School of Chemical and Process Engineering

**March 2025** 



I confirm that the work submitted is my own, except where work which has formed part of jointly authored publications has been included. My contribution and the other authors to this work has been explicitly indicated below. I confirm that appropriate credit has been given within the thesis where reference has been made to the work of others.

Parts of the results from Chapters 3 and 4 have been published in Computational Particle Mechanics: S. Saifoori, S. Nezamabadi, M. Ghadiri, Analysis of impact deformation of elastic-perfectly plastic particles, Comput. Part. Mech. (2024).

Saba Saifoori: data curation, analysis, investigation, methodology, validation, visualisation, original draft. Saeid Nezamabadi: software, conceptualisation, supervision, review editing. Mojtaba Ghadiri: project admin, conceptualisation, review editing, supervision, funding acquisition, resources.

Majority of the results from Chapter 5 and parts of the results from Chapter 6 have been submitted to Powder Technology: S. Saifoori, S. Hosseinhashemi, M. Alasossi, C. Schilde, S. Nezamabadi, M. Ghadiri, AI-Assisted Prediction of Particle Impact Deformation Simulated by Material Point Method "under review", Powder Technol. (2025).

Saba Saifoori: data curation, analysis, investigation, methodology, validation, visualisation, original draft. Somayeh Hosseinhashemi: analysis, original draft, visualisation. Mohammad Alasossi: data curation, small section of the analysis. Carsten Schilde: supervison. Saeid Nezamabadi: software, conceptualisation, supervision, review editing. Mojtaba Ghadiri: project admin, conceptualisation, review editing, supervision, funding acquisition, resources.

Also, Mr Stuart Micklethwaite, Mr John Harrington and Dr Fanchao Meng have contributed to parts of Chapter 6, as detailed in the corresponding Overview section.

This copy has been supplied on the understanding that it is copyright material and that no quotation from the thesis may be published without proper acknowledgement.



#### Acknowledgements

I would like to express my deepest gratitude to my primary supervisor, Professor Mojtaba Ghadiri, for his unconditional support, both academically and personally. His invaluable guidance, depth of knowledge, and insightful feedback have played a crucial role in shaping my research skills. I am forever grateful for the essential academic skills that I have learnt from him. His mentorship has not only helped me refine my academic approach, but has also contributed immensely to my growth in collaboration and communication, broadening my vision as a researcher.

I am also sincerely grateful to my co-supervisor, Professor Steven Milne, for his continued support, kindness and encouragement. I would like to extend my gratitude to Dr Saeid Nezamabadi, not only for allowing me to implement his proprietary code for this project, but also for his constant guidance, support, and mentorship. His expertise and willingness to share knowledge have been instrumental in enriching my understanding of the numerical component of the project, and have had a meaningful impact on my work.

I am incredibly fortunate to have had the support of my friend and colleague, Dr Wei Pin Goh, who has continuously provided invaluable guidance, both academically and personally. His encouragement, unique perspectives, and intellectual discussions have helped me see things from new angles and have been a source of strength during challenging times. His constructive comments have immeasurably contributed to my knowledge. I also extend my heartfelt appreciation to my friend and colleague, Dr James Middleton, for his constant earnest support and encouragement, which have meant a great deal to me.

I would like to express my sincere gratitude to Dr Harry Peirson for his continuous support with the aerosol deposition rig, his instrumental training, and his guidance in troubleshooting the system. Professor Andrew Mullis' valuable input and kind guidance are also deeply



appreciated, especially for recommending the use of solder balls in the impact experiments, and for his insightful discussions on the high strain rate deformation of copper particles. I would also want to sincerely thank Mr Robert Harris and Mr Robert Simpson, whose kind assistance, insights, and technical support have been invaluable in certain aspects of my research. I am truly grateful for their efforts.

I deeply appreciate the contributions of Miss Somayeh Hosseinhashemi, Mr Mohammad Alasossi, Dr Fanchao Meng, Mr Stuart Micklethwaite and Mr John Harrington to this project. Their help has been indispensable, and I am very grateful for their input.

All of the simulations presented in this work have been undertaken on ARC4, part of the High Performance Computing facilities at the University of Leeds, UK.

Finally, the financial support from the Engineering and Physical Sciences Research Council (EPSRC) via the Doctoral Training Partnership Studentship is gratefully appreciated.



#### **Abstract**

Particle impact is a common occurrence in numerous applications that involve handling and processing of powders. Depending on the impact details, it can have various implications for a process, e.g. it can affect the flow behaviour of powders due to kinetic energy dissipation, or influence the particle-particle and particle-substrate bonding mechanism, and consequently, the quality of the final film in coating processes such as cold spraying (CS). Thus, investigating the impact phenomenon is important for understanding and improving the efficiency of such processes. However, experimental investigation of particle impact is precarious, especially at high velocities, as the event takes place in an extremely short span of time. Therefore, numerical simulations provide a great means for the analysis of the phenomena taking place throughout impact. Discrete Element Method (DEM), Finite Element Method (FEM) and Molecular Dynamics (MD) are amongst the popular numerical methods used to date for the simulation of particle impact. However, these methods have certain limitations when dealing with the problem of impact, especially at large deformations. On the other hand, a method known as the Material Point Method (MPM) can be utilised to overcome such drawbacks. As MPM has seldom been used for the simulation of particle impact, it is adopted in the current work to carry out a comprehensive study of the impact phenomenon, especially when large deformation is concerned. Most studies on high-velocity impact processes like CS often overlook the influence of particle mechanical properties and density. Therefore, the present work considers a wide range of material properties and impact velocities to investigate their effect on the impact deformation behaviour.

To this end, MPM simulations are carried out for the impact of an elastic-perfectly plastic particle on a rigid wall. The results are analysed by focusing on variables and expressions that characterise the particle's plastic deformation and rebound behaviour. It is observed that the



plastic deformation of the particle is primarily governed by the incident kinetic energy and yield strength of the material. On the other hand, the recovery of deformation and material's resistance to it-particularly at small deformation-are intuitively influenced not only by these factors, but also by the material's Young's modulus. Empirical equations are suggested for the prediction of the coefficient of restitution and the compression ratio of the particle, leveraging dimensionless groups. Subsequently, the capability of Artificial Intelligence (AI), specifically Machine Learning (ML) techniques, in identifying the underlying trends in the simulation data and refining the empirical equations is examined. Accordingly, the simulation results are introduced to a hybrid AI framework, which successfully recognises meaningful relationships, when presented with the already identified dimensionless groups. The limitations of the framework are then highlighted, and recommendations are made for further improvement. In the end, impact experiments are carried out to assess the accuracy of the numerical simulations and empirical equations. Elastic impact is first examined using elastic balls to validate the simulation predictions against experimental measurements. Elastic-plastic impact is then investigated using metal particles impacted in a custom-built impact device, with the measured compression ratio and coefficient of restitution compared to empirical predictions. Lastly, the applicability of the empirical compression ratio equation to high strain rate impacts is evaluated by depositing fine copper particles via aerosol deposition. The results confirm that the simulations accurately model the elastic impact, and the empirical equations can reasonably predict the compression ratio. However, the predicted coefficient of restitution is underestimated compared to the experimental values, though it performs better than a number of other theoretical/empirical equations. It is also found that the compression ratio at high strain rates is better predicted by a higher representative yield strength, attributed to work hardening dominating the overall deformation. The study combines numerical modelling, AI-driven



analysis, and experimental validation, contributing to a deeper understanding of particle impact behaviour.



## **Table of Contents**

| Acknowledgements   | II   |
|--|------|
| Abstract   | IV   |
| Table of Contents  | VII  |
| List of Figures  | XI   |
| List of Tables   | XXII |
| Nomenclature   | XXVI |
| 1. Introduction  | 1    |
| 1.1. Motivation of the Present Work                      | 1    |
| 1.2. Aim, Objectives and Structure of the Thesis         | 3    |
| 2. Literature Review                                     | 6    |
| 2.1. Deformation Behaviour during Impact                 | 6    |
| 2.1.1. Deposition Mechanism in Cold Spraying             | 7    |
| 2.1.2. Parameters Affecting Deformation during CS        | 9    |
| 2.2. Numerical Methods for Simulation of Particle Impact | 12   |
| 2.2.1. Discrete Element Method (DEM)                     | 12   |
| 2.2.2. Finite Element Method (FEM)                       | 15   |
| 2.2.3. Molecular Dynamics (MD)                           | 19   |
| 2.2.4. Material Point Method (MPM)                       | 21   |
| 2.2.5. Critique of the Numerical Methods                 | 30   |
| 3. Numerical Methodology                                 | 32   |
| 3.1. Overview  | 32   |
| 3.2. MPM Formulation                                     | 32   |



| 3.3. Explicit Algorithm   |
|---|
| 3.4. Contact Algorithm  |
| 3.5. Sensitivity Analysis                                       |
| 3.5.1. Simulation Setup4  |
| 3.5.2. Material Points and Mesh Discretisation                  |
| 3.5.3. Time Step  |
| 3.5.4. Sensitivity Analysis Results                             |
| 3.5.5. Sensitivity Analysis Conclusions5.                       |
| 4. Simulation of Impact for Elastic-Perfectly Plastic Particles |
| 4.1. Overview50   |
| 4.2. Case Studies and Simulation Setup50                        |
| 4.3. Analysis of Deformation58                                  |
| 4.3.1. Method Scope   |
| 4.3.2. Equivalent Plastic Strain                                |
| 4.3.3. Normalised Deformed Height and Compression Ratio60       |
| 4.3.4. Ratio of Plastic Work to Incident Kinetic Energy         |
| 4.3.5. Coefficient of Restitution                               |
| 4.4. Contact Force-Displacement70                               |
| 4.4.1. Evolution of Contact Force with Displacement70           |
| 4.4.2. Comparison with Theoretical Contact Models7              |
| 4.4.3. Trends in the MPM Data                                   |
| 4.5. Concluding Remarks8'                                       |



| 5. AI-Assisted Analysis of MPM Simulation Data                      | 88  |
|---|-----|
| 5.1. Overview   | 88  |
| 5.2. AI Hybrid Approach   | 89  |
| 5.2.1. Pre-Processing and Augmentation Techniques                   | 90  |
| 5.2.2. Graph Attention Network (GATv2) Integration                  | 91  |
| 5.2.3. Data Augmentation Phase                                      | 91  |
| 5.2.4. Symbolic Regression and Mathematical Modelling               | 92  |
| 5.2.5. Input and Output Data  | 92  |
| 5.3. Trends and Equations Identified by the Framework               | 93  |
| 5.3.1. Equivalent Plastic Strain                                    | 93  |
| 5.3.2. Compression Ratio  | 97  |
| 5.3.3. Other Output Data  | 100 |
| 5.3.4. Numerical Verification                                       | 101 |
| 5.4. Critique and Concluding Remarks                                | 103 |
| 6. Impact Experiments   | 104 |
| 6.1. Overview   | 104 |
| 6.2. Impact of Elastic Balls  | 105 |
| 6.2.1. Methodology  | 105 |
| 6.2.2. Comparison between Simulation and Experimental Results       | 106 |
| 6.3. Impact of Metal Particles in the Single Particle Impact Tester | 109 |
| 6.3.1. Empirical Correlation for Impact Velocity in the Device      | 110 |
| 6.3.2. Impact of Metal Particles                                    | 118 |



| 6.4. Impact of Copper Particles in an Aerosol Deposition Rig            | 132 |
|---|-----|
| 6.4.1. Methodology  | 133 |
| 6.4.2. Compression Ratio  | 137 |
| 6.5. Concluding Remarks   | 139 |
| 7. Conclusions and Recommendations for Future Work                      | 140 |
| References  | 144 |
| Appendix A  | 159 |
| Sensitivity Analysis: Effect of Material Points and Mesh Discretisation | 159 |
| Sensitivity Analysis: Effect of Time Step                               | 161 |
| Appendix B  | 162 |
| Impact Deformation: Simulation Success of Case Studies                  | 162 |
| Impact Deformation: $\varepsilon_p$ as a function of $E/Y$              | 165 |
| Impact Deformation: $e$ as a function of $V_i/V_y$                      | 167 |
| Appendix C  | 169 |
| Particle Impact Velocity in the Single Particle Impact Tester           | 169 |
| Finding $C_1$ , $C_2$ , $C_3$ and $C_4$ for Equation (6-1)              | 171 |
| Comparison between the Experimental and Predicted values of $N_v^{1/3}$ | 175 |
| The Measured/Estimated Impact Velocity for the Metal Particles          | 177 |



## **List of Figures**

| Figure 1-1 Workflow of the thesis.  | 5  |
|---|----|
| Figure 2-1 Deposition efficiency versus particle velocity during impact, marking        |    |
| the so-called "deposition window" for aerosol deposition (AD) of                        |    |
| ceramics (area A) and CS of ductile metals (area C). No deposition takes                |    |
| place for velocities below the critical velocity (area N). CS of brittle                |    |
| materials and high particle velocities in both CS and AD lead to erosion                |    |
| of the substrate (area E). Modified by Hanft et al. [1] from Schmidt et                 |    |
| al. [35]  | 7  |
| Figure 2-2 Schematic illustration of metallic bonding formation during CS due           |    |
| to the plastic deformation of the metallic surfaces and the resultant                   |    |
| contact of fresh metallic surfaces. $\varepsilon$ denotes the interfacial strain. Taken |    |
| from [2]  | 9  |
| Figure 2-3 Discretisation in two different MPM formulations: (a) ULMPM,                 |    |
| where the space that the body occupies and will occupy is covered by                    |    |
| the background mesh and (b) TLMPM, where the background mesh                            |    |
| only discretises the space occupied by the body in the reference                        |    |
| configuration.  | 22 |
| Figure 2-4 Illustration of a typical explicit TLMPM computational cycle,                |    |
| Modified from [144]   | 23 |
| Figure 2-5 Taylor impact test for an OFHC copper projectile: (a) schematic              |    |
| drawing of the projectile's geometry before and after impact [143], and                 |    |
| (b) Initial and final configurations of the material points in TLMPM                    |    |
| simulations of de Vaucorbeil et al. [8]   | 25 |

| Figure 2-6 CS of a copper particle on a copper substrate simulated by Liu and                              |    |
|--|----|
| Xu [118]: comparison between (a) the ULMPM results and the   |    |
| experimental results of Li et al. [155] for oblique impact, and (b) the                                    |    |
| FEM and ULMPM results for normal impact. Taken from [118]  | 29 |
| Figure 3-1 Contact between two bodies $\alpha$ and $\beta$ : (a) normal unit vector $n_{pq}^{\alpha\beta}$ |    |
| oriented from material point $q$ in body $\beta$ to material point $p$ in body $\alpha$                    |    |
| and (b) making the unit vector $n_{pq}^{\alpha\beta}$ normal to the contact surface using                  |    |
| the positions of the boundary neighbouring points. Modified from   |    |
| [145]  | 38 |
| Figure 3-2 Contact conditions: (a) velocity-Signorini complementarity condition                            |    |
| illustrated by a graph relating the normal contact force, $f_n$ , to the relative                          |    |
| normal velocity, $v_n$ , and (b) Coulomb law of friction illustrated as a                                  |    |
| graph relating the tangential force, $f_t$ , to the relative tangential velocity,                          |    |
| $v_t$ , where $\mu_s$ is the friction coefficient. The dashed lines represent the                          |    |
| linear relationships extracted from the equations of motion. Modified                                      |    |
| from [145]   | 39 |
| Figure 3-3 Flowchart describing the explicit TLMPM and contact algorithms                                  | 41 |
| Figure 3-4 Visualisation of the modelled sphere for the sensitivity analysis,                              |    |
| detailing the initial and boundary conditions (illustration is not to scale                                |    |
| for presentation purposes). Created using ParaView version 5.11.0-RC1                                      |    |
| [174]  | 45 |
| Figure 3-5 Selecting the discretisation settings of each case study for the                                |    |
| sensitivity analysis based on the number of the material points per  |    |
| element (MP) and element size (ES) of the benchmark case, MP/ES  | 46 |
|  |    |

| Figure 3-6 Variation of the contact force and displacement with time for the                                    |    |
|---|----|
| impact of an elastic sphere undergoing small deformation (refer to  |    |
| Section 3.5.1), calculated using Johnson's [27] analytical approach   |    |
| (dashed lines) and MPM simulations (discrete symbols) considering a   |    |
| time step of 100 ns for (a) cases MP/ES, 2MP/ES and 4MP/ES, to  |    |
| highlight the effect of increasing the number of material points per  |    |
| element, and (b) cases MP/ES, MP/2ES and MP/4ES, to highlight the   |    |
| effect of increasing the element size, for the sensitivity analysis   | 51 |
| Figure 3-7 Variation of the contact force and displacement with time for the                                    |    |
| impact of an elastic sphere undergoing small deformation (refer to  |    |
| Section 3.5.1), calculated using Johnson's [27] analytical approach   |    |
| (dashed lines) and MPM simulations (discrete symbols) considering   |    |
| time steps of 1, 10 and 100 ns for (a) case MP/ES, (b) case 2MP/ES and  |    |
| (c) case 4MP/ES of the sensitivity analysis   | 53 |
| Figure 4-1 Visualisation of the modelled elastic-perfectly plastic particle                                     |    |
| impacting a rigid wall, detailing the initial and boundary conditions   |    |
| (illustration is not to scale for presentation purposes)  | 58 |
| Figure 4-2 Visualisation of the modelled particle after rebound for different                                   |    |
| cases: (a) $\rho$ =8,000 kg/m <sup>3</sup> , $E$ =100 GPa, $E/Y$ =160; (b) $\rho$ =8,000 kg/m <sup>3</sup> ,    |    |
| <i>E</i> =1 GPa, <i>E/Y</i> =40; (c) $\rho$ =2,000 kg/m <sup>3</sup> , <i>E</i> =1 GPa, <i>E/Y</i> =320 and (d) |    |
| $\rho$ =8,000 kg/m <sup>3</sup> , $E$ =1 GPa, $E/Y$ =160. The orientation is chosen randomly                    |    |
| to provide the best view of the extent of deformation   | 60 |
| Figure 4-3 The equivalent plastic strain, $\varepsilon_p$ , as a function of the ratio of Young's               |    |
| modulus to yield strength, $E/Y$ , for all the cases with an impact velocity                                    |    |
| of 50 m/s. For designation of the symbols, see Table 4-2  | 63 |



| Figure 4-4 The equivalent plastic strain, $\varepsilon_p$ , as a function of the dimensionless     |    |
|--|----|
| group $\rho V_i^2/Y$ , for all the case studies  | 65 |
| Figure 4-5 Contours of plastic strain in the impact direction $(\varepsilon^p_{zz})$ shortly after |    |
| rebound for case $\rho$ =2,000 kg/m <sup>3</sup> , $E$ =1 GPa and $E/Y$ =320, with the             |    |
| impact velocity of (a) 10, (b) 20, (c) 30, (d) 40 and (e) 50 m/s. The                              |    |
| contours are displayed on a plane slicing the particle in half (normal of                          |    |
| the plane is along the x axis)   | 66 |
| Figure 4-6 The deformation extent of the particle reflected by: (a) the normalised                 |    |
| deformed height, $H_d/D$ , and (b) the compression ratio, 1- $(H_d/D)$ , as a                      |    |
| function of $\rho V_i^2/Y$ , for all the cases   | 68 |
| Figure 4-7 The link between the equivalent plastic strain, $\varepsilon_p$ , and the compression   |    |
| ratio, 1- $(H_d/D)$  | 69 |
| Figure 4-8 The ratio of the plastic work to the incident kinetic energy, $W_p/W_i$ , as            |    |
| a function of the dimensionless group $\rho V_i^2/Y$   | 71 |
| Figure 4-9 The coefficient of restitution, $e$ , as a function of $V_i/V_y$ , for all the cases    |    |
| with an impact velocity of 50 m/s. For designation of the symbols, see                             |    |
| Table 4-3. Note that the data points in each data set correspond to                                |    |
| different densities  | 72 |
| Figure 4-10 The coefficient of restitution, $e$ , as a function of the dimensionless               |    |
| group $(V_i/V_y)/(E^*/Y)$ . The dashed line is the model of Wu et al. [110],                       |    |
| shown by Equation (4-8).   | 75 |
| Figure 4-11 The coefficient of restitution, $e$ , as a function of the dimensionless               |    |
| group $2.85(E/Y)^{-0.325} \exp[-2(\rho V_i^2/Y)^{0.325}]$  | 76 |
| Figure 4-12 The contact force-displacement relationship for all the cases with                     |    |
| $\rho$ =8,000 kg/m <sup>3</sup> , $E$ =100 GPa and $E/Y$ =80 at different impact velocities        | 78 |

| Figure 4-13 Change in: (a) the normalised maximum displacement, $\delta^*/R$ , and (b)           |     |
|--|-----|
| the normalised residual displacement, $\delta_{res}/R$ , as a function of $V_i/V_y$              | 81  |
| Figure 4-14 Change in: (a) the normalised maximum displacement, $\delta^*/R$ , and (b)           |     |
| the normalised residual displacement, $\delta_{res}/R$ , as a function of $\rho V_i^2/Y$         | 83  |
| Figure 4-15 The normalised maximum contact force, $F^*/F_y$ , as a function of $V_i$             |     |
| /V <sub>y</sub>  | 84  |
| Figure 4-16 The maximum contact force, $F^*$ , as a function of $\pi R^2 (Y \rho V_i^2)^{0.5}$   | 85  |
| Figure 4-17 The simulation results of the maximum contact force, $F^*$ , for cases               |     |
| shown in Table 4-5 using particle sizes of 100, 250, 750 and 1,000 $\mu m$ ,                     |     |
| as a function of (a) group $2\pi R^2 (Y\rho V_i^2)^{0.5}$ and (b) group $(Y\rho V_i^2)^{0.5}$ in |     |
| comparison with the values estimated by Equation (4-13)  | 87  |
| Figure 5-1 Flowchart of the implemented hybrid AI framework.                                     | 91  |
| Figure 5-2 The RFE and correlation scores of all the input variables for the                     |     |
| prediction of the equivalent plastic strain, $\varepsilon_p$ .                                   | 95  |
| Figure 5-3 The equivalent plastic strain, $\varepsilon_p$ , obtained from the MPM simulations:   |     |
| (a) as a function of Equation (5-4), identified by the AI framework, and                         |     |
| (b) in comparison with the values predicted by Equation (5-4) for all the                        |     |
| data points  | 97  |
| Figure 5-4 The RFE and correlation scores of all the input variables for the                     |     |
| prediction of the compression ratio, 1- $(H_d/D)$ .  | 98  |
| Figure 5-5 The compression ratio, $1-(H_d/D)$ , obtained from the MPM                            |     |
| simulations: (a) as a function of Equation (5-5), identified by the AI                           |     |
| framework, and (b) in comparison with the values predicted by                                    |     |
| Equation (5-5) for all the data points.  | 100 |

| Figure 5-6 1- $e^2$ , as a function of $W_p/W_i$ , both representing the ratio of the plastic |     |
|---|-----|
| work to the incident kinetic energy.  | 102 |
| Figure 6-1 The instant of maximum deformation upon impact for (a) Ball 1, (b)                 |     |
| Ball 2, and (c) Ball 3, captured from high-speed images of the balls, as                      |     |
| well as the visualisations of the simulated balls, including the overall                      |     |
| view and the corresponding contours of von Mises stress. The contours                         |     |
| are on the surface of a plane slicing the particle in half (normal of the                     |     |
| plane is along the x axis)  | 109 |
| Figure 6-2 Schematic drawing of the single particle impact tester device.                     | 111 |
| Figure 6-3 One frame of the high-speed images taken from a 1,000 $\mu m$ HDPE                 |     |
| particle during free fall through the single particle impact tester                           |     |
| acceleration tube (frame rate of 10 <sup>4</sup> fps)   | 114 |
| Figure 6-4 The experimental values of the dimensionless impact velocity, $N_{\nu,e}^{1/3}$ ,  |     |
| as a function of those predicted by Equation (6-6), $N_{v,p}^{1/3}$ , for all the             |     |
| sample particles.   | 119 |
| Figure 6-5 SEM images of the (a) 760, 500 and 350 $\mu m$ solder balls, (b) copper            |     |
| particles and (c) aluminium alloy particles, used in the impact tests                         |     |
| conducted in the single particle impact tester  | 121 |
| Figure 6-6 One frame of the high-speed images taken from a 760 $\mu m$ solder ball            |     |
| subjected to impact in the single particle impact tester at a 10 kPa                          |     |
| vacuum gauge pressure (frame rate of 2×10 <sup>4</sup> fps)                                   | 123 |
| Figure 6-7 The experimental values of the dimensionless impact velocity, $N_{v,e}^{1/3}$ ,    |     |
| as a function of those predicted by Equation (6-7), $N_{\nu,p}^{1/3}$ , for the solder        |     |
| balls and the particles originally used in developing the empirical                           |     |
| correlation.  | 124 |



| Figure 6-8 Examples of the SEM images used for determining the compression                     |     |
|--|-----|
| ratio, with the deformed area presented for viewing by the microscope:                         |     |
| (a) solder ball, (b) copper particle and (c) aluminium alloy particle                          | 125 |
| Figure 6-9 schematic diagram of the geometrical approach taken to estimate the                 |     |
| height of the deformed particle, $H_d$ , using the measured values of the                      |     |
| particle diameter, $D$ , and the diameter of the deformed area, $d_d$                          | 126 |
| Figure 6-10 The compression ratio, 1- $(H_d/D)$ , as a function of $\rho(V_i^2-V_y^2)/Y$ , for |     |
| (a) different sizes of the solder balls (SAC305), (b) aluminium alloy                          |     |
| particles (AA6061), and (c) copper particles (Cu), considering different                       |     |
| yield strengths shown in Table 6-10.   | 128 |
| Figure 6-11 The compression ratio, 1- $(H_d/D)$ , as a function of $\rho(V_i^2-V_y^2)/Y$ , for |     |
| the solder balls (SAC305), aluminium alloy particles (AA6061), and                             |     |
| copper particles (Cu) considering a yield strength of 162 MPa                                  | 130 |
| Figure 6-12 The measured values of the coefficient of restitution (e) for the                  |     |
| solder balls, in comparison with those predicted by the empirical                              |     |
| Equation (4-8) of Wu et al. [110], Equation (4-9), and the analytical                          |     |
| equations of Johnson [27] and Thornton [28], as a function of the ratio                        |     |
| of the measured impact velocity to the yield velocity $(V_i/V_y)$                              | 132 |
| Figure 6-13 Schematic drawing of the AD rig  | 135 |
| Figure 6-14 Impact tests in the AD rig: (a) SEM image of the feed copper                       |     |
| particles and (b) a cut section of the substrate where the particles are                       |     |
| deposited  | 136 |
| Figure 6-15 SEM images of (a) the top view of the copper particles deposited on                |     |
| the substrate (b) particle-free surface of the substrate (c) an example                        |     |

| of the particles analysed (the view is slightly tilted) and (d) cross-section          |      |
|--|------|
| of the same particle cut in half using an electron beam                                | .137 |
| Figure 6-16 Particle impact velocity in the AD rig as a function of particle size,     |      |
| determined by Dr Fanchao Meng (The University of Manchester, UK)                       |      |
| using his semi-analytical surrogate model [208], modified for the nozzle               |      |
| used in the current AD rig.  | .138 |
| Figure 6-17 Schematic drawing of the regions of the particle affected by thermal       |      |
| softening and work hardening during high strain rate impact.                           | .140 |
| Figure A-1 Variation of the contact force and displacement with time for the impact of |      |
| an elastic sphere undergoing small deformation, calculated using Johnson's [25]        |      |
| analytical approach (dashed lines) and MPM simulations (discrete symbols)              |      |
| considering a time step of 10 ns for (a) cases MP/ES, 2MP/ES and 4MP/ES, to            |      |
| highlight the effect of increasing the number of material points per element, and      |      |
| (b) cases MP/ES, MP/2ES and MP/4ES, to highlight the effect of increasing the          |      |
| element size.  | .149 |
| Figure A-2 Variation of the contact force and displacement with time for the impact of |      |
| an elastic sphere undergoing small deformation, calculated using Johnson's [25]        |      |
| analytical approach (dashed lines) and MPM simulations (discrete symbols)              |      |
| considering a time step of 1 ns for (a) cases MP/ES, 2MP/ES and 4MP/ES, to             |      |
| highlight the effect of increasing the number of material points per element, and      |      |
| (b) cases MP/ES, MP/2ES and MP/4ES, to highlight the effect of increasing the          |      |
| element size.  | .150 |
| Figure A-3 Variation of the contact force and displacement with time for the impact of |      |
| an elastic sphere undergoing small deformation, calculated using Johnson's [25]        |      |
| analytical approach (dashed lines) and MPM simulations (discrete symbols)              |      |



| considering time steps of 1, 10 and 100 ns for (a) case MP/2ES and (b) case                               |      |
|---|------|
| MP/4ES of the sensitivity analysis.   | .151 |
| Figure B-1 The equivalent plastic strain, $\varepsilon_p$ , as a function of the ratio of Young's modulus |      |
| to yield strength, $E/Y$ , for all the cases with an impact velocity of 10 m/s. For                       |      |
| designation of the symbols, see Table 4-2.  | .155 |
| Figure B-2 The equivalent plastic strain, $\varepsilon_p$ , as a function of the ratio of Young's modulus |      |
| to yield strength, $E/Y$ , for all the cases with an impact velocity of 20 m/s. For                       |      |
| designation of the symbols, see Table 4-2   | .155 |
| Figure B-3 The equivalent plastic strain, $\varepsilon_p$ , as a function of the ratio of Young's modulus |      |
| to yield strength, $E/Y$ , for all the cases with an impact velocity of 30 m/s. For                       |      |
| designation of the symbols, see Table 4-2.  | .156 |
| Figure B-4 The equivalent plastic strain, $\varepsilon_p$ , as a function of the ratio of Young's modulus |      |
| to yield strength, $E/Y$ , for all the cases with an impact velocity of 40 m/s. For                       |      |
| designation of the symbols, see Table 4-2.  | .156 |
| Figure B-5 The coefficient of restitution, $e$ , as a function of $V_i/V_y$ , for all the cases with      |      |
| an impact velocity of 10 m/s. For designation of the symbols, see Table 4-3.                              |      |
| Note that the data points in each data set correspond to different densities                              | .157 |
| Figure B-6 The coefficient of restitution, $e$ , as a function of $V_i/V_y$ , for all the cases with      |      |
| an impact velocity of 20 m/s. For designation of the symbols, see Table 4-3.                              |      |
| Note that the data points in each data set correspond to different densities                              | .157 |
| Figure B-7 The coefficient of restitution, $e$ , as a function of $V_i/V_y$ , for all the cases with      |      |
| an impact velocity of 30 m/s. For designation of the symbols, see Table 4-3.                              |      |
| Note that the data points in each data set correspond to different densities                              | .158 |

| Figure B-8 The coefficient of restitution, $e$ , as a function of $V_i/V_y$ , for all the cases with              |
|---|
| an impact velocity of 40 m/s. For designation of the symbols, see Table 4-3.                                      |
| Note that the data points in each data set correspond to different densities158                                   |
| Figure C-1 The impact velocity, $V_i$ , measured using high-speed imaging for different                           |
| sizes of (a) HDPE, (b) PP Homo, (c) PP RaCo particles and (d) 1000 μm glass                                       |
| beads, as a function of the vacuum gauge pressure, $P_{gauge}$ , in the single particle                           |
| impact tester   |
| Figure C-2 The experimental value of the dimensionless velocity, $N_v^{1/3}$ , as a function of                   |
| $P_{gauge}/\rho_{air}gh$ for (a) HDPE, (b) PP Homo, (c) PP RaCo particles for different                           |
| particle sizes and (d) glass beads for 1000 µm particles. The arithmetic mean                                     |
| value for the power indices of all the fitted lines is taken as the power index $C_2$                             |
| of Equation (6-1)162  |
| Figure C-3 Plot of $N_v^{1/3}/(P_{gauge}/\rho_{air}gh)^{0.464}$ as a function of $N_d^{1/3}$ for (a) HDPE, (b) PP |
| Homo and (c) PP RaCo particles at different vacuum gauge pressures. The   |
| arithmetic mean of the absolute value for the power of all the fitted lines is taken                              |
| as the power index $C_4$ of Equation (6-1). Glass beads are not included in this                                  |
| analysis as the corresponding data are only available for one particle size164                                    |
| Figure C-4 Plot of $C_i$ as a function of (S-1) for all the sample materials. The slope and                       |
| absolute value of the power of the fitted line are taken as the empirical constant                                |
| $C_1$ and power index $C_3$ of Equation (6-1), respectively   |
| Figure C-5 Comparison between the experimental (solid symbols) and predicted (hollow                              |
| symbols) values of the dimensionless impact velocity, $N_{\nu}^{1/3}$ , at different vacuum                       |
| gauge pressures for (a) HDPE, (b) PP Homo and (c) PP RaCo particles166  |



| Figure   | C-6 Comparison between the experimental and predicted values of the                  |
|----------|--|
|          | dimensionless impact velocity, $N_v^{1/3}$ , at different vacuum gauge pressures for |
|          | 1000 μm glass beads  |
| Figure ( | C-7 The impact velocity, $V_i$ , measured using high-speed imaging for different     |
|          | sizes of the solder balls (SAC305), and estimated using Equation (6-7) for           |
|          | copper (Cu) and aluminium alloy (AA6061) particles, as a function of the             |
|          | vacuum gauge pressure, $P_{gauge}$ , in the single particle impact tester            |



## **List of Tables**

| Table 2-1 Influence of process parameters on CS coating properties. NCV denotes "no                     |     |
|---|-----|
| common view", ↑ denotes increase, and ↓ denotes decrease. DS and DE denote                              |     |
| "deposition strength" and "deposition efficiency", respectively. Taken from                             |     |
| [50]  | .11 |
| Table 2-2 Taylor impact test for an OFHC copper projectile: the diameter ( $D^{\text{Taylor}}$ ), bulge |     |
| (W), and length $(L)$ of the projectile after impact, as measured experimentally                        |     |
| [149,150] and predicted by TLMPM [8] and ULMPM [142]. Note that the                                     |     |
| impact velocity in all the cases is 190 m/s, and the initial values for the diameter,                   |     |
| bulge and length before impact are 7.6, 7.6, and 25.4 mm, respectively.                                 | 26  |
| Table 3-1 Discretisation settings for the cases used in the sensitivity analysis                        | 47  |
| Table 3-2 Calculation of the critical time step for the sensitivity analysis: values of                 |     |
| $ES/(c_{dil}+ V_i )$ for the cases discussed in Section 3.5.2.  | .49 |
| Table 3-3 Mean absolute error (MAE) and mean squared error (MSE) values for $F/F^*$                     |     |
| and $\delta/\delta^*$ corresponding to cases MP/ES and 2MP/ES, in reference to case                     |     |
| 4MP/ES  | 50  |
| Table 3-4 Computational time required for generation of one output file for all of the case             |     |
| studies in the sensitivity analysis.  | 54  |
| Table 4-1 Various materials that exhibit both elastic and plastic properties, taken from                |     |
| [180]. NA denotes "not applicable"  | 60  |
| Table 4-2 Symbol reference for Figure 4-3, and Figures B-1 to B-4 of Appendix B                         | 62  |
| Table 4-3 Symbol reference for Figure 4-9, and Figures B-5 to B-8 of Appendix B                         | 72  |
| Table 4-4 The maximum contact force, $F^*$ , obtained from the MPM simulations for cases                |     |
| with $\rho$ =8,000 kg/m <sup>3</sup> , $E$ =100 GPa and $E/Y$ =80 at all the impact velocities (Figure  |     |



| 4-12), compared to the values predicted by the KE [/0] and JG [6/] contact                                     |      |
|--|------|
| models, using the MPM displacement values  | 79   |
| Table 4-5 The material properties and impact velocities of the cases for which additional                      |      |
| simulations are carried out using particle sizes of 100, 250, 750 and 1,000 $\mu m,$                           |      |
| to examine the validity of Equation (4-13)   | 86   |
| Table 5-1 MAE, MSE and R <sup>2</sup> values for the equivalent plastic strain, $\varepsilon_p$ , predicted by |      |
| Equation (5-4), with respect to the MPM data.  | 96   |
| Table 5-2 MAE, MSE and $R^2$ values for the compression ratio, 1- $(H_d/D)$ , predicted by                     |      |
| Equation (5-5), with respect to the MPM data.  | 99   |
| Table 5-3 Material properties of lead (Pb) and nickel (Ni) used in the MPM simulations                         |      |
| for the verification of Equations (5-4) and (5-5). Taken from [180]  | .103 |
| Table 5-4 The equivalent plastic strain, $\varepsilon_p$ , for lead and nickel particles, as obtained from     |      |
| the MPM simulations, in comparison with the predictions of Equation (5-4)                                      |      |
| identified by the AI framework.  | .103 |
| Table 5-5 The compression ratio, $1-(H_d/D)$ , for lead and nickel particles, as obtained                      |      |
| from the MPM simulations, in comparison with the predictions of Equation                                       |      |
| (5-5) identified by the AI framework.  | .104 |
| Table 6-1 Material properties and impact velocity of the balls used in the elastic impact                      |      |
| experiments  | .107 |
| Table 6-2 Comparison between the experimental and simulation values of the total                               |      |
| contact time, $t_{tot}$ , for the impact of elastic balls.   | .109 |
| Table 6-3 Comparison between the experimental and simulation values of the ratio of the                        |      |
| particle height to the original particle diameter at the instant of maximum                                    |      |
| deformation, $H_e/D$ , for the impact of elastic balls.  | .110 |



| Table 6-4 Comparison between the experimental and simulation values of the coefficient                    |     |
|---|-----|
| of restitution, e, for the impact of elastic balls.   | 110 |
| Table 6-5 The measured density of the sample particles used in developing an empirical                    |     |
| correlation for predicting the particle impact velocity in the single particle                            |     |
| impact tester.  | 112 |
| Table 6-6 Initial values determined for the empirical constant and power indices of                       |     |
| Equation (6-1), developed for predicting the particle impact velocity in the                              |     |
| single particle impact tester.  | 116 |
| Table 6-7 The coefficient of determination (R <sup>2</sup> ) for $N_v^{1/3}$ values predicted by Equation |     |
| (6-1) using the initial $C_1$ , $C_2$ , $C_3$ and $C_4$ values (Table 6-6), with respect to the           |     |
| experimental values calculated by Equation (6-2) using the measured impact                                |     |
| velocities  | 117 |
| Table 6-8 Modified values determined for the empirical constant and power indices of                      |     |
| Equation (6-1), developed for predicting the particle impact velocity in the                              |     |
| single particle impact tester.  | 117 |
| Table 6-9 The coefficient of determination (R <sup>2</sup> ) for $N_v^{1/3}$ values predicted by Equation |     |
| (6-1) using the modified $C_1$ , $C_2$ , $C_3$ and $C_4$ values (Table 6-8), with respect to              |     |
| the experimental values calculated by Equation (6-2) using the measured impact                            |     |
| velocities  | 118 |
| Table 6-10 Material properties of the copper particles (Cu), solder balls (SAC305), and                   |     |
| aluminium alloy particles (AA6061) used for the impact experiments in the                                 |     |
| single particle impact tester.  | 122 |
| Table 6-11 The analytical equations developed by Johnson [27] and Thornton [28] for                       |     |
| predicting the coefficient of restitution, <i>e</i>   | 131 |



| Table 6-12 The measured values of the compression ratio, $1-(H_d/D)$ , and those predicted |     |
|--|-----|
| by Equation (5-5) using the yield strength values of 270 and 446.6 MPa                     | 139 |
| Table B-1 Case studies for the impact of an elastic-perfectly plastic particle at 10 m/s,  |     |
| colour coded based on the simulation success: red signifies the cases for which            |     |
| no result is obtained, green represents the cases for which the simulation is              |     |
| successful and orange denotes the cases that do not undergo plastic deformation            |     |
| and therefore are dismissed from further analysis.   | 152 |
| Table B-2 Case studies for the impact of an elastic-perfectly plastic particle at 20 m/s,  |     |
| colour coded based on the simulation success: red signifies the cases for which            |     |
| no result is obtained, green represents the cases for which the simulation is              |     |
| successful and orange denotes the cases that do not undergo plastic deformation            |     |
| and therefore are dismissed from further analysis.   | 152 |
| Table B-3 Case studies for the impact of an elastic-perfectly plastic particle at 30 m/s,  |     |
| colour coded based on the simulation success: red signifies the cases for which            |     |
| no result is obtained, and green represents the cases for which the simulation is          |     |
| successful   | 153 |
| Table B-4 Case studies for the impact of an elastic-perfectly plastic particle at 40 m/s,  |     |
| colour coded based on the simulation success: red signifies the cases for which            |     |
| no result is obtained, and green represents the cases for which the simulation is          |     |
| successful   | 153 |
| Table B-5 Case studies for the impact of an elastic-perfectly plastic particle at 50 m/s,  |     |
| colour coded based on the simulation success: red signifies the cases for which            |     |
| no result is obtained, and green represents the cases for which the simulation is          |     |
| successful   | 154 |



#### Nomenclature

#### **Acronyms and Abbreviations**

AA6061 Aluminium Alloy 6061

AD Aerosol Deposition

Ag Silver

AI Artificial Intelligence

ASI Adiabatic Shear Instability

CD Contact Dynamics

CFD Computational Fluid Dynamics

CS Cold Spraying

Cu Copper

DA Dimensional Analysis

DEM Discrete Element Method

DE Deposition Efficiency

DNN Deep Neural Networks

DS Deposition Strength

EOS Equation of State

FEA Finite Element Analysis

FEM Finite Element Method

FST Fragment Selection Technique

GA Genetic Algorithms

GAT Graph Attention Networks

GCN Graph Convolutional Networks

HDPE High Density Polyethylene

HPO Hyperparameter Optimisation

JC Johnson-Cook

JG Jackson and Green

KE Kogut and Etsion

MAE Mean Absolute Error



MD Molecular Dynamics

ML Machine Learning

MPM Material Point Method

MPFEM Material Point Finite Element Method

MSE Mean Squared Error

MTS Mechanical Threshold Stress

MW Ma-Wang

Ni Nickel

Pb Lead

PINN Physics-Informed Neural Networks

PP Homo Polypropylene Homopolymer

PP RaCo Polypropylene Random Copolymer

PTW Preston-Tonks-Wallace

R<sup>2</sup> Coefficient of Determination

RFE Recursive Feature Elimination

SAC305 Solder Alloy of 96.5% Sn, 3% Ag and 0.5% Cu

SEM Scanning Electron Microscope

SR Symbolic Regression

TLMPM Total Lagrangian Material Point Method

ULMPM Updated Lagrangian Material Point Method

ZA Zerilli-Armstrong

#### **Latin Symbols**

a acceleration

*a<sub>i</sub>* nodal acceleration

a<sup>t</sup> time step multiplier

b body force

A, B material-dependent constants of JC model

c maximum wave speed

 $c_{dil}$  dilatational wave speed

 $c_m$  speed of sound in the material (Mie-Grüneisen EOS)



C, M, N material-dependent constants of JC model

 $C_1$ ,  $C_2$ ,  $C_3$ ,  $C_4$  constants in equation for  $N_V$ 

 $C_i$  dimensionless group used in developing equation for  $N_v$ 

D particle diameter

 $D_1, D_2, D_3, D_4, D_5$  material-dependent constants of JC failure model

 $d_d$  diameter of the deformed area after impact

 $D_{JC}$  damage in JC failure model

 $D^{\text{Taylor}}$  diameter of projectile in Taylor impact test

e coefficient of restitution

E Young's modulus

 $E_m$  internal energy per initial volume (Mie-Grüneisen EOS)

E\* effective Young's modulus

ES element size

 $\hat{f}$  prescribed load

 $f_i^C$  nodal contact forces

 $f_i^{C, \alpha}$  nodal contact forces corresponding to node i of body  $\alpha$ 

 $f_i^{C,\beta}$  nodal contact forces corresponding to node j of body  $\beta$ 

 $f_i^{int}$  internal force vector

 $f_i^{ext}$  external force vector

*f*<sub>i</sub><sup>S</sup> surface tractions

 $f_n$  normal contact force

 $f_{pq}^{C, \alpha\beta}$  contact force between point p in body  $\alpha$  and point q in body  $\beta$ 

 $\sum_{\alpha} f_{\alpha} C_{\alpha} \alpha \gamma$  contact forces of other bodies in contact with point p in body  $\alpha$ 

 $\sum_{\gamma} f_{ar}^{C, \beta \gamma}$  contact forces of other bodies in contact with point q in body  $\beta$ 

 $f_t$  tangential contact force

F contact force

 $F^*$  maximum contact force

 $F_{\nu}$  contact force at onset of yield

g gravitational acceleration

 $G_{ip}^{e}$  gradient of the shape function



h full length of the acceleration tube in in-house device

H hardness

 $H_d$  deformed particle height

 $H_e$  particle height at maximum elastic deformation

I identity matrix

 $k_n$  offset normal force

 $k_t$  offset tangential force

L length of projectile in Taylor impact test

m mass

 $m_p$  Mass of material point p

 $M_{ii}$  lumped mass matrix

n outward unit normal vector

 $n_d$  number of the data points

 $n_t$  number of time steps selected to generate an output file

 $n_{pq}^{\alpha\beta}$  normal unit vector from point q in body  $\beta$  to point p in body  $\alpha$ 

 $N_d$  dimensionless particle size

 $N_{ip}^{e}$  shape function matrix

 $N_p$  number of the material points

 $N_{\nu}$  dimensionless particle impact velocity in in-house device

 $N_{v,p}$ ,  $N_{v,e}$  predicted and experimental values of  $N_v$ 

p hydrostatic pressure (Mie-Grüneisen EOS)

 $p_0$  maximum contact pressure

 $p_{0y}$  maximum contact pressure at onset of yield

 $p_H$  pressure on the Hugoniot curve (Mie-Grüneisen EOS)

 $p_m$  mean contact pressure

 $\bar{p_y}$  contact yield stress defined by Thornton

*P*<sub>i</sub> nodal momentum

 $P_{gauge}$  vacuum gauge pressure

R radius

S Parameter in equation for  $N_{\nu}$ 



S<sub>H</sub> material parameter (Mie- Grüneisen EOS)

Sn tin

t time

 $t_{tot}$  total contact time

 $t_{pq}^{\alpha\beta}$  tangential unit vector from point q in body  $\beta$  to point p in body  $\alpha$ 

 $T_m$  melting temperature

 $T_{room}$  room temperature

U deformation gradient

*u* displacement

*û* prescribed displacement

*v<sub>air</sub>* kinematic viscosity of air

 $v_i$  nodal velocity

 $v_n$  relative normal velocity

 $v_p$  velocity of material point p

 $v_p^{\alpha}$  velocity vector for material point p in body  $\alpha$ 

 $v_q^{\beta}$  velocity vector for material point q in body  $\beta$ 

 $v_t$  relative tangential velocity

 $V_i$  impact velocity

 $V_{p0}$  material point volume in the initial configuration

 $V_r$  rebound velocity

 $V^s$  specific volume

 $V_{y}$  yield velocity

 $V_{\nu}^{T}$  yield velocity defined by Thornton

 $V^z$  particle velocity in the impact direction (z axis)

W bulge of projectile in Taylor impact test

 $W_i$  incident kinetic energy

 $W_p$  plastic work

x position in deformed configuration

X position in initial configuration

Y yield strength



#### **Greek Symbols**

 $\alpha, \beta$  deformable bodies in contact

 $\delta$  displacement of particle centre

 $\delta_{res}$  residual displacement

 $\delta^*$  maximum displacement of particle centre

 $\delta_y$  displacement of particle centre at onset of yield

 $\varepsilon_p$  equivalent plastic strain

 $\varepsilon^{p}_{ij}$  deviatoric plastic strain

 $\varepsilon_{r}^{f}$  failure strain in JC failure model

 $\dot{\varepsilon_p}^*$  normalised equivalent plastic strain rate

 $\varepsilon^p_{zz}$  plastic strain in the impact direction (z axis)

 $\eta$  Grüneisen parameter

 $\Gamma_0$  surface of body in initial configuration

λ first Lamé constant

μ shear modulus

 $\mu_{air}$  dynamic viscosity of air

v Poisson's ratio

 $\Omega_0$  domain in MPM

 $\partial\Omega_0$  external boundary of domain

 $\Omega_0^e$  domain occupied by the *e*th element of background mesh

 $\partial \Omega_0^{\rm f}$  Neumann boundaries

 $\partial \Omega_0^{\rm u}$  Dirichlet boundaries

 $\Pi$  first Piola-Kirchhoff stress tensor

 $\rho$  density

 $\rho_{air}$  air density

 $\rho_p$  particle density

φ parameter in Mie-Grüneisen EOS

 $\sigma$  flow stress

 $\bar{\sigma}$  von Mises effective stress

 $\sigma_m$  mean stress



 $\sigma^*$ 

stress triaxiality



#### 1. Introduction

#### 1.1. Motivation of the Present Work

The impact of particles with surfaces is of great interest in various technological applications, including particle dispersion, deposition, coating, and surface contamination, as well as in natural events such as hailstorms. In particular, the study of high-velocity particle impact is essential for techniques such as shot peening, sandblasting and abrasive waterjet cutting, as well as advanced coating techniques like cold spraying (CS) and aerosol deposition (AD). CS in particular has attracted significant attention within the past two decades, as it circumvents the common challenges associated with high-temperature coating processes like thermal spraying and sintering, e.g. high energy consumption, oxidation, adverse structural changes, uninvited chemical reactions and residual stresses [1,2]. In CS, preheated micronsized metal particles are accelerated to high velocities (200 to 1,500 m/s [3]) by a pressurised, preheated gas. The particle-laden gas passes through a converging-diverging nozzle and impinges the particles on a substrate. The particles plastically deform and adhere to the substrate as a result of the high-velocity impact. The subsequent impacts and deformation of the ensuing particles result in the build-up of a film on the substrate. Since the temperature of the carrier gas is always lower than the melting point of the particle material, the technique is considered a solid-state method [2].

Even though CS is a well-established technique, several aspects of the process remain poorly explored, most notably, the deformation behaviour of the impacting particles, which significantly influences the quality of the final coating. In fact, the majority of studies on CS focus on the effect of particle size and process parameters, often overlooking the role of particle mechanical properties and density, both of which strongly affect deformation. Moreover, experimental investigation of high-velocity impact processes such as CS is inherently



challenging due to the extremely short time scales and small particle sizes involved, making numerical simulations a more practical and insightful alternative for studying the underlying phenomena. However, the numerical methods commonly used for simulating particle impact, e.g. Discrete Element Method (DEM) [4], Finite Element Method (FEM) [5], and on occasion Molecular Dynamics (MD) [6], often encounter limitations when dealing with large deformation, which is characteristic of CS. A promising alternative is the Material Point Method (MPM) [7], which effectively accommodates large plastic deformation while avoiding the numerical instabilities associated with traditional approaches. Nevertheless, only a limited number of studies have applied MPM to impact problems (refer to Section 2.2.4), with the majority implementing the classical updated Lagrangian formulation of MPM (ULMPM) [7], which is prone to cell-crossing instabilities and high computational costs.

Considering the lack of studies regarding the influence of material properties on particle deformation behaviour during CS, the limitations of conventional numerical methods in handling large deformations, the scarce application of MPM to the problem of particle impact, and the prevalent reliance on the less stable ULMPM variant, the present work aims to address these gaps by employing the new, more stable total Lagrangian formulation of MPM (TLMPM) [8], to investigate the particle impact phenomena across a broad range of material properties.

In the simulation of high-velocity impact processes, a material model that accounts for strain rate and temperature effects is typically required for accurate predictions. However, due to the complexity of such models, material behaviour is often approximated by an elastic-perfectly plastic model for initial analysis in engineering practices [9]. An elastic-perfectly plastic material exhibits a linear elastic behaviour up to the point of yielding, after which its flow stress stays constant as the yield stress. As MPM is still an emerging approach, a study that applies the TLMPM formulation to impact problems, particularly with a focus on material properties, is missing from the literature. Therefore, the current work implements the more



straightforward elastic-perfectly plastic material model, as an initial step to assess the limitations and capabilities of MPM in modelling deformation within a dynamic impact framework, for a wide range of material properties. The insights gained from this study can serve as a foundation for future research, where more advanced constitutive models can be incorporated to further improve the predictive accuracy of MPM in simulating high-velocity impact processes for a broad range of materials.

#### 1.2. Aim, Objectives and Structure of the Thesis

The overall aim of this research work is to investigate the relationship between the deformation behaviour of elastic-perfectly plastic particles during high-velocity impact processes, and their mechanical properties, density and impact velocity. To achieve this, MPM simulations of particle impact are performed considering a wide range of material properties and impact velocities. The work comprises computational and experimental components, with the following key objectives:

- To establish the criteria for selecting the appropriate time step and discretisation settings in MPM simulations of impact;
- To characterise the impact deformation of elastic-perfectly plastic particles with different material properties and impact velocities using MPM simulations;
- To identify the relationship between particle deformation, material properties and impact velocity;
- To develop empirical equations that describe this relationship;
- To evaluate the potential of Artificial Intelligence (AI) in recognising and optimising these empirical equations;
- To validate the simulation results through experimental impact tests.



The structure of the thesis is as follows:

- Chapter 2 outlines the literature review on the deformation behaviour of a particle during impact and the numerical methods that have so far been employed to simulate particle impact.
- 2. Chapter 3 details the MPM approach that is employed in this work, followed by a sensitivity analysis to determine the criteria for selecting the optimal time step and discretisation settings for simulation of particle impact.
- 3. In Chapter 4, MPM simulations are performed to investigate the normal impact of an elastic-perfectly plastic particle with a rigid wall, covering a wide range of material properties and impact velocities. The plastic deformation and rebound behaviour of the particle, along with the evolution of contact force and displacement are studied. Consequently, empirical equations are suggested for prediction of the compression ratio and coefficient of restitution, as a function of the material properties and impact velocity.
- 4. Chapter 5 presents the processing of the MPM simulation results using a hybrid AI framework, proprietary of the Institute for Particle Technology (Technische Universität Braunschweig, Germany). This analysis evaluates the effectiveness of AI in identifying the trends within the MPM simulation data and refining the empirical equations proposed in Chapter 4.
- In Chapter 6, impact experiments are conducted to assess the accuracy of the MPM
  approach and the empirical equations in predicting the deformation behaviour
  during impact.
- 6. Chapter 7 presents a summary of the key findings of the thesis, concluding remarks and recommended future work.



A workflow summarising the thesis objectives and their corresponding chapters is displayed in Figure 1-1, below.

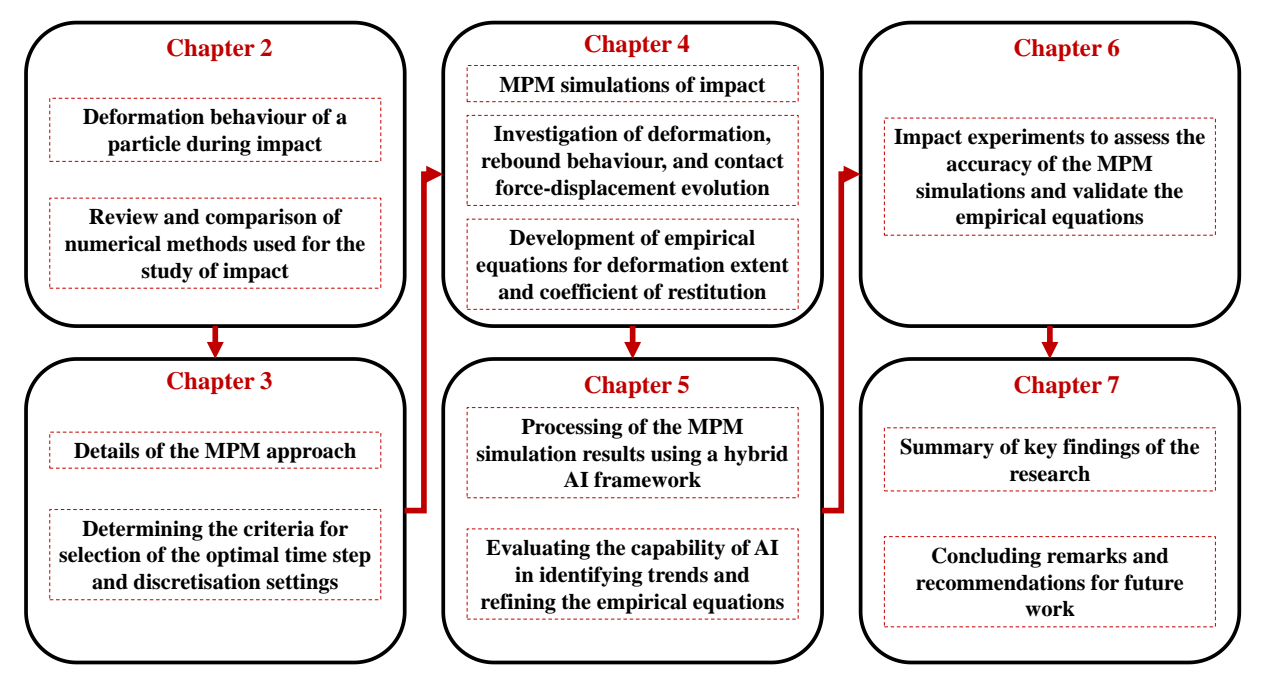


Figure 1-1 Workflow of the thesis.



## 2. Literature Review

# 2.1. Deformation Behaviour during Impact

During the impact of two deformable bodies at moderate velocities, a fraction of the initial kinetic energy of the impact is stored in the contacting bodies as recoverable elastic strain energy. The remaining fraction is primarily dissipated by propagation of elastic waves and, if the initial kinetic energy is sufficiently high to induce yielding, plastic deformation. While elastic wave propagation is inherent in any impact regardless of the impact velocity, it has been shown experimentally and analytically that energy losses due to this mechanism are typically less than 3-4% of the initial kinetic energy [10–13], given that the number of the stress wave propagation reflections within the contact duration are more than one [14]. However, for impacts involving yielding, plastic deformation becomes the dominant mechanism for energy dissipation [14]. Therefore, plastic deformation of impacting deformable bodies has conventionally been studied through investigating their rebound behaviour, experimentally [15–26] or analytically [27–34].

According to Johnson [27], an elastic-plastic material reaches the limits of elastic behaviour at a point beneath the surface, when the maximum contact pressure  $p_0$  reaches the value 1.6Y, where Y is the yield strength of the softer body, governed by von Mises's shear strain-energy criterion. When the yield point is first exceeded, the plastic region is small and fully contained by elastic material. As the load increases and the deformation becomes more severe, the plastic zone eventually breaks out to the free surface, and the displaced material is free to escape by plastic flow. Therefore, depending on the load, the deformation regime can be classified as fully elastic, elastic-plastic (contained) and fully plastic (uncontained) [27].

At higher velocities, the plastic deformation becomes extreme, and the impact response is heavily influenced by the mechanical properties of the impacting bodies. Moreover, the



dissipated energy results in localised temperature rise, which can alter the material properties [27]. This extreme deformation regime is characteristic of high-velocity impact processes like CS, where material deposition typically occurs through intense plastic deformation rather than melting. Given the relevance of this phenomenon, providing an account of the literature on the deposition mechanism in CS and the factors affecting the particle deformation behaviour seems appropriate.

## 2.1.1. Deposition Mechanism in Cold Spraying

CS is mainly utilised for the deposition of ductile metallic particles, and successful deposition is assumed to initiate when impact velocity surpasses a critical velocity [3,35,36]. Together with another critical velocity at which the particles erode the substrate, a so-called "deposition window" is presumed for successful deposition of metallic particles using CS, as displayed in Figure 2-1 [35,37].

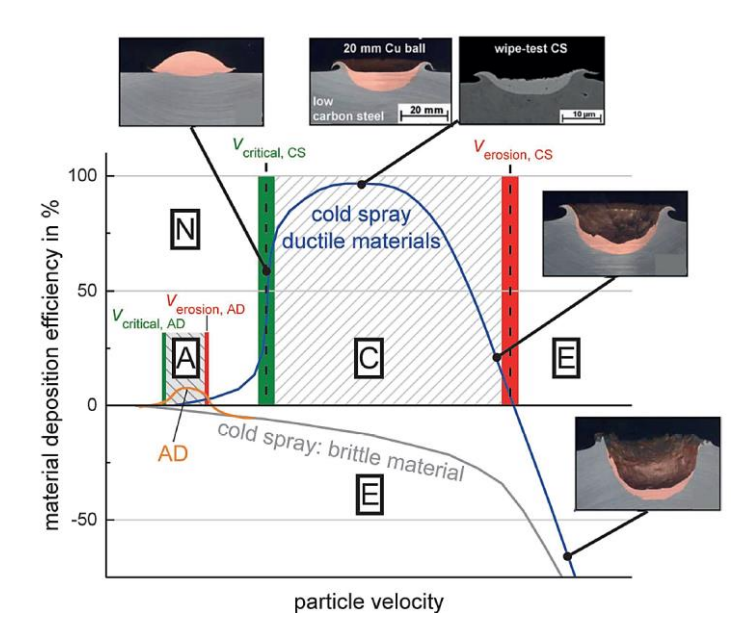


Figure 2-1 Deposition efficiency versus particle velocity during impact, marking the so-called "deposition window" for aerosol deposition (AD) of ceramics (area A) and CS of ductile metals (area C). No deposition takes place for velocities below the critical velocity (area N). CS of brittle materials and high particle velocities in both CS and AD lead to erosion of the substrate (area E). Modified by Hanft et al. [1] from Schmidt et al. [35].



Successful bonding at particle-substrate and particle-particle interfaces in CS has been explained through adiabatic shear instability (ASI) and severe shear plastic deformation [35,38]. The concept is as follows: kinetic energy of the impacting particle supplies the work required for viscoplastic deformation of the material. Simultaneously, a major fraction of the kinetic energy is converted to heat which can dissipate through conduction. However, at timescales as small as that of the CS process, and provided that the system dimension (particle diameter in this instance) is notably greater than the thermal diffusion distance (which is dependent on the thermal diffusivity and process time), the generated heat cannot be dissipated. Due to this adiabatic heating, thermal softening dominates over strain and strain-rate hardening and the particle experiences an overall strain softening. Strain softening leads to a sudden disturbance in the homogeneity of the ongoing plastic deformation and at a critical strain, this shear instability results in the localisation of strain and shear banding. Beyond the critical strain, the overall strain remains almost constant, while the local strain at the shear band rapidly increases to considerably high values. This substantial local strain at the contact point stretches and flattens the interfacial region significantly, leading to jetting. Consequently, the surface oxide layers, which prevent bonding between the surfaces at the solid state, are broken up. Thus, atomically-flat, clean surfaces of the particle and the substrate are brought into contact (see Figure 2-2). This intimate contact of the surfaces at atomic level is postulated to be the cause of bonding in CS [2]. Experimental and modelling results [38,39] suggest that ASI takes place at or beyond the critical velocity, and thus can be used as a criterion for bonding [40].



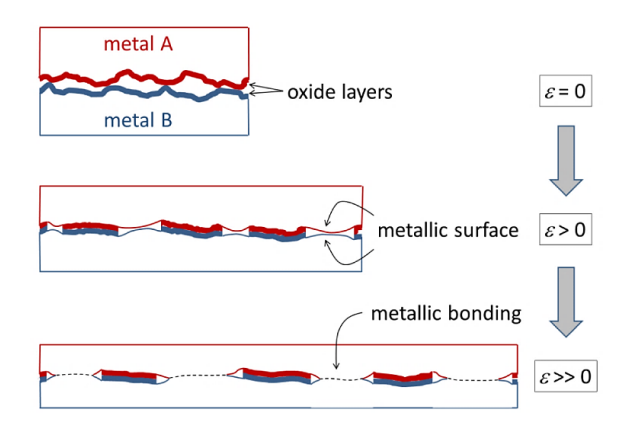


Figure 2-2 Schematic illustration of metallic bonding formation during CS due to the plastic deformation of the metallic surfaces and the resultant contact of fresh metallic surfaces.  $\varepsilon$  denotes the interfacial strain. Taken from [2].

#### 2.1.2. Parameters Affecting Deformation during CS

Most publications on CS identify the particle velocity and temperature as the major parameters affecting the deformation behaviour during CS [35,41,42]. As these parameters in turn depend on feedstock powder properties and process parameters [43], a summary of the findings from the literature on the influence of the aforementioned on the CS process are provided below.

Particle size affects the critical velocity of deposition and consequently, the success of bonding between the particle and substrate [3]. The optimal particle size required for effective deposition is governed by an interplay between thermal and mechanical phenomena. Smaller particles are more difficult to deposit as their high surface area to volume ratio leads to rapid heat dissipation, which can hinder the onset of ASI essential for bonding. The cooling rate (which decreases with an increase in particle size) must be sufficiently low to promote plastic deformation and shear instability, but high enough to ensure the solidification of the bond after impact [44]. Additionally, for a given impact velocity, larger particles experience a longer impact event, as the deformation wave travels through a larger volume. This increases the maximum temperature and the time available for bonding, resulting in an increase in the

bonding quality [3]. This trade-off establishes an ideal particle size range that allows for both sufficient plastic deformation and adequate thermal conditions for bonding. Considering the aforementioned, Schmidt et al. [3] propose an equation for the critical particle size above which the particles adhere to the substrate, based on the particle density, velocity, thermal conductivity, and specific heat.

Another factor affecting the critical deposition velocity for CS is the oxygen content of the feedstock powder. The works of Li et al. [45] and Kang et al. [46] with copper, stainless steel, nickel alloy and aluminium powders show that the critical velocity increases with an increase in the oxygen content of the feed powder. This is attributed to the fact that most of the impact energy is spent on the removal of the surface oxide layers rather than plastic deformation and consequently, successful bonding. Kang et al. [46] also report that the aluminium particles with a higher oxygen content exhibit a lower flattening ratio upon impact, with the resulting coatings being more porous, due to the residual oxygen layers obstructing adhesion between the particle and substrate.

As for the process parameters, the type of the carrier gas can influence the impact velocity of the particles. The carrier gases that are typically used for CS are air, nitrogen and helium [47]. Even though helium has been reported to accelerate the feed particles to higher velocities and enhance their deformation, its substantial cost remains a barrier to widespread adoption of the gas for CS [48,49]. Therefore, a mixture of helium and nitrogen is typically used for industrial applications [50].

The powder feed rate is also one of the factors influencing the particle impact velocity. Increase in the feed rate leads to lower particle impact velocities, as more particles in the gas stream result in more particle-gas interactions. Therefore, the feed rate should be carefully selected [51,52].



Ultimately, the nozzle parameters affect the deformation of the particles and the quality of the final coating [50]. The nozzle transverse speed controls the amount of the powder impacting the substrate. Denser coatings with better adhesion strength are achieved using lower nozzle transverse velocities [53–57]. However, high transverse speeds are preferred for CS as low velocities contribute to residual stresses in the interface between the coating and the substrate [58]. Additionally, the nozzle stand-off distance can influence the impact velocity and deposition efficiency: the deposition efficiency increases with the stand-off distance up to a critical optimal point (which is material-dependent), after which it decreases [53]. The spray angle is another nozzle parameter that can affect the deposition efficiency. The highest deposition efficiency is typically achieved with a spray angle between 70° and 90°, with 90° being the optimum. When the angle is not perpendicular, the normal component of the velocity contributes to particle adhesion, while the tangential component can erode or remove the already deposited splats [59,60]. Adaan-Nyiak et al. [50] provide a table summarising the effect of different process parameters on the CS coating properties, as displayed in Table 2-1.

Table 2-1 Influence of process parameters on CS coating properties. NCV denotes "no common view", ↑ denotes increase, and ↓ denotes decrease. DS and DE denote "deposition strength" and "deposition efficiency", respectively. Taken from [50].

| Parameter                      | Degree   | DS           | Adhesion     | DE           | Porosity     | Residual Stress |
|--------------------------------|----------|--------------|--------------|--------------|--------------|-----------------|
| Gas Pressure                   | 1        | <b>↑</b>     | 1            | 1            | <b>↓</b>     | <b>↑</b>        |
| Gas Temperature                | <b>↑</b> | <b>↑</b>     | 1            | <b>↑</b>     | $\downarrow$ | <b>↑</b>        |
| Gas Molecular Weight           | <b>↑</b> | $\downarrow$ | $\downarrow$ | $\downarrow$ | <b>↑</b>     | $\downarrow$    |
| Particle Velocity <sup>a</sup> | 1        | <b>↑</b>     | 1            | <b>↑</b>     | <b>↑</b>     | $\downarrow$    |
| <b>Powder Feed Rate</b>        | 1        | $\downarrow$ | $\downarrow$ | $\downarrow$ | <b>↑</b>     | <b>↑</b>        |
| <b>Stand-off Distance</b>      | 1        | NCV          | NCV          | NCV          | NCV          | NCV             |
| Spray Angle                    | <b>↑</b> | <b>↑</b>     | <b>↑</b>     | <b>↑</b>     | <b>↑</b>     | <b>↑</b>        |

<sup>&</sup>lt;sup>a</sup> Although an increase in particle velocity increases adhesion and DE, new findings show they decrease at very high velocities [61,62].



# 2.2. Numerical Methods for Simulation of Particle Impact

Analysing the deformation behaviour of impacting particles is essential for gaining a deeper understanding of the deposition mechanisms in high-velocity impact processes like CS. However, experimental investigation of particle impact is challenging due to the extremely short duration of the event, making direct observation and measurement difficult. Therefore, numerical simulations serve as a powerful tool for analysing the underlying phenomena throughout the impact process. Accordingly, a brief overview of the numerical methods commonly used for simulating particle impact is provided, including the Discrete Element Method (DEM), Finite Element method (FEM), Boundary Element Method (BEM) and Molecular Dynamics (MD). Additionally, the Material Point Method (MPM) is described in detail, as it is the method employed in the current work. In the end, a comparative critique of these methods is presented, highlighting their respective strengths and limitations.

#### 2.2.1. Discrete Element Method (DEM)

DEM is a numerical simulation method introduced by Cundall and Strack [4], which estimates the motion of particles in a system using Newton's law of motion. Each particle in the system is a discrete entity with its own properties, and is assigned with an initial position and velocity. The net force on the particle, which is the sum of the contact forces and other interaction forces, is used to determine the acceleration of each particle based on Newton's second law of motion. Consequently, the velocities and positions of the particles are updated using numerical integration techniques, and the simulation proceeds iteratively until a specific condition is met.

In DEM, particles are considered as rigid bodies that are "deformable", in that the particles are allowed to "overlap" during contact [63]. Contact forces are calculated based on the relative



overlap, through a "contact model" that relates the two. The contact model is often determined analytically or empirically, using the distribution of the contact pressure over the contact area.

The more recent available contact models that can be applied to the normal impact of elastic-perfectly plastic particles are piecewise with regards to the deformation regime. For the elastic regime, the linear spring [4] or Hertz [64] models are commonly used. When yielding occurs, some models consider a single equation for the elastic-plastic phase [28,65–76], while others suggest separate equations for the elastic-plastic and fully plastic regimes [29,77–81]. It should be noted that in most of the aforementioned studies, the case of indentation (rigid sphere pressed into a deformable half-space) is considered, rather than flattening (deformable sphere pressed against a rigid half-space). Even though these contact conditions may be equivalent in the elastic regime, they differ in the elastic-plastic and fully plastic regimes [82,83]: in the case of a deformable sphere, the displaced material can expand freely, whereas for a deformable half-space, it is confined by the rigid spherical indenter and the elastic bulk of the half-space [70]. Consequently, care must be taken when selecting a contact model, to ensure its applicability to the studied case. It is also worth mentioning that there are several elastic-plastic normal contact models that also account for adhesion. These include the contact mechanics based models of Thornton and Ning [84], Tomas [85] and Martin [86], as well as the piecewise linear models of Luding [87–89], and Pasha et al. [90].

The application of DEM to the field of particle technology has been growing so rapidly that it is challenging to review all the publications on the subject. Nevertheless, there are a number of review papers covering different aspects and applications of the method, e.g. the works of Zhu et al. [91] on theoretical advances in the field, Mishra [92,93] on tumbling mills, and Bertrand et al. [94] on mixing.



It is also worth mentioning that there have been attempts to couple DEM with the Boundary Element Method (BEM) [95], which only requires the discretisation of the bounding surface, rather than the entire volume of a material domain. As BEM performs very well in infinite domain problems [96,97], coupling it with DEM allows for improved multi-scale modelling capabilities. There are instances of older studies that couple DEM and BEM for quasi-static problems [98,99]. In a more recent work, Nadimi et al. [100] use a coupled DEM-BEM approach to investigate the effect of the surface roughness of individual particles on the bulk behaviour of granular materials. They create a BEM model of compression between two particles, taking into account the elastic-plastic deformation of the asperities on the particle surfaces. A set of normal contact force-displacement curves for particles with different degrees of roughness are then generated, from which a contact model is extracted by curve fitting. The model is then plugged into the DEM simulations of a particle bed under quasi-static compression. The results suggest that increasing the particle surface roughness increases the stiffness of the granular bed. Moreover, rough particles produce a more widespread distribution of normal contact forces, but experience less tangential slip, indicating that smoother particles slide past each other more easily.

There are few studies that apply the coupled DEM-BEM method to dynamic problems: Barros et al. [101] introduce a new coupled DEM-BEM scheme and apply it to the problem of one-dimensional wave propagation in an elastic rod (modelled as finite, semi-infinite homogeneous, and semi-infinite non-homogeneous) under Heaviside load. The results suggest that the formulation performs well for the infinite and semi-infinite examples, and the importance of careful time step adjustment is highlighted. In a more recent work, Barros et al. [102] extend their formulation to two-dimensions for fully dynamic problems of a rod under load, and a cylindrical cavity under uniform pressure in infinite space. Despite the good agreement between their numerical results and analytical solutions, the authors once again



emphasise the importance of the time step selection. This is due to the fact that smaller time steps benefit the DEM, but lead to numerical instabilities for the BEM. Therefore, the use of a staggered scheme is suggested by the authors as a solution for future work.

#### 2.2.2. Finite Element Method (FEM)

FEM is a mesh-based numerical method in which the domain of the problem is discretised into a finite number of small elements. The characteristics of the domain are then estimated by assembling the contributions from the similar properties of the elements to the whole system [5,103]. Several studies have employed FEM to model the contact between an elastic-plastic sphere and a rigid surface [67,70,104–108] in a quasi-static analysis. There are also a number of FEM studies that consider the impact of an elastic sphere with an elastic-plastic substrate (indentation case), as detailed below:

Li et al. [29] modify Johnson's contact model [27] by deriving a more detailed pressure distribution function using FEM, accounting for the changes in the contact curvature. They provide analytical expressions for the contact force-displacement relationship in static contact problems, and coefficient of restitution for dynamic impacts, and validate the results using FEM. Wu et al. [14] use FEM to investigate the energy dissipation during normal impact of an elastic particle on either an elastic, or elastic-plastic substrate. Their results suggest that for the case of an elastic substrate, if more than one stress wave reflection occurs during contact, energy dissipation due to wave propagation is negligible. However, when no reflections occur, a noticeable portion of the incident kinetic energy is lost due to stress wave propagation. In the case of an elastic-plastic substrate, the contribution of stress wave propagation to energy loss is negligible, with plastic deformation being the primary mechanism of energy dissipation. Moreover, the study identifies two regimes of impact separated by a critical impact velocity.



i.e. elastoplastic and finite-plastic-deformation, where the trend of decrease in the coefficient of restitution with increase in the normalised impact velocity is more rapid for the latter. Mukhopadhyay et al. [109] propose a theoretical model for estimating the coefficient of restitution for the impact of an elastic sphere with an elastoplastic surface, by considering a radially uniform pressure distribution in the central contact region and incorporating the effects of nonlocal plasticity. They use FEM and experiments to validate their results for a wide range of impact velocities, demonstrating improved predictions for the coefficient of restitution, contact force and contact time compared to Thornton's model [28].

It appears that Wu et al.'s work [110] is the only FEM study where the specific case of contact between an elastic-perfectly plastic sphere with a rigid surface (flattening case) is modelled in the dynamic framework. Additionally, the case of impact between an elastic sphere and an elastic-perfectly plastic half-space is studied (indentation case). The authors conduct FEM simulations considering different impact velocities and mechanical properties, to investigate the evolution of the contact pressure distribution and coefficient of restitution. Their results for the contact pressure distribution are in perfect agreement with Hertz theory before the maximum pressure reaches 1.6Y (elastic regime), and consistent with the observation of others [111–114] when yield occurs. Moreover, once the pressure profiles are fully established, the maximum pressure remains approximately constant at 2.7Y, comparable to the results of Tabor [115] and others [27,111,113]. The authors also identify a critical velocity above which the sphere undergoes finite plastic deformation. At lower velocities, the coefficient of restitution is only dependent on the ratio of the impact velocity to the yield velocity  $(V_i/V_y)$ . However, at velocities higher than the critical value, the coefficient of restitution is not only dependent on  $(V_i/V_v)$ , but also on the ratio of the effective Young's modulus to the yield strength  $(E^*/Y)$  of the sphere. Based on these findings, Wu et al. propose equations for the coefficient of restitution for both small and finite plastic deformation regimes.



FEM has also been widely used for the simulation of particle impact and deformation during CS, using both Eulerian and Lagrangian formulations. A comprehensive review of the numerous studies utilising the method is provided by Fardan et al. [116]. Since CS is commonly used for deposition of metal particles, most FEM studies implement material models that account for strain rate and temperature effects. The Cauchy stress tensor can be expressed as the sum of its isotropic part, i.e. the hydrostatic pressure (*p*), and the deviatoric stress. For high-velocity impact processes, the hydrostatic pressure is typically determined using the Mie-Grüneisen equation of state (EOS), as it takes account of temperature effects. When the material is under compression, the pressure is calculated using the equations below [117,118]:

$$p = p_H \left( 1 - \frac{\eta \varphi}{2} \right) + \eta_0 E_m \tag{2-1}$$

$$p_{H} = \frac{\rho_{0}c_{m0}^{2}\varphi(1+\varphi)}{\left[1-(S_{H}-1)\varphi\right]^{2}}$$
 (2-2)

In Equations (2-1) and (2-2), the subscript 0 denotes the values at the reference state. Also,  $p_H$ ,  $E_m$ ,  $\rho$ ,  $c_m$ , and  $S_H$  are the pressure on the Hugoniot curve, internal energy per initial volume, density, speed of sound in the material, and a material-dependent parameter, respectively. Finally,  $\eta$  is the Grüneisen parameter satisfying  $\eta/V^s = \eta_0/V_0^s$ , with  $V^s$  being the specific volume equal to  $1/\rho$ , and  $\varphi = \rho/\rho_0$ -1. When the material is under expansion, p is calculated using Equation (2-3), below:

$$p = \rho_0 c_{m0}^2 \varphi + \eta_0 E_m \tag{2-3}$$

The deviatoric part of the stress tensor can be modelled using different constitutive equations, with the most popular being the Johnson-Cook plasticity model (JC) [119]. The JC formulation can model the material response at high strain rates and temperatures, as expressed by the following equation:

$$\sigma = \left(A + B\varepsilon_p^N\right) \left(1 + C\ln\dot{\varepsilon}_p^*\right) \left(1 - \left[\frac{T - T_{room}}{T_m - T_{room}}\right]^M\right)$$
(2-4)

where  $\sigma$  is the flow stress,  $\varepsilon_p$  is the equivalent plastic strain and  $\varepsilon_p^*$  is the equivalent plastic strain rate normalised with respect to a reference strain rate, normally taken as 1 s<sup>-1</sup>. Moreover,  $T_{room}$  and  $T_m$  are the respective reference and melting temperatures and A, B, N, C and M are constants dependent on the material.

The Johnson-Cook constitutive model is typically complemented by a Johnson-Cook failure model [120] that signifies fracture. In this model, the failure strain is calculated by:

$$\varepsilon_{p}^{f} = \left(D_{1} + D_{2} e^{D_{3}\sigma^{*}}\right) \left(1 + D_{4} \ln \dot{\varepsilon}_{p}^{*}\right) \left(1 + D_{5} \left[\frac{T - T_{room}}{T_{m} - T_{room}}\right]\right)$$
(2-5)

where  $D_1$  to  $D_5$  are material parameters, and  $\sigma^* = \sigma_m/\bar{\sigma}$  is the stress triaxiality, with  $\sigma_m$  and  $\bar{\sigma}$  being the mean stress and von Mises effective stress, respectively. The damage is accumulated with time as:

$$D_{JC} = \sum \frac{\Delta \varepsilon_p}{\varepsilon_p^f}$$
 (2-6)

When the damage reaches the threshold value of unity, the material fails.



Other constitutive models describing the plastic behaviour of the material include: the Preston-Tonks-Wallace (PTW) model [121] for plastic flow of metals under explosive loading and high-velocity impacts, the Mechanical Threshold Stress (MTS) model [122] for simulation of high strain rates and extreme deformations, the Zerilli-Armstrong (ZA) model [123] and its modifications [124,125] for describing the flow stress of metals at high temperatures based on dislocation mechanics, and the more recent Ma-Wang (MW) model [126], which accounts for a wide range of strain rates during CS.

#### 2.2.3. Molecular Dynamics (MD)

MD is a computational tool suitable for the study of physical and mechanical properties of materials at small length scales (in the nanometre range), using inter-atomic potentials. This method implements the Newtonian equations of motion for calculation of movements and interactions of atoms/molecules and allows for analysis of field variables such as stress, strain and temperature [6,127]. The method is specifically used to study the impact behaviour of brittle particles during aerosol deposition (AD) [128–133], as the feed particles are in the nanometre size range. However, there are a number of studies that implement it for the study of CS.

Gao et al. [134] employ MD to investigate the deposition dynamics and structural evolution of nanoscale gold particles deposited on a gold substrate. The study indicates that both the particle and substrate (which are modelled as clusters of atoms) lose their crystalline structure during deformation upon impact. However, this is restored after relaxation. Thermal analysis reveals that the impact region undergoes localised melting, while the temperature of the other regions remains below the melting point. The results also demonstrate that an increase



in the cluster size or impact velocity results in stronger interactions between the particle and the substrate, attributed to an increase in the incident kinetic energy.

Malama et al. [135] observe similar trends using MD simulations of CS for nickel and titanium nanoparticles on a titanium substrate. Moreover, they find that higher temperatures of both particles and substrate result in a stronger bond between the two.

Joshi and James [136,137] utilise MD simulations to investigate the effect of impact velocity, particle size and impact angle on the deposition of copper nanoparticles on a copper substrate during CS. They emphasise the importance of maintaining the impact velocity in a certain range to optimise the coating quality. Additionally, the authors reveal a trade-off between the coating thickness and uniformity depending on the impact angle, where a 90° impact results in the highest deposition height, and a 60° impact angle produces more uniform coatings. Regarding the influence of particle size, the study indicates that increasing the particle size up to 20 Å enhances the coating quality, while further increase beyond this threshold yields no additional benefits. Further analysis of the von Mises stress and plastic strain points towards the presence of shear instabilities at higher impact velocities, improving the bonding strength between the particle and the substrate.

Rahmati et al. [138] also investigate the CS of copper nanoparticles on copper substrates using MD, identifying three deformation stages for particles larger than 10 nm. The first stage is the onset of plastic deformation characterised by dislocation nucleation and glide at the bottom edges of the particle. This is followed by the formation of a dislocation network in the lower part of the particle, while the upper part stays undeformed. In the end, the particle completely flattens as the deformation reaches the upper part. The results also reveal fluid-like behaviour at the particle-substrate interface, with jetting resulting from the flow of material from the centre towards the edges of the particle.



Temitope Oyinbo and Jen [139] carry out MD simulations of CS for the deposition of nanoscale aluminium, nickel, copper and silver particles on copper substrates. The results demonstrate a three stage deformation process similar to that pointed out by Rahmati et al. [138]. Moreover, the authors attribute the jetting phenomenon to the interaction of the pressure waves with the particle-substrate interface, leading to localisation of softening in this region. In a later work [140], the authors simulate the impact of agglomerates of palladium particles with a copper substrate, revealing that bonding forms without melting of the materials involved, with stronger bonds forming at elevated temperatures.

#### 2.2.4. Material Point Method (MPM)

MPM, which has been developed by Sulsky et al. [7,141,142], comprises two concepts: Lagrangian material points that carry the full physical state of the material, and a background Eulerian mesh used for the discretisation of the continuous fields, i.e. the displacement field. The method can be regarded as "FEM with moving integration points", since it utilises Lagrangian material points (rather than a mesh) to discretise the material domain. The material points are tracked during the deformation process and each of them is assigned with a position and carries the state variables. Mass is automatically conserved in MPM as each point is associated with a fixed amount of mass at all times. The classical MPM developed by Sulsky et al. is an updated Lagrangian formulation of MPM (ULMPM), where the background mesh discretises the space occupied by the body in both the reference and current configurations, as shown in Figure 2-3 (a). Alternatively, in the somewhat novel total Lagrangian MPM formulation (TLMPM) [8], the background mesh only covers the space occupied by the body in the reference configuration, as illustrated in Figure 2-3 (b) [143,144]. Typically, ULMPM defines the reference configuration based on the configuration of the previous time step. This can lead to cell-crossing instability as the material points might not lie at an optimal position



inside the background mesh elements. Moreover, the reference configuration is updated at each time step, which makes ULMPM relatively computationally expensive. In TLMPM, the reference configuration is fixed and the material points are always associated with their initial positions. This provides an efficient approach in terms of numerical stability and computational expenses [145].

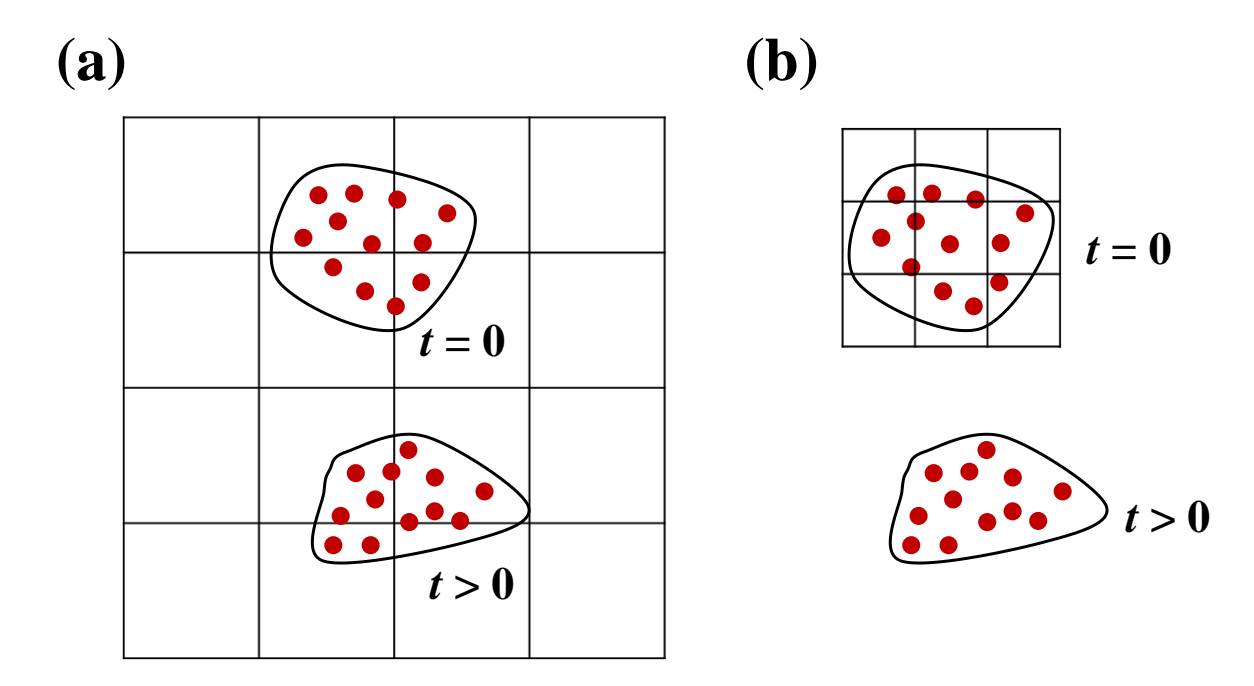


Figure 2-3 Discretisation in two different MPM formulations: (a) ULMPM, where the space that the body occupies and will occupy is covered by the background mesh and (b) TLMPM, where the background mesh only discretises the space occupied by the body in the reference configuration.

A basic explicit algorithm of TLMPM is shown in Figure 2-4 and works as follows: Initially, information is mapped from the material points to the mesh nodes (P2M), as the mesh is reset at every cycle. Then, the solution to the momentum equations is calculated on the mesh nodes (Mesh Update). Subsequently, the nodal solution is mapped back to the particles to update their position and state variables (M2P). It should be noted that in TLMPM, all of the mapping and interpolations are done in the undeformed reference configuration (taken as the initial state), in which both the material points and the background mesh (which only exists in



the initial state) are fixed [144]. An account of the studies that use MPM to investigate the impact process is provided below.

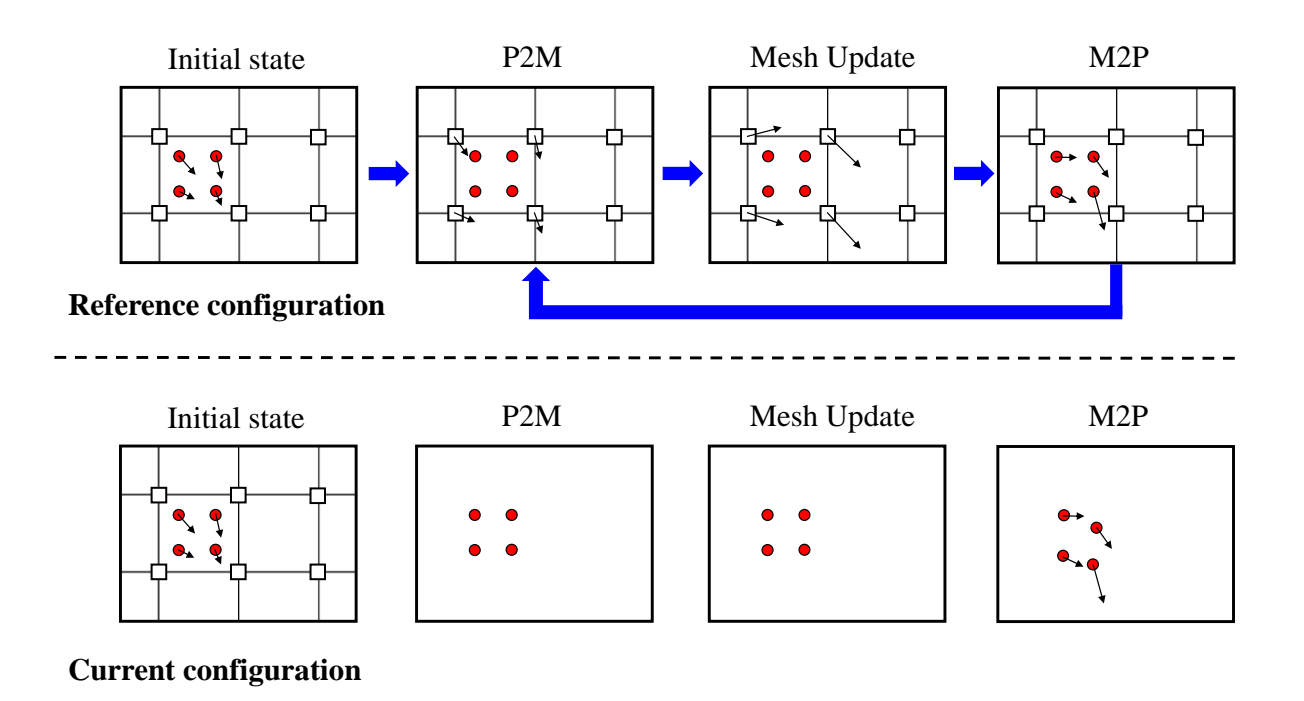


Figure 2-4 Illustration of a typical explicit TLMPM computational cycle, Modified from [144].

Li et al. [146] implement ULMPM to model the impact of elastic-perfectly plastic disks with different mechanical properties on a rigid target at different velocities. Their results show that the normalised contact law (force normalised by the contact force at yield and displacement normalised by the radius of the particle) depends on and can be determined from the ratio of the effective Young's modulus to the yield strength,  $E^*/Y$ , and that of the impact velocity to the yield velocity,  $V_i/V_y$ . Moreover, when the coefficient of restitution is expressed in terms of  $V_i/V_y$ , three distinct zones of deformation behaviour are identified: small deformation, full plasticity and large deformation. The authors suggest that the coefficient of restitution is only dependent on  $V_i/V_y$  in the first two zones. They express this dependency by formulating their own analytical expressions. For the third zone, their numerical results are in perfect agreement with Wu et al.'s [110] equation for the coefficient of restitution.



Liu et al. [147] investigate the high-velocity impact of micron sized aluminium particles on a thick aluminium plate using ULMPM. The Mie-Grüneisen EOS [117] and JC constitutive model [119,120] are employed. After impacting the particles individually and as an assembly at different angles and impact velocities, they study the impact response and dimensions of the craters generated on the plate. Depending on the impact angle, different modes of crater morphology are identified for the impact of the particle assembly, and the results are in good agreement with experimental and empirical findings.

A typical problem for assessing the performance of numerical methods in modelling large deformation during high-velocity impacts is the Taylor impact test [148]. The test comprises a cylindrical projectile impacting a rigid wall at a high velocity, and is used by Johnson and Holmquist [149,150] to compare different constitutive models for Oxygen-Free High Conductivity (OFHC) copper and Armco iron. In their work, Johnson and Holmquist use experiments to determine the material parameters for different constitutive models, and compare the models using numerical simulations. Sulsky and Schreyer [142] use the experimental and numerical results of Johnson and Holmquist [149,150] to test the applicability of their ULMPM code to the Taylor impact problem for OFHC copper. They employ a JC constitutive model [119] to describe the deformation of the impacting projectile, and compare the measured and predicted values of the diameter, bulge, and length of the projectile after impact. Their results demonstrate a good agreement with those obtained by Johnson and Holmquist [149,150]. For an illustration of the aforementioned parameters, refer to Figure 2-5 (a). Note that the bulge is the diameter of the deformed projectile measured at 0.2 times the original length up from the impact surface.

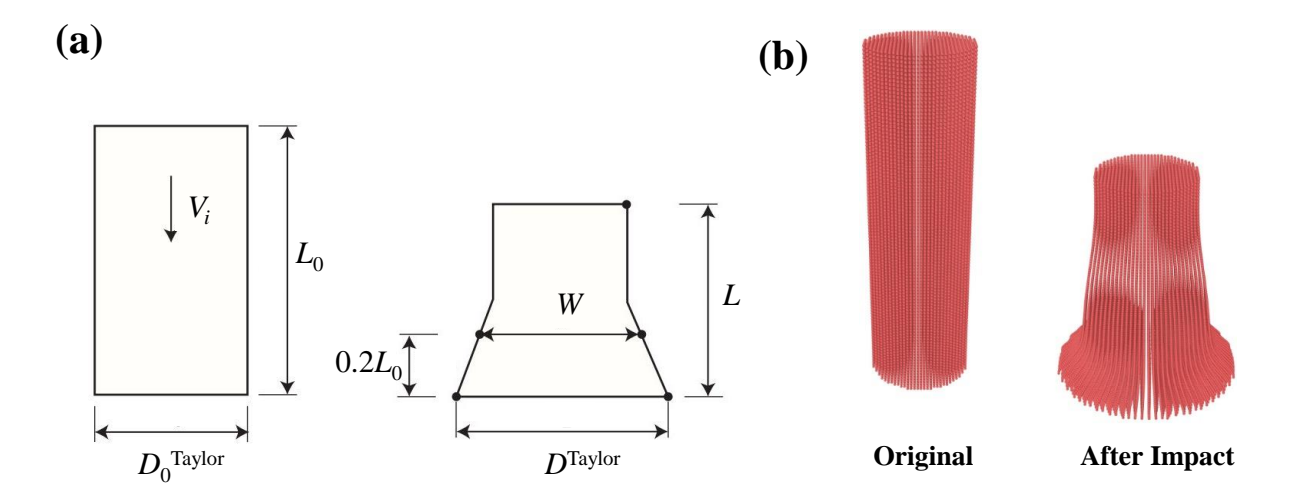


Figure 2-5 Taylor impact test for an OFHC copper projectile: (a) schematic drawing of the projectile's geometry before and after impact [143], and (b) Initial and final configurations of the material points in TLMPM simulations of de Vaucorbeil et al. [8].

In a more recent work, de Vaucorbeil et al. [8] test their TLMPM code against the ULMPM predictions of Sulsky and Schreyer [142]. They use a modified Mie-Grüneisen EOS [117] that accounts for damage to calculate the hydrostatic pressure, and the JC constitutive model [119,120] for calculating the deviatoric stress. The initial and final configurations of the material points in de Vaucorbeil et al.'s work [8] are shown in Figure 2-5 (b). The values of the diameter, bulge, and length of the projectile after impact, as measured by Johnson and Holmquist [149,150], and predicted by the TLMPM [8] and ULMPM [142] formulations are displayed in Table 2-2, confirming the better performance of TLMPM in modelling the high-velocity impact problem.



Table 2-2 Taylor impact test for an OFHC copper projectile: the diameter ( $D^{Taylor}$ ), bulge (W), and length (L) of the projectile after impact, as measured experimentally [149,150] and predicted by TLMPM [8] and ULMPM [142]. Note that the impact velocity in all the cases is 190 m/s, and the initial values for the diameter, bulge and length before impact are 7.6, 7.6, and 25.4 mm, respectively.

| Geometry      | Experimental | TLMPM | ULMPM |
|---------------|--------------|-------|-------|
| D Taylor (mm) | 13.5         | 13.9  | 14.6  |
| W (mm)        | 10.1         | 9.4   | 9.1   |
| L (mm)        | 16.2         | 16.2  | 18.3  |

Telikicherla and Moutsanidis [151] also consider the Taylor impact test as part of their performance evaluation of ULMPM and TLMPM in modelling various solid mechanics problems. Different constitutive models are used depending on the problem. They compare the methods by implementing various shape functions (interpolation functions that link the material points to the mesh nodes, refer to Section 3.2). This is because the use of shape functions results in oscillations in the stress profiles. The authors also propose their own "projection technique" to remedy the oscillations by improving the stress tensor through modifying either the deformation gradient or the velocity gradient (depending on the problem). By comparing their numerical results with the experimental and FEM results of Wilkins et al. [152] for the Taylor test, they find that TLMPM supplemented by their projection method produces the smoothest stress profiles and good predictions for the final projectile geometry. However, it is important to note that while TLMPM without the projection technique results in oscillations in the stress profile, it still yields the same predictions as when the projection technique is applied. The authors conclude that TLMPM is a notably better alternative to ULMPM, in terms of energy conservation, computational cost, and overcoming cell-crossing instabilities.

de Vaucorbeil et al. [144] simulate the high-velocity impact (1,160 m/s) of an elastic steel disk on an elastic-perfectly plastic aluminium substrate using both ULMPM and TLMPM as a



numerical example. They note that when a linear shape function is used for both methods, TLMPM produces much smoother stress profiles compared to ULMPM, though the ULMPM stress fields improve with the use of a higher order shape function. Nevertheless, TLMPM with a linear shape function is 21% faster than ULMPM with a higher order shape function. The authors also find that the deformed surface of the substrate is smoother using TLMPM due to the absence of numerical fracture in the method. In the end, it is concluded that TLMPM is more accurate than ULMPM in all the numerical examples presented in the study.

Li et al. [153] complement ULMPM with a novel contact algorithm, and as a numerical example, model the impact of two elastic rods approaching each other at 100 m/s using different shape functions. They compare the numerical values of the peak stress along the rods, to the analytical values obtained from the one-dimensional wave propagation theory. Strong oscillations in the stress profile are observed using ULMPM with a linear shape function. However, the profile gets smoother and the results become more accurate as the shape function order is increased.

Liu and Xu [118] use ULMPM to simulate the cold spraying of copper particles on copper substrates. They consider single-particle and multiple-particle impacts, using the Mie-Grüneisen EOS [117] and JC constitutive model [119,120] to describe the material behaviour. The final configurations of the single particle and substrate are investigated, revealing a good agreement between the ULMPM results and those of FEM and experimental studies (see Figure 2-6). In the case of impact for multiple particles, the authors observe that the jetting of the substrate is supressed by consecutive impacts, and the particles in the lower layer get embedded in the substrate. Consequently, it is concluded that metal jetting and mechanical interlocking are important bonding factors in CS.



Even though the findings of Liu and Xu [118] highlight the role of mechanical interlocking in CS, it is important to note that their simulations do not directly incorporate the bonding process. Therefore, in a very recent work, Hirmand et al. [154] introduce a bonding criterion that is directly incorporated into their ULMPM simulations of CS. They assume that successful bonding is governed by a critical threshold value that can be defined by the level of material jetting. Consequently, a "bonding parameter" is assigned to each boundary material point. The bonding parameter is a history-dependent variable used to track the evolution of jetting on the surface of the contacting bodies. With the progress of the simulation, the bonding parameter is integrated in time, until the equivalent interface bonding parameter reaches the threshold value of unity at a mesh node. Thereafter, contact detection algorithm halts and a bond condition is applied to the node by adding a bond force to the nodal forces, i.e. free surfaces are converted to a continuous domain. To calibrate the material constants used in their bonding model, the authors run ULMPM simulations of CS for an aluminium/aluminium system using the Mie-Grüneisen EOS [117] and PTW constitutive model [121]. After calibration, they compare the bonding outcome of their simulations at different velocities with experimental findings in the literature, finding good agreement. It is important to note that this model can only determine the occurrence of bonding and cannot provide any quantitative measure of the bonding strength. However, the work makes a valuable contribution in laying a foundation for future research.

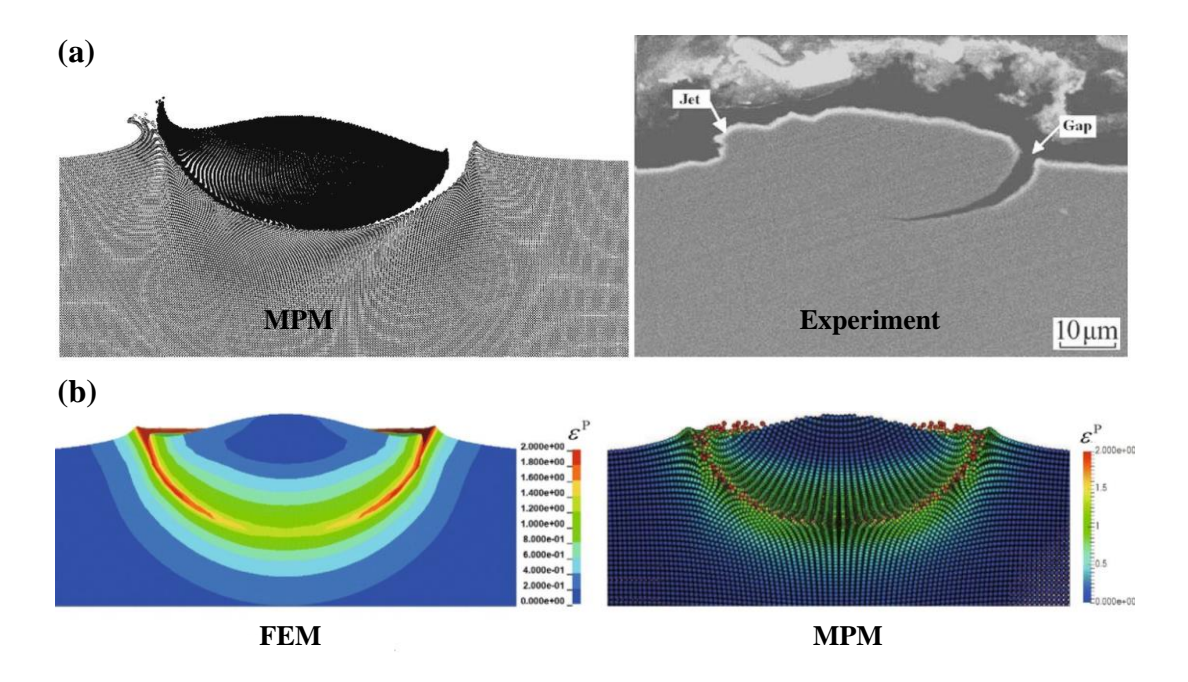


Figure 2-6 CS of a copper particle on a copper substrate simulated by Liu and Xu [118]: comparison between (a) the ULMPM results and the experimental results of Li et al. [155] for oblique impact, and (b) the FEM and ULMPM results for normal impact. Taken from [118].

As a final remark, it is worth mentioning that MPM has also been combined with other numerical methods for simulation of high-velocity impacts. For instance, Zhang et al. [156] have developed a material point finite element method (MPFEM) that discretises a body by a mesh of finite elements, and uses an additional mesh in the regions prone to large deformation. The nodes covered by the second mesh are treated as material points, and the rest are treated as finite element nodes [143]. They apply their method to the Taylor impact test, and achieve satisfactory results. Furthermore, Liu et al. [157] conduct MD simulations to determine the equations of state of different materials, and implement them into ULMPM simulations of impact for different numerical examples, getting good agreements with experimental and numerical results from the literature. Additional examples of MPM coupled with other methods are provided in the textbook of Zhang et al. [158].



#### 2.2.5. Critique of the Numerical Methods

DEM is quite well-established and provides thorough dynamic information on particulate systems, with the advantage of access to many well-studied contact models. However, the method is best for explaining the bulk behaviour of the system and monitoring of the physical processes rather than modelling of real-scale problems. Moreover, as DEM models materials as assemblies of discrete particles, it cannot accurately capture the continuous nature of materials undergoing large deformations, which leads to inaccuracies in representing the material behaviour.

FEM provides a good means for particle interface tracing. However, analysis of problems involving large strains is typically difficult using FEM, especially in the Lagrangian formulation. During large deformation problems, mesh distortion and element entanglement are inevitable and adversely affect the accuracy of the calculations. In order to tackle this problem, a mesh-rezoning technique can be used to restore the mesh cells. In this technique, the fields of variables are mapped from the distorted mesh to a new one. However, remeshing and remapping require high computational effort, and if not handled correctly, can result in more errors. The Eulerian formulation on the other hand is not adequate for following material free surfaces and requires a fine mesh and high computational effort to obtain accurate results [63,116].

MD allows for modelling of extreme deformations and particle-substrate interactions during high-velocity impact problems. Also, it offers the advantage of understanding the impact mechanism at the atomic level. Nevertheless, while MD can handle systems with millions of atoms, this is still minute in comparison with the number of atoms in a macroscopic material. This limitation in length scale means that simulating bulk material properties or large-scale phenomena can be difficult, making the application of MD limited to modelling of nano-



sized particles. Additionally, the description of the interatomic interactions and equations of motion poses difficulties: the entire simulation is fundamentally limited by the accuracy of the applied force fields, which describe the potential energy of the system and the forces between the atoms [116,159].

MPM circumvents the problem of mesh distortion and element entanglement as the material domain is discretised by moving integration points, and the momentum equations are solved on an Eulerian background mesh. Moreover, the similarity of MPM and FEM offers the advantage of access to numerous existing well-studied algorithms. However, the enforcement of boundary conditions and formal analysis in terms of convergence, error and stability is comparatively more difficult in MPM. Additionally, MPM has a lower accuracy than FEM for small deformation problems [143].

Considering the discussions above, MPM seems like a viable candidate for simulation and analysis of high-velocity impact processes like CS.



# 3. Numerical Methodology

## 3.1. Overview

This chapter outlines the details of the numerical method used in this work for the study of particle impact, followed by the sensitivity analysis carried out to determine the most suitable time step and discretisation settings. In this work, an explicit formulation of TLMPM [143–145] is coupled with a new implicit contact algorithm to model the particle. The current study utilises TLMPM to compensate for the drawbacks of ULMPM (refer to Section 2.2.4). An implicit formulation of ULMPM coupled with Contact Dynamics (CD) method for the treatment of frictional contact can be found in [160–163]. Part of the sensitivity analysis results in this chapter has been published in [164]. All of the simulations presented in this work have been undertaken on ARC4, part of the High Performance Computing facilities at the University of Leeds, UK.

## 3.2. MPM Formulation

To describe a continuum body in its initial (reference) configuration, a domain  $\Omega_0$  is considered in  $\mathbb{R}^D$ , D being the domain dimension, with an external boundary  $\partial\Omega_0$ . The body is subjected to prescribed displacements and forces on its separate complementary parts of the boundary, i.e. the Dirichlet boundaries,  $\partial\Omega_0^u$  and the Neumann boundaries,  $\partial\Omega_0^f$ . The conservation of linear momentum of the body is expressed by Equation (3-1) below:

$$\nabla \cdot \mathbf{\Pi}(\mathbf{X}, t) + \mathbf{b}(\mathbf{X}, t) = \rho(\mathbf{X}, t)\mathbf{a}(\mathbf{X}, t) \qquad \text{in } \Omega_0, \tag{3-1}$$

where  $\Pi$ , b,  $\rho$  and a are respectively the first Piola-Kirchhoff stress tensor, the body force, the density and the acceleration of a point at position X in its initial configuration at time t. In the MPM, mass is automatically conserved as the body is divided into material points with a fixed amount of mass. The boundary conditions are described by:

$$\begin{cases} \boldsymbol{u}(\boldsymbol{X},t) = \hat{\boldsymbol{u}}(\boldsymbol{X},t) & \text{on } \partial\Omega_0^{\mathrm{u}}, \\ \boldsymbol{\Pi}(\boldsymbol{X},t).\boldsymbol{n} = \hat{\boldsymbol{f}}(\boldsymbol{X},t) & \text{on } \partial\Omega_0^{\mathrm{f}}, \end{cases}$$
(3-2)

where u and  $\hat{u}$  are the displacement and the prescribed displacement fields, respectively. The displacement of a material point is the difference between its position in the deformed configuration, x and its position in the initial configuration, i.e. u=x-X. The terms  $\hat{f}$  and n respectively denote a prescribed load and the outward unit normal vector to  $\partial \Omega_0$ .

In order to solve Equation (3-1), the principle of virtual work and the boundary conditions shown by Equation (3-2) can be used to write the weak form of Equation (3-1) as:

$$\int_{\Omega_0} \rho \mathbf{a} \cdot \delta \mathbf{u} \, d\Omega + \int_{\Omega_0}^T \mathbf{\Pi} : \delta \mathbf{U} \, d\Omega = \int_{\Omega_0} \mathbf{b} \cdot \delta \mathbf{u} \, d\Omega + \int_{\partial \Omega_0^f} \hat{\mathbf{f}} \cdot \delta \mathbf{u} \, d\Gamma_0$$
(3-3)

where  $\Gamma_0$  is the surface of the body in its initial configuration and U is the deformation gradient defined as  $U=\partial x/\partial X=I+\nabla u$ , with I being the identity matrix. It is important to note that MPM is similar to FEM with the difference that the integration points are material points, rather than elements. Thus, Equation (3-3) is first discretised into Finite elements, as shown below:

$$\sum_{e} \int_{\Omega_{0}^{e}} \rho \mathbf{a} \cdot \delta \mathbf{u} \, d\Omega + \sum_{e} \int_{\Omega_{0}^{e}}^{T} \mathbf{\Pi} : \delta \mathbf{U} \, d\Omega = \sum_{e} \int_{\Omega_{0}^{e}} \mathbf{b} \cdot \delta \mathbf{u} \, d\Omega + \int_{\partial \Omega_{0}^{f}} \hat{\mathbf{f}} \cdot \delta \mathbf{u} \, d\Gamma_{0}$$
(3-4)



where  $\Omega_0^e$  is the domain occupied by the *e*th element of the background mesh, in the initial configuration. Subsequently, MPM discretises the above integrals using a Dirac delta function, taking the material points as integration points. Ultimately, Equation (3-4) in its discretised form can be written as follows:

$$\boldsymbol{M}_{ii}\boldsymbol{a}_{i}(t) = \boldsymbol{f}_{i}^{\text{int}}(t) + \boldsymbol{f}_{i}^{\text{ext}}(t)$$
(3-5)

where  $a_i$  is the nodal acceleration associated with node i and

$$\boldsymbol{M}_{ii} = \sum_{e} \sum_{p} \boldsymbol{N}_{ip}^{e} m_{p}$$
 Lumped mass matrix,

$$f_i^{\text{int}}(t) = -\sum_{e} \sum_{p} G_{ip}^{e} \Pi_p(t) V_{p_0}$$
 Internal force vector,

$$f_i^{ext}(t) = \sum_e \sum_p N_{ip}^e b_p(t) + f_i^S(t)$$
 Sum of body forces and surface tractions,  $f_i^S$ .

where  $m_p$  and  $V_{p0}$  represent the material point mass and volume in the initial configuration for a material point p.  $N_{ip}^{e}$  is the shape function matrix (interpolation matrix) for a material point p and its function is to relate the quantities associated with the material point to the variables associated with the nodes of the element e to which the material point belongs, at the initial configuration.  $G_{ip}^{e}$  denotes the gradient of the shape function  $N_{ip}^{e}$ . It should be noted that  $f_{i}^{S}$  also includes the nodal contact forces,  $f_{i}^{C}$  between several bodies. Evidently, the contributions of each element's nodal variables are combined into the global nodal variables, which represent the entire computational domain [145].

# 3.3. Explicit Algorithm

The explicit algorithm of the TLMPM adopted for this work is as follows [145]: first, a finite set of Lagrangian material points is used to discretise the particle. The material points are then assigned with their initial conditions and a background Eulerian mesh is defined for the particle. The time integration algorithm is subsequently initiated. The procedure explained below is followed for all the time steps:

- 1. Information (position, velocity, mass, density, deformation gradient, stress tensor, etc.) is mapped from the material points to the background mesh.
- 2. Equation (3-5) is solved from time *t* to time  $t+\Delta t$ , explicitly:
  - a. In order to determine the nodal velocities  $v_i$  associated with node i from the material point velocities  $v_p$ , a weighted squares approach is adopted:

$$\mathbf{P}_{i}(t) = \mathbf{M}_{ii} \mathbf{v}_{i}(t) = \sum_{e} \sum_{p} \mathbf{N}_{ip}^{e} \ m_{p} \ \mathbf{v}_{p}(t)$$
(3-6)

where  $P_i$  is the nodal momentum associated with node i.

b. The increments of the deformation gradient at the material points are calculated using the equation below:

$$\Delta \boldsymbol{U}_{p} = \Delta t \sum_{k} \boldsymbol{G}_{kp}^{e} \boldsymbol{v}_{k}(t) \tag{3-7}$$

where k denotes the nodes associated with element e.

c. The deformation gradients of the material points are then updated, as shown below:

$$\boldsymbol{U}_{p}(t+\Delta t) = \boldsymbol{U}_{p}(t) + \Delta \boldsymbol{U}_{p} \tag{3-8}$$



- d. The constitutive model is used to compute the stresses associated with each material point.
- e. Equation (3-5) is utilised to compute the internal and external nodal force vectors.

  The contact interactions between particles (if present) are also determined in this step.
- f. The nodal velocity is updated using Equation (3-5):

$$\mathbf{v}_{i}(t+\Delta t) = \mathbf{v}_{i}(t) + \Delta t \left[ \mathbf{f}_{i}^{\text{int}}(t) + \mathbf{f}_{i}^{\text{ext}}(t) \right] / \mathbf{M}_{ii}$$
(3-9)

3. The positions and velocities of the material points are updated:

$$\mathbf{v}_{p}(t+\Delta t) = \mathbf{v}_{p}(t) + \Delta t \sum_{k} N_{kp}^{e} \mathbf{a}_{k}(t)$$
(3-10)

$$\boldsymbol{x}_{p}(t+\Delta t) = \boldsymbol{x}_{p}(t) + \Delta t \sum_{k} N_{kp}^{e} \, \boldsymbol{v}_{k}(t+\Delta t) \tag{3-11}$$

4. In the end, t is set to  $t+\Delta t$  and the procedure is repeated from step 1.

## 3.4. Contact Algorithm

In this section, the contact algorithm used in the current study is explained in the context of two deformable bodies discretised by material points, interacting at several contact points depending on their degree of deformation and spatial resolution [145]. The contact forces should be computed by a contact algorithm that accounts for the Coulomb friction law, as well as the constraint of impenetrability of the bodies at their surfaces (in this case, imposed between neighbouring material points on the bodies' boundaries). This is achieved by utilising the

Contact Dynamics (CD) method, which is a mathematical framework that imposes unilateral constraints at contact points and is based on non-smooth mechanics, i.e. it allows the velocities of the mechanical system to undergo jumps as a result of multi-contact collisions and the non-smooth feature of the Coulomb friction law [165–167]. In the current contact algorithm, contact forces are computed directly on the material points, though there are previous studies that use a multi-mesh mapping algorithm which computes the contact forces on the nodes of a common background mesh [161,162,168,169].

Considering two deformable bodies  $\alpha$  and  $\beta$ , each material point at the bodies' external boundaries is treated as a spherical rigid particle with a diameter equal to the mean distance between material points. This is to avoid introducing excess volume in the bodies by making the volume of the spherical rigid particle closely equal to the volume of the boundary material points, as the material points are located in the centre of their appointed volume. It should be noted that upon contact, each material point associated with one body can be in contact with multiple material points associated with the other bodies.

Considering the positions, velocities and masses of the material points, for each pair of material points p (in body  $\alpha$ ) and q (in body  $\beta$ ) that are likely to come into contact, a normal unit vector  $n_{pq}^{\alpha\beta}$  positioned from body  $\beta$  to body  $\alpha$  is determined, as shown in Figure 3-1 (a). The contact normal vectors are specified to be normal to the contact surface, using the positions of the boundary neighbouring points, as demonstrated in Figure 3-1 (b). Additionally, a tangential unit vector  $t_{pq}^{\alpha\beta}$  is defined by Equation (3-12), where  $v_p^{\alpha}$  and  $v_q^{\beta}$  are the velocity vectors for material points p and q, respectively:

$$t_{pq}^{\alpha\beta} = \frac{\left(v_p^{\alpha} - v_q^{\beta}\right) - \left(v_p^{\alpha} - v_q^{\beta}\right) \cdot n_{pq}^{\alpha\beta} n_{pq}^{\alpha\beta}}{\left|\left(v_p^{\alpha} - v_q^{\beta}\right) - \left(v_p^{\alpha} - v_q^{\beta}\right) \cdot n_{pq}^{\alpha\beta} n_{pq}^{\alpha\beta}\right|}$$
(3-12)

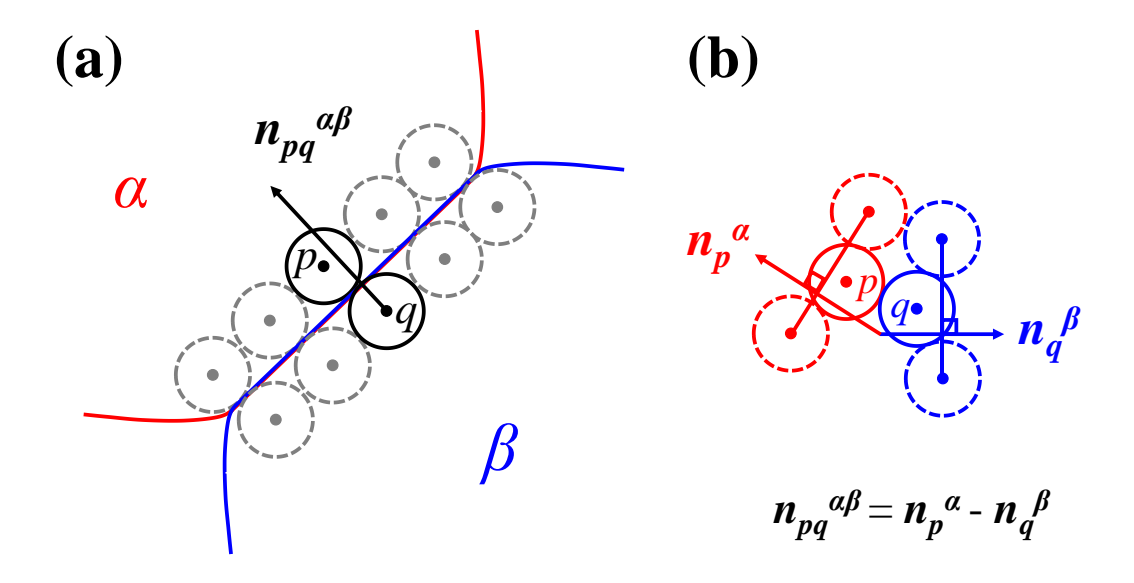


Figure 3-1 Contact between two bodies  $\alpha$  and  $\beta$ : (a) normal unit vector  $n_{pq}^{\alpha\beta}$  oriented from material point q in body  $\beta$  to material point p in body  $\alpha$  and (b) making the unit vector  $n_{pq}^{\alpha\beta}$  normal to the contact surface using the positions of the boundary neighbouring points. Modified from [145].

As long as the normal relative velocity,  $v_n$ , remains positive,

$$v_n = \left(v_p^{\alpha} - v_q^{\beta}\right). \, n_{pq}^{\alpha\beta} > 0 \tag{3-13}$$

the contact force  $f_n$  is zero. However, if  $v_n$  is zero, a repulsive (non-negative) normal contact force,  $f_n$ , is initiated at the contact point. These conditions describe the velocity-Signorini complementarity condition [170,171], as shown in Figure 3-2 (a). In order to solve the equations of motion along with the velocity-Signorini condition at all the potential contact points, the equations of motion should be expressed in terms of  $f_n$  and  $v_n$ , as follows:

$$m_{p}^{\alpha}a_{p}^{\alpha} = f_{pq}^{C,\alpha\beta} + \sum_{\gamma} f_{pr}^{C,\alpha\gamma}$$

$$m_{q}^{\beta}a_{q}^{\beta} = -f_{pq}^{C,\alpha\beta} + \sum_{\gamma} f_{qr}^{C,\beta\gamma}$$
(3-14)

where  $f_{pq}{}^{C, \alpha\beta}$  is the potential contact force between bodies  $\alpha$  and  $\beta$ , and  $\sum_{\gamma} f_{pr}{}^{C, \alpha\gamma}$  and  $\sum_{\gamma} f_{qr}{}^{C, \beta\gamma}$  denote the contact forces of other bodies at this contact point. Using Equation (3-14), a linear relationship between  $f_n = f_{pq}{}^{C, \alpha\beta}$ .  $n_{pq}{}^{\alpha\beta}$  and  $v_n$  can be found, as shown by Equation (3-15):

$$f_n = \frac{2}{\Delta t} \frac{m_p^{\alpha} m_q^{\beta}}{m_p^{\alpha} + m_q^{\beta}} v_n + k_n \tag{3-15}$$

where  $k_n$  is an offset force which depends on other contact forces applied by the neighbouring bodies of  $\alpha$  and  $\beta$ . With regards to Figure 3-2 (a), Equation (3-15) intersects the velocity-Signorini graph at a single point, depending on  $k_n$  and consequently, the other contact forces. Therefore, an iterative process is carried out to determine the normal contact forces at all of the contact points.

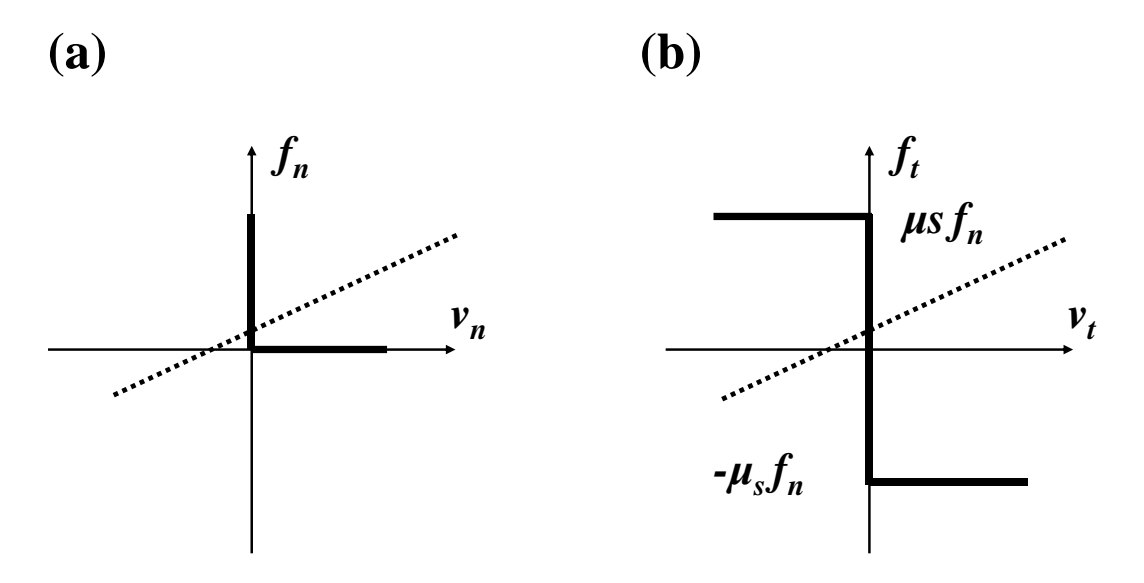


Figure 3-2 Contact conditions: (a) velocity-Signorini complementarity condition illustrated by a graph relating the normal contact force,  $f_n$ , to the relative normal velocity,  $v_n$ , and (b) Coulomb law of friction illustrated as a graph relating the tangential force,  $f_t$ , to the relative tangential velocity,  $v_t$ , where  $\mu_s$  is the friction coefficient. The dashed lines represent the linear relationships extracted from the equations of motion. Modified from [145].

The Coulomb law for dry friction is analogously a complementarity relationship between the tangential force,  $f_t$ , and the relative tangential velocity,  $v_t = (v_p^{\alpha} - v_q^{\beta}).t_{pq}^{\alpha\beta}$ , as illustrated in Figure 3-2 (b). Subsequently, in the same fashion as before, the equations of motion are expressed in terms of  $f_t$  and  $v_t$ :

$$f_t = \frac{2}{\Delta t} \frac{m_p^{\alpha} m_q^{\beta}}{m_p^{\alpha} + m_q^{\beta}} v_t + k_t \tag{3-16}$$

Equation (3-16) is intersected with the Coulomb graph displayed in Figure 3-2 (b) to simultaneously compute the tangential force,  $f_t$ , at all contact points within the same iteration process used for calculation of the normal contact force.

Finally, the contact force  $f_{pq}{}^{C,\ \alpha\beta} = f_n\ n_{pq}{}^{\alpha\beta} + f_t\ t_{pq}{}^{\alpha\beta}$  is projected onto the background mesh to compute the nodal contact forces  $f_i{}^{C,\ \alpha}$  corresponding to node i of body  $\alpha$ , and the nodal contact forces  $f_j{}^{C,\ \beta}$  corresponding to node j of body  $\beta$ , as shown by Equation (3-17). As stated before,  $f_i{}^{C,\ \alpha}$  and  $f_j{}^{C,\ \beta}$  are embedded in the nodal external forces,  $f_i{}^{ext}$ , shown in Equation (3-5), for bodies  $\alpha$  and  $\beta$ , respectively.

$$f_i^{C,\alpha} = \sum_e \sum_p N_{ip}^e f_{pq}^{C,\alpha\beta}$$

$$f_j^{C,\beta} = \sum_e \sum_q N_{jq}^e f_{pq}^{C,\alpha\beta}$$
(3-17)

A flowchart summarising the MPM and contact algorithms during one time step is shown in Figure 3-3.

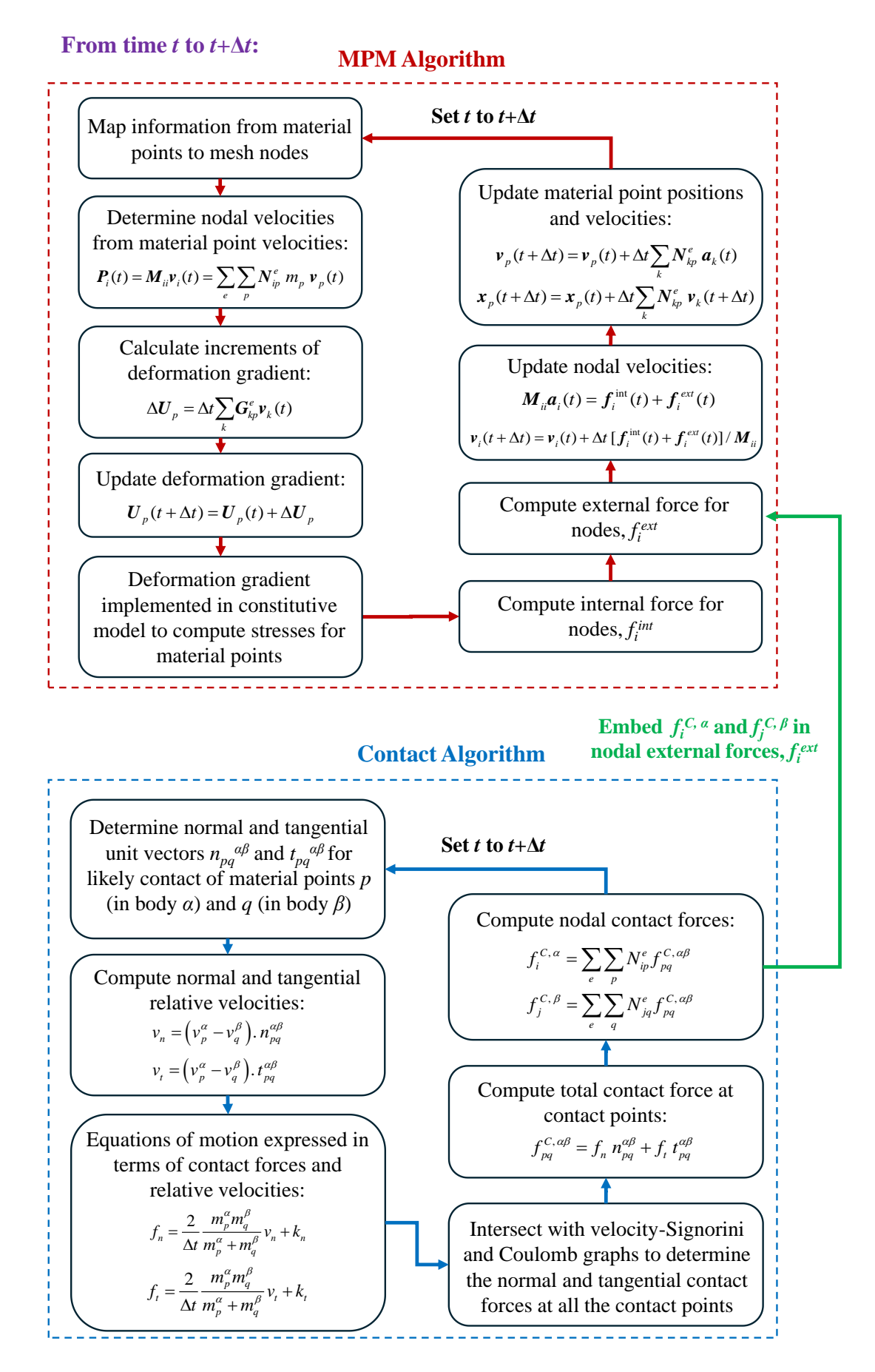


Figure 3-3 Flowchart describing the explicit TLMPM and contact algorithms.



# 3.5. Sensitivity Analysis

In order to model the impact of a spherical particle with a rigid wall, the abovementioned MPM-CD approach is adopted by utilising an in-house C++ code, proprietary of Dr Saeid Nezamabadi (University of Montpellier, France). To define the initial configuration of a simulation using the code, parameters including the particle radius, initial velocity, density, Young's modulus, Poisson's ratio and yield strength are inserted as input. Moreover, the problem domain is specified as two-dimensional or three-dimensional, and the position of the rigid wall is adjusted. To model the material behaviour, one of the following three constitutive relations can be selected: linear elastic, elastic-perfectly plastic and bilinear plastic. For each simulation, the time step, material points and mesh discretisation need to be decided. Therefore, a sensitivity analysis is necessary to determine the time step and discretisation settings that not only ensure accuracy and stability, but also are applicable to various cases and offer an efficient computational cost. For problems involving particle deformation, the accuracy of simulation results is typically verified using a contact model relevant to the problem. However, a comprehensive study by Wang et al. [172] comparing the available elastic-perfectly plastic contact models (18 different models) reveals notable discrepancies in prediction of impact behaviour by the models. A more reliable approach for verification is thereby adopted following Johnson [27], who suggests that Hertz [64] model can be used as the contact law for the impact of an elastic sphere with a rigid wall undergoing small deformation, as shown by Equation (3-18):

$$F = \frac{4}{3}R^{1/2}E^*\delta^{3/2} \tag{3-18}$$

where F, R and  $\delta$  denote the contact force, radius of the sphere, and displacement of the centre of the particle, respectively.  $E^*$  is the effective Young's modulus of the sphere defined as  $E^*$ =



 $E/(1-v^2)$ , with v being the Poisson's ratio. The relationship between  $\delta$  and time t is given by [27]:

$$t = \frac{\delta^*}{V_i} \int \frac{d(\delta/\delta^*)}{\left[1 - (\delta/\delta^*)^{5/2}\right]^{1/2}}$$
(3-19)

where:

$$\delta^* = \left(\frac{15mV_i^2}{16R^{1/2}E^*}\right)^{2/5} \tag{3-20}$$

in which  $V_i$  is the impact velocity,  $\delta^*$  is the maximum displacement of the centre of the particle during impact, and m is the mass of the particle. Deresiewicz [173] has evaluated Equation (3-19) numerically, providing the values for  $\delta/\delta^*$  and  $2t/t_{tot}$ , with  $t_{tot}$  being the total contact time given by Johnson [27] according to Equation (3-21):

$$t_{tot} = 2.87 \left( \frac{m^2}{RE^{*2}V_i} \right)^{1/5}$$
 (3-21)

By calculating the maximum contact force,  $F^*$ , from Equations (3-18) and (3-20), the change in contact force and displacement with time can be obtained in a dimensionless form. The sensitivity analysis is thus carried out by simulating normal impact of an elastic sphere (three-dimensional domain) with a rigid wall using various time steps and discretisation settings, and the results are compared with the analytical contact model provided by Johnson [27] for verification.



### 3.5.1. Simulation Setup

For all the simulations, an impact velocity of 1 m/s is considered in the -z direction, and the wall is placed 1.5 mm below the sphere to ensure that the material points are not in contact with the wall at the start of the simulation and mark the start of contact (Figure 3-4). The properties of the sphere are as follows: Radius, R=12.5 mm, Young's modulus, E=4.9 MPa, Poisson's ratio, v=0.25 and density,  $\rho=1,404$  kg/m<sup>3</sup>. Damping and friction are not applied and the cubic spline shape function is used.

The evolution of a simulation is followed using output files that contain the whole configuration and parameters of a simulation at a given time. These are generated every  $n_t$  time steps, where  $n_t$  is user-defined ( $n_t \ge 1$ ). The value of  $n_t$  should be sufficiently small to provide enough output data for a clear understanding of the process, but not so small that it leads to extensive computational cost. As a matter of personal preference,  $n_t$  is always adjusted so that ten output files are generated before impact, with respect to the time step and the distance between the sphere and the wall. The contact force printed in an output file is the arithmetic mean of all the contact forces calculated at each of the  $n_t$  time steps between the time of the output file and that of its predecessor (considering only the time steps where contact is detected). The time corresponding to the first output file with a non-zero contact force is taken as the instant of contact. The total contact time is considered from this instant to the time of the last output file with a non-zero contact force. For consistency, the position (z component here) of the centre of the sphere corresponding to an output file is taken as the arithmetic mean of the value printed in the current and the preceding output files. Subsequently, the displacement is calculated with reference to the position of the sphere centre at the instant of contact. Note that a simulation will continue running until it is stopped by the user. Typically, simulations are halted when the energy curves plateau after rebound. Since the focus of the current sensitivity analysis is on the contact force and displacement, the simulations are stopped after

contact is lost. The procedure for the selection of the time step and discretisation settings is described below.

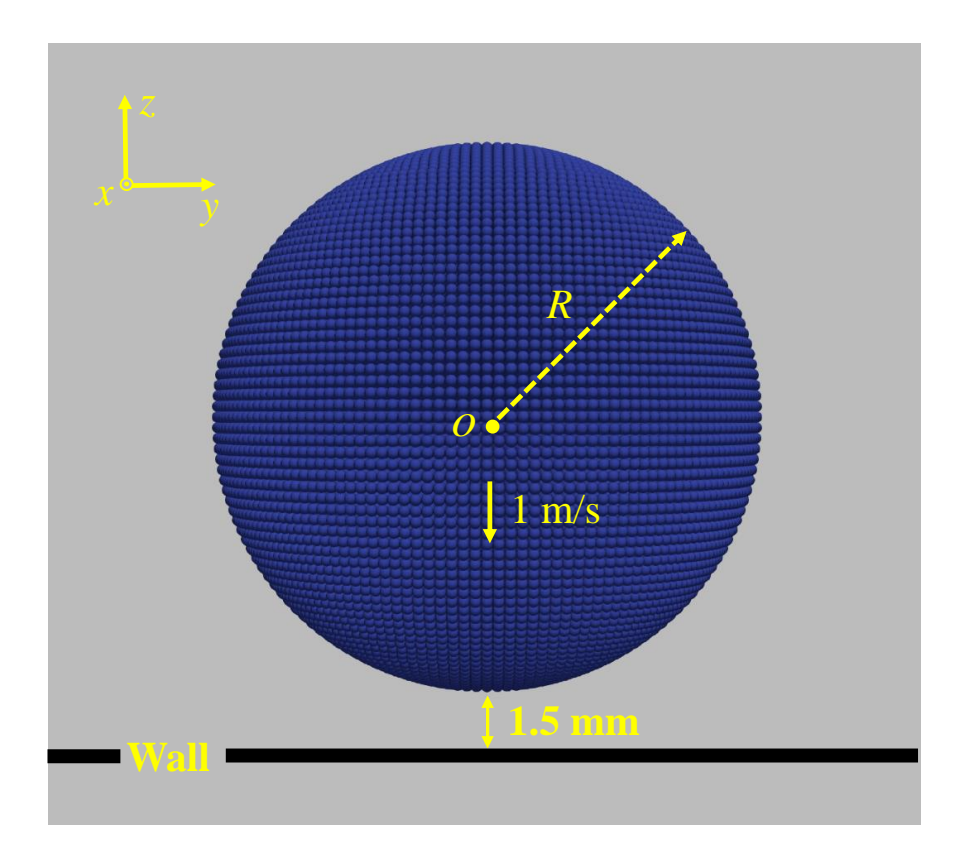


Figure 3-4 Visualisation of the modelled sphere for the sensitivity analysis, detailing the initial and boundary conditions (illustration is not to scale for presentation purposes). Created using ParaView version 5.11.0-RC1 [174].

#### 3.5.2. Material Points and Mesh Discretisation

The code allows for specifying the number of the material points used to discretise the diameter of the sphere in the initial configuration (*initial point density*). This determines the initial distance between the material points, i.e. the *point contact diameter*, which in turn is used by the code to construct the sphere from the material points. The size of the background mesh elements (hexahedral elements are used) can be determined by specifying the ratio of the element size to the initial distance between the material points in each dimension (*element to point ratio*). For the sensitivity analysis, a benchmark case comprising 50 material points to

discretise the diameter and a value of 1.05 for the element to point ratio is considered. Trial and error has shown that these settings perform very well across various cases. Hereafter, the benchmark case is denoted by "MP/ES" with MP and ES signifying the initial number of the material points per element and element size of the benchmark case, respectively. Subsequently, four additional cases are considered by maintaining either the element size or the number of the material points per element of the benchmark case, while doubling and quadrupling the other, as demonstrated in Figure 3-5. The resulting discretisation settings for each case are provided in Table 3-1.

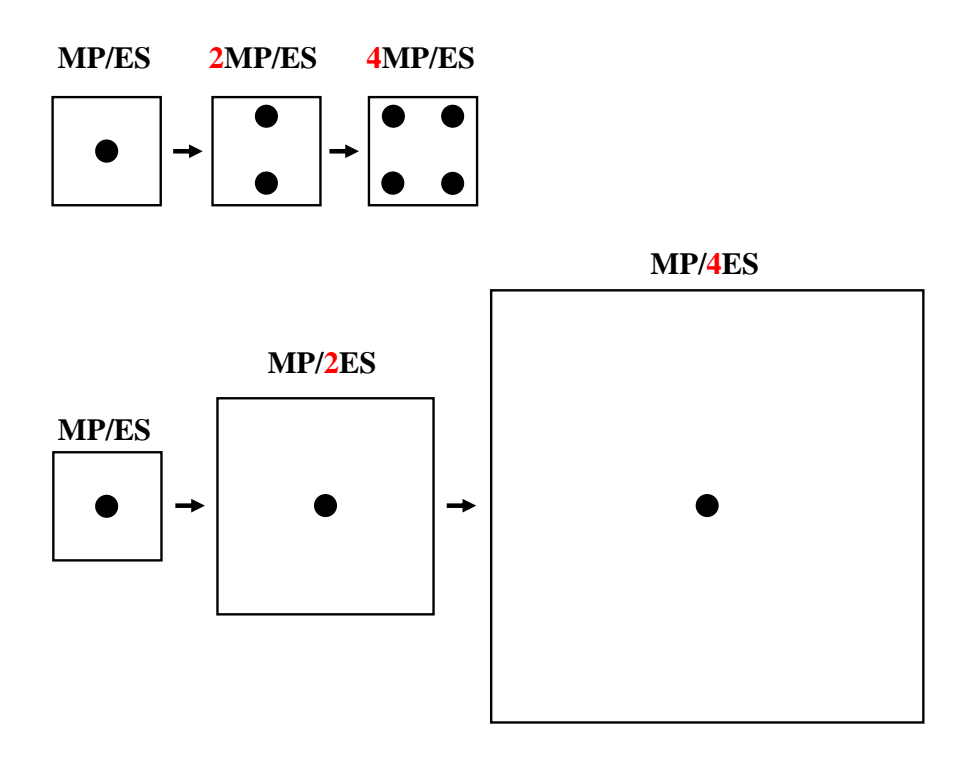


Figure 3-5 Selecting the discretisation settings of each case study for the sensitivity analysis based on the number of the material points per element (MP) and element size (ES) of the benchmark case, MP/ES.

| Discretisation Settings          | MP/ES   | 2MP/ES  | 4MP/ES  | MP/2ES | MP/4ES |
|----------------------------------|---------|---------|---------|--------|--------|
| Initial Point Density (-)        | 50      | 62      | 80      | 25     | 13     |
| Point Contact Diameter (mm)      | 0.5     | 0.4     | 0.312   | 1      | 1.923  |
| Total No. of Material Points (-) | 74,227  | 137,963 | 290,245 | 9,357  | 1,513  |
| Element to Point Ratio (-)       | 1.05    | 1.3     | 1.68    | 1.05   | 1.05   |
| Element Size (mm)                | 0.525   | 0.525   | 0.525   | 1.05   | 2.1    |
| Material Points per Element (-)  | ~1      | ~2      | ~4      | ~1     | ~1     |
| Total No. of Elements (-)        | 132,651 | 132,651 | 132,651 | 19,683 | 4,913  |

Table 3-1 Discretisation settings for the cases used in the sensitivity analysis.

# **3.5.3. Time Step**

Due to the conditional stability of explicit time integrations, a time step smaller than a critical value should be selected for the explicit TLMPM used in this work. Typically, rather than using a fixed time step, explicit MPM simulations employ an adaptive time step that is adjusted based on the velocity of the material points, as follows [143]: First, the dilatational wave speed,  $c_{dil}$ , is calculated using the Lamé constants  $\lambda$  and  $\mu$ , where  $\lambda$  is the first Lamé constant and  $\mu$  denotes the shear modulus:

$$c_{dil} = \sqrt{\frac{\lambda + 2\mu}{\rho}} \tag{3-22}$$

$$\lambda = \frac{\upsilon E}{(1+\upsilon)(1-2\upsilon)} \tag{3-23}$$

$$\mu = \frac{E}{2(1+\nu)} \tag{3-24}$$

Subsequently, the maximum wave speed is calculated using Equation (3-25) [175]:

$$\mathbf{c} = \left( \max_{p} (c_{dil} + |v_{p}^{x}|), \max_{p} (c_{dil} + |v_{p}^{y}|), \max_{p} (c_{dil} + |v_{p}^{z}|) \right)$$
(3-25)

where  $v_p^x$ ,  $v_p^y$  and  $v_p^z$  are the x, y and z components of the material point p's velocity. Ultimately, the time step  $\Delta t$  is chosen as follows:

$$\Delta t = a^t \min\left(\frac{ES^x}{c_x}, \frac{ES^y}{c_y}, \frac{ES^z}{c_z}\right)$$
 (3-26)

where  $ES^x$ ,  $ES^y$  and  $ES^z$  denote the element size in the x, y and z directions, and  $a^t$  is a time step multiplier between 0 and 1.

The code utilised in this work currently only allows for employing a fixed time step. Considering that  $c_{dil}$  is a constant material-dependent parameter, a fixed value for the critical time step is determined by considering the highest velocity attained by the material points throughout the simulation, and the smallest element size. As the mesh elements are hexahedral and the maximum velocity of any of the material points throughout the simulation does not exceed the initial/impact velocity ( $V_i$ ) in the impact direction (z axis here), Equation (3-26) reduces to:

$$\Delta t = a^t \frac{ES}{c_{dil} + |V_i|} \tag{3-27}$$

Subsequently,  $ES/(c_{dil}+|V_i|)$  is calculated for each of the cases in Section 3.5.2 with regards to the element size (refer to Table 3-1), and the results are displayed in Table 3-2. Accordingly, considering only the order of magnitude of the smallest values shown in Table 3-2, i.e. 1  $\mu$ s, three different time steps-100 ns, 10 ns and 1 ns-are selected for all the cases, corresponding to



values of 0.1, 0.01 and 0.001 for  $a^t$ , respectively. This results in a total of 15 case studies for the sensitivity analysis. Note that with regards to the aforementioned time step values (and the discussion in Section 3.5.1),  $n_t$  is adjusted for each case so that an output file is generated every 150  $\mu$ s in the simulation.

Table 3-2 Calculation of the critical time step for the sensitivity analysis: values of  $ES/(c_{dil}+|V_i|)$  for the cases discussed in Section 3.5.2.

| Cases                     | MP/ES | 2MP/ES | 4MP/ES | MP/2ES | MP/4ES |
|---------------------------|-------|--------|--------|--------|--------|
| $ES/(c_{dil}+ V_i )$ (µs) | 8     | 8      | 8      | 16     | 32     |

# 3.5.4. Sensitivity Analysis Results

## 3.5.4.1. Effect of material points and mesh discretisation

Figure 3-6 shows the change in contact force and displacement over time obtained from the simulations, with the analytical results [27] overlaid for comparison. Figure 3-6 (a) emphasises the effect of increase in the number of material points per element, while Figure 3-6 (b) highlights the effect of increase in the element size. For brevity, only the results for the time step of 100 ns are presented here. The results for the time steps of 10 and 1 ns are provided in Figures A-1 and A-2 of Appendix A, respectively.

Considering Figures 3-6 (a) and (b), in general, the numerical results are in agreement with the analytical curves. With regards to Figure 3-6 (a), there is a small difference between the values of  $F/F^*$  and  $\delta/\delta^*$  during the unloading phase of cases MP/ES, 2MP/ES and 4MP/ES. However, this discrepancy becomes noticeably more prominent with increase in the element size, comparing cases MP/ES, MP/2ES and MP/4ES, as seen in Figure 3-5 (b). Considering Figures A-1 and A-2 of Appendix A, a decrease in the time step slightly diminishes this disparity between the cases. All in all, it appears that compared to cases MP/2ES and MP/4ES, cases MP/ES and 2MP/ES can reproduce the numerical results of the most refined case study



(4MP/ES) with a higher accuracy. This is also confirmed by the insignificant values of the mean absolute error (MAE) and mean squared error (MSE) for  $F/F^*$  and  $\delta/\delta^*$  corresponding to cases MP/ES and 2MP/ES, in reference to case 4MP/ES (refer to Table 3-3). MAE and MSE are calculated using Equations (3-28) and (3-29), shown below:

$$MAE = \frac{\sum_{i=1}^{n_d} \left| y_{case,i} - y_{reference,i} \right|}{n_d}$$
(3-28)

$$MSE = \frac{\sum_{i=1}^{n_d} (y_{case,i} - y_{reference,i})^2}{n_d}$$
(3-29)

where y denotes an output variable ( $F/F^*$  and  $\delta/\delta^*$  here) and  $n_d$  is the number of the data points. Subscript *case* refers to cases MP/ES and 2MP/ES, and *reference* to case 4MP/ES.

Table 3-3 Mean absolute error (MAE) and mean squared error (MSE) values for  $F/F^*$  and  $\delta/\delta^*$  corresponding to cases MP/ES and 2MP/ES, in reference to case 4MP/ES.

|        | MA                  | <b>AE</b>          | MSE                |                    |  |
|--------|---------------------|--------------------|--------------------|--------------------|--|
| Cases  | $F/F^*$             | $\delta/\delta^*$  | <i>F/F</i> *       | $\delta/\delta^*$  |  |
| MP/ES  | 13×10 <sup>-3</sup> | 8×10 <sup>-3</sup> | 2×10 <sup>-4</sup> | 2×10 <sup>-4</sup> |  |
| 2MP/ES | 9×10 <sup>-3</sup>  | 3×10 <sup>-3</sup> | 2×10 <sup>-4</sup> | 3×10 <sup>-5</sup> |  |

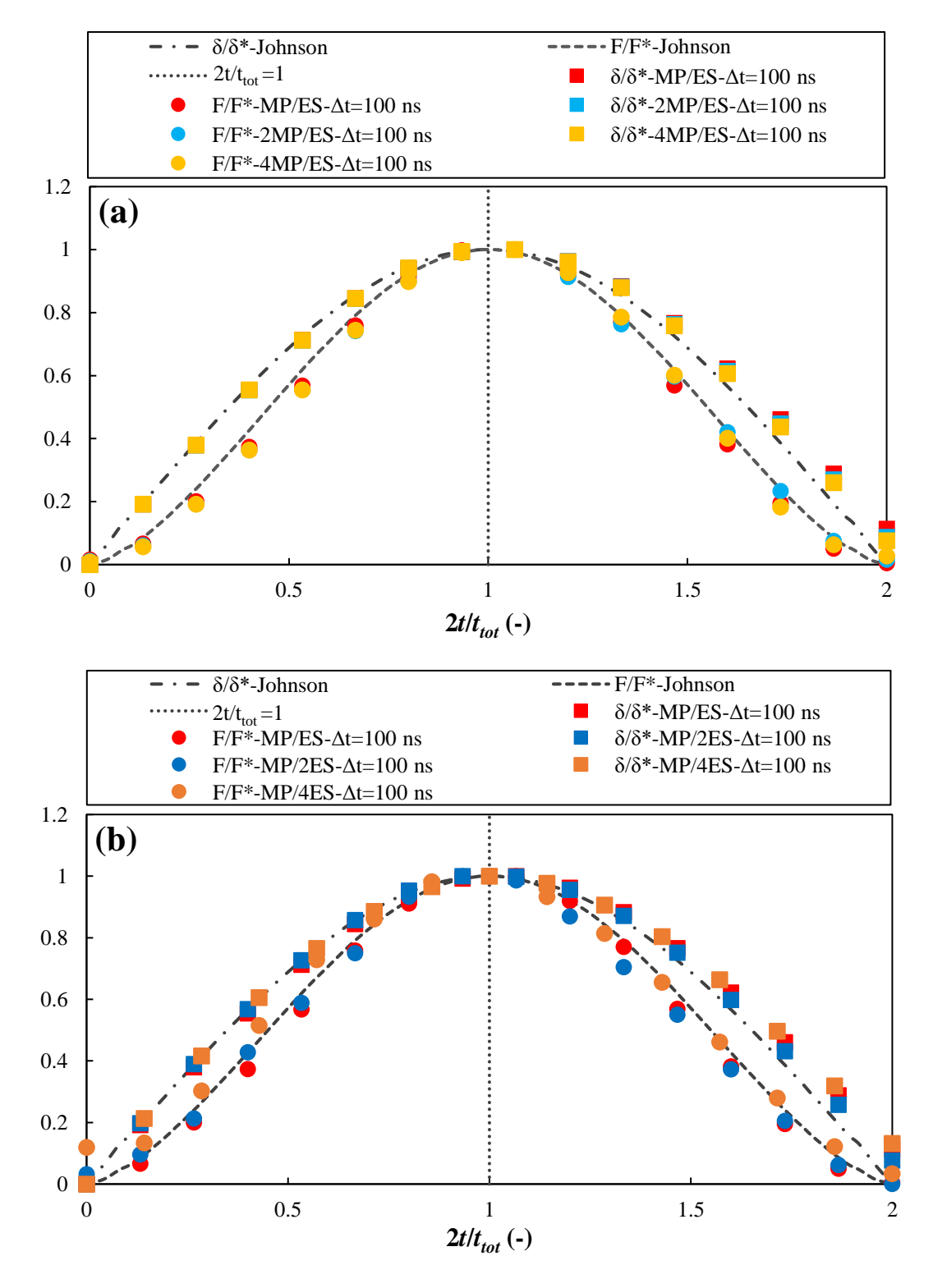


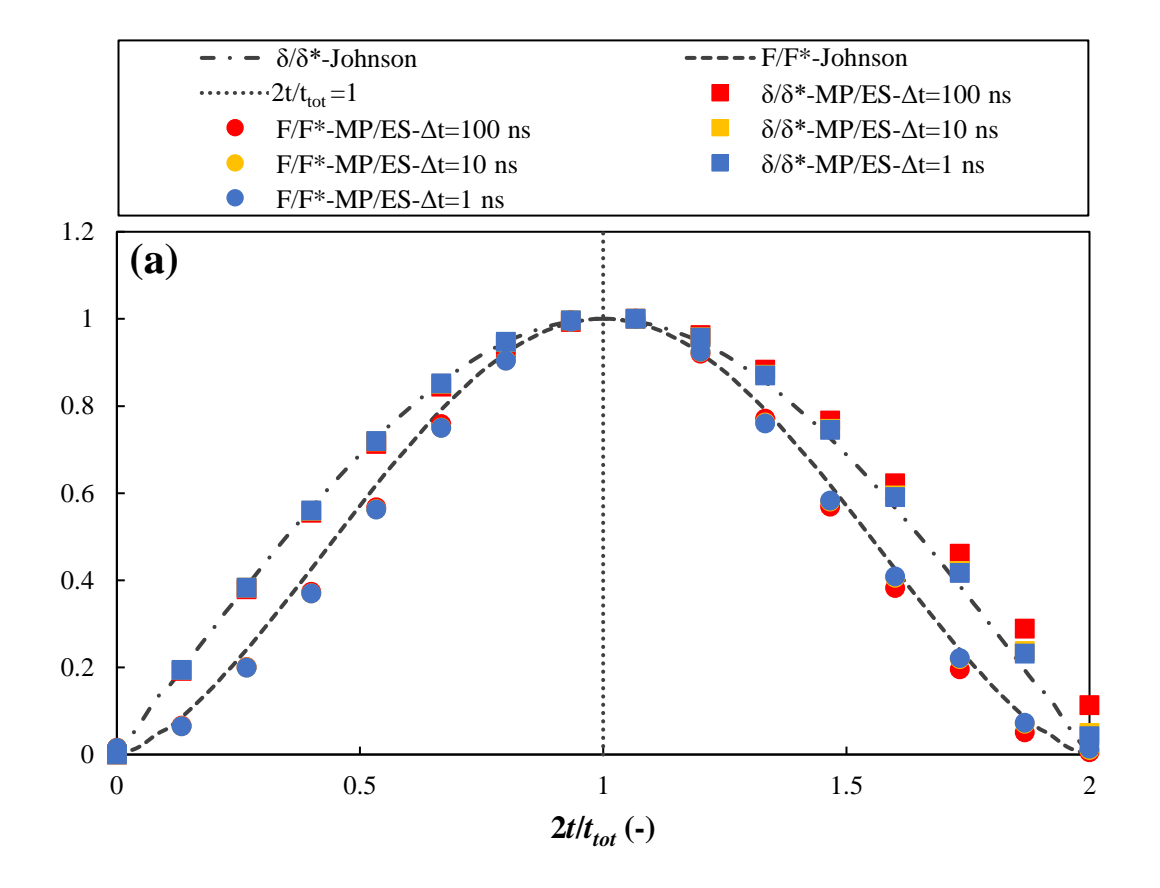
Figure 3-6 Variation of the contact force and displacement with time for the impact of an elastic sphere undergoing small deformation (refer to Section 3.5.1), calculated using Johnson's [27] analytical approach (dashed lines) and MPM simulations (discrete symbols) considering a time step of 100 ns for (a) cases MP/ES, 2MP/ES and 4MP/ES, to highlight the effect of increasing the number of material points per element, and (b) cases MP/ES, MP/2ES and MP/4ES, to highlight the effect of increasing the element size, for the sensitivity analysis.



# 3.5.4.2. Effect of Time Step

Variation of contact force and displacement with time using different time steps is shown in Figure 3-7 for cases MP/ES, 2MP/ES and 4MP/ES. Similar graphs are presented in Figure A-3 of Appendix A for cases MP/2ES and MP/4ES.

With regards to Figure 3-7, decreasing the time step intuitively results in a better agreement between the numerical and analytical values of  $F/F^*$  and  $\delta/\delta^*$ . Nevertheless, all of the selected time steps lead to acceptable numerical results, as verified by the analytical curves [27].



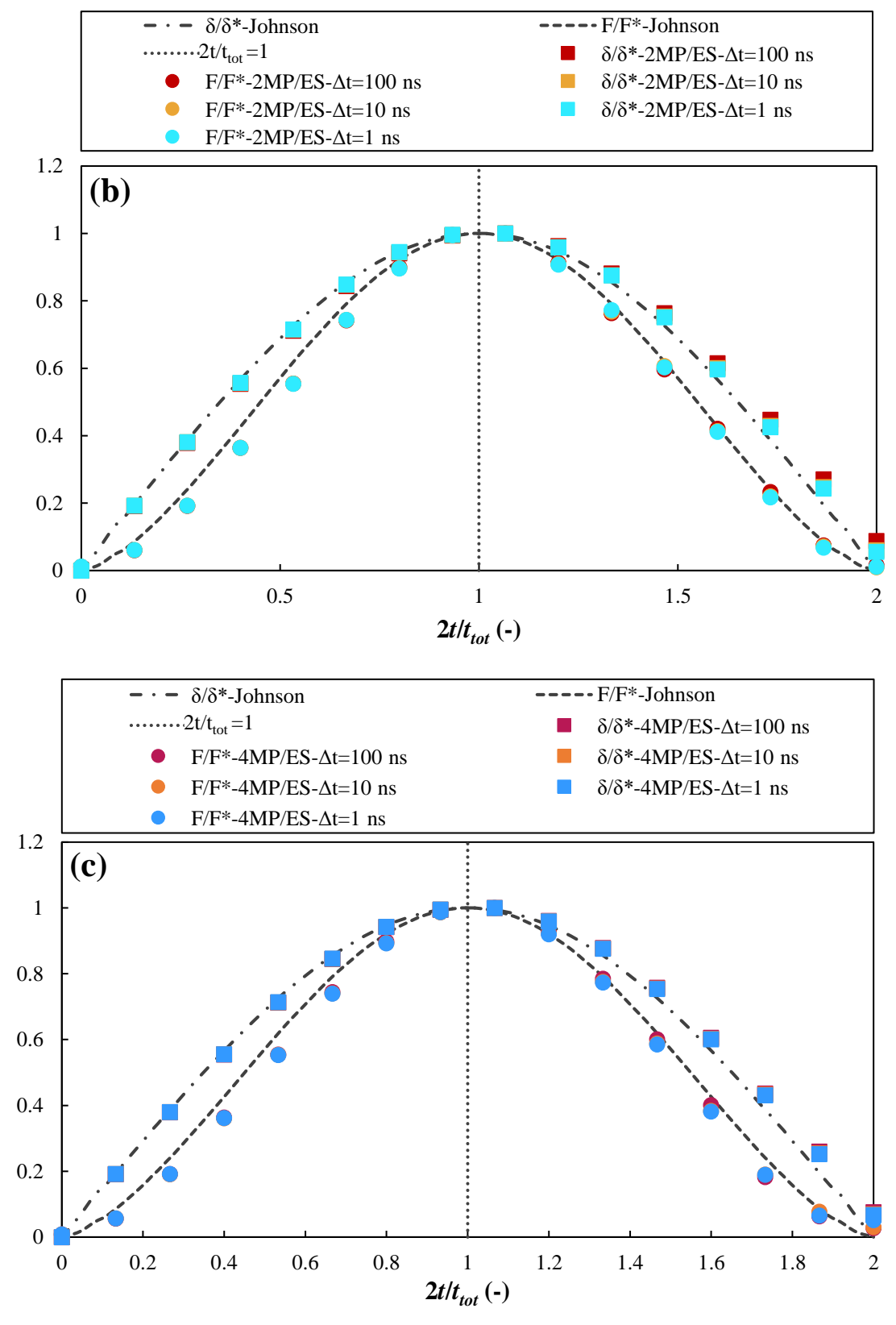


Figure 3-7 Variation of the contact force and displacement with time for the impact of an elastic sphere undergoing small deformation (refer to Section 3.5.1), calculated using Johnson's [27] analytical approach (dashed lines) and MPM simulations (discrete symbols) considering time steps of 1, 10 and 100 ns for (a) case MP/ES, (b) case 2MP/ES and (c) case 4MP/ES of the sensitivity analysis.



### 3.5.4.3. Computational Cost

The total computational time for a simulation is calculated by multiplying the computational time required for the generation of one output file, by the total number of the output files (one-core PC with 4GB allocated RAM). For the current sensitivity analysis, the latter depends on contact duration, which in turn is influenced by the impact conditions and material properties. Thus, as the currently considered case studies share the same impact conditions and material properties, they have approximately the same number of output files (24 or 25 output files). On the other hand, the computational time per output file is greatly affected by the number of material points, mesh discretisation, and time step. Therefore, the computational time required to generate one output file is presented in Table 3-4, for all of the case studies. With regards to Table 3-4, the computational time per output file increases with the number of material points, or more noticeably, with a decrease in the time step. On the other hand, increasing the element size reduces the computational time per output file. It should be noted that the current sensitivity analysis is based on a small deformation case. In scenarios involving large deformation, the number of output files and the total computational time will increase significantly. Therefore, in order to manage the computational time effectively, it is crucial to carefully select the time step and discretisation settings.

Table 3-4 Computational time required for generation of one output file for all of the case studies in the sensitivity analysis.

| Computational Time per Output File (min) |       |        |        |        |        |
|--|-------|--------|--------|--------|--------|
| Time Step (ns)                           | MP/ES | 2MP/ES | 4MP/ES | MP/2ES | MP/4ES |
| 100                                      | 3     | 5      | 10     | <1     | <1     |
| 10                                       | 28    | 46     | 93     | 3      | <1     |
| 1  | 261   | 449    | 864    | 32     | 4      |



# 3.5.5. Sensitivity Analysis Conclusions

Based on the observations in Section 3.5.4.1 and the fact that increasing the number of material points generally enhances the representation of continuum material behaviour, it is deduced that compared to cases MP/2ES and MP/4ES, cases MP/ES, 2MP/ES and 4MP/ES yield more accurate results. Thus, the material point and mesh discretisation settings of these cases can be used as a benchmark for further simulations. The results from Section 3.5.4.2 suggest that considering only the order of magnitude of  $ES/(c_{dil}+|V_i|)$  for a certain case, either of the values 0.1, 0.01 and 0.001 for  $a^i$  ensure the stability of a simulations, as well as the accuracy of the results. When selecting the appropriate time step and discretisation settings, it is important to consider not only stability and accuracy, but also the computational cost. Therefore, based on the computational time for all the case studies discussed in Section 3.5.4.3, the settings for case MP/ES and a value of 0.1 for  $a^i$  appear to be the most suitable for further simulations.



# 4. Simulation of Impact for Elastic-Perfectly Plastic Particles

# 4.1. Overview

In this chapter, the numerical method detailed in Chapter 3 is implemented to investigate the normal impact of an elastic-perfectly plastic particle with a rigid wall, covering a wide range of material properties and impact velocities. Experimental investigation of the impact phenomenon is arduous due to its dynamic nature, while the nonlinearity of the problem leads to inadequacy of the analytical models that use simplified assumptions. Therefore, numerical simulations provide a great means for the analysis of the phenomena taking place throughout impact. The current analysis focusses on variables and expressions that provide insights into the plastic deformation and rebound behaviour of the particle during impact. Additionally, the evolution of the contact force and displacement is briefly studied. The objective of these analyses is to establish the link between the impact behaviour of the particle, and its material properties and impact velocity. Consequently, empirical equations are suggested where possible. Parts of the results from this chapter have been published in [164]. All of the simulations presented in this work have been undertaken on ARC4, part of the High Performance Computing facilities at the University of Leeds, UK.

# 4.2. Case Studies and Simulation Setup

The elastic-perfectly plastic particle is modelled as a sphere with radius R=250  $\mu$ m and Poisson's ratio  $\nu$ =0.35, normally impacting a rigid wall (in the -z direction) at five different impact velocities ( $V_i$ ) of 10, 20, 30, 40 and 50 m/s (Figure 4-1). In order to include a wide range of material properties, four different densities ( $\rho$ ) of 1,000, 2,000, 4,000 and 8,000 kg/m<sup>3</sup> are considered for the particle. For each density, three different values of 1, 10 and 100 GPa for

Young's modulus (E), and eight different values of 20, 40, 80, 160, 320, 640, 1,280 and 2,560 for the ratio of Young's modulus to yield strength (E/Y, where Y denotes the yield strength) are taken into account. This leads to a total of 480 cases being investigated. It should be noted that group E/Y is selected to represent the mechanical properties of the material, as it repeatedly emerges in formulae connected to plastic deformation in fundamental studies, e.g. [27,176–178] and more recent studies such as [110,146,179].

With regards to the sensitivity analysis results (Section 3.5.5) favouring case MP/ES (refer to Table 3-1), the following settings are used: the particle is discretised into 74,227 material points, and the wall is placed 30 µm below the particle (3 times the distance between the material points, consistent with case MP/ES). This is to ensure that the material points are not in contact with the wall at the start of the simulation. Initially, the mesh size is adjusted based on an element to point ratio of 1.05 for all the cases (consistent with case MP/ES). Subsequently, a time step of 10 ps is selected for all the cases, considering a multiplier of  $a^t$ =0.1, and the order of magnitude of the cases having the smallest  $ES/(c_{dil}+|V_i|)$  value (0.1 ns), i.e. cases with  $\rho=1,000 \text{ kg/m}^3$ , E=100 GPa and  $V_i=50 \text{ m/s}$ . However, it is found that for cases undergoing a comparatively small deformation (all cases with E=100 GPa and cases with E=10GPa when  $\rho$ =1,000 and 2,000 kg/m<sup>3</sup>), these settings would lead to notable scatter in the data for the coefficient of restitution. As seen in Sections 3.5.4.1 and 3.5.4.2, the unloading phase and consequently, the coefficient of restitution are affected by the number of material points per element and the time step. Thus, increasing the former or decreasing the latter is expected to somewhat remedy the issue. As selecting a smaller time step would significantly increase the computational cost, it is preferred to increase the number of material points per element instead. Therefore, the element to point ratio is changed to 1.5 for all the cases with E=100 GPa and cases with E=10 GPa when  $\rho=1,000$  and 2,000 kg/m<sup>3</sup>. These setting result in a total of 50,653 and 132,651 hexahedral elements for the mesh, corresponding to the element to point

ratios of 1.5 and 1.05, respectively. Damping and friction are not applied. A cubic-spline shape function is used and the von Mises yield criterion is considered.

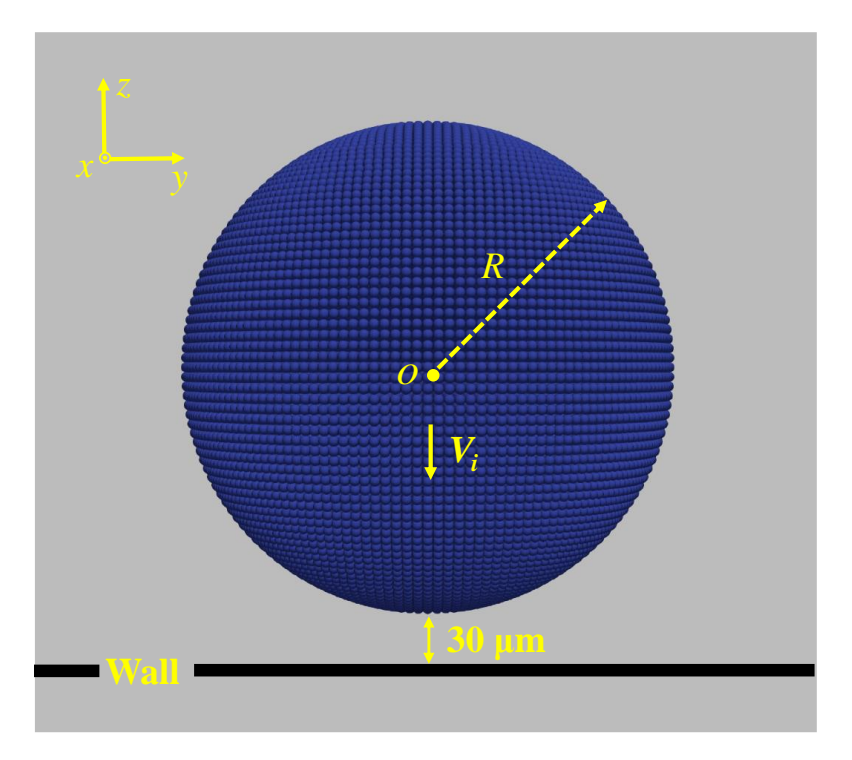


Figure 4-1 Visualisation of the modelled elastic-perfectly plastic particle impacting a rigid wall, detailing the initial and boundary conditions (illustration is not to scale for presentation purposes).

# 4.3. Analysis of Deformation

# 4.3.1. Method Scope

To illustrate the diversity in the modelled range of deformation, visualisations of the particle after rebound are shown in Figure 4-2 for four different cases, as examples. Considering Figure 4-2 (d), it is clear that the method allows for modelling very large deformation. However, for several cases exhibiting the two extremes of deformation, i.e. extensive or slight, no results/inaccurate results are obtained. This is highlighted in Tables B-1 to B-5 of Appendix B, which show that instances of slight deformation occur at lower velocities (10 and 20 m/s) for cases having a high Young's modulus and a low ratio of Young's

modulus to yield strength. As the impact velocity increases, cases with a low Young's modulus and a high ratio of Young's modulus to yield strength begin to undergo extensive deformation at high densities, and with further increase in the impact velocity, at all densities. It is well known that MPM does not generally perform well for cases of small deformation, as the material points might not lie at optimal positions for numerical integration [143]. Also, at very high impact velocities, temperature and strain rate effects can influence the material behaviour, and the use of an elastic-perfectly plastic material model may no longer be appropriate for certain cases. Nevertheless, it is important to note that in the case of the failed examples here, materials with such properties do not exist in reality. Therefore, it is expected that the constitutive laws derived from real materials fail to model such hypothetical materials. For comparison, various real materials that exhibit both elastic and plastic properties are listed in Table 4-1.

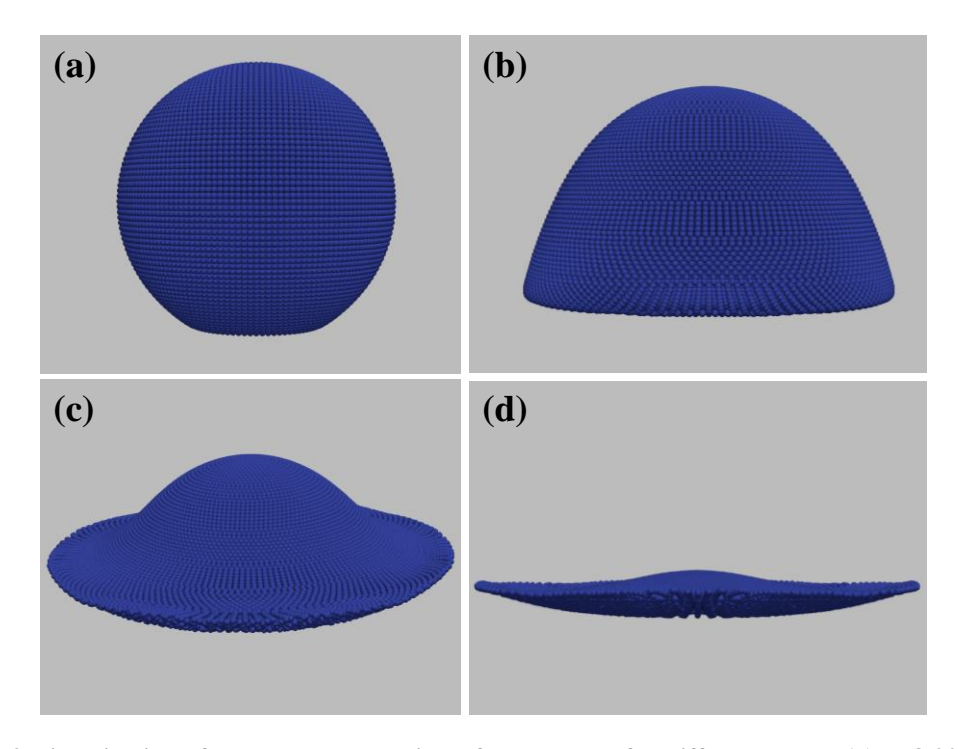


Figure 4-2 Visualisation of the modelled particle after rebound for different cases: (a)  $\rho$ =8,000 kg/m³, E=100 GPa, E/Y=160; (b)  $\rho$ =8,000 kg/m³, E=1 GPa, E/Y=40; (c)  $\rho$ =2,000 kg/m³, E=1 GPa, E/Y=320 and (d)  $\rho$ =8,000 kg/m³, E=1 GPa, E/Y=160. The orientation is chosen randomly to provide the best view of the extent of deformation.



Table 4-1 Various materials that exhibit both elastic and plastic properties, taken from [180]. NA denotes "not applicable".

| Material                                 | $\rho$ (kg/m <sup>3</sup> ) | E (GPa)  | Y (MPa)  | <i>E</i> / <i>Y</i> (-) |
|--|-----------------------------|----------|----------|-------------------------|
| Copper                                   | 8,960                       | 128      | 69-365   | 351-1,855               |
| Pure Aluminium                           | 2,700                       | 70.2     | 10-30    | 2,340-7,020             |
| Ti6Al4V (Titanium Alloy)                 | 4,430                       | 114      | 830      | 137.3                   |
| Aluminium Alloys                         | NA                          | 68-82    | 30-500   | 136-2,733               |
| Nickle Alloys                            | NA                          | 190-220  | 70-1,100 | 173-3,143               |
| High Density Polyethylene (HDPE)         | 940-960                     | 0.6-1.4  | 18-30    | 20-78                   |
| Polypropylene (PP)                       | 900-915                     | 1.3-1.8  | 25-40    | 32-72                   |
| Polystyrene (PS)                         | 1,050                       | 3.1-3.3  | 50       | 62-66                   |
| Un-plasticised Polyvinyl Chloride (UPVC) | 1,380-1,400                 | 2.7-3    | 50-60    | 45-60                   |
| Polytetrafluoroethylene (PTFE)           | 2,130-2,230                 | 0.4-0.75 | 11.7     | 34-64                   |

The limits of the deformation range that the code successfully models for elastic-perfectly plastic impact are marked by the equivalent plastic strain,  $\varepsilon_p$ , calculated at the instant of rebound from Equation (4-1), where  $\varepsilon^p_{ij}$  is the deviatoric plastic strain. The **instant of rebound** is taken as the first instant at which the velocity of the particle in the impact direction reaches a constant value, after contact is lost. The particle velocity in the impact direction ( $V^z$ ) is calculated for each time step using Equation (4-2), where  $m_p$  and  $v_p^z$  are respectively the mass of the material point p and its velocity in the impact direction (z axis here), and  $N_p$  is the number of the material points. Accordingly, the capability of the code in modelling deformation for an elastic-perfectly plastic material is limited to the equivalent plastic strain values ranging from  $2.6 \times 10^{-6}$  (slight deformation) to 1.53 (extensive deformation).

$$\varepsilon_p = \sqrt{\frac{2}{3} \varepsilon_{ij}^p \varepsilon_{ij}^p} \tag{4-1}$$

$$V^{z} = \sum_{p=1}^{N_{p}} m_{p} v_{p}^{z} / \sum_{p=1}^{N_{p}} m_{p}$$
 (4-2)

It should also be noted that four additional cases are dismissed from further analysis as they do not undergo plastic deformation (refer to Tables B-1 and B-2 of Appendix B). This is due to the fact that for these cases, the impact velocity of the particle is lower than its yield velocity,  $V_{\nu}$ , defined by Johnson [27] using Equation (4-3), below:

$$V_{y} = \left(\frac{26Y}{\rho}\right)^{1/2} \left(\frac{Y}{E^{*}}\right)^{2} \tag{4-3}$$

## 4.3.2. Equivalent Plastic Strain

To highlight the effect of the material properties on the plastic deformation induced by the impact, the equivalent plastic strain,  $\varepsilon_p$ , is plotted against the ratio of Young's modulus to yield strength, E/Y, for all the cases with the impact velocity of 50 m/s, as displayed in Figure 4-3. Similar graphs for the rest of the impact velocities are presented in Figures B-1 to B-4 of Appendix B. Due to the high number of the case studies, no legends are displayed on any of the aforementioned graphs, and the reader is referred to Table 4-2 for the designation of the symbols.

Table 4-2 Symbol reference for Figure 4-3, and Figures B-1 to B-4 of Appendix B.

| Legend              |       |          |       |       |  |
|---------------------|-------|----------|-------|-------|--|
| $ ho~({ m kg/m^3})$ |       |          |       |       |  |
| E (GPa)             | 1,000 | 2,000    | 4,000 | 8,000 |  |
| 1                   | •     | <b>A</b> | •     | •     |  |
| 10                  | •     | <b>A</b> |       | •     |  |
| 100                 | •     | <b>A</b> |       | •     |  |

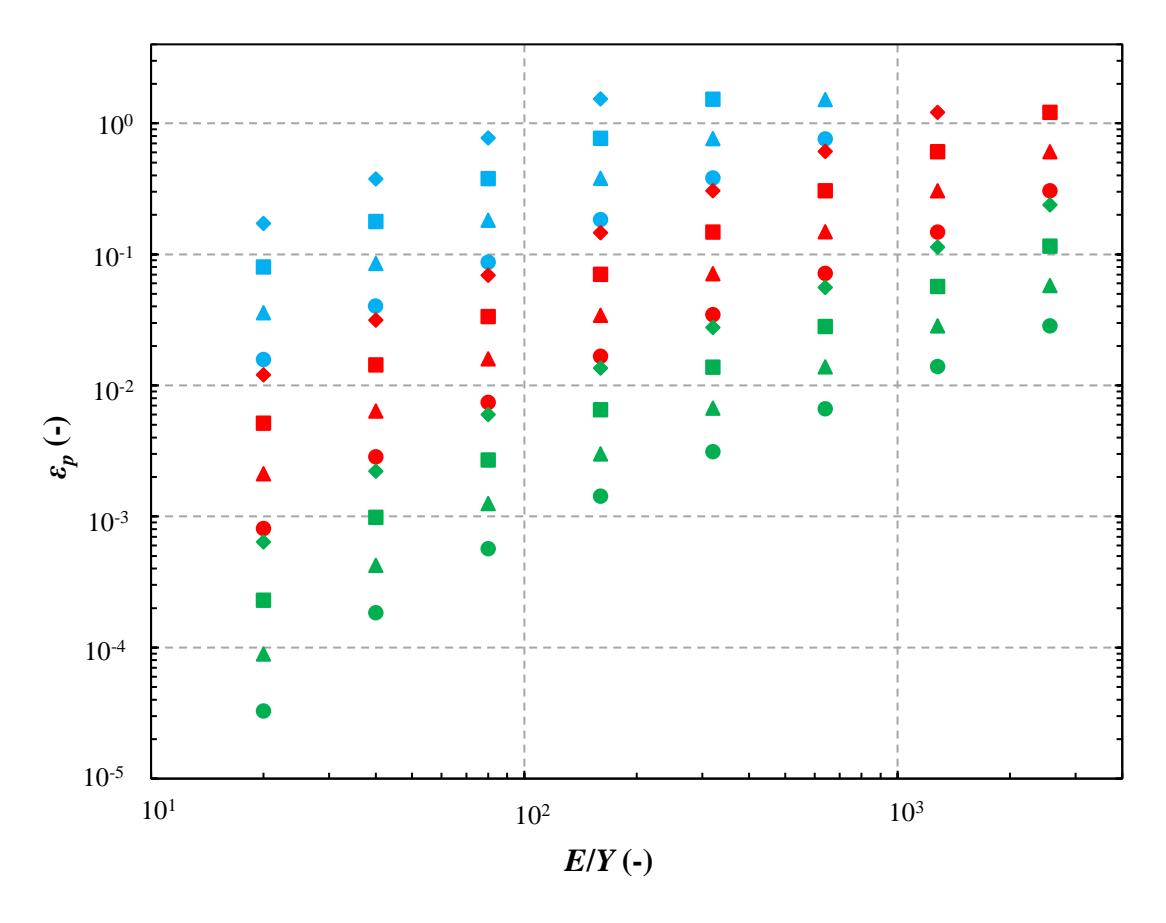


Figure 4-3 The equivalent plastic strain,  $\varepsilon_p$ , as a function of the ratio of Young's modulus to yield strength, E/Y, for all the cases with an impact velocity of 50 m/s. For designation of the symbols, see Table 4-2.

With regards to Figure 4-3, for cases with the same density and Young's modulus, the equivalent plastic strain,  $\varepsilon_p$ , intuitively increases with an increase in the ratio of Young's modulus to yield strength, E/Y, which corresponds to a decrease in the material yield strength. For cases with the same E/Y and density,  $\varepsilon_p$  increases as the yield strength decreases. Moreover, when both E/Y and Young's modulus (and consequently, the yield strength) are constant,  $\varepsilon_p$  increases with the density of the material. This is due to the fact that, for particles of the same size and impact velocity, an increase in the material density leads to a higher kinetic energy upon impact, resulting in a larger plastic deformation.

To include the effect of particle impact velocity and the kinetic energy of impact,  $\varepsilon_p$  is plotted as a function of the dimensionless group  $\rho V_i^2/Y$  for all the case studies, as shown in

Figure 4-4. This group is used by Johnson [27] to distinguish between various regimes of deformation behaviour during the impact of metal particles. Considering Figure 4-4,  $\varepsilon_p$  increases with an increase in  $\rho V_i^2/Y$ , which is expected as the increase in the latter is due to the decrease in the yield strength of the material or increase in the incident kinetic energy. Moreover, the data points remarkably unify for all the cases, suggesting that the extent to which an elastic-perfectly plastic particle undergoes plastic strain is only affected by the yield strength and incident kinetic energy of the particle, with no sensitivity to Young' modulus. Consequently, the equation of the fitted line in Figure 4-4 can be used to estimate the equivalent plastic strain for the impact of an elastic-perfectly plastic particle, as shown by Equation (4-4) below:

$$\varepsilon_p = 0.474 \left( \frac{\rho V_i^2}{Y} \right) \tag{4-4}$$

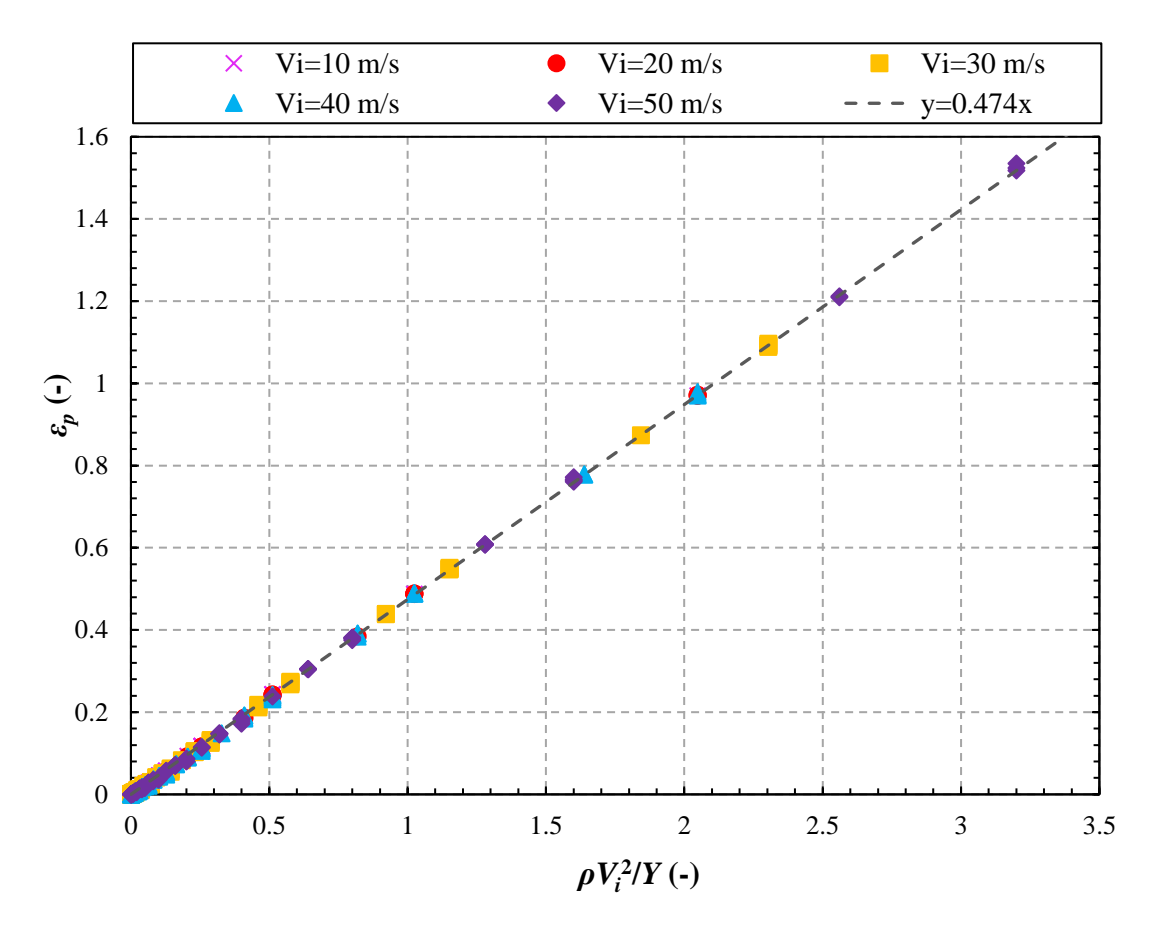


Figure 4-4 The equivalent plastic strain,  $\varepsilon_p$ , as a function of the dimensionless group  $\rho V_i^2/Y$ , for all the case studies.

Figure 4-5 illustrates the distribution of the plastic strain within the particle, shown as contours of the plastic strain in the impact direction ( $\varepsilon^{\rho}_{zz}$ ) shortly after rebound. This example uses the cases with  $\rho$ =2,000 kg/m³, E=1 GPa and E/Y=320, across all the impact velocities. It should be noted that the contours are displayed on the surface of a plane slicing the particle in half, with the plane normal pointing towards the observer (along the x axis). Considering Figure 4-5 (a), for  $V_i$ =10 m/s, the plastic strain is primarily concentrated in the contact area and the maximum strain (-0.41) is located beneath the contact surface, where the plastic deformation is potentially initiated. The top part of the particle remains undeformed, while a slight positive strain of 0.003 is observed at the top edges of the contact area, attributed to material displacement. With regards to Figure 4-5 (b) to (e), higher impact velocities lead to larger

plastic deformation, with  $\varepsilon^p_{zz}$  reaching up to -3.3 at 50 m/s, and the maximum strain shifting to the contact area. Moreover, the top part of the particle experiences a small positive strain, potentially due to the reflection of the compressive elastic waves as tensile waves, or material displacement. As shown in Figure 4-5 (d), the bottom edges of the particle begin to exhibit jetting when the impact velocity reaches 40 m/s.

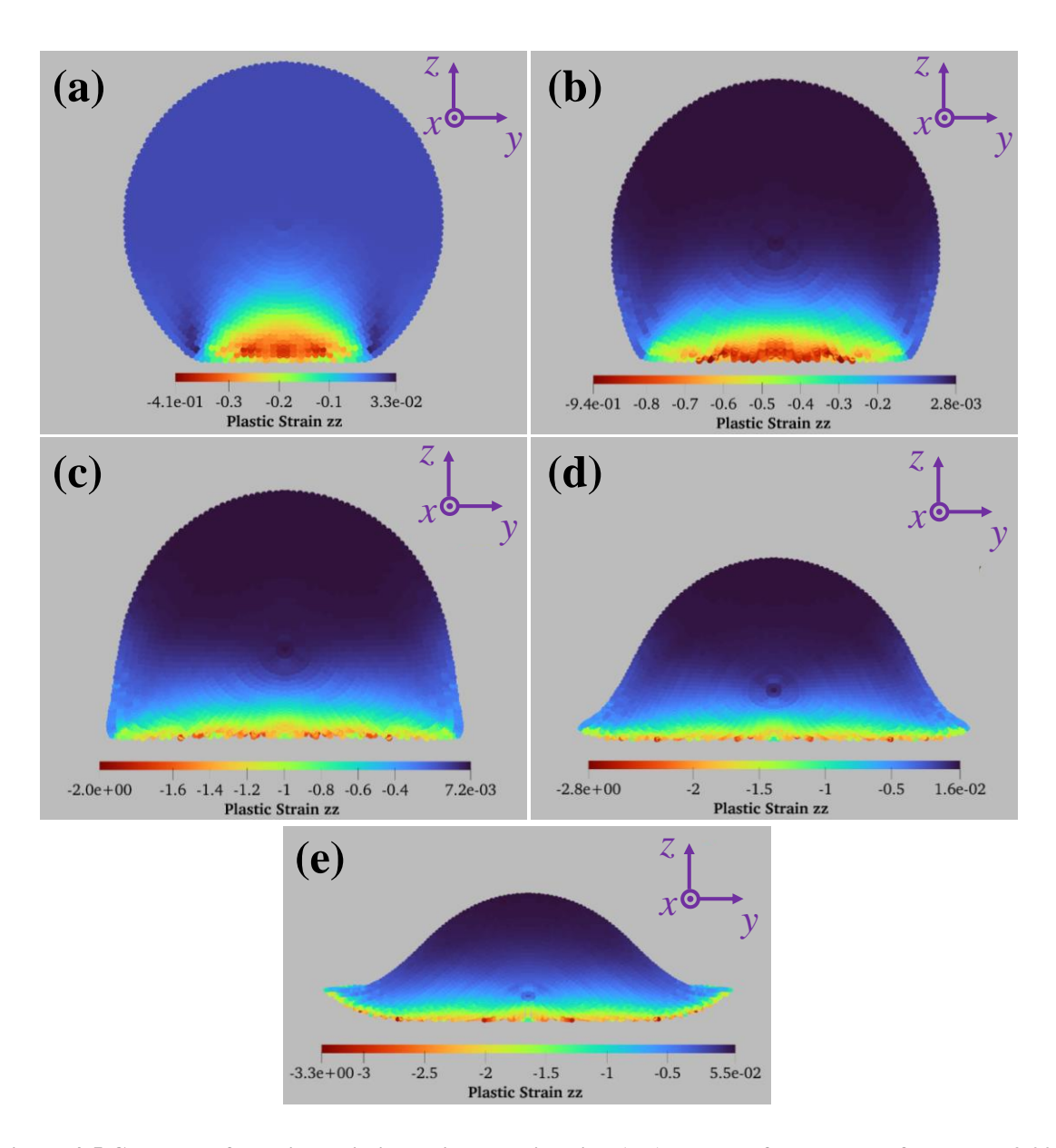


Figure 4-5 Contours of plastic strain in the impact direction  $(\varepsilon^p_{zz})$  shortly after rebound for case  $\rho$ =2,000 kg/m³, E=1 GPa and E/Y=320, with the impact velocity of (a) 10, (b) 20, (c) 30, (d) 40 and (e) 50 m/s. The contours are displayed on a plane slicing the particle in half (normal of the plane is along the x axis).



### 4.3.3. Normalised Deformed Height and Compression Ratio

Another approach for the study of plastic deformation is by investigating the extent to which the particle flattens due to impact. To this end, the deformation extent of the particle is estimated using the "normalised deformed height",  $H_d/D$ , and the "compression ratio", 1-( $H_d/D$ ), where D is the particle diameter before impact, and  $H_d$  is the length of the imaginary centre line connecting the top and bottom of the particle, parallel to the impact direction, after rebound, as shown in Figure 4-6 (a). A lower normalised deformed height indicates a greater deformation extent, while a higher value corresponds to a smaller deformation extent. The opposite is true for the compression ratio. It should be mentioned that  $H_d$  is measured after rebound as an arithmetic mean value, due to the fluctuations caused by the elastic waves within the particle, since damping is not considered. Subsequently,  $H_d/D$  is plotted as a function of  $\rho V_i^2/Y$  for all the case studies, resulting in a master curve, as shown in Figure 4-6 (a).

Considering Figure 4-6 (a),  $H_d/D$  is intuitively decreasing with an increase in  $\rho V_i^2/Y$ , i.e. an increase in the incident kinetic energy or a decrease in the yield strength of the particle. The unification of the data suggests that  $H_d/D$  can be predicted based on the value of the yield strength and incident kinetic energy. However, fitting a curve to the data in Figure 4-6 (a) proves challenging. On the other hand, when 1- $(H_d/D)$  is plotted against  $\rho V_i^2/Y$ , a good fit to the data can be found, as seen in Figure 4-6 (b). Accordingly, the compression ratio increases with a decrease in the yield strength of the material or an increase in the incident kinetic energy. The deformation extent caused by the impact of an elastic-perfectly plastic particle can be estimated using the compression ratio, as defined in Equation (4-5), below:

$$1 - \frac{H_d}{D} = 0.34 \left(\frac{\rho V_i^2}{Y}\right)^{0.66} \tag{4-5}$$

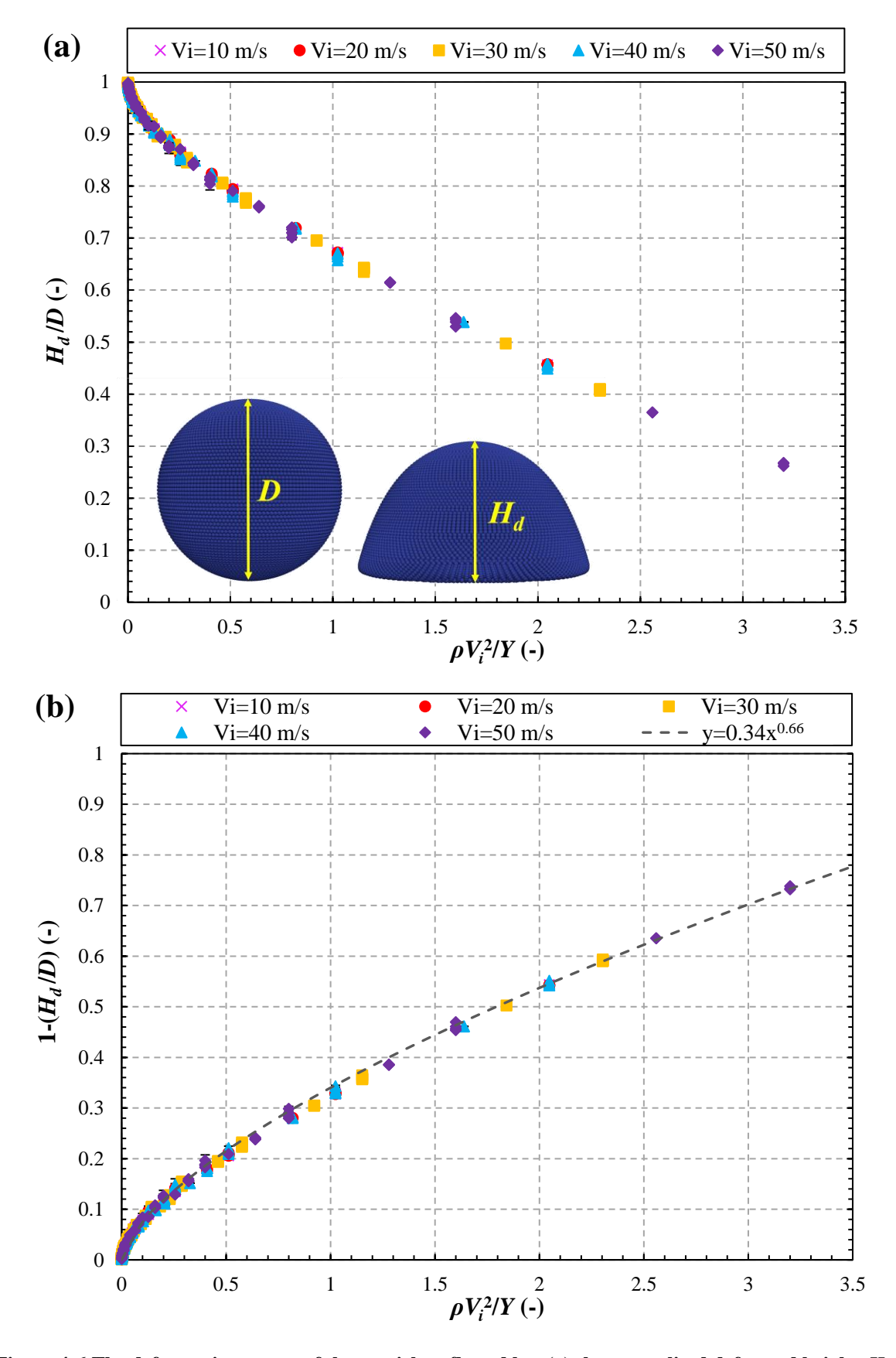


Figure 4-6 The deformation extent of the particle reflected by: (a) the normalised deformed height,  $H_d/D$ , and (b) the compression ratio, 1- $(H_d/D)$ , as a function of  $\rho V_i^2/Y$ , for all the cases.

It is important to note that Equation (4-5) allows for the estimation of the deformation extent based on the material properties and impact velocity. This is particularly valuable for coating techniques such as aerosol deposition and cold spraying, where the compression ratio of the particles influences the final coating quality, in terms of porosity, cohesive strength, bonded area, etc. [36]. Specifically, the impact velocity required to achieve a desired deformation can be determined based on the material properties of the feed particles.

Considering Equations (4-4) and (4-5), the equivalent plastic strain and compression ratio are linked to each other via Equation (4-6). This is further displayed in Figure 4-7, where the data fall perfectly on the line of equality when  $\varepsilon_p$  is plotted as a function of 2.43[1-( $H_d/D$ )]<sup>3/2</sup>.

$$\varepsilon_p = 2.43 \left( 1 - \frac{H_d}{D} \right)^{3/2} \tag{4-6}$$

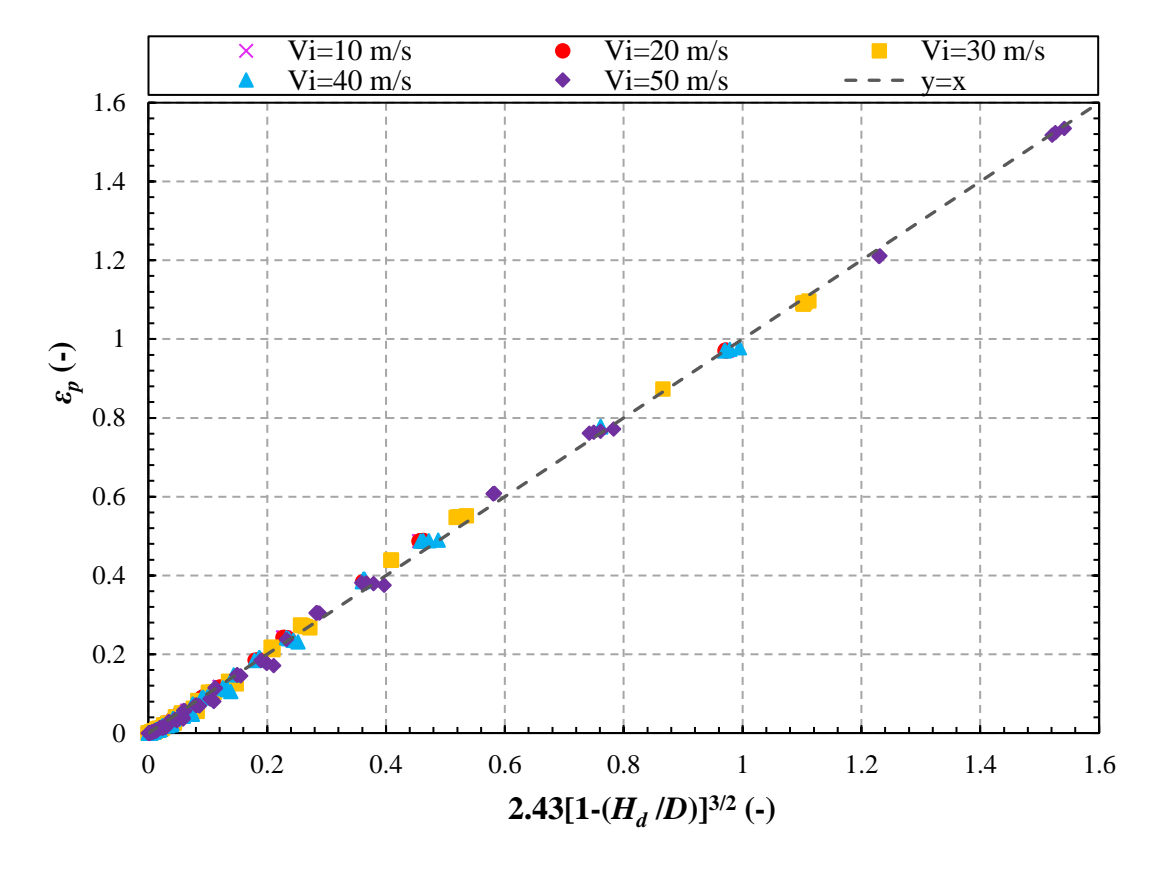


Figure 4-7 The link between the equivalent plastic strain,  $\varepsilon_p$ , and the compression ratio, 1- $(H_d/D)$ .



### 4.3.4. Ratio of Plastic Work to Incident Kinetic Energy

The ratio of the plastic work/energy to the incident kinetic energy,  $W_p/W_i$ , is plotted against  $\rho V_i^2/Y$ , as shown in Figure 4-8. Here,  $W_p$  and  $W_i$  denote the plastic work and incident kinetic energy, respectively. The plastic work,  $W_p$ , is calculated by subtracting the elastic strain energy from the total deformation energy for each time step after rebound, as obtained from the stress-strain relationship. It should be noted that the use of shape functions in MPM leads to minor oscillations in the stress values across element boundaries, and consequently, in the calculated energies [151]. Thus, arithmetic mean values are calculated for  $W_p$ .

Considering Figure 4-8, as  $\rho V_i^2/Y$  increases (corresponding to an increase in the incident kinetic energy or a decrease in the yield strength of the material), the fraction of the incident kinetic energy expended by plastic work increases. The trend is notably fast for smaller values of  $\rho V_i^2/Y$ , especially for cases with a smaller E/Y, and slows down as  $\rho V_i^2/Y$  approaches unity. Moreover, for  $\rho V_i^2/Y < 1$ , the data points group together based on the value of E/Y, suggesting that for this range,  $W_p/W_i$  not only depends on the incident kinetic energy and yield strength of the material, but also on its Young's modulus. This is intuitive since  $W_p/W_i$  is calculated using the elastic strain energy, which is influenced by E. As  $\rho V_i^2/Y$  exceeds unity, the fraction of the initial kinetic energy which is converted to plastic work stays almost constant at approximately 0.95, independent of  $\rho V_i^2/Y$  and E/Y. This is in line with the findings of Johnson [27], who states that when  $\rho V_i^2/Y > 1$ , "the inertia of the deforming material becomes more important than its yield strength, so it behaves more like an ideal fluid than a plastic solid".

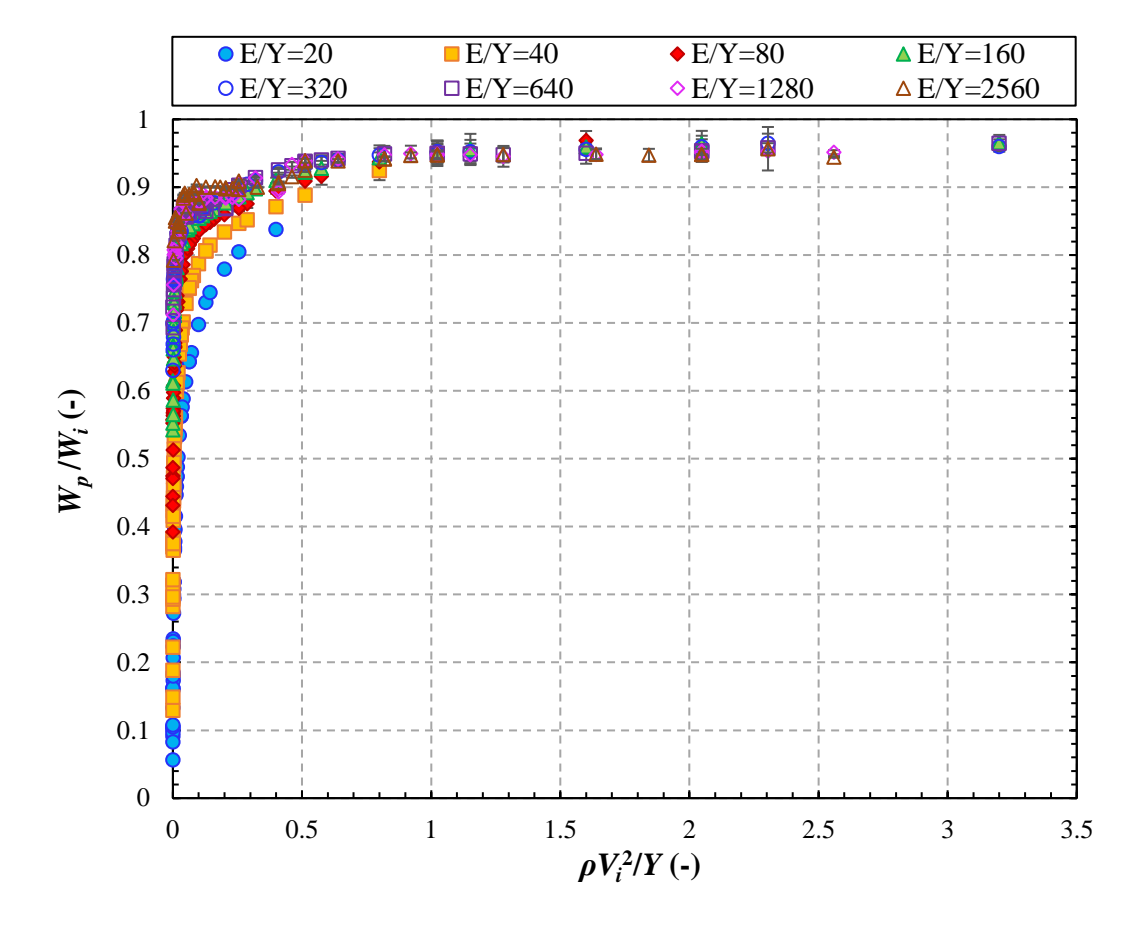


Figure 4-8 The ratio of the plastic work to the incident kinetic energy,  $W_p/W_i$ , as a function of the dimensionless group  $\rho V_i^2/Y$ .

### 4.3.5. Coefficient of Restitution

The coefficient of restitution, e, is calculated using Equation (4-7), where the rebound velocity,  $V_r$ , is taken as the particle velocity in the impact direction, calculated using Equation (4-2), at the instant of rebound (as defined in Section 4.3.1).

$$e = \left| \frac{V_r}{V_i} \right| \tag{4-7}$$

Wu et al. [110] emphasise the influence of the ratio of the impact velocity to the yield velocity,  $V_i/V_y$ , on the coefficient of restitution for an elastic-perfectly plastic particle. Note that  $V_y$  is calculated using Equation (4-3). Therefore, the coefficient of restitution obtained from Equation (4-7) is plotted against  $V_i/V_y$  for all the case studies with  $V_i$ =50 m/s, as presented in



Figure 4-9. Similar graphs for the rest of the impact velocities are presented in Figures B-5 to B-8 of Appendix B. Due to the high number of the case studies, no legends are displayed on any of the aforementioned graphs, and the reader is referred to Table 4-3 for the designation of the symbols.

Table 4-3 Symbol reference for Figure 4-9, and Figures B-5 to B-8 of Appendix B.

|        | Legend |          |          |
|--------|--------|----------|----------|
|        |        | E (GPa)  |          |
| E/Y(-) | 1      | 10       | 100      |
| 20     | •      | •        | <b>A</b> |
| 40     | •      | <u> </u> | _        |
| 80     | •      | •        | <b>A</b> |
| 160    | •      |          | <b>A</b> |
| 320    | •      |          | <b>A</b> |
| 640    | •      |          | <b>A</b> |
| 1,280  | •      | •        | <b>A</b> |
| 2,560  | •      |          | <b>A</b> |

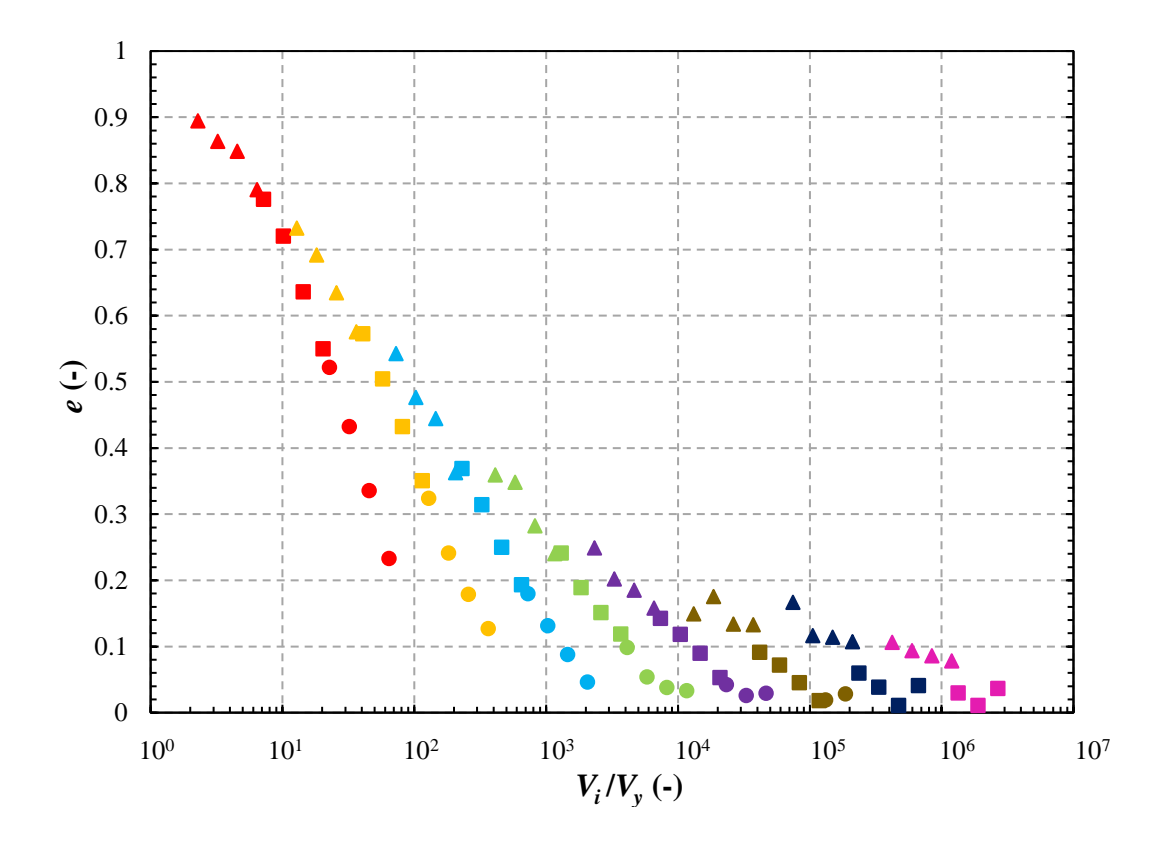


Figure 4-9 The coefficient of restitution, e, as a function of  $V_i/V_y$ , for all the cases with an impact velocity of 50 m/s. For designation of the symbols, see Table 4-3. Note that the data points in each data set correspond to different densities.

Considering Figure 4-9, and Figures B-5 to B-8 of Appendix B, when the coefficient of restitution is plotted as a function of  $V_i/V_y$ , a family of curves emerges where all the data points corresponding to a specific value of E/Y group together (in line with the findings of Wu et al. [110]). As a general trend, the coefficient of restitution decreases as  $V_i/V_v$  increases. This is expected as  $V_i$  is constant for all the cases in each graph, and the increase in  $V_i/V_y$  is simply due to a decrease in  $V_{\nu}$ . This decrease in  $V_{\nu}$  (as a result of a decrease in Y or an increase in  $\rho$ ) leads to an earlier onset of plastic deformation, thereby reducing the recovered elastic energy. The trend is rapid for the smaller values of E/Y (which generally correspond to small deformation) and slows down with further increase in E/Y. Moreover, for cases with the same value of E/Y, the coefficient of restitution decreases as the Young's modulus of the material decreases, which results from a reduction in the material yield strength, considering that E/Y is constant. It should be noted that for some of the cases with an impact velocity of 10 and 20 m/s (Figures B-5 and B-6 of Appendix B, respectively), i.e. cases corresponding to a relatively smaller deformation, there is scatter in the data. This can be attributed to the numerical errors arising from the sensitivity of the unloading dynamics to the selected time step or the number of the material points per element (especially for very small deformation), as discussed in Section 4.2. A potential solution to reduce such errors could be a further reduction in the time step, which is not pursued in this study due to time restrictions.

According to Wu et al. [110], when  $(V_i/V_y)/(E^*/Y)^2 \ge 0.008$ , the particle is considered to have undergone large deformation and the coefficient of restitution can be determined from Equation (4-8).

$$e = 0.62 \left(\frac{V_i / V_y}{E^* / Y}\right)^{-1/2} \tag{4-8}$$



Consequently, the coefficient of restitution for all the cases that fit this criterion is plotted as a function of  $(V_i/V_v)/(E^*/Y)$ , as shown in Figure 4-10, along with the model of Wu et al. superimposed for comparison. As seen in the graph, even though displaying e based on  $(V_i)$  $(V_y)/(E^*/Y)$  unifies the data to a certain extent, there is discrepancy between Wu et al.'s model (dashed line) and the MPM simulation results. This can in part be attributed to the use of a lumped mass matrix in the current MPM approach; while computationally efficient and better for impulsive loading problems [181], a lumped mass matrix results in energy dissipation [143,182], leading to underestimation and numerical errors in calculating the coefficient of restitution. However, this underestimation does not alter the observed trend, which still shows a separation between the curves corresponding to specific values of E/Y. It should also be noted that Wu et al. consider a smaller number of case studies (two and six different values for Young's modulus and yield strength, respectively and one value for density), whereas the current work studies a much wider range of material properties. Moreover, the criterion suggested by Wu et al. to mark the boundary between small and large deformation is not deemed reasonable based on the results of the current work, as there are multiple cases that fit the criterion yet exhibit plastic strain in the impact direction of no more than 1% of the original particle diameter.

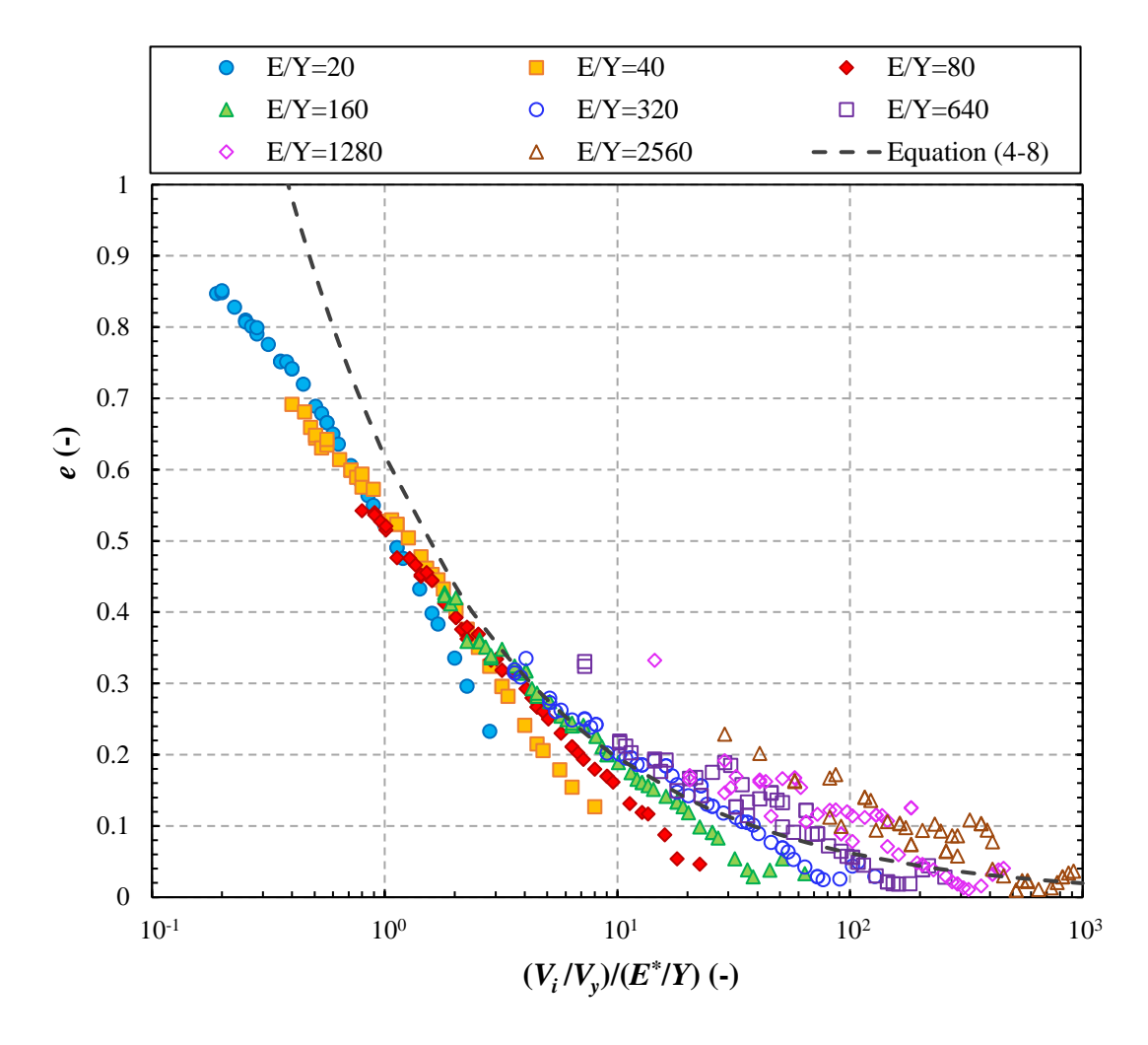


Figure 4-10 The coefficient of restitution, e, as a function of the dimensionless group  $(V_i/V_y)/(E^*/Y)$ . The dashed line is the model of Wu et al. [110], shown by Equation (4-8).

Whilst using the dimensionless group  $(V_i/V_y)/(E^*/Y)$  does not fully unify the data for such a wide range of material properties, the MPM results indicate that the coefficient of restitution can be related to the material properties and impact velocity using Equation (4-9). This relationship is further demonstrated in Figure 4-11, where the data points fall close to the line of equality when e is plotted as a function of the group at the right-hand side of Equation (4-9). In line with previous observations, Figure 4-11 shows that an increase in either E/Y or  $\rho V_i^2/Y$  results in a decrease in the coefficient of restitution, due to the decrease in the yield strength of the material, or an increase in the incident kinetic energy. Moreover, there is scatter in the data, notably for cases with the impact velocities of 10 and 20 m/s, similar to the observations from

Figures B-5 and B-6 of Appendix B. It is important to note that while Equation (4-9) effectively reveals the trend in the coefficient of restitution with respect to the material properties and impact velocity, the actual values of e may be higher than those predicted by the equation, due to the energy dissipation caused by the use of a lumped mass matrix.

$$e \approx 2.85 \left(\frac{E}{Y}\right)^{-0.325} \exp\left[-2\left(\frac{\rho V_i^2}{Y}\right)^{0.325}\right]$$
 (4-9)

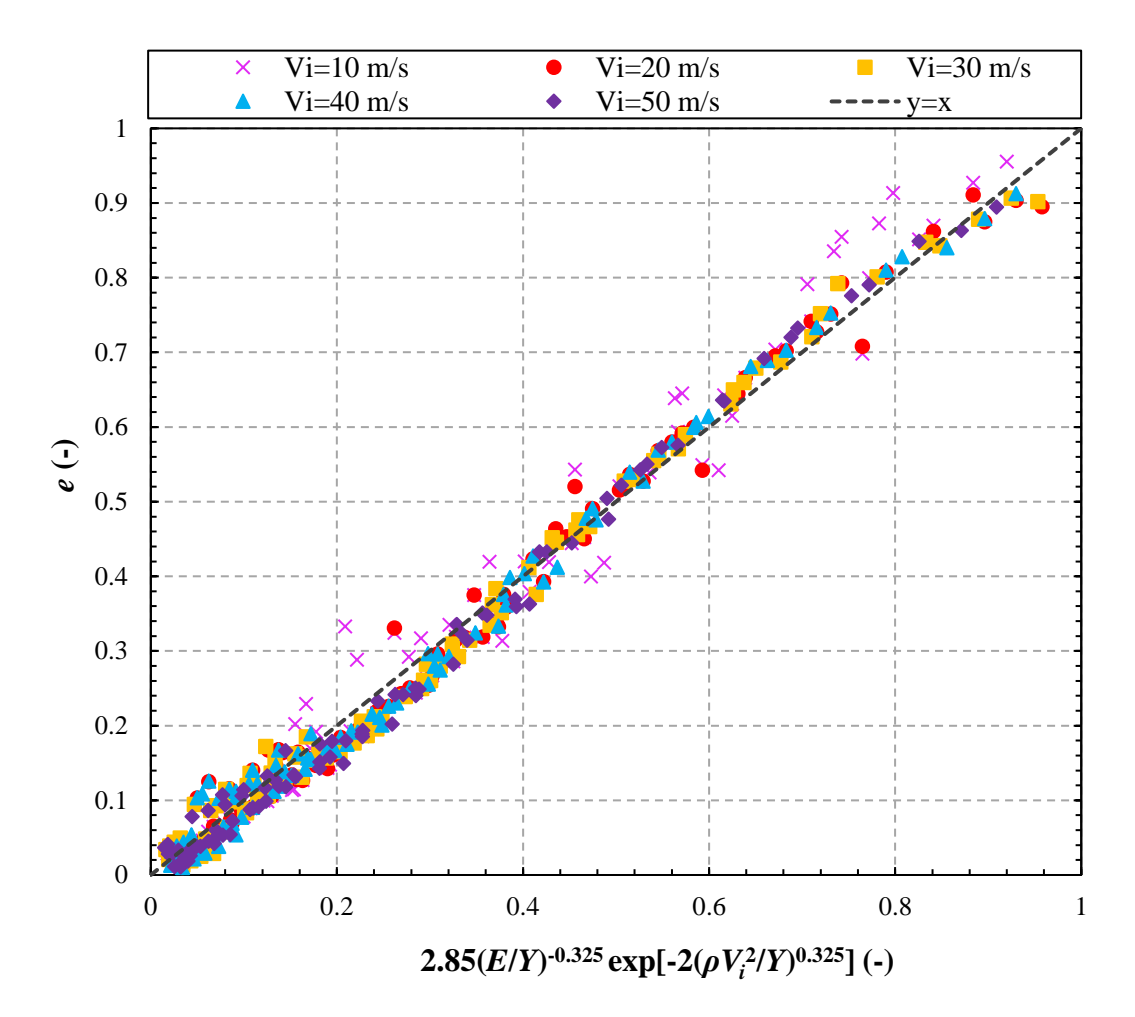


Figure 4-11 The coefficient of restitution, e, as a function of the dimensionless group  $2.85(E/Y)^{-0.325} \exp[-2(\rho V_i^2/Y)^{0.325}]$ .



# 4.4. Contact Force-Displacement

### 4.4.1. Evolution of Contact Force with Displacement

To display the evolution of the contact force (F) with displacement ( $\delta$ ) throughout impact, as an example, the contact force-displacement relationship for cases with  $\rho$ =8,000 kg/m<sup>3</sup>, E=100 GPa and E/Y=80 at all the impact velocities is shown in Figure 4-12 (F and  $\delta$  are calculated as described in Section 3.5.1). Here, F and  $\delta$  are normalised by their analytical values at the onset of yield,  $F_y$  and  $\delta_y$ , given by Equations (4-10) and (4-11), respectively, where  $p_{0y}$ =1.6Y is the maximum contact pressure at the onset of yield [27].

$$F_{y} = \frac{\pi^{3} p_{0Y}^{3} R^{2}}{6E^{*2}} \tag{4-10}$$

$$\delta_{y} = \frac{\pi^{2} p_{0Y}^{2} R}{4E^{*2}} \tag{4-11}$$

The contact force-displacement trends shown in Figure 4-12 align with the observations of Wu et al. [110] for the impact of an elastic sphere ( $\rho$ =7,850 kg/m³, E=208 GPa) with an elastic-perfectly plastic half-space ( $\rho$ =7,850 kg/m³, E=208 GPa and Y=1.35 GPa). During the loading phase, all the curves follow a common trajectory, where the contact force initially increases gradually at very small displacements, then transitions to a steeper, nearly constant slope as the displacement grows. On the other hand, the slope of the unloading curve increases with an increase in the impact velocity. Wu et al. [110] attribute this behaviour to a reduction in the contact curvature caused by increased plastic deformation. The variation in the unloading slope with impact velocity signifies changes in the ratio of the work done during unloading to that during loading-and consequently, in the coefficient of restitution-as a function of impact velocity [110].

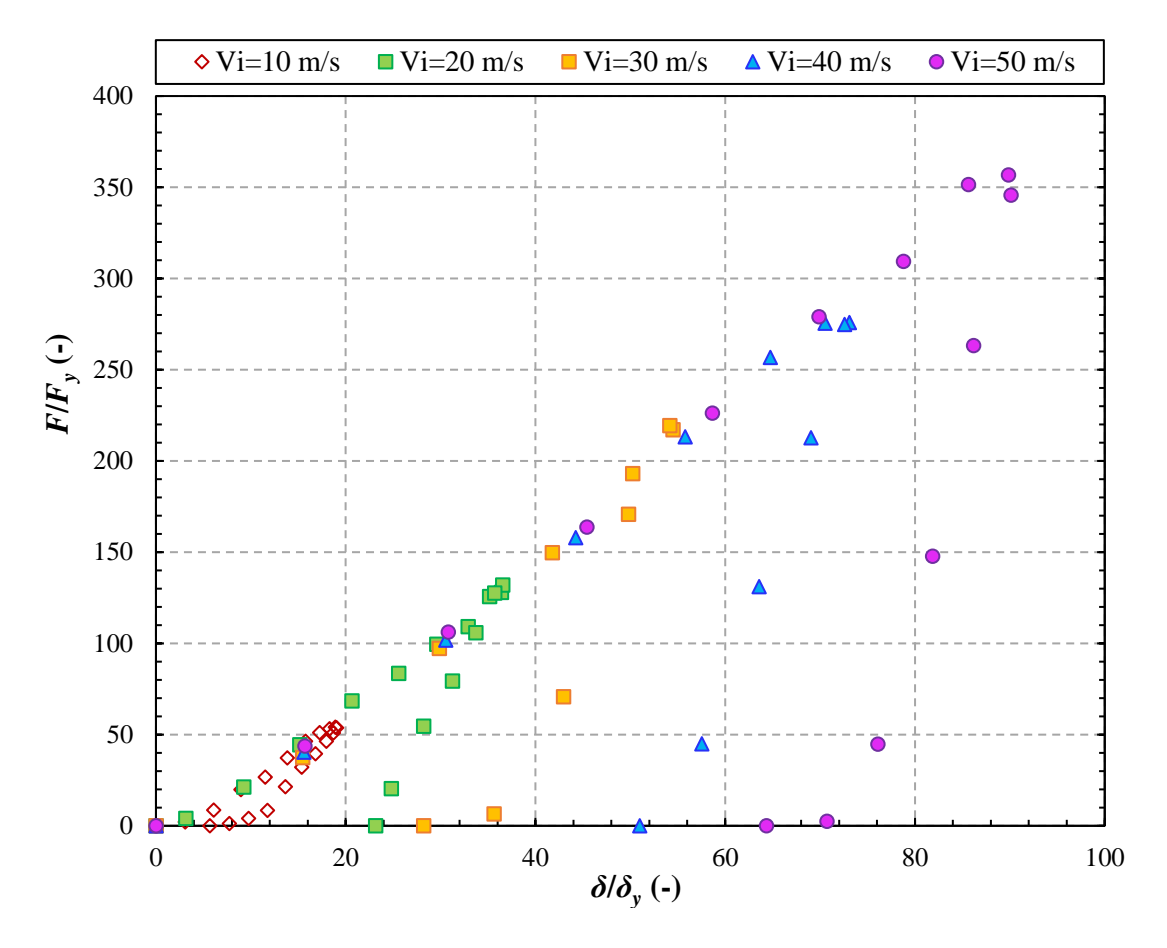


Figure 4-12 The contact force-displacement relationship for all the cases with  $\rho$ =8,000 kg/m³, E=100 GPa and E/Y=80 at different impact velocities.

### 4.4.2. Comparison with Theoretical Contact Models

As mentioned in Section 3.5, Wang et al. [172] identify discrepancies between the available theoretical contact models in predicting the impact behaviour of an elastic-perfectly plastic particle. Nevertheless, they show that at low impact velocities, the models of Kogut and Etsion (KE) [70] and Jackson and Green (JG) [67] are in good agreement with their Finite Element Analysis (FEA) results in predicting the maximum contact force, maximum indentation/flattening, and impact duration. To this end, the maximum contact force ( $F^*$ ) for the cases shown in Figure 4-12 (obtained from the MPM simulations) is compared with the



predictions from the KE and JG models using the MPM displacement values, as presented in Table 4-4.

Similar to the findings of Wang et al. [172], at lower impact velocities (up to 30 m/s), the MPM values of  $F^*$  are close to the values predicted by the KE and JG models. However, at higher impact velocities, the theoretical models (notably the KE model) overestimate the maximum contact force compared to the MPM results. Jackson and Green [67] compare the dimensionless contact force and contact area predicted by both their model and the KE model with the experimental results of Johnson [111] for the contact of a copper sphere with a rigid steel surface. Their findings indicate that both JG and KE models overestimate the contact force and contact area, with the discrepancy becoming more pronounced as the deformation increases. Therefore, the contact force values obtained from the MPM simulations are deemed more reasonable than those predicted by the KE and JG models.

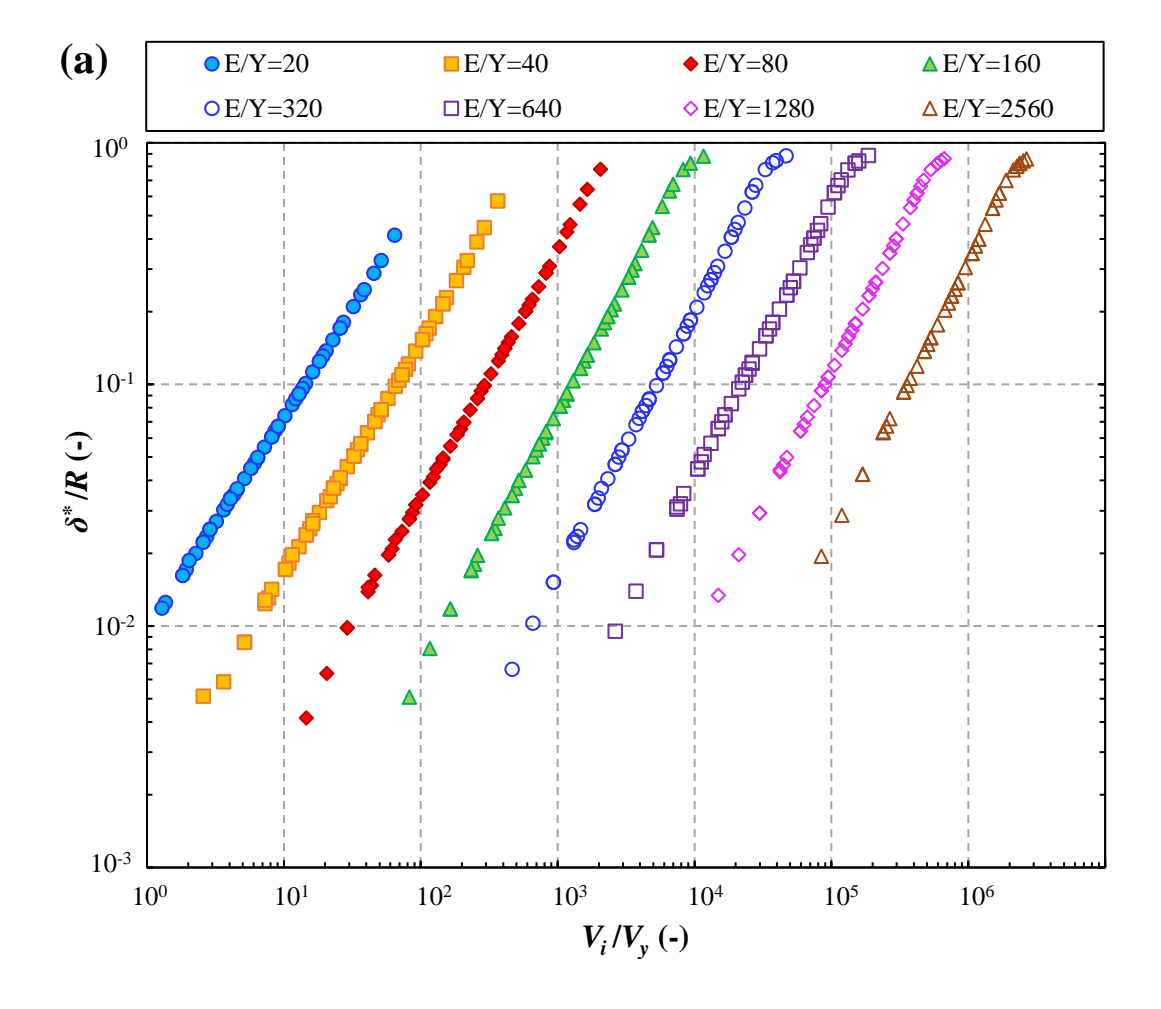
Table 4-4 The maximum contact force,  $F^*$ , obtained from the MPM simulations for cases with  $\rho$ =8,000 kg/m³, E=100 GPa and E/Y=80 at all the impact velocities (Figure 4-12), compared to the values predicted by the KE [70] and JG [67] contact models, using the MPM displacement values.

|             |      | <i>F</i> * (N) |      |
|-------------|------|----------------|------|
| $V_i$ (m/s) | KE   | JG             | MPM  |
| 10          | 11.8 | 11.8           | 10.7 |
| 20          | 26.8 | 26.5           | 26.2 |
| 30          | 44.4 | 42.2           | 43.6 |
| 40          | 64.3 | 58.6           | 54.9 |
| 50          | 85.1 | 74.6           | 70.9 |

#### 4.4.3. Trends in the MPM Data

The ULMPM simulation results of Li et al. [146] demonstrate that during the impact of an elastic-perfectly plastic particle with a rigid wall, the normalised maximum displacement ( $\delta^*$ /R) and residual displacement ( $\delta_{res}$ /R)-with R being the particle radius-group together for a

given E/Y value, when plotted as a function of  $V_i/V_y$ . A similar trend is observed in this study, when  $\delta^*/R$  and  $\delta_{res}/R$  are plotted as a function of  $V_i/V_y$ , as displayed in Figures 4-13 (a) and (b), respectively. Accordingly, as E/Y increases and the particle undergoes more severe plastic deformation,  $\delta^*/R$  and  $\delta_{res}/R$  approach unity. Note that in the current work,  $\delta_{res}$  is the displacement calculated for the first output file where the contact is lost. Consequently, there is scatter in the  $\delta_{res}/R$  data for the bottom tail of the curves corresponding to the lower E/Y values (cases undergoing small deformation), as the contact duration is very short for such cases, and the output file interval  $(n_t)$  is not fine enough to precisely capture the moment when the contact force becomes zero.



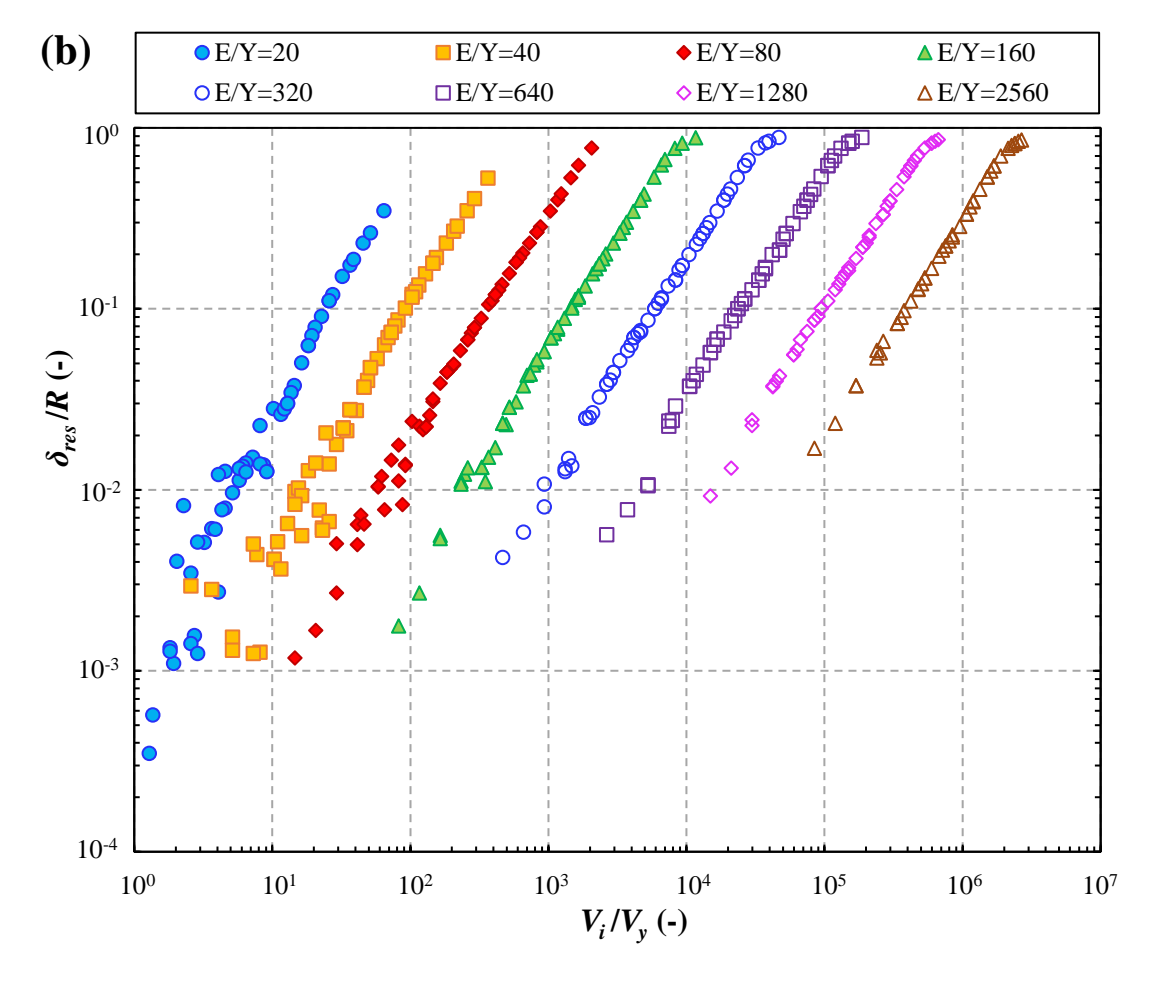


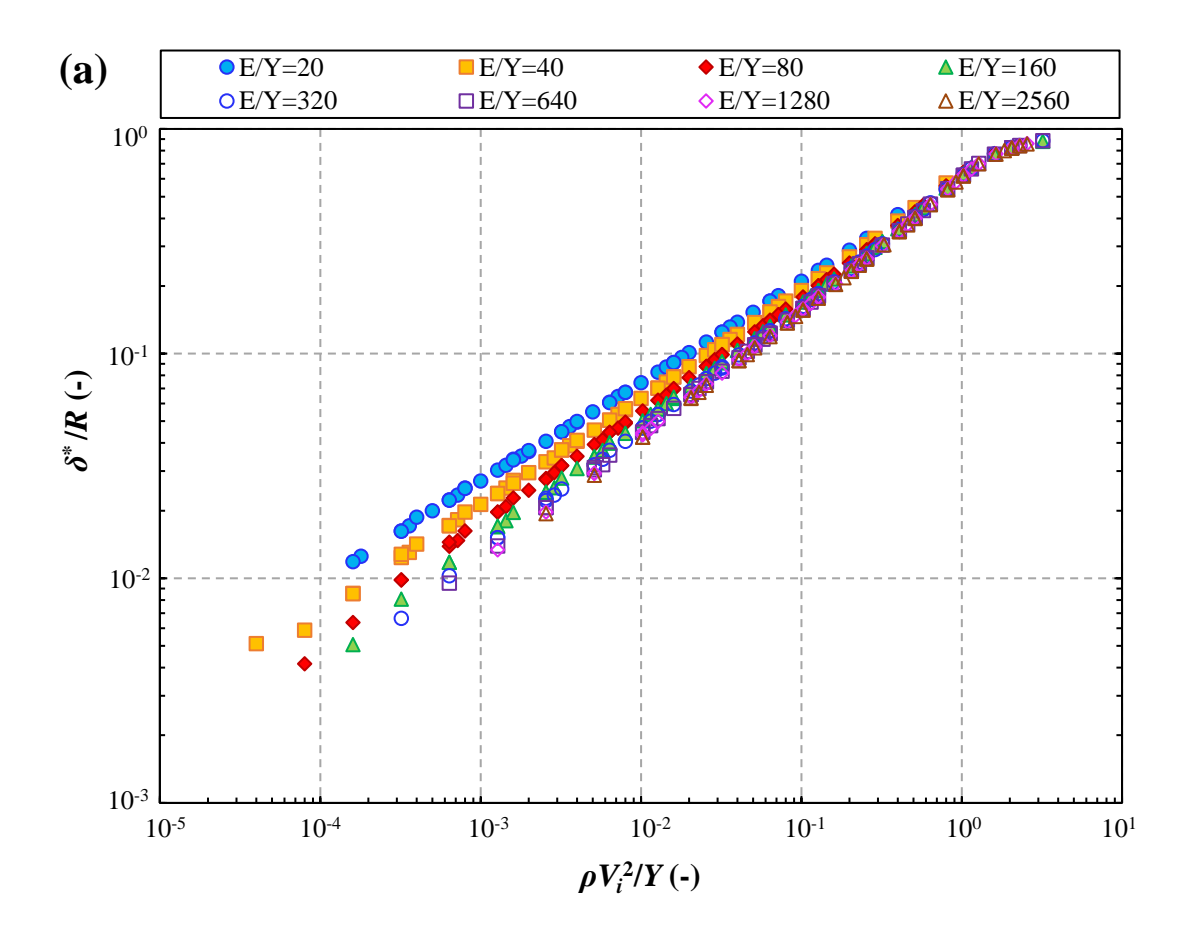
Figure 4-13 Change in: (a) the normalised maximum displacement,  $\delta^*/R$ , and (b) the normalised residual displacement,  $\delta_{res}/R$ , as a function of  $V_i/V_y$ .

It is important to highlight that the separation of data in Figure 4-13 based on E/Y values is due to the strong dependence of  $V_i/V_y$  on the group  $E^*/Y$ , and consequently, E/Y (as all cases in this study share the same Poisson's ratio), as indicated by Equation (4-12), below:

$$\frac{V_i}{V_y} = V_i \left(\frac{\rho}{26Y}\right)^{0.5} \left(\frac{E^*}{Y}\right)^2 = 0.2 \left(\frac{\rho V_i^2}{Y}\right)^{0.5} \left(\frac{E^*}{Y}\right)^2 \tag{4-12}$$

To better observe the trends in the data,  $\delta^*/R$  and  $\delta_{res}/R$  are plotted against the group  $\rho V_i^2/Y$ , as shown in Figures 4-14 (a) and (b), respectively. Accordingly, both  $\delta^*/R$  and  $\delta_{res}/R$  intuitively increase with an increase in  $\rho V_i^2/Y$ , i.e. an increase in the incident kinetic energy or a decrease

in the yield strength of the material. From Figure 4-14 (a), for  $\rho V_i^2/Y < 1$ , the  $\delta^*/R$  data shows separation based on E/Y values up to E/Y=80, suggesting that for small deformations, the maximum displacement depends not only on the incident kinetic energy and yield strength, but also on Young's modulus. Furthermore, the rate of increase in  $\delta^*/R$  with  $\rho V_i^2/Y$  is higher for larger values of E/Y. As deformation increases and  $\rho V_i^2/Y$  approaches unity, the dependency of  $\delta^*/R$  on E/Y diminishes, and the curves converge. With respect to Figure 4-14 (b), it is difficult to draw firm conclusions for  $\delta_{res}/R$  up to  $\rho V_i^2/Y$ =0.04, due to the scatter in the data. However, comparing Figure 4-14 (a) and (b) within the range  $0.04 < \rho V_i^2/Y < 1$ , unlike the maximum displacement, the residual displacement shows no dependency on E/Y. Consistent with the observations in Section 4.3.4, a clear transition point occurs for both  $\delta^*/R$  and  $\delta_{res}/R$  at  $\rho V_i^2/Y$ =1, marking the onset of fluid-like behaviour; at this point, the slopes of all the curves noticeably decrease as  $\delta^*/R$  and  $\delta_{res}/R$  approach unity.



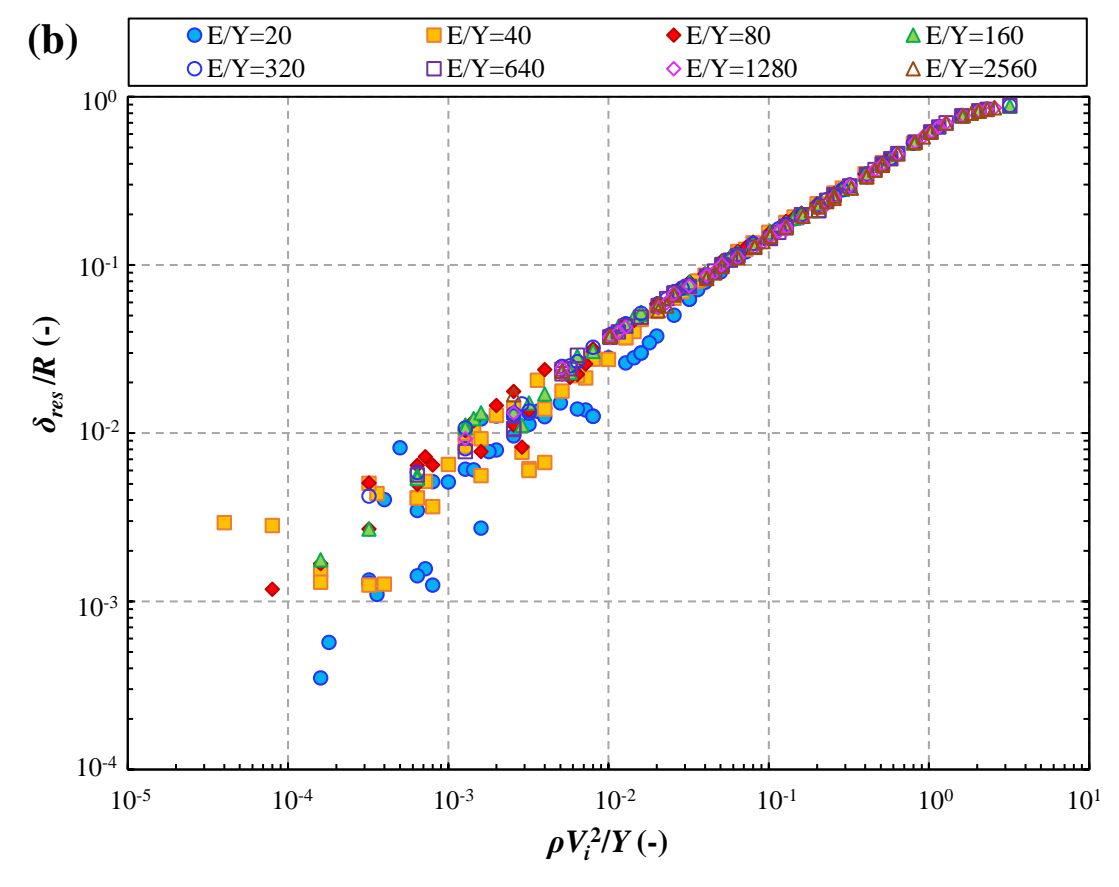


Figure 4-14 Change in: (a) the normalised maximum displacement,  $\delta^*/R$ , and (b) the normalised residual displacement,  $\delta_{res}/R$ , as a function of  $\rho V_i^2/Y$ .

Li et al. [146] also demonstrate that, similar to the trend observed for  $\delta^*/R$  and  $\delta_{res}/R$ , when the normalised maximum contact force,  $F^*/F_y$  is plotted against  $V_i/V_y$ , the data cluster together based on  $E^*/Y$ . Following this approach, the same graph is plotted for the results of the current study, as shown in Figure 4-15. The graph reveals that while cases with the same E/Y value group together, all the data follow a common linear trend, where  $F^*/F_y$  increases with E/Y.

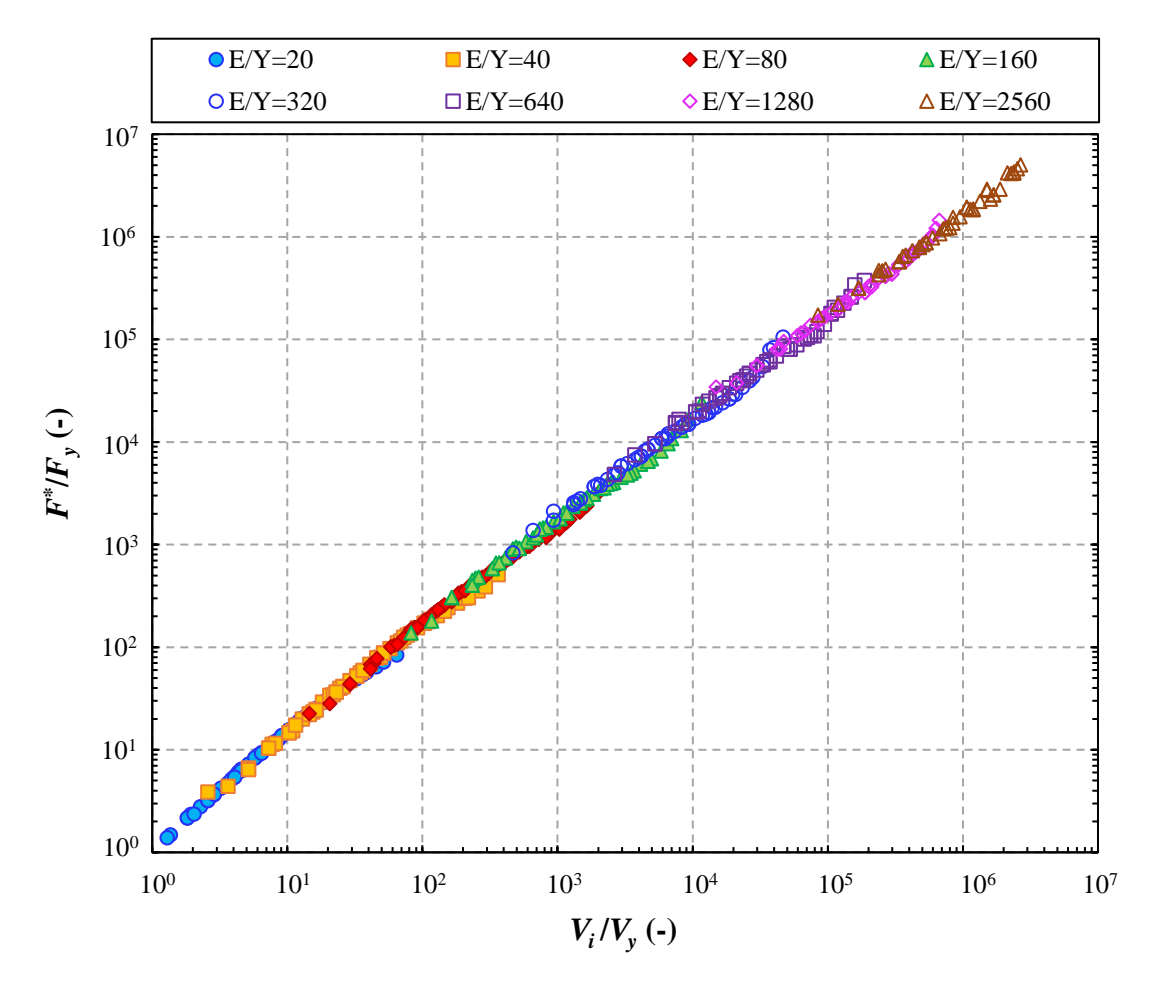


Figure 4-15 The normalised maximum contact force,  $F^*/F_y$ , as a function of  $V_i/V_y$ .

From Figure 4-15, it can be observed that  $F^*/F_y$  is proportional to  $V_i/V_y$ . Therefore, considering Equations (4-10) and (4-12), it can be deduced that  $F^* \propto \pi R^2 (Y \rho V_i^2)^{0.5}$ . This intuitively shows that the maximum force is the highest for high-energy impact of less deformable particles, and the lowest for low-energy impact of highly deformable particles. Accordingly,  $F^*$  is plotted as a function of  $\pi R^2 (Y \rho V_i^2)^{0.5}$ , as displayed in Figure 4-16. Considering the slope of the fitted line, Equation (4-13) can be used to estimate  $F^*$ :

$$F^* \approx 2\pi R^2 \left(Y \rho V_i^2\right)^{0.5}$$
 (4-13)

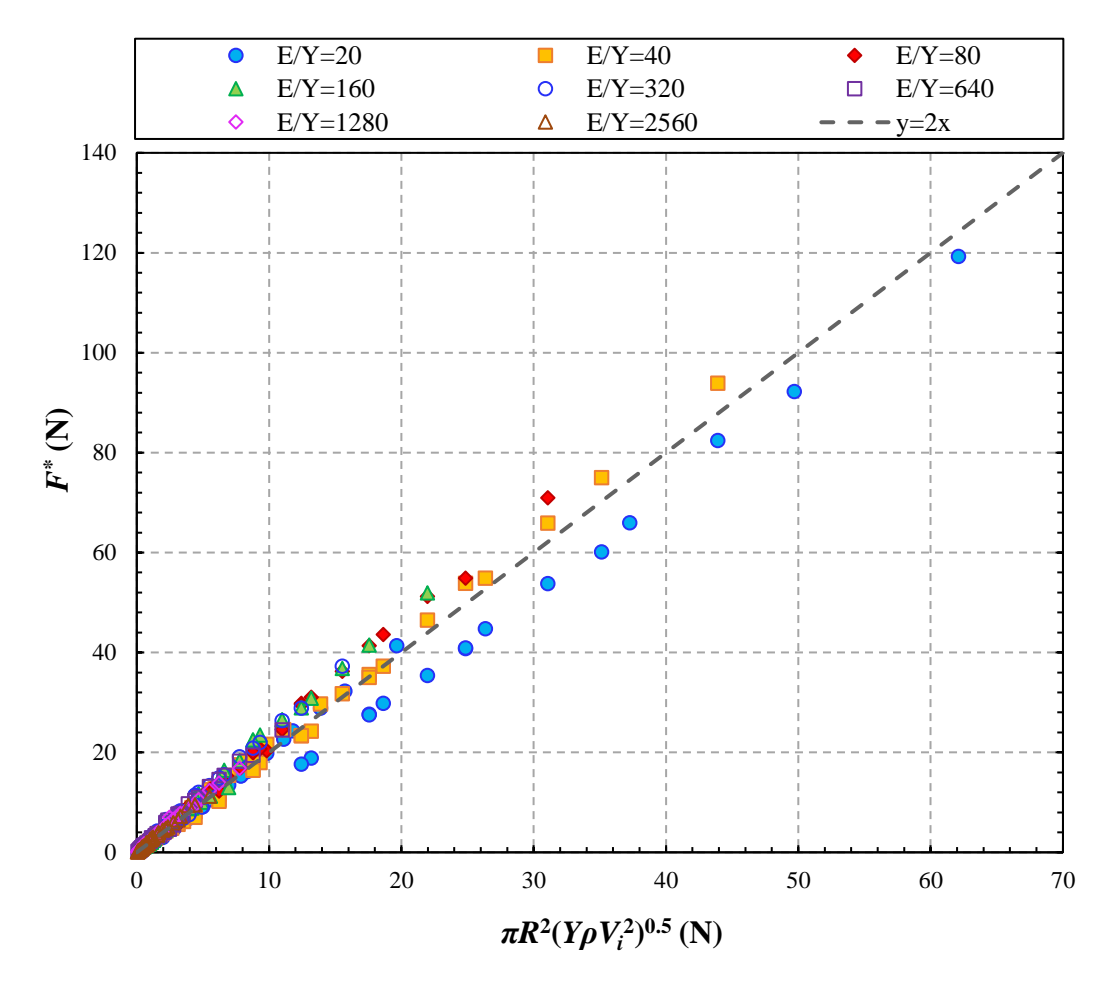


Figure 4-16 The maximum contact force,  $F^*$ , as a function of  $\pi R^2 (Y \rho V_i^2)^{0.5}$ .

Since all the cases studied thus far share the same particle size (500  $\mu$ m), to examine the validity of Equation (4-13), additional simulations are carried out using particle sizes of 100, 250, 750 and 1,000  $\mu$ m. Three of the previously studied cases (500  $\mu$ m) that exhibit noticeably different values of  $F^*$  are selected for this purpose. In total, 12 simulations are performed, considering these three cases and the four particle sizes. The material properties and impact velocities for the cases are summarised in Table 4-5.



Table 4-5 The material properties and impact velocities of the cases for which additional simulations are carried out using particle sizes of 100, 250, 750 and 1,000  $\mu$ m, to examine the validity of Equation (4-13).

|        | $V_i$ (m/s) | $\rho$ (kg/m <sup>3</sup> ) | E (GPa) | Y (MPa) |
|--------|-------------|-----------------------------|---------|---------|
| Case 1 | 30          | 1,000                       | 1       | 50      |
| Case 2 | 40          | 2,000                       | 10      | 250     |
| Case 3 | 50          | 4,000                       | 100     | 5,000   |

The simulation results are presented in Figure 4-17 (a) as the plot of  $F^*$  versus  $2\pi R^2(Y\rho V_t^2)^{0.5}$ . With regards to the graph, for smaller values of  $2\pi R^2(Y\rho V_t^2)^{0.5}$ , the simulation results for the maximum contact force closely match the values estimated by Equation (4-13). However, for larger values of  $2\pi R^2(Y\rho V_t^2)^{0.5}$ , Equation (4-13) overestimates  $F^*$  compared to the simulation values. This discrepancy is more clearly illustrated when the simulation and estimated values of  $F^*$  are plotted as a function of  $(Y\rho V_t^2)^{0.5}$ , as displayed in Figure 4-17 (b). Considering the graph, Equation (4-13) provides accurate estimates of  $F^*$  when  $(Y\rho V_t^2)^{0.5} < 10$ . However, for  $10 < (Y\rho V_t^2)^{0.5} < 100$ , the estimated  $F^*$  values are underestimated compared to the simulation results, whereas for  $(Y\rho V_t^2)^{0.5} > 100$ , they are overestimated. The reason for this behaviour is unclear, though it is suspected that the proportionality constant in Equation (4-13) may be influenced by the material properties or impact velocity through a dimensionless expression.

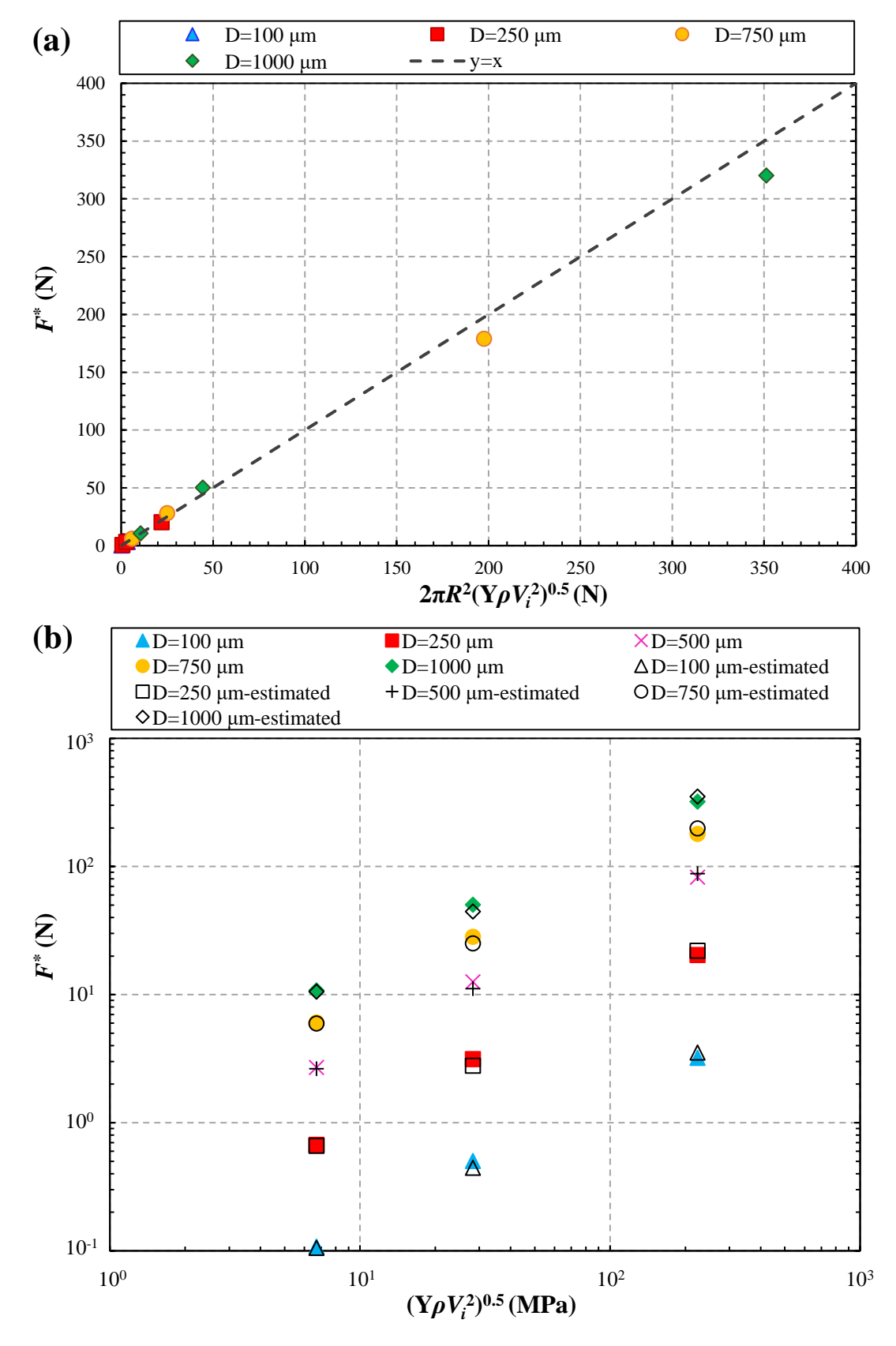


Figure 4-17 The simulation results of the maximum contact force,  $F^*$ , for cases shown in Table 4-5 using particle sizes of 100, 250, 750 and 1,000  $\mu$ m, as a function of (a) group  $2\pi R^2 (Y\rho V_i^2)^{0.5}$  and (b) group  $(Y\rho V_i^2)^{0.5}$  in comparison with the values estimated by Equation (4-13).



# 4.5. Concluding Remarks

The results from this chapter exhibit how the impact behaviour of an elastic-perfectly plastic particle is influenced by its material properties and impact velocity. As intuitively expected, it is observed that the variables which represent the plastic deformation of the particle, i.e. the equivalent plastic strain, compression ratio, and residual (permanent) displacement, are solely dependent on the incident kinetic energy and yield strength of the material. However, the variables that are linked to the deformation recovery/resistance behaviour of the particle, i.e. the coefficient of restitution, the ratio of the plastic work to the incident kinetic energy, and the maximum displacement during loading, are additionally affected by the Young's modulus of the material, especially for small deformation. The importance of the dimensionless groups E/Y and  $\rho V_i^2/Y$  in recognising the trends in the particle impact behaviour is highlighted, and the groups are used in the development of empirical equations that predict the equivalent plastic strain, compression ratio and coefficient of restitution. As suggested by Johnson [27], group  $\rho V_i^2/Y$  is a great marker for understanding the deformation behaviour of an impacting particle.

It is worth noting that there are plans for a future publication to further expand on the contact force-displacement work in this chapter, aiming to develop a contact model and compare it with existing contact models.



# 5. AI-Assisted Analysis of MPM Simulation Data

### 5.1. Overview

In Chapter 4, the trends in the TLMPM simulation data were identified by examining various combinations of input and output parameters, a process that is both labour-intensive and time-consuming. Nevertheless, with the rapid growth of Artificial Intelligence (AI) in recent years, particularly Machine Learning (ML), large datasets can now be analysed intelligently and efficiently. Therefore, in collaboration with the Institute for Particle Technology (iPAT), Technische Universität Braunschweig (Braunschweig, Germany), the MPM simulation results are processed using a custom-developed hybrid AI framework (proprietary of iPAT) to examine the efficiency of AI in recognising the trends in the MPM simulation data and improve the equations proposed in Section 4.3. To this end, the framework is used to identify the link between the simulation input parameters (material properties and impact velocity) and the resulting output (parameters describing the deformation behaviour of the impacting particle). The data analysis using the framework has been carried out by Miss Somayeh Hosseinhashemi (Technische Universität Braunschweig, Germany), who has also provided the description of the methodology outlined in Section 5.2, up to Section 5.2.4. Modification of the flowchart (Figure 5-1), data curation (MPM data), as well as the contents of the remaining sections, including the interpretation, discussion, visualisation and verification are the contributions of the thesis author, who has also provided insight during data processing by Miss Somayeh Hosseinhashemi. Majority of the results from this chapter have been submitted for publication in [183].



# 5.2. AI Hybrid Approach

The hybrid AI framework implements Symbolic Regression (SR) [184], integrated with Deep Neural Networks (DNN) [185], Genetic Algorithms (GA) [186], and Graph Attention Networks (GAT) [187]. A comprehensive description of the employed AI techniques (DNN, GA and GAT) can be found in [188,189]. A brief description of the general workflow, shown by Figure 5-1, is as follows: The first step in the workflow is typically Dimensional Analysis (DA), where the input and output data are analysed to determine dimensionless groups that represent the physics of the process. These groups are then used to update the original dataset, in order to refine the input for the subsequent stages. After DA, the process moves to the next stage, in which Symbolic Regression (SR) techniques are used. In this stage, several tools and techniques such as GPLearn [190], Graph Attention Networks (GAT), Fragment Selection Techniques (FST, developed in-house) are utilised to identify the potential mathematical relationships within the data. If the first round of SR does not produce satisfactory solutions, the workflow calls for iteration. This includes revisiting the results to make any necessary recalibrations to refine the model outputs, after which SR is applied again. In case the modified results are still unsatisfactory, the process is extended to a deeper level of problem solving, involving deep neural networks (DNN) that are improved through Hyperparameter Optimisation (HPO). This approach is used to tune the model parameters to best fit the data. During this stage, the DNN employs a user-provided equation library (based on prior knowledge of the system) to check for existing patterns and solutions. It should be noted that the aforementioned stages are iterative, continuously looping back to earlier steps as needed until a solution is found. After finding a successful solution, the model selects the configuration with the highest fitness from the tested SR outputs and completes the process.

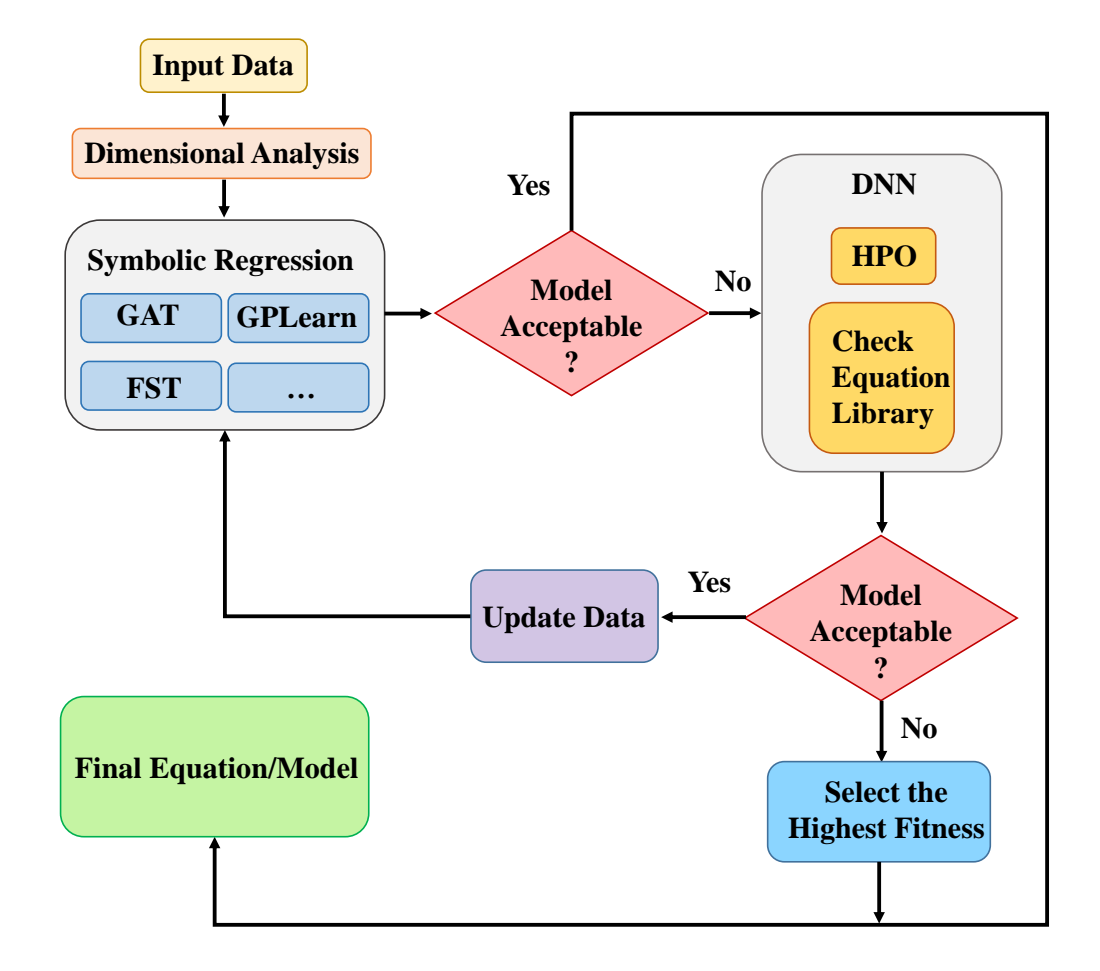


Figure 5-1 Flowchart of the implemented hybrid AI framework.

In the current study, the best results are achieved with the GAT model combined with preprocessing and data preparation strategies. Therefore, a detailed description of these stages of the framework is provided in the following sections. Other components, such as DNNs, are not directly applied to the final results of this study, and therefore are not discussed here.

### **5.2.1. Pre-Processing and Augmentation Techniques**

Initially, the process begins by fetching the raw dataset, named "original\_data", which often includes a variety of redundant or irrelevant features. To refine this dataset, Recursive Feature Elimination (RFE) [191] driven by a Random Forest Algorithm is applied to select only the most significant variables. This step is crucial for reducing dimensionality, thereby enhancing both the accuracy and interpretability of the models. Alongside RFE, Spearman's



correlation analysis [192] is employed (preferred over that of Pearson for its ability to capture non-linear relationships), to further inspect the feature interactions through heat map visualization. The results are expressed as scores, assisting in identification and elimination of redundant or collinear features. The approach for calculating the RFE and correlation scores is detailed in the Supplementary Data file, modified from the description provided by Miss Somayeh Hosseinhashemi. Following RFE, the "original\_data" undergoes an 'Expand & Reorder' process where transformations such as cropping and rotating are applied. This enhances data diversity and robustness, resulting in the augmented dataset "train\_data", which improves the generalizability of the subsequent modelling phases.

#### 5.2.2. Graph Attention Network (GATv2) Integration

The Graph Attention Network (GATv2) [193] is defined with specific configurations to intelligently handle the complexities of the graph-structured data. GATv2 builds upon traditional Graph Convolutional Networks (GCNs) [194,195] by integrating dynamic attention mechanisms that adjust the influence of node interactions based on their relevance, refining the model adaptability and interpretability. At this stage, the "train\_data" is split into training and validation subsets, with 80% used for training and the remaining 20% for validation. This ensures the model learns to generalise beyond the training data and accurately performs on new, unseen data.

#### 5.2.3. Data Augmentation Phase

New data points, called "predict\_data", are generated from the existing "train\_data" using the trained GATv2 model. These "predict\_data" points are then combined with the "train\_data", and the combined dataset is saved as "predict\_data". This phase assesses the framework's capability to handle unfamiliar or novel data scenarios. The "predict data"



undergoes further refinement, where outliers are removed and biases adjusted, ensuring the data remains representative and accurate for further analysis.

### 5.2.4. Symbolic Regression and Mathematical Modelling

In this study, Symbolic Regression (SR) using GPLearn techniques is systematically applied to three datasets: "original\_data", "train\_data", and "predict\_data". The details of how the GPLearn model is applied as an SR model are described in detail in [188,189]. Each application of SR serves a distinct purpose. Initially, SR interprets the basic input-output relationships in "original\_data". Subsequently, the generalisation ability of the model is examined with "train\_data". Finally, the prediction accuracy and practical utility of the model are evaluated using "predict\_data". This multi-level application helps validate the interactions and relationships captured by the model. The framework employs symbolic manipulation tools to identify and extract stable, recurring mathematical patterns across these datasets. These patterns represent the underlying physical laws and result in a unified symbolic equation or set of equations that concisely describe the data across all scenarios.

### 5.2.5. Input and Output Data

Initially, only the material properties and impact velocity ( $V_i$ ,  $\rho$ , E and Y) are inserted as input for the framework. However, the framework is unable to derive rational equations, emphasising the necessity for the user to have an understanding of the underlying physics of the problem. Consequently, based on the equations derived in Chapter 4, groups E/Y and  $\rho V_i^2/Y$  are introduced as inputs for the framework. Additionally, group  $\rho(V_i^2-V_y^2)/Y$  is considered as an input. This group not only considers the effect of all the input variables (by including  $V_y$ ), it also accounts for the portion of the incident kinetic energy that is available for inducing plastic deformation, i.e. by deducting the incident kinetic energy required for onset of yielding (represented by  $\rho V_y^2$ ) from the total kinetic energy (represented by  $\rho V_i^2$ ).

The considered output data include: the equivalent plastic strain,  $\varepsilon_p$ , the compression ratio, 1- $(H_d/D)$ , the coefficient of restitution, e, and the ratio of plastic work/energy to the incident kinetic energy, expressed by  $W_p/W_i$ , as well as 1- $e^2$ .

The performance of the framework and the fit of the predicted models to the MPM data are evaluated using the mean absolute error (MAE), mean squared error (MSE) and the coefficient of determination (R<sup>2</sup>), shown by the equations below:

$$MAE = \frac{\sum_{i=1}^{n_d} |y_{pred,i} - y_{MPM,i}|}{n_d}$$
 (5-1)

MSE = 
$$\frac{\sum_{i=1}^{n_d} (y_{pred,i} - y_{MPM,i})^2}{n_d}$$
 (5-2)

$$R^{2} = 1 - \frac{\sum_{i=1}^{n_{d}} \left( y_{pred,i} - y_{MPM,i} \right)^{2}}{\sum_{i=1}^{n_{d}} \left( y_{pred,i} - \frac{1}{n_{d}} \sum_{i=1}^{n_{d}} y_{MPM,i} \right)^{2}}$$
(5-3)

where  $y_{pred}$  and  $y_{MPM}$  are respectively the predicted and MPM values of an output, and  $n_d$  is the number of the data points.

## 5.3. Trends and Equations Identified by the Framework

# 5.3.1. Equivalent Plastic Strain

The RFE and correlation scores of all the input variables for the prediction of the equivalent plastic strain,  $\varepsilon_p$ , are presented in Figure 5-2. Considering both RFE and correlation



scores, the yield strength of the material is the most important variable in influencing the equivalent plastic strain, as intuitively expected. This is followed by the particle impact velocity, density, yield velocity and Young's modulus, respectively.

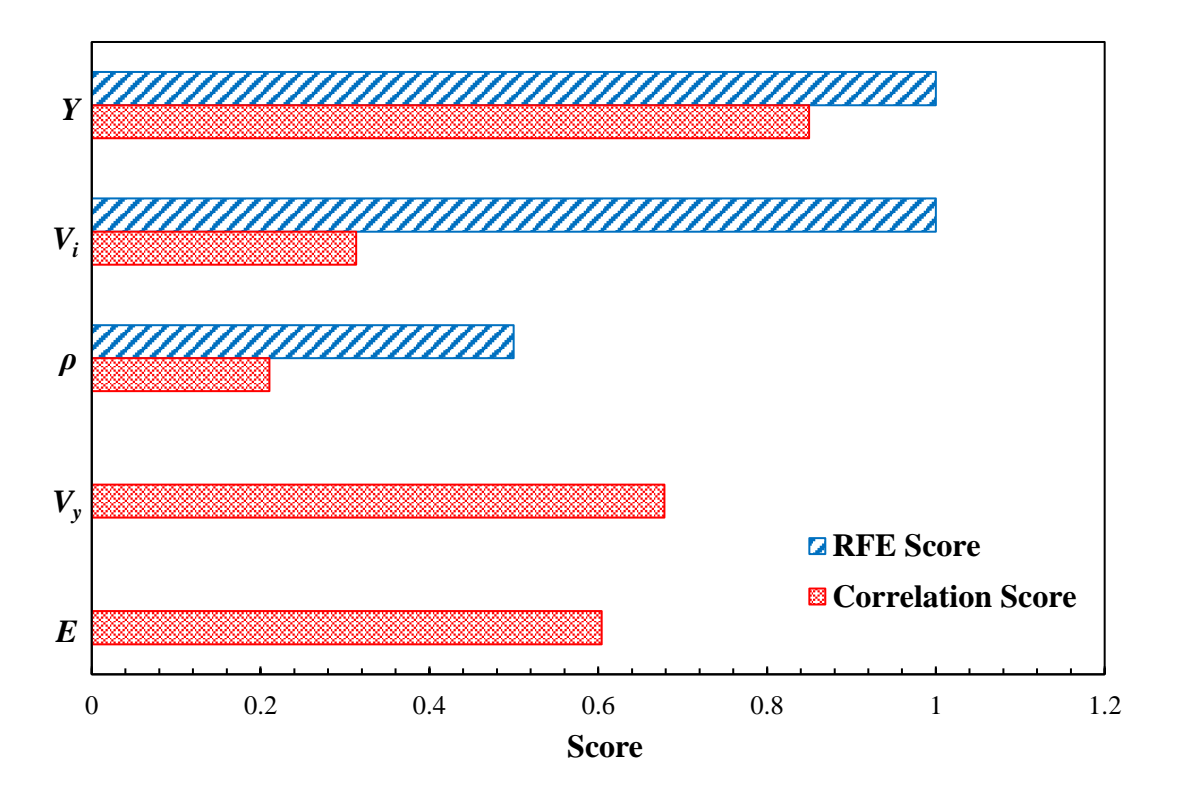


Figure 5-2 The RFE and correlation scores of all the input variables for the prediction of the equivalent plastic strain,  $\varepsilon_p$ .

The framework identifies Equation (5-4) for the equivalent plastic strain,  $\varepsilon_p$ . The corresponding MAE, MSE and R<sup>2</sup> values with respect to the MPM data are displayed in Table 5-1, demonstrating the excellent fit of the identified equation to the MPM data. This is further demonstrated in Figure 5-3 (a), where the  $\varepsilon_p$  values obtained from the MPM simulations fall perfectly on the line of equality when plotted as a function of the correlation identified by the framework. Moreover, the predicted values of  $\varepsilon_p$  are very close to the MPM values for all the data points, as shown in Figure 5-3 (b).



Considering Equation (5-4) and Figure 5-3 (a),  $\varepsilon_p$  intuitively increases with an increase in  $\rho(V_i^2-V_y^2)/Y$ , as the increase in the latter is due to a decrease in the yield strength of the material, or an increase in the portion of the incident kinetic energy available for plastic deformation. It is important to note that Equation (5-4) is very similar to the previously identified Equation (4-4). However, it alternatively accounts for the portion of the incident kinetic energy that is expended on inducing plastic deformation.

$$\varepsilon_p = 0.475 \left\lceil \frac{\rho \left( V_i^2 - V_y^2 \right)}{Y} \right\rceil \tag{5-4}$$

Table 5-1 MAE, MSE and  $R^2$  values for the equivalent plastic strain,  $\varepsilon_p$ , predicted by Equation (5-4), with respect to the MPM data.

| Identified Equation | MAE   | MSE                    | $\mathbb{R}^2$ |
|---------------------|-------|------------------------|----------------|
| Equation (5-4)      | 0.003 | 1.556×10 <sup>-5</sup> | 0.999          |

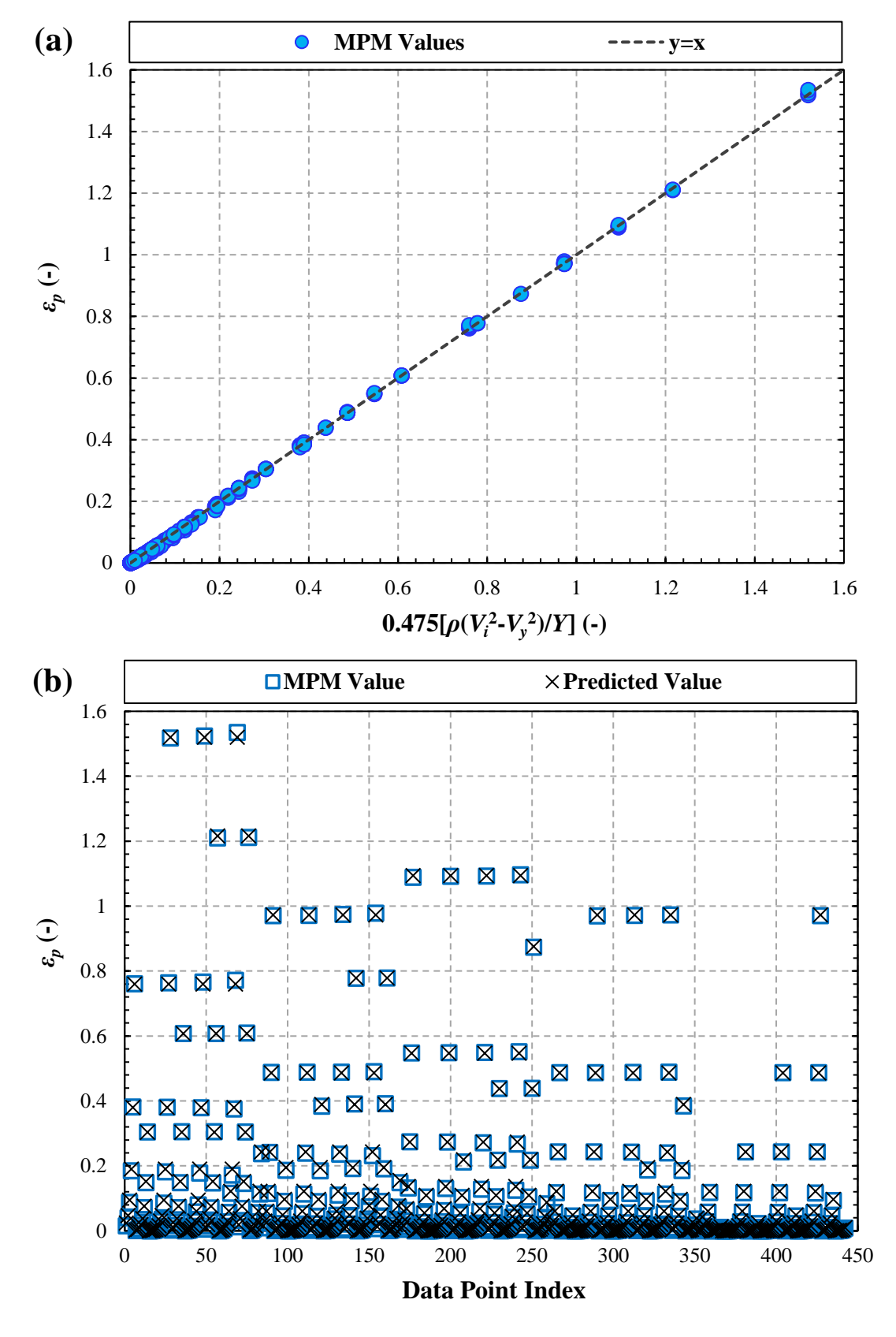


Figure 5-3 The equivalent plastic strain,  $\varepsilon_p$ , obtained from the MPM simulations: (a) as a function of Equation (5-4), identified by the AI framework, and (b) in comparison with the values predicted by Equation (5-4) for all the data points.



### 5.3.2. Compression Ratio

The RFE and correlation scores of all the input variables for the prediction of the compression ratio, 1- $(H_d/D)$ , are displayed in Figure 5-4. Accordingly, groups  $\rho(V_i^2-V_y^2)/Y$  and  $\rho V_i^2/Y$  strongly influence the compression ratio. This is respectively followed by the yield velocity, impact velocity, yield strength, Young's modulus, group E/Y, and particle density.

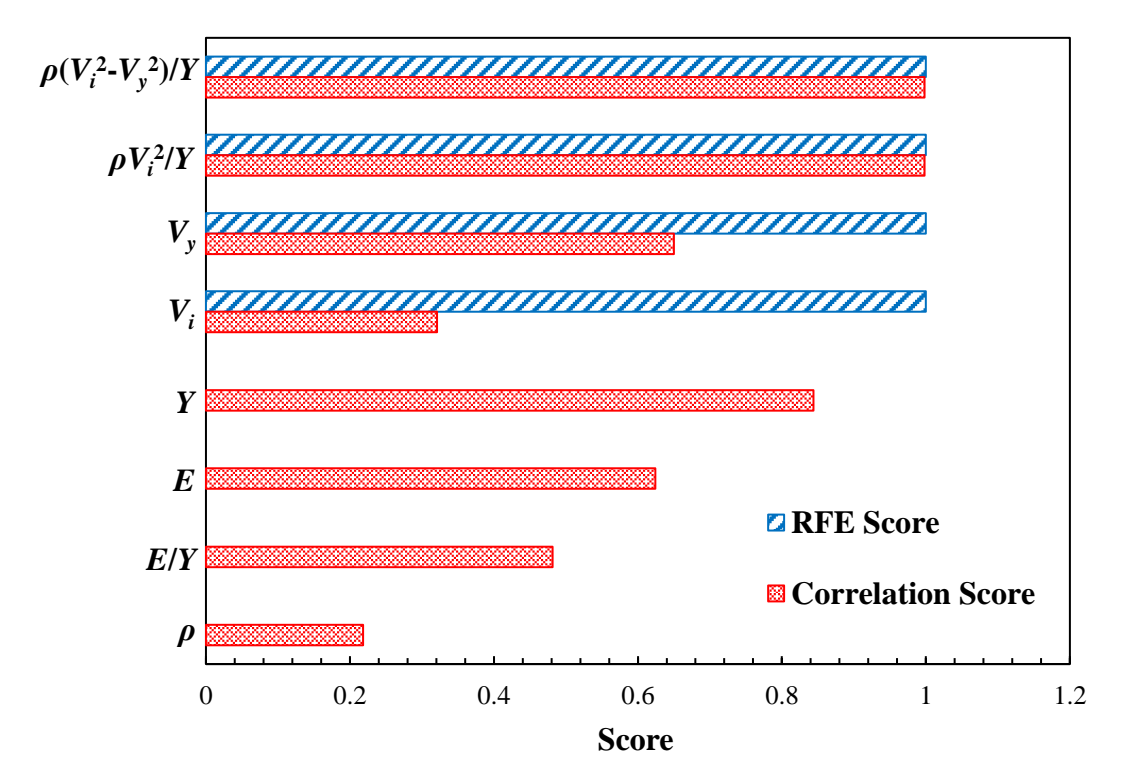


Figure 5-4 The RFE and correlation scores of all the input variables for the prediction of the compression ratio,  $1-(H_d/D)$ .

The equation identified by the framework for the compression ratio, along with the corresponding MAE, MSE and  $R^2$  values with respect to the MPM data are shown in Equation (5-5) and Table 5-2, respectively. Moreover, 1-( $H_d/D$ ) is plotted as a function of the identified equation, as shown in Figure 5-5 (a), and the predicted values for all the data points are compared to the MPM values, given in Figure 5-5 (b). Considering the MAE, MSE and  $R^2$  values in Table 5-2, the identified equation is a good fit to the MPM data, though Figure 5-5



(a) and (b) suggest that the predicted values are slightly underestimated with respect to the MPM values, especially for large deformation. Nevertheless, the equation identified by the framework provides a fair prediction of the MPM values. Although Equation (5-5) is similar to the previously identified Equation (4-5), it is deemed more suitable for predicting the compression ratio, as it accounts for the portion of the incident kinetic energy that is available for inducing plastic deformation.

Based on the identified equation and consistent with the observations for  $\varepsilon_p$ , the compression ratio for an elastic-perfectly plastic particle impacting a rigid wall depends on the yield strength of the material, as well as the portion of the incident kinetic energy available for plastic deformation, as intuitively expected. Additionally, Figure 5-5 (a) suggests that 1-( $H_d$ /D) increases with a decrease in the yield strength of the material, or an increase in the energy available for inducing plastic flow. It is important to note that the identified equation allows for prediction of the compression ratio based on the material properties and impact velocity. This is valuable for coating techniques like aerosol deposition and cold spraying, where the compression ratio of the particles affects the quality of the final coating, i.e. the impact velocity required to induce a desired extent of deformation can be determined based on the material properties of the feed particles.

$$1 - \frac{H_d}{D} = 0.33 \left[ \frac{\rho \left( V_i^2 - V_y^2 \right)}{Y} \right]^{0.66}$$
 (5-5)

Table 5-2 MAE, MSE and  $R^2$  values for the compression ratio, 1- $(H_d/D)$ , predicted by Equation (5-5), with respect to the MPM data.

| Identified Equation | MAE   | MSE                    | $\mathbb{R}^2$ |
|---------------------|-------|------------------------|----------------|
| Equation (5-5)      | 0.006 | 4.855×10 <sup>-5</sup> | 0.997          |

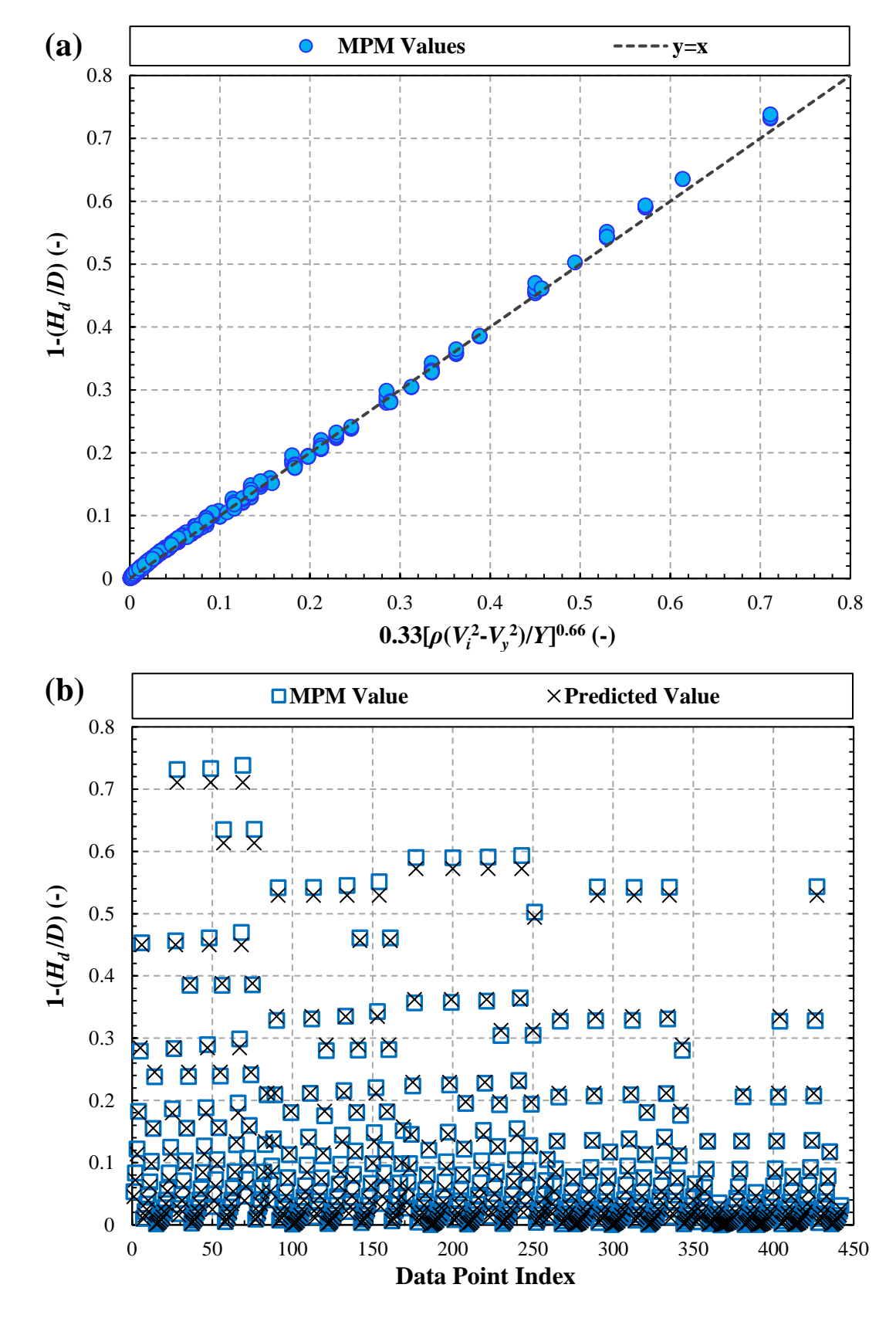


Figure 5-5 The compression ratio, 1- $(H_d/D)$ , obtained from the MPM simulations: (a) as a function of Equation (5-5), identified by the AI framework, and (b) in comparison with the values predicted by Equation (5-5) for all the data points.



### 5.3.3. Other Output Data

With regards to the other output variables (e,  $W_p/W_i$  and  $1-e^2$ ), the framework struggles to identify equations of physical significance which provide an acceptable fit to the MPM data. As seen in Section 4.3.5, Equation (4-9) can be fitted to the MPM data to predict the coefficient of restitution, yet the framework fails to identify this relationship. This is attributed to the fact that DNNs (and their built-in equation library) are not applied to the MPM data. However, it is not certain that the user-defined equation library of the framework (refer to Table 2 of [188]) would be capable of identifying Equation (4-9), as the library does not include such a relationship.

Nonetheless, the framework is able to detect a close link between  $1-e^2$  and  $W_p/W_i$ , as shown in Figure 5-6. Both  $1-e^2$  and  $W_p/W_i$  determine the ratio of the plastic work to the incident kinetic energy, albeit using different methods;  $1-e^2$  represents deducting the rebound energy  $(1/2mV_r^2)$  from the incident kinetic energy  $(1/2mV_i^2)$  to find the plastic work (and dividing it by the incident kinetic energy), while  $W_p/W_i$  deducts the recovered elastic energy from the total deformation energy, using the stress-strain relationship. Considering the graph,  $1-e^2$  intuitively increases with an increase in  $W_p/W_i$ , since the rebound velocity of the particle decreases as most of the incident kinetic energy is spent on plastic work. Even though it is anticipated that the data points in Figure 5-6 lie very close to the identity line, the values obtained from  $1-e^2$  are overestimated compared to those obtained from  $W_p/W_i$ . This discrepancy potentially arises from the underestimation of e by the MPM approach, as well as the high sensitivity of the coefficient of restitution to the selected time step (as discussed in Section 4.3.5). Consistent with the previous observations, there is scatter in the data corresponding to the cases with the impact velocities of 10 and 20 m/s.

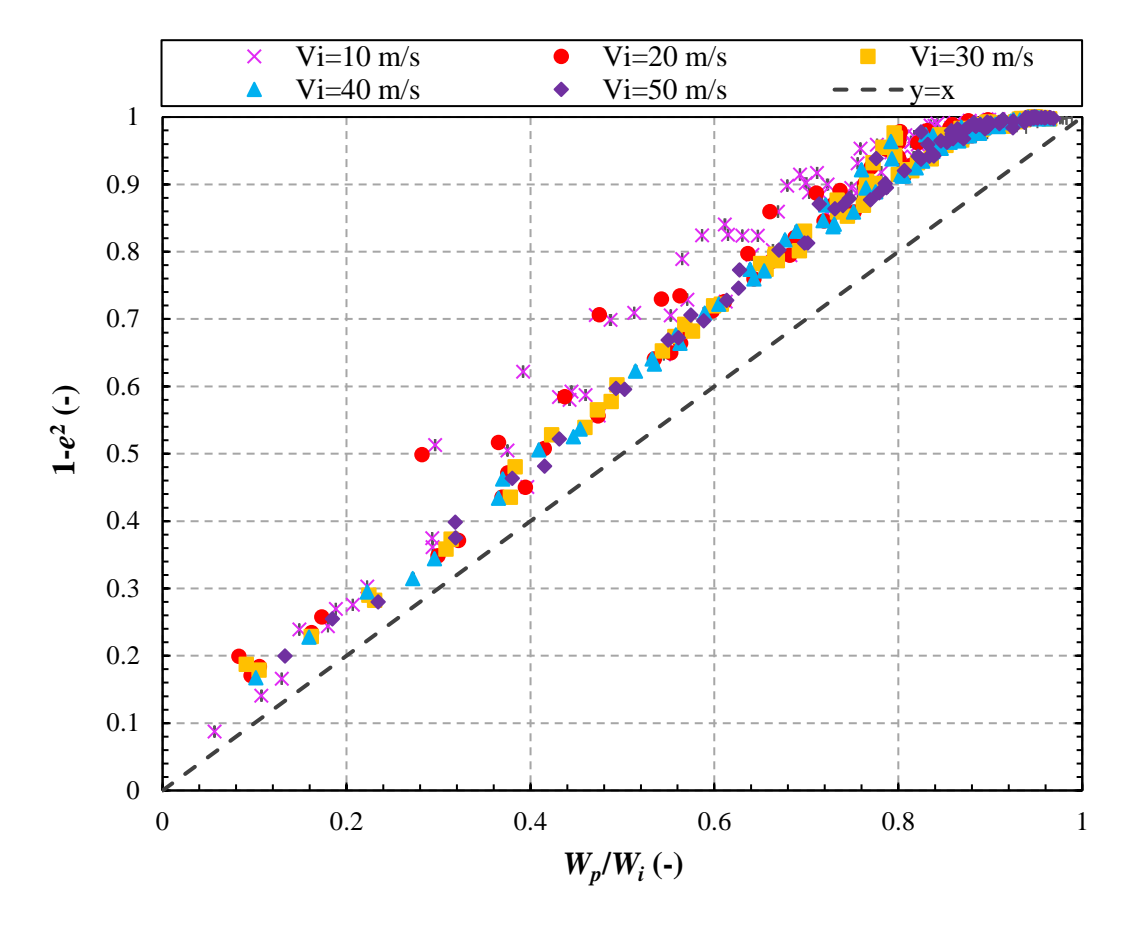


Figure 5-6 1- $e^2$ , as a function of  $W_p/W_i$ , both representing the ratio of the plastic work to the incident kinetic energy.

#### 5.3.4. Numerical Verification

In order to verify the adequacy of the identified equations for the equivalent plastic strain and compression ratio, MPM simulations are carried out for two further cases with material properties and impact velocities outside the original input data range. Subsequently, the MPM values of the equivalent plastic strain and compression ratio are compared to the values obtained using Equations (5-4) and (5-5). For the first case, a lead particle with an impact velocity of 5 m/s is considered. The second case addresses the impact of a nickel particle at 80 m/s. The material properties for both of the particles are taken from [180], as shown in Table 5-3. For both cases, the particle is modelled as a 500 µm sphere impacting a rigid wall placed 30 µm below it. The discretisation settings and time step are the same as discussed in Section



4.2. However, the mesh size is adjusted here in a way that the ratio of the element size to the distance between the material points in each dimension is 1.5 for the nickel particle and 1.05 for the lead particle.

Table 5-3 Material properties of lead (Pb) and nickel (Ni) used in the MPM simulations for the verification of Equations (5-4) and (5-5). Taken from [180].

| Material | $\rho$ (kg/m <sup>3</sup> ) | E (GPa) | Y (MPa) | v (-) |
|----------|-----------------------------|---------|---------|-------|
| Pb       | 11,400                      | 15.8    | 5.9     | 0.44  |
| Ni       | 8,900                       | 204     | 148     | 0.31  |

Tables 5-4 and 5-5 respectively provide the MPM values of  $\varepsilon_p$  and 1- $(H_d/D)$  for lead and nickel particles, compared to those calculated using the equations identified by the framework. As expected, the nickel particle undergoes larger deformation (17% of its original diameter) compared to the lead particle (5% of its original diameter), as it has a significantly higher impact velocity. The predicted values by the framework for both  $\varepsilon_p$  and 1- $(H_d/D)$  are very close to the MPM values, despite the fact that the material properties and impact velocities of the tested cases are outside the range of the original input data that have been used to develop the equations. This verifies the adequacy of the equations and confirms the capability of the framework in finding equations that describe the relationship between the input and output data, given that the input data are appropriately structured.

Table 5-4 The equivalent plastic strain,  $\varepsilon_p$ , for lead and nickel particles, as obtained from the MPM simulations, in comparison with the predictions of Equation (5-4) identified by the AI framework.

|          |      | $\varepsilon_p$ (-) |
|----------|------|---------------------|
| Material | MPM  | Equation (5-4)      |
| Pb       | 0.02 | 0.02                |
| Ni       | 0.17 | 0.18                |



Table 5-5 The compression ratio,  $1-(H_d/D)$ , for lead and nickel particles, as obtained from the MPM simulations, in comparison with the predictions of Equation (5-5) identified by the AI framework.

|          | 1-( <i>H</i> | $(I_d/D)$ (-)  |
|----------|--------------|----------------|
| Material | MPM          | Equation (5-5) |
| Pb       | 0.05         | 0.04           |
| Ni       | 0.17         | 0.17           |

# 5.4. Critique and Concluding Remarks

The AI framework is capable of finding meaningful equations when provided with well-structured input data, showing its potential as a valuable tool for equation discovery. However, its dependence on user-prepared dimensionless groups, inability to generalise to raw input data, and failure to identify complex equations due to the absence of an equation library reveal several areas for improvement. These shortcomings can be addressed by improving the pre-processing procedure, extending the analysis to DNNs, and expanding the incorporated library. Moreover, integrating more advanced techniques such as Physics-Informed Neural Networks (PINNs) can improve the predictive capabilities of the framework by incorporating physical laws directly into the learning process, as traditional Neural Networks only rely on data rather than physical principles [196].



# 6. Impact Experiments

### 6.1. Overview

In this chapter, impact tests are conducted to evaluate the accuracy of the MPM approach in predicting the deformation behaviour during impact. First, elastic impact is examined using elastic balls, and simulations are performed to compare measurable experimental parameters to their predicted values. Subsequently, elastic-plastic impact is investigated by subjecting copper, solder and aluminium alloy particles to impact in an in-house device. The resulting compression ratio, and where possible, the coefficient of restitution are measured and compared against empirical Equations (5-5) and (4-9). Finally, a methodology is explored to assess the applicability of Equation (5-5) to hyper-velocity impacts. This is achieved by depositing fine copper particles using an aerosol deposition rig. The results of this analysis offer a preliminary assessment of whether Equation (5-5) can be extended to high strain rate conditions.

Mr Mohammad Alasossi (University of Leeds, UK) has contributed to the data curation for the impact of metal particles in the in-house device as part of his MSc project. His contributions include the complete dataset for the aluminium alloy particles and portions of the data for the solder and copper particles. Additionally, he has assisted in modifying the coefficients of the empirical equation developed for predicting particle impact velocity in the device. Mr Stuart Micklethwaite and Mr John Harrington at Leeds electron microscopy and spectroscopy centre, LEMAS (University of Leeds, UK) have contributed to imaging and sectioning the deposited copper particles. Finally, the contribution of Dr Fanchao Meng (The University of Manchester, UK) in estimating the particle impact velocity in the aerosol deposition rig's nozzle is gratefully acknowledged. The methodology, investigation, all the other data curation (aside from the aforementioned), analysis, validation, visualisation and



discussions are the contributions of the thesis author. A part of the results from this chapter has been submitted for publication in [183].

### 6.2. Impact of Elastic Balls

### **6.2.1.** Methodology

To validate the accuracy of the MPM approach in modelling elastic impact, impact tests are conducted using three different bouncy balls. A digital calliper is used to measure the diameter of the balls, and their density is determined from their weight and volume. The Young's modulus of each ball is inferred from the contact force-displacement relationship measured by the Instron Mechanical Tester 5566 (Instron European Headquarters, Buckinghamshire, UK), assuming Hertzian contact and a Poisson's ratio of 0.25 for all the balls (five loading-unloading measurements per ball). Subsequently, the balls are normally impacted on a clean laboratory tabletop, and their impact velocity is measured by high-speed imaging using Photron Fastcam SA5 camera. This is repeated several times for each ball until three measurements resulting in close values for the impact velocity are achieved and taken as the main measurements. The measured properties and velocities of the balls (mean values for the Young's modulus and impact velocity), as shown in Table 6-1, are then used to conduct threedimensional simulations of the impact tests. For all the simulations, the ball is modelled as a sphere discretised into 74,227 material points, and the wall is placed 1.5 mm below the particle (3 times the distance between the material points). A time step of 1 ns is selected and the mesh size is adjusted based on an element to point ratio of 1.05. The linear elastic constitutive law is used, and damping and friction are not applied.

Table 6-1 Material properties and impact velocity of the balls used in the elastic impact experiments.

|        | D (mm) | $\rho$ (kg/m <sup>3</sup> ) | E (MPa)       | v (-) | $V_i$ (m/s) |
|--------|--------|-----------------------------|---------------|-------|-------------|
| Ball 1 | 25     | 889                         | 2.57±0.13     | 0.25  | 4.30±0.27   |
| Ball 2 | 25     | 894                         | $3.55\pm0.42$ | 0.25  | 5.41±0.16   |
| Ball 3 | 25     | 1,404                       | 4.90±0.28     | 0.25  | 5.74±0.19   |

### 6.2.2. Comparison between Simulation and Experimental Results

Figure 6-1 illustrates the instant of maximum deformation upon impact, observed from the high-speed images of the balls, as well as the visualisations of the simulated balls, including the overall view and the corresponding contours of von Mises stress. It should be noted that the contours are on the surface of a plane slicing the particle in half with the normal of the plane pointing towards the observer (normal is along the x axis). Moreover, Tables 6-2, 6-3, and 6-4 provide a comparison between the experimental and simulation results for the total contact time ( $t_{tot}$ ), the ratio of the particle height to the original particle diameter at the instant of maximum deformation ( $H_e/D$ ), and the coefficient of restitution (e), respectively.

Qualitative observation of Figure 6-1 suggests that the simulations predict an intuitive deformation behaviour for the balls, with the stress being concentrated in the vicinity of the impact point. Considering the von Mises stress values from the contour scale bars, Ball 3 experiences higher stress upon impact compared to Balls 2 and 1. This is intuitively expected, as Ball 3 has the highest impact energy and Young's modulus. It should be mentioned that the sequences (animations) of the simulation visualisations and high-speed images (not shown in this report) are also in perfect agreement in displaying the transmission of the elastic waves through the balls.

With regards to Tables 6-2 and 6-3, there is a good agreement between the experimental and simulation values of  $t_{tot}$  and  $H_e/D$ . Considering Table 6-2, in line with Equation (3-21) from Johnson [27], the contact duration decreases moving from Ball 1 to Ball 3, as Balls 1 and



2 have a relatively lower Young's modulus and impact velocity compared to Ball 3. Moreover, as seen in Table 6-3, Ball 3 has the lowest  $H_e/D$ , since its impact energy is higher than Balls 1 and 2. From Table 6-4, for all the balls, the measured coefficient of restitution is smaller than the value obtained from the simulation. This discrepancy is expected, as the simulations do not account for energy losses due to several factors such as friction, adhesion, and elastic wave propagation [14]. Ideally, the simulation values for the coefficient of restitution should be 1. However, the use of a lumped mass matrix leads to an underestimation of e (by approximately 2% here) due to energy dissipation resulting from simplifying the mass matrix. There is also a slight reduction in the measured coefficient of restitution moving from Ball 1 to 3. This could potentially be due to the differences in the contact time between the balls, as shown in Table 6-2; the longer the contact duration, the higher the likelihood that the propagated elastic waves will reflect from the impact surface back into the ball, increasing the coefficient of restitution.

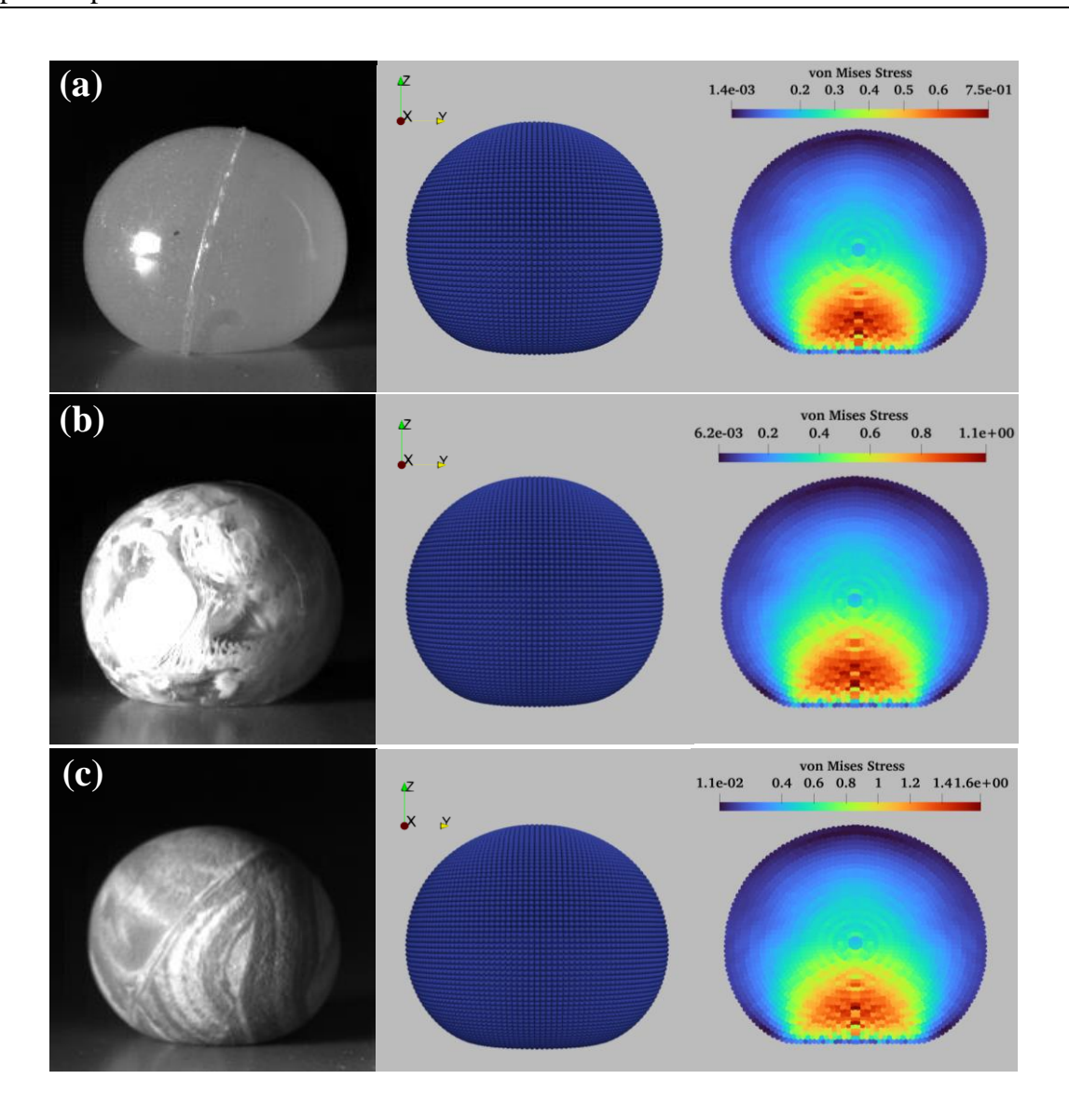


Figure 6-1 The instant of maximum deformation upon impact for (a) Ball 1, (b) Ball 2, and (c) Ball 3, captured from high-speed images of the balls, as well as the visualisations of the simulated balls, including the overall view and the corresponding contours of von Mises stress. The contours are on the surface of a plane slicing the particle in half (normal of the plane is along the *x* axis).

Table 6-2 Comparison between the experimental and simulation values of the total contact time,  $t_{tot}$ , for the impact of elastic balls.

|            |           | $t_{tot}$ (ms) |               |
|------------|-----------|----------------|---------------|
|            | Ball 1    | Ball 2         | Ball 3        |
| Experiment | 1.57±0.24 | $1.39\pm0.23$  | $1.30\pm0.28$ |
| MPM        | 1.60      | 1.36           | 1.40          |



Table 6-3 Comparison between the experimental and simulation values of the ratio of the particle height to the original particle diameter at the instant of maximum deformation,  $H_e/D$ , for the impact of elastic balls.

|            |                 | $H_e/D$ (-)   |                 |
|------------|-----------------|---------------|-----------------|
|            | Ball 1          | Ball 2        | Ball 3          |
| Experiment | $0.88 \pm 0.02$ | $0.88\pm0.01$ | $0.87 \pm 0.02$ |
| MPM        | 0.89            | 0.88          | 0.87            |

Table 6-4 Comparison between the experimental and simulation values of the coefficient of restitution, e, for the impact of elastic balls.

|            |               | e (-)           |               |
|------------|---------------|-----------------|---------------|
|            | Ball 1        | Ball 2          | Ball 3        |
| Experiment | $0.89\pm1.01$ | $0.87 \pm 0.56$ | $0.86\pm1.94$ |
| MPM        | 0.98          | 0.98            | 0.98          |

# 6.3. Impact of Metal Particles in the Single Particle Impact Tester

In this section, the empirical equations identified in Chapters 4 and 5 for predicting the coefficient of restitution and compression ratio (Equations (4-9) and (5-5), respectively) are examined for their validity. To this end, impact experiments are conducted in an in-house device called the "single particle impact tester", shown in Figure 6-2, using metal particles. The device comprises an air eductor which is connected to a collection chamber via an acceleration tube. The collection chamber, in which the target assembly is located, is connected to a vacuum pump with adjustable pressure. By adjusting the vacuum pump, the pressure difference between the collection chamber and the inlet of the device (where particles are fed) generates different air velocities in the acceleration tube, resulting in different particle impact velocities. To study the impact deformation of particles using this device, it is crucial to determine their impact velocity. While high-speed imaging can be used to measure the impact velocity of particles larger than 350 µm, particles smaller than this size cannot be tracked using

this method. Therefore, the impact velocity for large particles of different materials is first established against the applied vacuum, and the results are used to develop a non-dimensional empirical correlation for predicting the particle impact velocity in the device, as detailed in Section 6.3.1. Subsequently, metal particles are subjected to impact in the device, and their measured compression ratio and coefficient of restitution is compared to Equations (5-5) and (4-9), respectively (Sections 6.3.2.3 and 6.3.2.4).

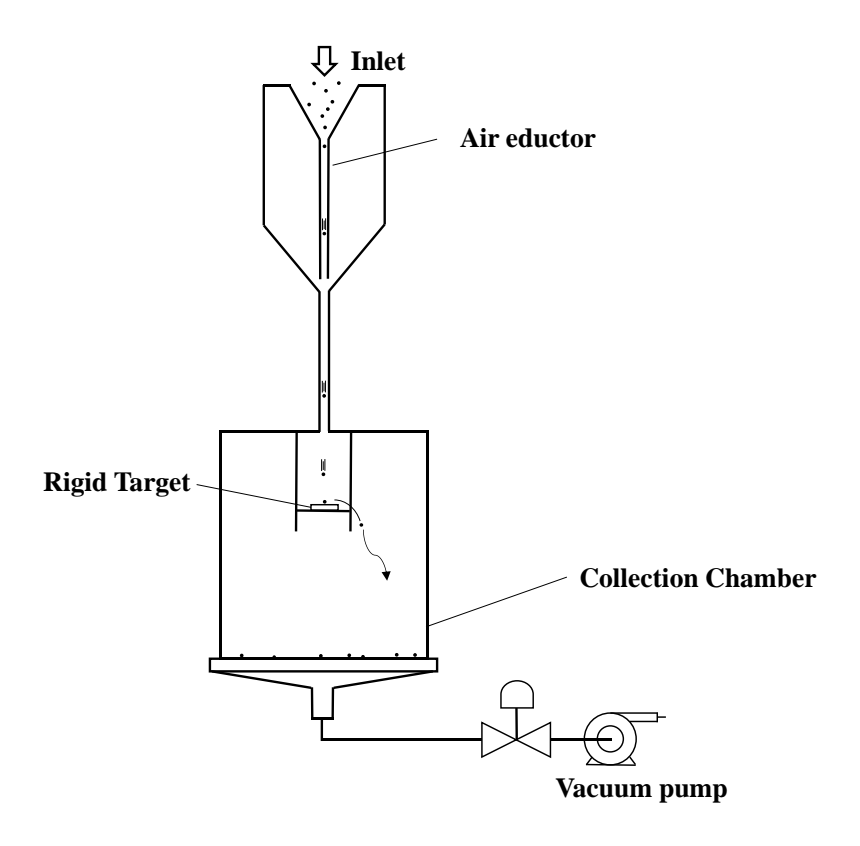


Figure 6-2 Schematic drawing of the single particle impact tester device.

### **6.3.1.** Empirical Correlation for Impact Velocity in the Device

### 6.3.1.1. Sample Preparation and Impact Velocity Measurement

The sample test materials used in this part of the work are spherical particles of high density polyethylene (HDPE), polypropylene homopolymer (PP Homo) and polypropylene random copolymer (PP RaCo), obtained from LyondellBasell (Italy) and spherical glass beads

obtained from Sigmund Lindner GmbH (Warmensteinach, Germany). In order to make the velocity measurements precise and also measure the particle densities, near-mesh size particles are prepared for the tests as follows: sample particles are mechanically sieved with an amplitude of 1 mm for 10 minutes (10 second time intervals) using the Haver EML digital plus test sieve shaker (Haver & Boecker, Oelde, Germany) and the BS 410 sieve type. Subsequently, only the particles stuck in the mesh apertures of the sieves are collected by brushing. A sufficient number of particles with sizes of 500, 710 and 1,000 µm are collected for the polymer samples in the aforementioned manner. Due to time constraints, only 1,000 µm particles are collected for the glass beads. As near-mesh size particles are used, it is expected that all of the test particles of the same size have approximately the same volume. Thus, particle density is measured by weighing a specific number of the 1,000 µm particles and dividing the measured weight by their total volume. The measurements are conducted with different numbers of particles, gradually increased until a constant value for density is achieved, and the results are shown in Table 6-5.

Table 6-5 The measured density of the sample particles used in developing an empirical correlation for predicting the particle impact velocity in the single particle impact tester.

| Sample      | $\rho$ (kg/m <sup>3</sup> ) |
|-------------|-----------------------------|
| HDPE        | 745                         |
| PP Homo     | 859                         |
| PP Raco     | 902                         |
| Glass Beads | 2,545                       |

To measure the particle impact velocities, Photron Fastcam SA5 camera is used to capture individual particles falling through the acceleration tube. Above the target assembly, a ruler is fixed on the transparent acceleration tube, so that the distance travelled by the falling particle can be captured (see Figure 6-3). The particles are introduced from the top of the rig and four vacuum gauge pressures of 4, 8, 12 and 16 kPa (absolute vacuum pressures of 97.325, 93.325,

89.325 and 85.325 kPa) are selected to accelerate the particles to a wide range of velocities. The polymer particles are additionally imaged during free fall (0 vacuum gauge pressure). A frame rate of 10<sup>4</sup> fps for the free fall measurements and 4×10<sup>4</sup> fps for the rest of the measurements are used. The measurements for the polymer particles are repeated five times for different combinations of size and vacuum gauge pressure, yielding a total of 225 measurements (three sample materials, three sizes, five vacuum gauge pressures and five repeats). In addition, 20 measurements are conducted for the glass beads (one sample material, one size, four vacuum gauge pressures and five repeats). The impact velocities are then measured through analysing the captured high-speed images, as described below:

Time per frame is determined based on the frame rate for each of the measurements. Subsequently, the number of the frames it takes the particle to travel a certain distance on the ruler is multiplied by the time per frame to yield the time of travel. The travelled distance (displacement) is then divided by the time of travel to determine the particle impact velocity for each of the measurements. Ultimately, the arithmetic mean of the impact velocity values obtained from the five repeated measurements is taken as the impact velocity of the particle. As the time intervals for the measurements are really short (0.025-0.1 ms), the measured velocities can be taken as instantaneous particle velocities. Plots of the measured particle impact velocities as a function of the vacuum gauge pressure are presented in Figure C-1 of Appendix C, for all the test particles.

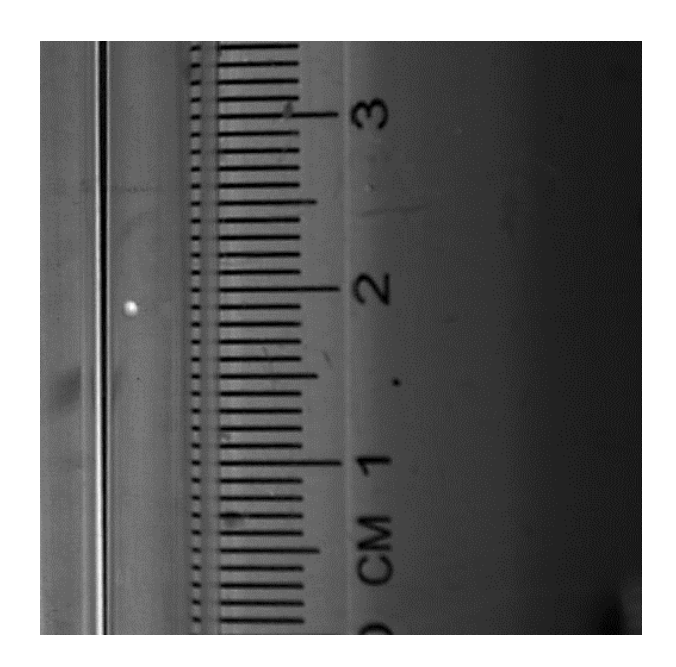


Figure 6-3 One frame of the high-speed images taken from a 1,000  $\mu$ m HDPE particle during free fall through the single particle impact tester acceleration tube (frame rate of  $10^4$  fps).

### 6.3.1.2. Empirical Correlation

Figure C-1 of Appendix C demonstrates that the particle impact velocity in the device increases with the vacuum gauge pressure, and decreases as the particle size or density increases, which is intuitively expected. These trends align with the empirical correlation of Bonakdar et al. [197] for predicting the particle impact velocity in the Aero S disperser of Malvern Panalytical Mastersizer 3000 (Malvern Panalytical, Worcestershire, UK). Accordingly, the correlation of Bonakdar et al. [197], which is in the form of Equation (6-1), is modified for the single particle impact tester by using the impact velocities and particle properties measured in the previous section, to find constant  $C_1$ , and power indices  $C_2$ ,  $C_3$  and  $C_4$ :

$$N_{v}^{1/3} = C_{1} \left[ \frac{\left( \frac{P_{gauge}}{\rho_{air} gh} \right)^{C_{2}}}{\left( S - 1 \right)^{C_{3}} \left( N_{d} \right)^{C_{4}/3}} \right]$$
 (6-1)

where  $N_v$  and  $N_d$  are dimensionless particle impact velocity and size, respectively.  $P_{gauge}$  is the vacuum gauge pressure in Pa (positive values),  $\rho_{air}$  is the air density in kg/m<sup>3</sup>, g is the gravitational acceleration in m/s<sup>2</sup> and h is the full length of the acceleration tube (0.401 m).  $S=\rho_p/\rho_{air}$  where  $\rho_p$  is the particle density in kg/m<sup>3</sup>.  $N_v$  and  $N_d$  can be calculated from Equations (6-2) and (6-3), respectively, where  $v_{air}=\mu_{air}/\rho_{air}$  is the kinematic viscosity of air in m<sup>2</sup>/s, with  $\mu_{air}$  being the dynamic viscosity of air.

$$N_{v}^{1/3} = V_{i} \left[ \frac{3}{4gv_{air}(S-1)} \right]^{1/3}$$
 (6-2)

$$N_d^{1/3} = D \left[ \frac{4g(S-1)}{3v_{qir}^2} \right]^{1/3}$$
 (6-3)

The measured impact velocities are first used to calculate  $N_v^{1/3}$  from Equation (6-2). Subsequently,  $N_v^{1/3}$  is plotted against  $P_{gauge}/\rho_{air}gh$  and the power law equation of the fitted line is used to find the power index  $C_2$  by regression in the Microsoft Excel software. This is done for different combinations of particle size and vacuum gauge pressure for all the test materials, and the arithmetic mean of all the values is taken as  $C_2$  (refer to Figure C-2 of Appendix C). After determining  $C_2$ ,  $N_v^{1/3}$  is divided by  $(P_{gauge}/\rho_{air}gh)^{C_2}$ , and the resultant values are plotted as a function of  $N_d^{1/3}$  to find the power index  $C_4$  in the same way  $C_2$  is calculated (refer to Figure C-3 of Appendix C). It should be noted that as the measurements for the glass beads are



conducted with only one particle size, the initial value found for  $C_4$  is only based on the data from the polymer particles.

In order to determine  $C_1$  and  $C_3$ , group  $C_i$  is first calculated for all the data using Equation (6-4). As  $C_i$  is density/material-dependent, the arithmetic mean of the values found for different combinations of size and vacuum gauge pressure corresponding to a specific test material is taken as the  $C_i$  of that material. In the end,  $C_i$  is plotted as a function of (S-1) to determine the pre-exponential constant  $C_1$  and power index  $C_3$ , as shown in Figure C-4 of Appendix C. The initial values found for  $C_1$ ,  $C_2$ ,  $C_3$  and  $C_4$  are shown in Table 6-6.

$$C_{i} = \frac{N_{v}^{1/3} \times (N_{d})^{C_{4}/3}}{\left(\frac{P_{gauge}}{\rho_{air}gh}\right)^{C_{2}}} = \frac{C_{1}}{(S-1)^{C_{3}}}$$
(6-4)

Table 6-6 Initial values determined for the empirical constant and power indices of Equation (6-1), developed for predicting the particle impact velocity in the single particle impact tester.

| <i>C</i> <sub>1</sub> | $C_2$ | <i>C</i> <sub>3</sub> | C4   |
|-----------------------|-------|-----------------------|------|
| 158.26                | 0.464 | 0.55                  | 0.22 |

To evaluate the performance of the correlation using the initial  $C_1$ ,  $C_2$ ,  $C_3$  and  $C_4$  values in Table 6-6, the coefficient of determination (R<sup>2</sup>) is calculated using Equation (6-5) for all the data, where  $N_{\nu,p}^{1/3}$  and  $N_{\nu,e}^{1/3}$  denote the predicted and experimental values of  $N_{\nu}^{1/3}$  obtained from Equations (6-1) and (6-2), respectively, and  $n_d$  is the number of the data points. The results corresponding to each of the sample materials are reported in Table 6-7.



$$R^{2} = 1 - \frac{\sum_{i=1}^{n_{d}} \left(N_{v,p_{i}}^{1/3} - N_{v,e_{i}}^{1/3}\right)^{2}}{\sum_{i=1}^{n_{d}} \left(N_{v,p_{i}}^{1/3} - \frac{1}{n_{d}} \sum_{i=1}^{n_{d}} N_{v,e_{i}}^{1/3}\right)^{2}}$$
(6-5)

Table 6-7 The coefficient of determination ( $\mathbb{R}^2$ ) for  $N_{\nu}^{1/3}$  values predicted by Equation (6-1) using the initial  $C_1$ ,  $C_2$ ,  $C_3$  and  $C_4$  values (Table 6-6), with respect to the experimental values calculated by Equation (6-2) using the measured impact velocities.

| Material       | HDPE | PP Homo | PP RaCo | Glass Beads |
|----------------|------|---------|---------|-------------|
| $\mathbb{R}^2$ | 0.98 | 0.99    | 0.99    | 0.71        |

With regards to Table 6-7,  $R^2$  is small for the glass beads, indicating that using the initial values for the empirical constant and power indices (Table 6-6) cannot provide a universally adequate prediction of the impact velocity. This is due to the fact that glass beads cannot be included in the calculations for  $C_4$ , as only one particle size is used in the corresponding measurements. Thus, other values for  $C_4$  (and consequently  $C_1$  and  $C_3$ ) are explored by trial and error until the difference between the measured and predicted values produces acceptably low errors for all the test materials. Accordingly, the final modified values for  $C_1$ ,  $C_2$ ,  $C_3$  and  $C_4$ , as well as the corresponding  $R^2$  values for  $N_{\nu}^{1/3}$  are shown in Tables 6-8 and 6-9, respectively.

Table 6-8 Modified values determined for the empirical constant and power indices of Equation (6-1), developed for predicting the particle impact velocity in the single particle impact tester.

| $C_1$  | $C_2$ | $C_3$ | C <sub>4</sub> |
|--------|-------|-------|----------------|
| 371.23 | 0.464 | 0.673 | 0.235          |



Table 6-9 The coefficient of determination ( $\mathbb{R}^2$ ) for  $N_{\nu}^{1/3}$  values predicted by Equation (6-1) using the modified  $C_1$ ,  $C_2$ ,  $C_3$  and  $C_4$  values (Table 6-8), with respect to the experimental values calculated by Equation (6-2) using the measured impact velocities.

| Material       | HDPE | PP Homo | PP RaCo | Glass Beads |
|----------------|------|---------|---------|-------------|
| R <sup>2</sup> | 0.98 | 0.99    | 0.99    | 0.99        |

Table 6-9 shows that compared to the initial values for  $C_1$ ,  $C_2$ ,  $C_3$  and  $C_4$ , the modified values provide a much better prediction for the glass beads, while the  $R^2$  values for the polymer particles do not change. As the modified values lead to acceptable results for all the test materials, the correlation for impact velocity in the device takes the form of Equation (6-6):

$$N_{v}^{1/3} = 371.23 \left[ \frac{\left( \frac{P_{gauge}}{\rho_{air}gh} \right)^{0.464}}{\left( S - 1 \right)^{0.673} \left( N_{d} \right)^{0.235/3}} \right]$$
 (6-6)

Comparison between the experimental values of the dimensionless impact velocity,  $N_{\nu}^{1/3}$ , and those predicted by Equation (6-6) is given in Figure C-5 of Appendix C for different sizes of the polymer particles at different vacuum gauge pressures. As the data for the glass beads correspond to only one particle size, experimental and predicted values of the dimensionless impact velocity are plotted for different vacuum gauge pressures instead, as shown in Figure C-6 of Appendix C. The graphs suggest that the developed correlation provides acceptable predictions of the impact velocity for all the particles. This is further demonstrated by Figure 6-4, where the data fall on the identity line when the experimental values of the dimensionless impact velocity,  $N_{\nu,e}^{1/3}$ , are plotted as a function of those predicted by Equation (6-6),  $N_{\nu,p}^{1/3}$ .

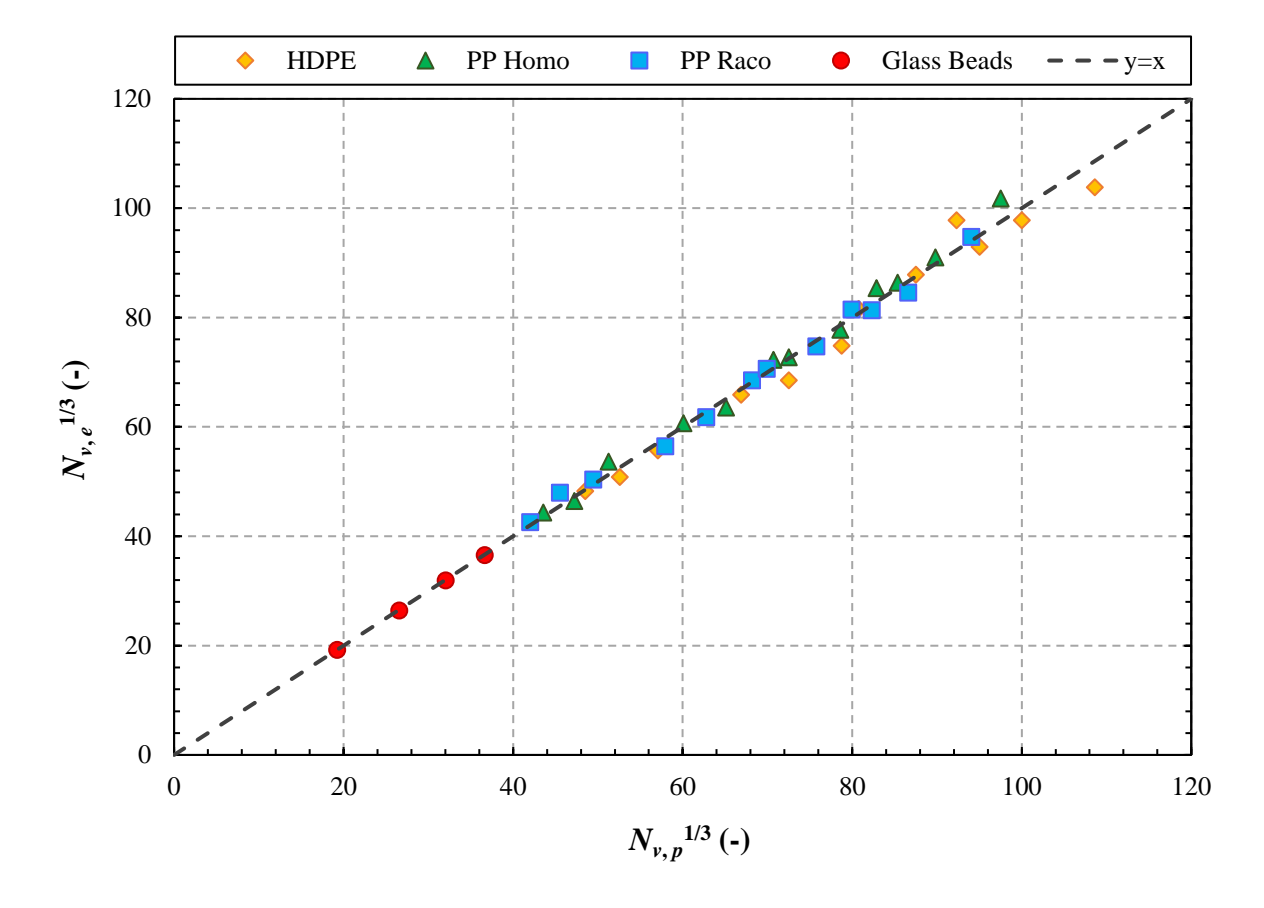


Figure 6-4 The experimental values of the dimensionless impact velocity,  $N_{\nu,e}^{1/3}$ , as a function of those predicted by Equation (6-6),  $N_{\nu,p}^{1/3}$ , for all the sample particles.

### **6.3.2. Impact of Metal Particles**

### 6.3.2.1. Sample Particles

For the impact tests, the following metal particles are used: 350, 500 and 760 µm SAC305 solder balls composed of 96.5% Sn, 3% Ag and 0.5% Cu (Chip Quik Inc., Ontario, Canada), copper particles with a maximum size of 150 µm (Goodfellow Cambridge Limited, Huntingdon, UK), and aluminium alloy 6061 particles with a maximum size of 63 µm (Goodfellow Cambridge Limited, Huntingdon, UK). Scanning Electron Microscope (SEM) images of the particles are captured using a Hitachi TM3030 table top microscope (Hitachi Ltd., Tokyo, Japan), as shown in Figure 6-5. The solder balls and copper particles are highly spherical, while the aluminium alloy particles consist of both spherical and irregular particles.

It should be noted that the impact experiments with these particles are used in the validation of Equations (4-9) and (5-5), which are derived considering an elastic-perfectly plastic constitutive law. However, most metal particles exhibit strain rate sensitivity, the effect of which is not accounted for by an elastic-perfectly plastic material model. Nevertheless, with reference to the work of Mao et al. [198], the copper particles used in this section are expected to have a very small strain rate sensitivity (for strain rates smaller than 10<sup>3</sup> s<sup>-1</sup>), as their grain size does not exceed 10 µm. Moreover, Noh et al. [199] and Ma'at et al. [200] suggest that even though aluminium alloy 6061 shows a high strain rate sensitivity at elevated temperatures, its mechanical properties are not affected by strain rate at room temperature. Regarding the solder balls, most available studies [201,202] focus on material behaviour at strain rates close to 10<sup>3</sup> s<sup>-1</sup>, which marks the lower end of the range encountered in cold spraying [126]. Even though it is challenging to determine the strain rate of the particles upon impact in the single particle impact tester, the impact velocities do not exceed 40 m/s, which is considerably lower than the velocity range of cold spraying (200 to 1,500 m/s [3]). However, in the study by Lall et al. [203], which examines relatively lower strain rates (10-75 s<sup>-1</sup>), the mechanical properties of SAC305 solder balls are not noticeably affected by strain rate at room temperature. Therefore, it is assumed that the solder balls used in the current work do not exhibit strain rate sensitivity.

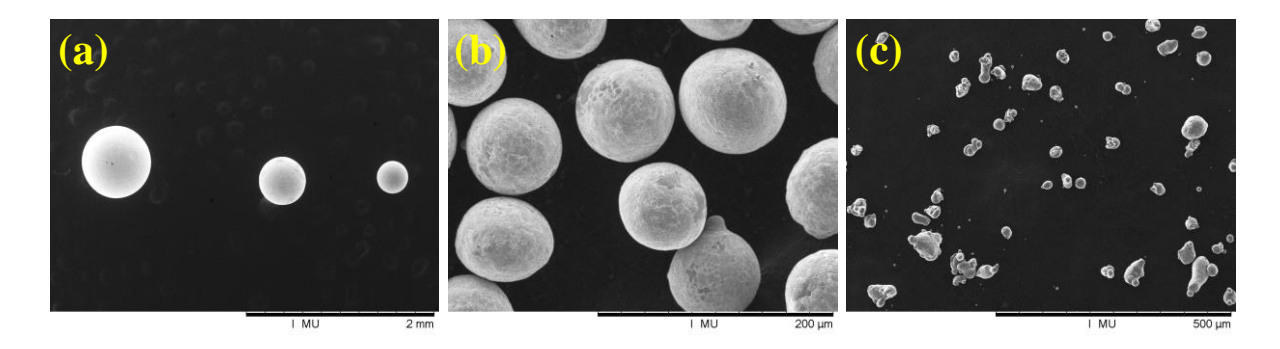


Figure 6-5 SEM images of the (a) 760, 500 and 350  $\mu$ m solder balls, (b) copper particles and (c) aluminium alloy particles, used in the impact tests conducted in the single particle impact tester.

The material properties of all the metal particles are shown in Table 6-10. The mechanical properties of the particles are measured by nano-indentation in the NanoTest device (Micro Materials Ltd., Wrexham, UK). Accordingly, the particles are cold mounted in resin and polished to provide a flat surface for indentation. For each sample material, the indentations are carried out on the surface of various particles using a Berkovic indenter, following a loadcontrolled method (maximum load of 50 mN). The measurements are repeated five times for the copper (Cu) and aluminium alloy (AA6061) particles, and fifteen times for the solder balls (SAC305). The arithmetic mean values of these measurements are then used to determine the Young's modulus and hardness (H). The yield strength of the particles is subsequently inferred from the measured hardness by assuming H/Y=2.8 [115]. It should be noted that the density and Poisson's ratio of the AA6061 particles, as well as all the material properties of the Cu particles are provided by the supplier. However, the reported values of the yield strength for Cu vary widely in the range 54 to 270 MPa for soft and hard particles, respectively. Thus, an average value is additionally considered, based on the arithmetic mean value of the aforementioned. The density of the SAC305 balls is measured by the method explained in Section 6.3.1.1 for the polymer particles and glass beads, and their Poisson's ratio is assumed to be that of Sn [180], as it comprises 96.5% of the material composition.



Table 6-10 Material properties of the copper particles (Cu), solder balls (SAC305), and aluminium alloy particles (AA6061) used for the impact experiments in the single particle impact tester.

| Sample | $\rho$ (kg/m <sup>3</sup> ) | E (GPa)                          | Y (MPa)   | v (-)             |
|--------|-----------------------------|----------------------------------|---|-------------------|
| Cu     | 8,960ª                      | 129.8 <sup>a</sup> , 125.18±2.49 | 54 <sup>a</sup> , 162 <sup>b</sup> , 270 <sup>a</sup> , 446.62±0.02 | 0.343             |
| SAC305 | 7,274                       | 59.82±8.60                       | 97.59±0.01  | 0.33              |
| AA6061 | 2,700 <sup>a</sup>          | 36.08±1.24                       | 345.44±0.04   | 0.33 <sup>a</sup> |

<sup>&</sup>lt;sup>a</sup> Provided by the supplier.

#### 6.3.2.2. Methodology

As the solder balls are large enough to be handled and tracked, individual particles are subjected to impact in the single particle impact tester, and the Photron Fastcam SA5 camera is used to capture their impact and rebound. To this end, single particles from each size class (350, 500 and 760  $\mu$ m) are subjected to impact using the vacuum gauge pressures of 10, 15, and 20 kPa. A frame rate of  $2\times10^4$  fps for the 760  $\mu$ m particles, and  $4\times10^4$  fps for the 350 and 500  $\mu$ m particles is used. The tests are repeated three times for each size class and vacuum gauge pressure, resulting in a total of 27 measurements. The data from these measurements are used to determine both the coefficient of restitution and compression ratio. To have a more comprehensive dataset for the coefficient of restitution, additional measurements are later conducted using the vacuum gauge pressures of 0 (free fall) and 5 kPa (for these samples, the compression ratio is not measured). To fully capture the impact and rebound of the particles on the impact target, instead of using a ruler outside of the acceleration tube (which is at a distance from the target assembly), the screws beside the target are marked at 1 cm intervals (refer to Figure 6-6). This distance is used as a reference for measuring the impact and rebound

<sup>&</sup>lt;sup>b</sup> Arithmetic mean of the values provided by the supplier.

velocities to determine the coefficient of restitution, following the approach detailed in Section 6.3.1.1.

For the copper and aluminium alloy samples, a small amount of the particles is fed to the single particle impact tester using a vibratory trough, at vacuum gauge pressures of 10, 15, and 20 kPa. Note that it is not feasible to directly measure the coefficient of restitution for these particles, as they are not large enough to be tracked using the high-speed camera. Therefore, they are only analysed for their compression ratio.

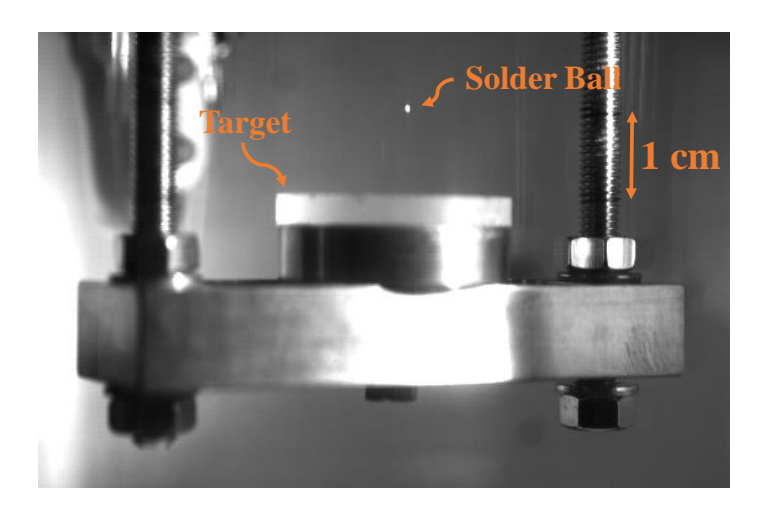


Figure 6-6 One frame of the high-speed images taken from a 760  $\mu$ m solder ball subjected to impact in the single particle impact tester at a 10 kPa vacuum gauge pressure (frame rate of  $2\times10^4$  fps).

Upon comparing the measured velocities of the solder balls with the values predicted by Equation (6-6), small discrepancies are observed. This is due to the fact that Equation (6-6) is developed using vacuum gauge pressures and particle properties that differ from those used in the current tests. Therefore, Equation (6-6) is upgraded to Equation (6-7), by adding the measured impact velocities of the solder balls to the previous data and correcting coefficients  $C_1$ ,  $C_2$ ,  $C_3$  and  $C_4$  (conducted by Mr Mohammad Alasossi). Comparison between the experimental values of the dimensionless impact velocity,  $N_{v,e}^{1/3}$ , and those predicted by

Equation (6-7),  $N_{\nu,p}^{1/3}$ , is provided in Figure 6-7, for the solder balls and the particles originally used in developing the empirical correlation.

$$N_{v}^{1/3} = 240.527 \left[ \frac{\left( \frac{P_{gauge}}{\rho_{air}gh} \right)^{0.472}}{\left( S - 1 \right)^{0.624} \left( N_{d} \right)^{0.221/3}} \right]$$
 (6-7)

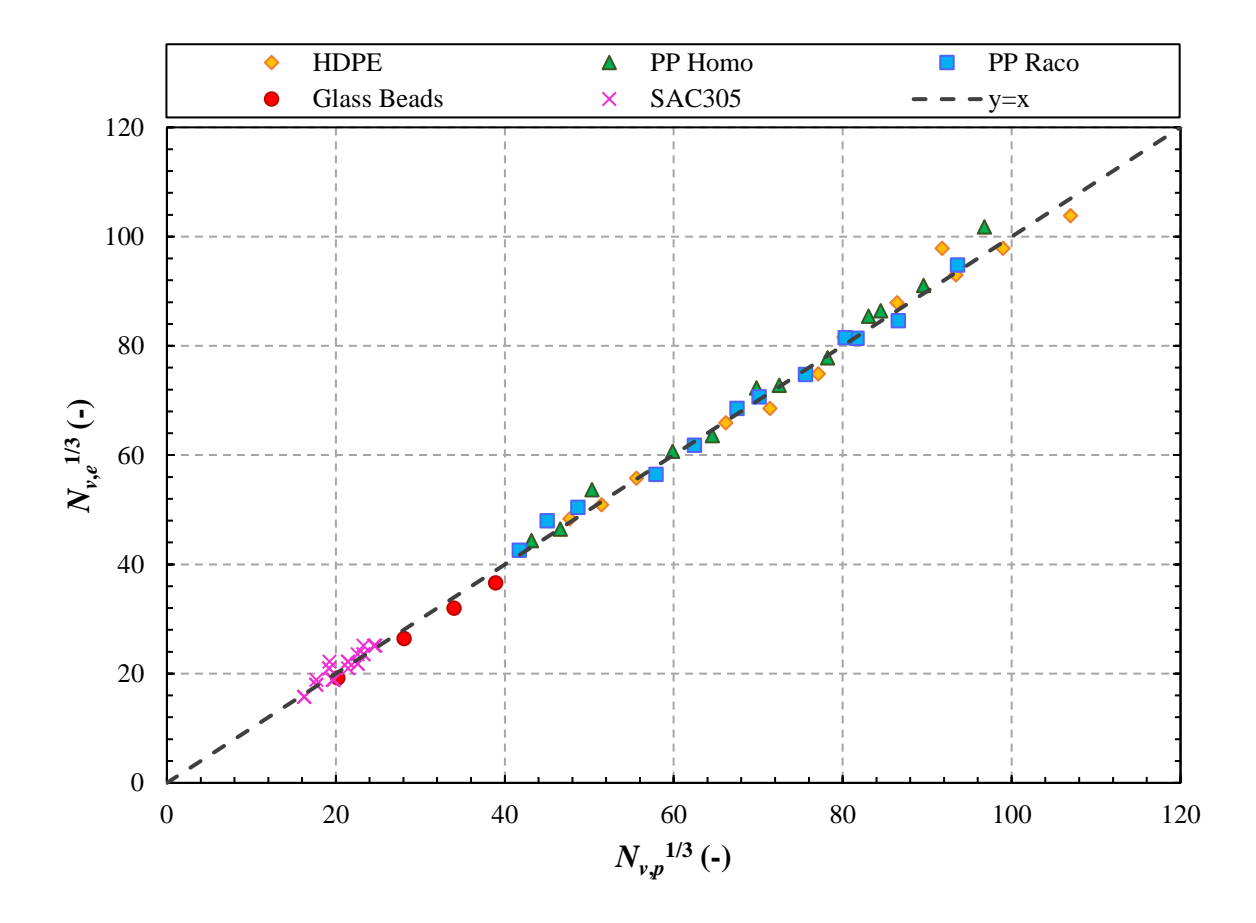


Figure 6-7 The experimental values of the dimensionless impact velocity,  $N_{\nu,e}^{1/3}$ , as a function of those predicted by Equation (6-7),  $N_{\nu,\rho}^{1/3}$ , for the solder balls and the particles originally used in developing the empirical correlation.

To measure the compression ratio after impact, the particles are collected from the collection chamber in order to image their deformed area using SEM. For the copper and

aluminium alloy samples, the collected particles are poured onto a glass slide and gently shaken to propel them to settle on their plane of maximum stability, i.e. their deformed area. For the solder balls, each individual particle is placed on a glass slide under an optical microscope (Olympus Corporation, Tokyo, Japan) for better visibility, so that it can be gently manipulated with tweezers until it falls on its deformed surface. Subsequently, an SEM stub with carbon adhesive tape is gently pressed onto the particles to pick them up. A Hitachi TM3030 table top microscope (Hitachi Ltd., Tokyo, Japan) is then used to capture images of the particles showcasing their deformed area (refer to Figure 6-8). Note that for the copper and aluminium alloy samples, after thorough examination of the stub under the SEM microscope, only near-spherical particles with a clear view of the deformed area are imaged. Consequently, the analysis includes 35 distinct copper particles, and 12 distinct aluminium alloy particles.

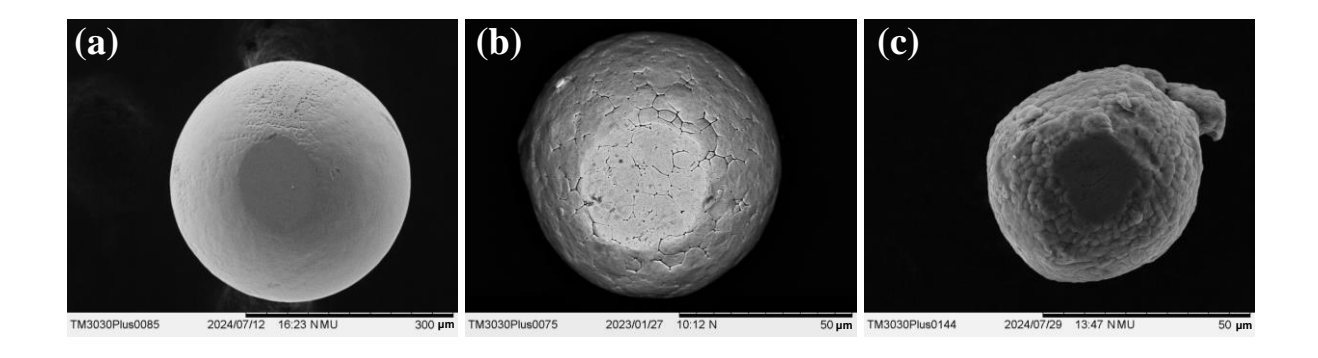


Figure 6-8 Examples of the SEM images used for determining the compression ratio, with the deformed area presented for viewing by the microscope: (a) solder ball, (b) copper particle and (c) aluminium alloy particle.

Fiji ImageJ software [204] is subsequently used to measure the projected area of the particle along with the deformed area, from which the particle diameter, D, and diameter of the deformed area,  $d_d$ , are obtained, respectively.  $H_d$  is then estimated from D and  $d_d$ , following a geometrical assumption, as illustrated in Figure 6-9. For the copper and aluminium alloy

particles,  $N_d$  is calculated using the measured D from Equation (6-3), and inserted in Equation (6-7) to find  $N_v$ . Finally,  $V_i$  is obtained from Equation (6-2).

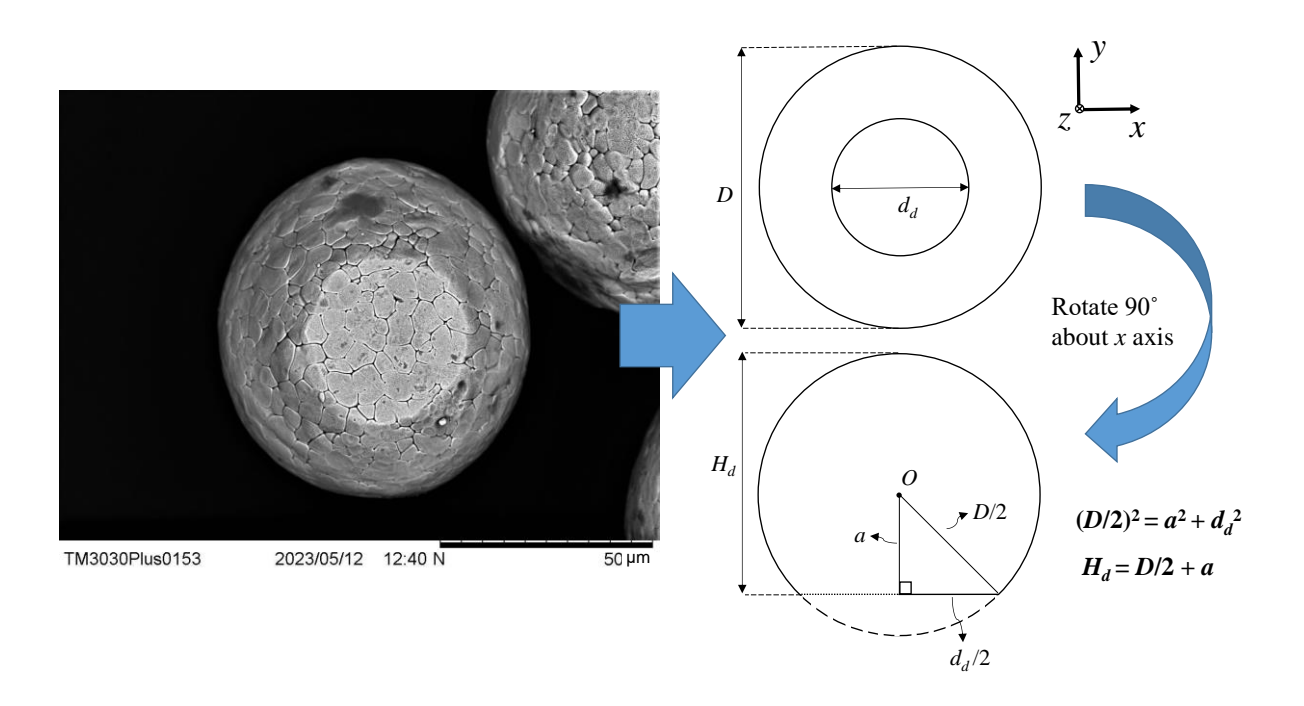
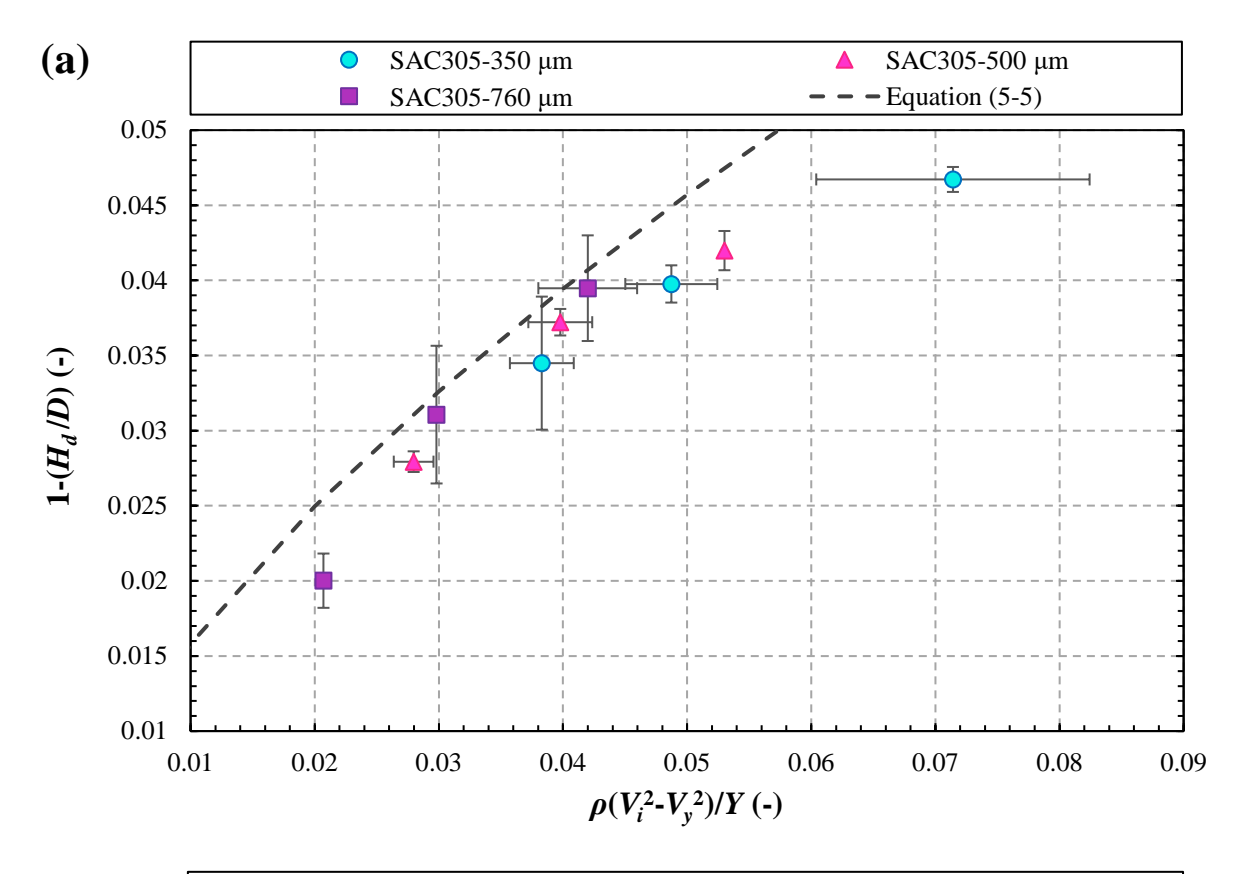


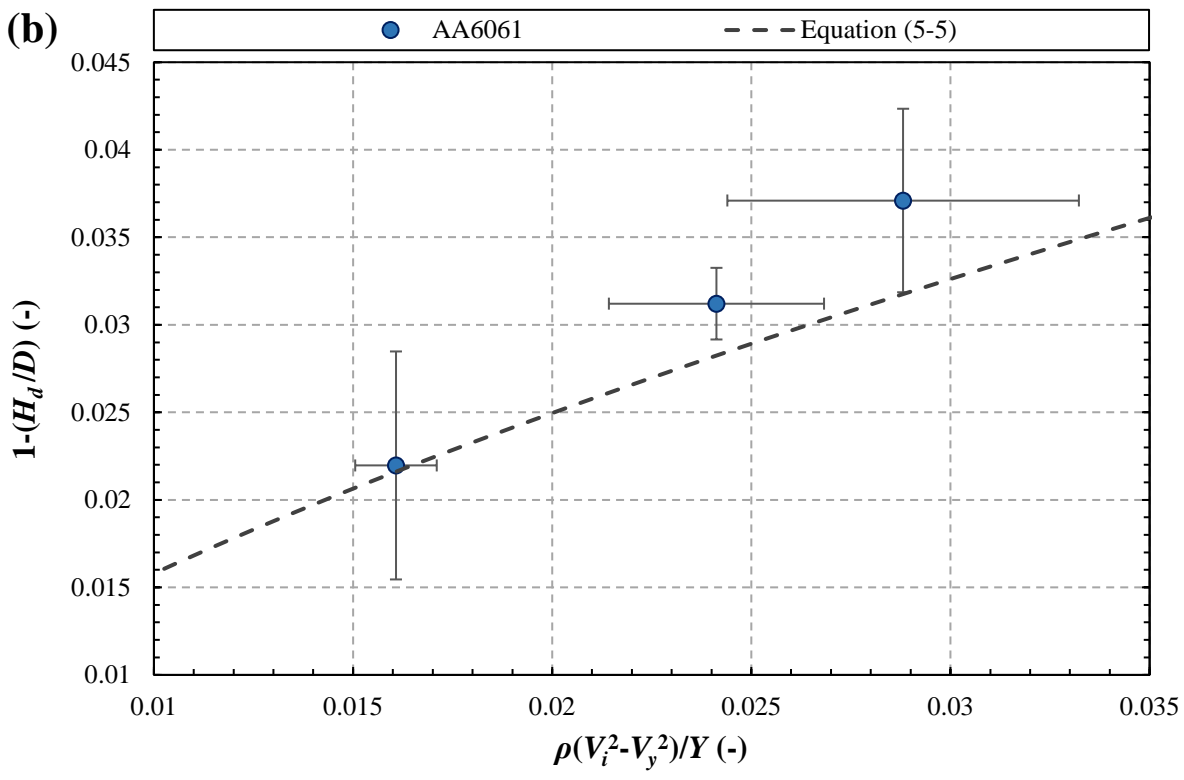
Figure 6-9 schematic diagram of the geometrical approach taken to estimate the height of the deformed particle,  $H_d$ , using the measured values of the particle diameter, D, and the diameter of the deformed area,  $d_d$ .

### 6.3.2.3. Compression Ratio

Figures 6-10 (a) to (c) show the plot of the measured compression ratio, 1- $(H_d/D)$ , as a function of  $\rho(V_i^2-V_y^2)/Y$ , for the solder balls (SAC305), aluminium alloy particles (AA6061), and copper particles (Cu), respectively. In all the graphs, Equation (5-5) is overlaid for comparison, and the data points are presented as the arithmetic mean of the 1- $(H_d/D)$  and  $\rho(V_i^2-V_y^2)/Y$  values corresponding to different vacuum gauge pressures. For reference, the measured/estimated impact velocities for all the sample particles are presented in Figure C-7 of Appendix C as a function of the vacuum gauge pressure. Note that four datasets are presented

for the copper particles in Figure 6-10 (c), each reflecting different yield strengths shown in Table 6-10, which result in varying  $\rho(V_i^2-V_y^2)/Y$  values.





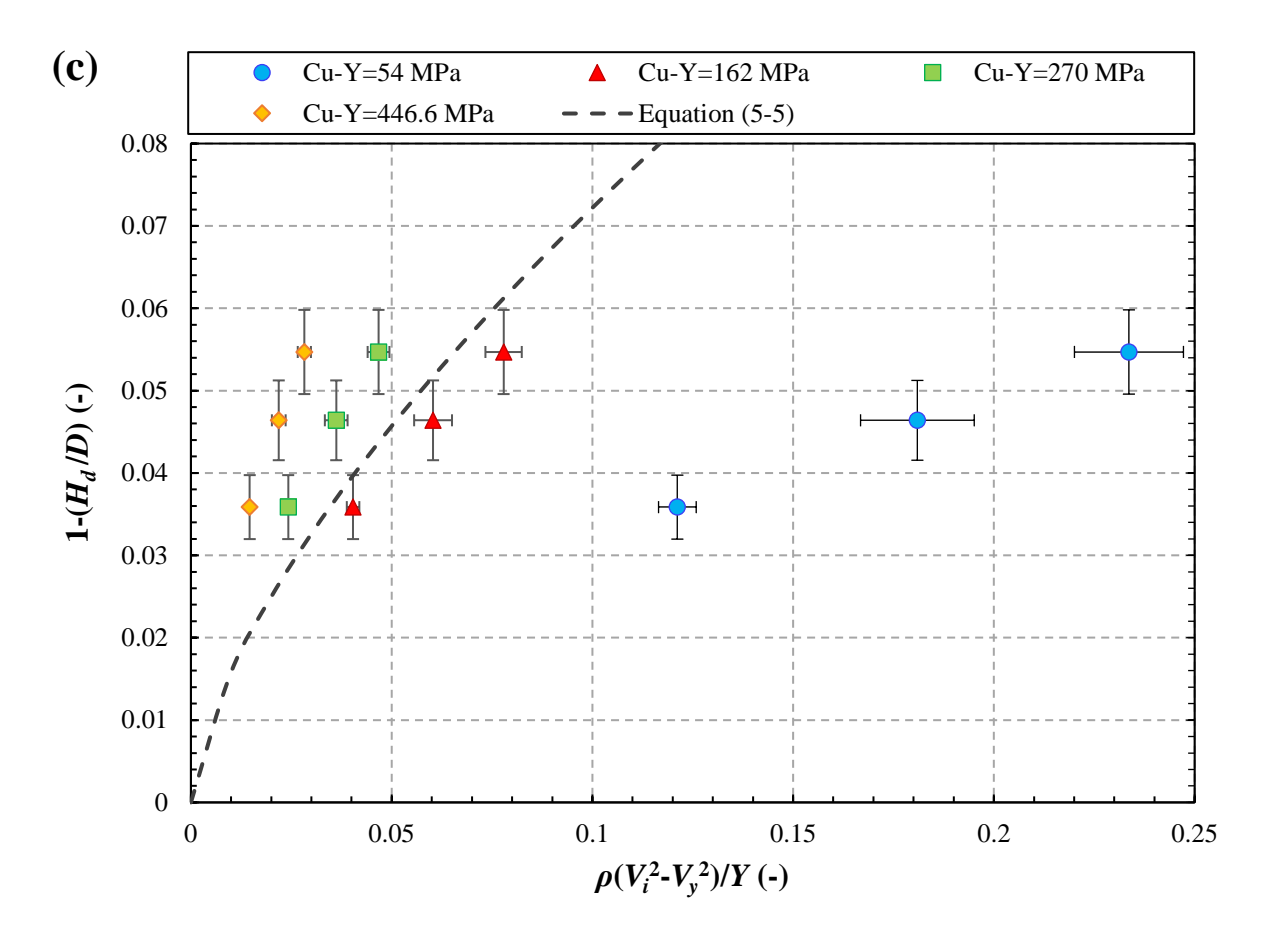


Figure 6-10 The compression ratio, 1- $(H_d/D)$ , as a function of  $\rho(V_i^2 - V_y^2)/Y$ , for (a) different sizes of the solder balls (SAC305), (b) aluminium alloy particles (AA6061), and (c) copper particles (Cu), considering different yield strengths shown in Table 6-10.

Considering Figures 6-10 (a) and (b), the measured values of the compression ratio for the solder balls and aluminium alloy particles are close to those predicted by Equation (5-5). Moreover, as a general trend for the solder balls, the compression ratio intuitively increases with a decrease in the particle size, as smaller particles accelerate to higher impact velocities (with the exclusion of free fall). With regards to Figure 6-10 (c), the measured values of the compression ratio for the copper particles are in good agreement with the predicted values only when the yield strength is considered to be 162 MPa. This highlights the fact that the precision of the predictions by Equation (5-5) is highly dependent on the accuracy of the mechanical properties used in the calculations.

The plot of 1-( $H_d/D$ ) versus  $\rho(V_i^2$ - $V_y^2)/Y$  is compiled in Figure 6-11 for all the sample particles (considering a yield strength of Y=162 MPa for the copper particles). To reduce the error bars, the data points are presented as arithmetic mean values corresponding to similar or close values of  $\rho(V_i^2$ - $V_y^2)/Y$ . As observed in the graph, the measured values of 1-( $H_d/D$ ) closely follow the trajectory of the curve for Equation (5-5), indicating that the empirical equation provides a reasonable prediction of 1-( $H_d/D$ ). However, more measurements are needed to reduce the deviations in the results. In general, the copper particles experience higher compression ratios, followed by the solder balls and the aluminium alloy particles. This highlights the collective effect of the material properties and impact velocity on the compression ratio, which is reflected through  $\rho(V_i^2$ - $V_y^2)/Y$ .

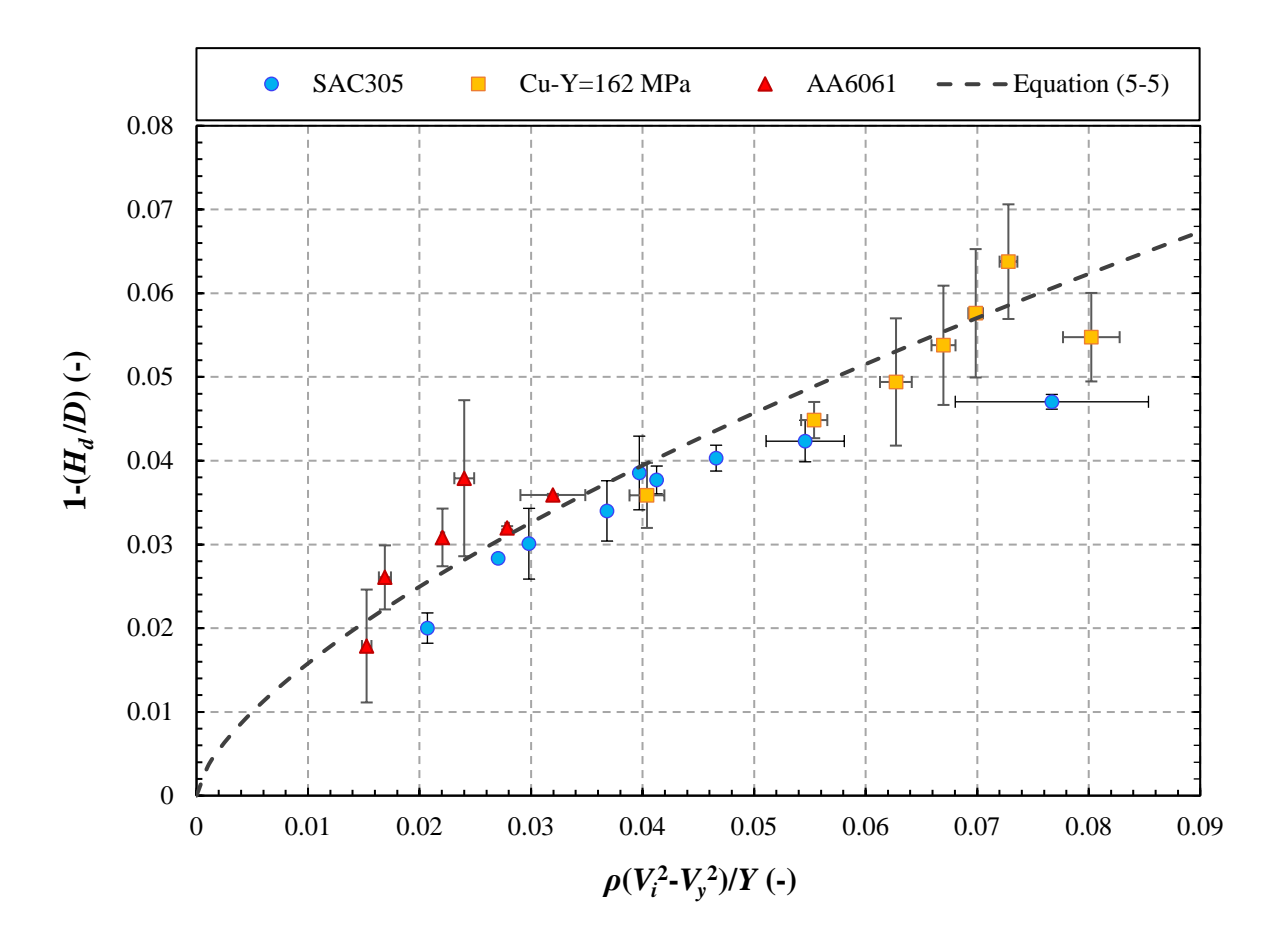


Figure 6-11 The compression ratio, 1- $(H_d/D)$ , as a function of  $\rho(V_i^2-V_y^2)/Y$ , for the solder balls (SAC305), aluminium alloy particles (AA6061), and copper particles (Cu) considering a yield strength of 162 MPa.

### 6.3.2.4. Coefficient of Restitution

Figure 6-12 compares the measured values of the coefficient of restitution (e) for the solder balls, with those predicted by the empirical Equation (4-8) of Wu et al. [110], Equation (4-9), and the analytical equations of Johnson [27] and Thornton [28], as a function of the ratio of the measured impact velocity to the yield velocity ( $V_i/V_y$ ). Note that the measured coefficient of restitution and  $V_i/V_y$  are presented as arithmetic mean values with respect to the vacuum gauge pressure and particle size of the solder balls. Table 6-11 summarises the analytical models of Johnson [27] and Thornton [28], as modified for the case of a sphere impacting a rigid surface. Johnson's equation [27] is simplified by assuming a constant mean contact pressure of  $p_m$ =3Y

at full plasticity. In Thornton's equation [28],  $V_y^T$  is defined as the yield velocity, expressed by Equation (6-8):

$$V_{y}^{T} = \left(\frac{\pi}{2E^{*}}\right)^{2} \left(\frac{2\bar{p}_{y}^{5}}{5\rho}\right)^{1/2}$$
 (6-8)

where  $\bar{p_y}$  is termed the "contact yield stress" (referred to as the "cut-off pressure" by Wu et al. [110]), which is assumed to remain constant during loading. Based on the findings of Wu [205], when the impact velocity exceeds the yield velocity, by assuming  $\bar{p_y}$ =2.8Y, Thornton's equation provides a reasonable prediction of the coefficient of restitution. As the impact velocity of the solder balls in the current analysis surpasses their yield velocity (refer to Figure C-7 of Appendix C),  $V_y^T$  is calculated by the same assumption.

Table 6-11 The analytical equations developed by Johnson [27] and Thornton [28] for predicting the coefficient of restitution, *e*.

| Reference | Equation   |  |  |  |
|-----------|--|--|--|--|
| Johnson   | $e \approx 3.465 \left(\frac{\rho V_i^2}{Y}\right)^{-1/8} \left(\frac{Y}{E^*}\right)^{1/2}$  |  |  |  |
| Thornton  | $e = \left(\frac{6\sqrt{3}}{5}\right)^{1/2} \left[1 - \frac{1}{6} \left(\frac{V_y^T}{V_i}\right)^2\right]^{1/2} \left[\frac{(V_y^T/V)_i}{(V_y^T/V)_i + 2\sqrt{6/5 - (1/5)(V_y^T/V_i)^2}}\right]^{1/4}$ |  |  |  |

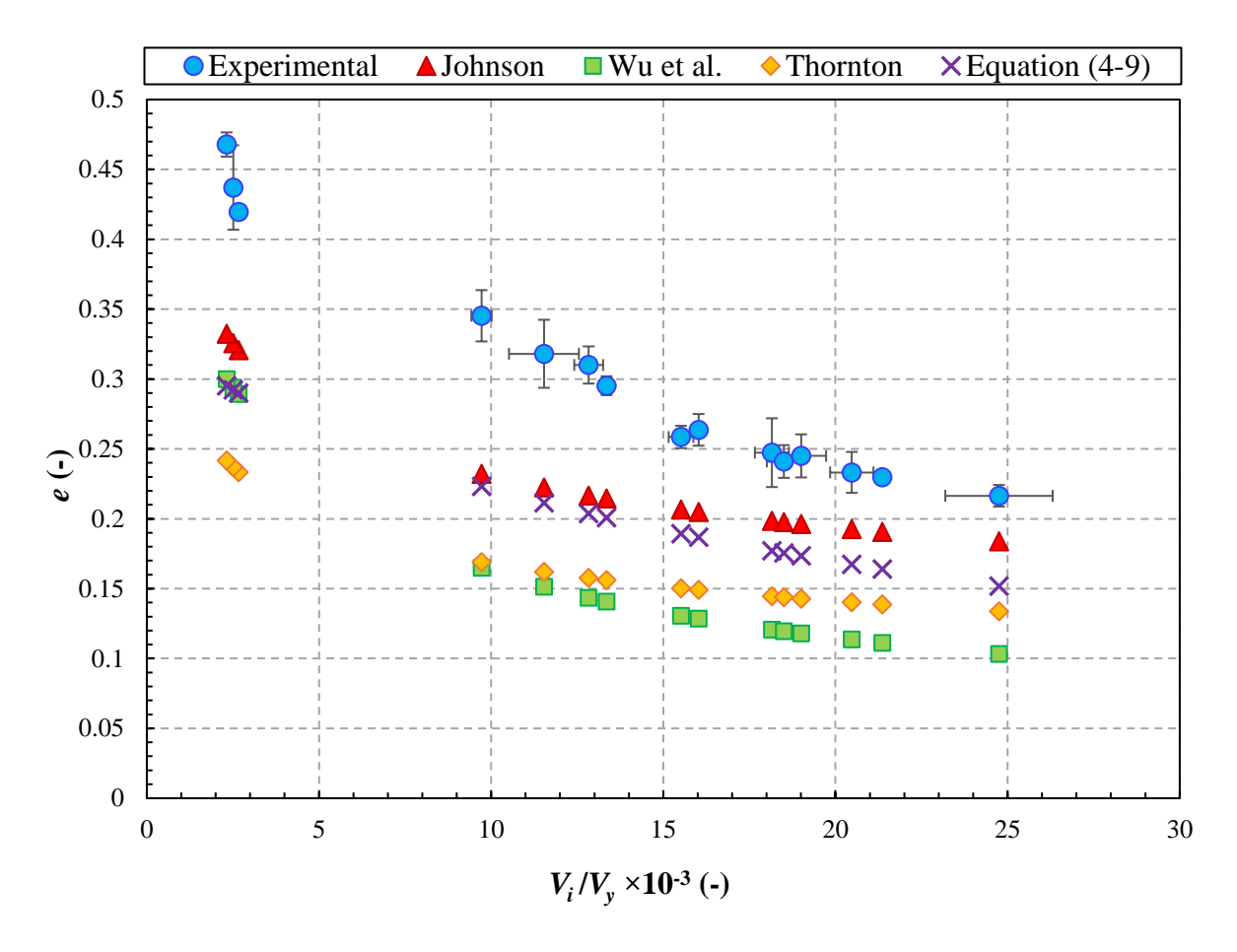


Figure 6-12 The measured values of the coefficient of restitution (e) for the solder balls, in comparison with those predicted by the empirical Equation (4-8) of Wu et al. [110], Equation (4-9), and the analytical equations of Johnson [27] and Thornton [28], as a function of the ratio of the measured impact velocity to the yield velocity  $(V_i/V_y)$ .

With regards to Figure 6-12, the coefficient of restitution decreases as the impact velocity increases for both the measured and predicted values (the yield velocity is constant). This is consistent with the observations from Figure 4-12 in Section 4.4.1, where the ratio of the work done during unloading to that during loading, and consequently the coefficient of restitution, decreases with an increase in the impact velocity. The trend is fast for smaller velocities, and slows down as the impact velocity increases, in line with the observations of Tabor [15] for brass and cast steel.

All the empirical and analytical equations underestimate the coefficient of restitution. Overall, Johnson's model [27] provides the closest prediction for e, respectively followed by Equation (4-9), Thornton's model [28], and Wu et al.'s model [110]. In line with the discussion in Section 4.3.5, the underestimation of e by Equation (4-9) is expected as the equation is developed using simulation results that have numerical errors due to energy dissipation. Regarding Johnson [27] and Thornton [28] models, the discrepancy could be attributed to the assumption of a constant contact curvature during loading, which contradicts the Finite Element analyses of Wu et al. [110]. In fact, Mesarovic and Fleck [82], Vu-Quoc and Zhang [68], and Li et al. [29] show that the radius of the contact curvature changes with time. Another contributor to the underestimated predictions of Thornton's model [28] is the assumption of a constant  $\vec{p}_y$ , which is later corrected in [29] by allowing  $\vec{p}_y$  to vary with the contact radius. For  $V_i/V_y$  values smaller than 5,000, Wu et al.'s model [110] performs better than Thornton's model [28], and agrees well with Equation (4-9). It should be noted that for  $V_i/V_y$  values higher than 10,000, the data from Wu et al.'s model [110] exhibit a curvature similar to that of the measured data, i.e. the predicted values of e are consistently about half the measured values.

# 6.4. Impact of Copper Particles in an Aerosol Deposition Rig

As seen in Section 6.3.2.3, the moderate impact conditions provided by the single particle impact tester limit the validation of Equation (5-5) to relatively small compression ratios. To investigate larger deformations, impact tests can be conducted in a cold spraying (CS) or aerosol deposition (AD) rig, which subjects the particles to extreme plastic deformation. However, at such extreme deformation extents, strain rate and temperature effects can no longer be ignored. Therefore, it is not appropriate to apply Equation (5-5) directly, as it is developed based on an elastic-perfectly plastic constitutive law. Nevertheless, the effect of

thermal softening and strain rate hardening is still reflected in the yield behaviour of the particle. Acknowledging the aforementioned limitations, and assuming that the strain rate and temperature effects can be accounted for by a mean representative value of the particle yield strength, it is assessed whether Equation (5-5) remains predictive by adjusting the yield strength accordingly. This analysis is by no means intended as a validation of Equation (5-5), but rather an exploration of a methodology to assess its applicability to high strain rate and temperature conditions. To this end, copper particles are deposited on a hard steel substrate in an in house-AD rig, and their compression ratio is measured, as detailed in the forthcoming sections. AD, which has specifically been developed for fabrication of ceramic coatings, is somewhat similar to CS and offers the same advantages of low processing temperatures. The difference between the two techniques is that in AD, the deposition chamber is under vacuum, and the carrier gas is not preheated and has a lower pressure compared to that of CS. These conditions lead to lower temperature rises upon impact and lower particle velocities (100 to 600 m/s) compared to CS [1,206,207].

#### **6.4.1.** Methodology

The AD rig (illustrated in Figure 6-13) has recently been developed by Professor Steven Milne's group at the School of Chemical and Process Engineering, University of Leeds, UK. The rig comprises an aerosol chamber and a deposition chamber. The two chambers are connected, and the deposition chamber is kept under vacuum by a pump. The aerosol chamber is mounted on a vibrating table and is connected to a carrier gas (nitrogen) supply with a flow controller. The carrier gas passes through a powder sample which is placed on a filter paper within the aerosol chamber and creates a fluidised bed, thereby generating an aerosol. The pressure difference between the two chambers delivers the aerosol to the deposition chamber through a nozzle. The nozzle accelerates the aerosol to velocities up to several hundred meters

per second, creating a focused jet at the outlet. The jet collides with a substrate controlled by a programmable X-Y stage, leading to deformation/deposition of the particles on the substrate.

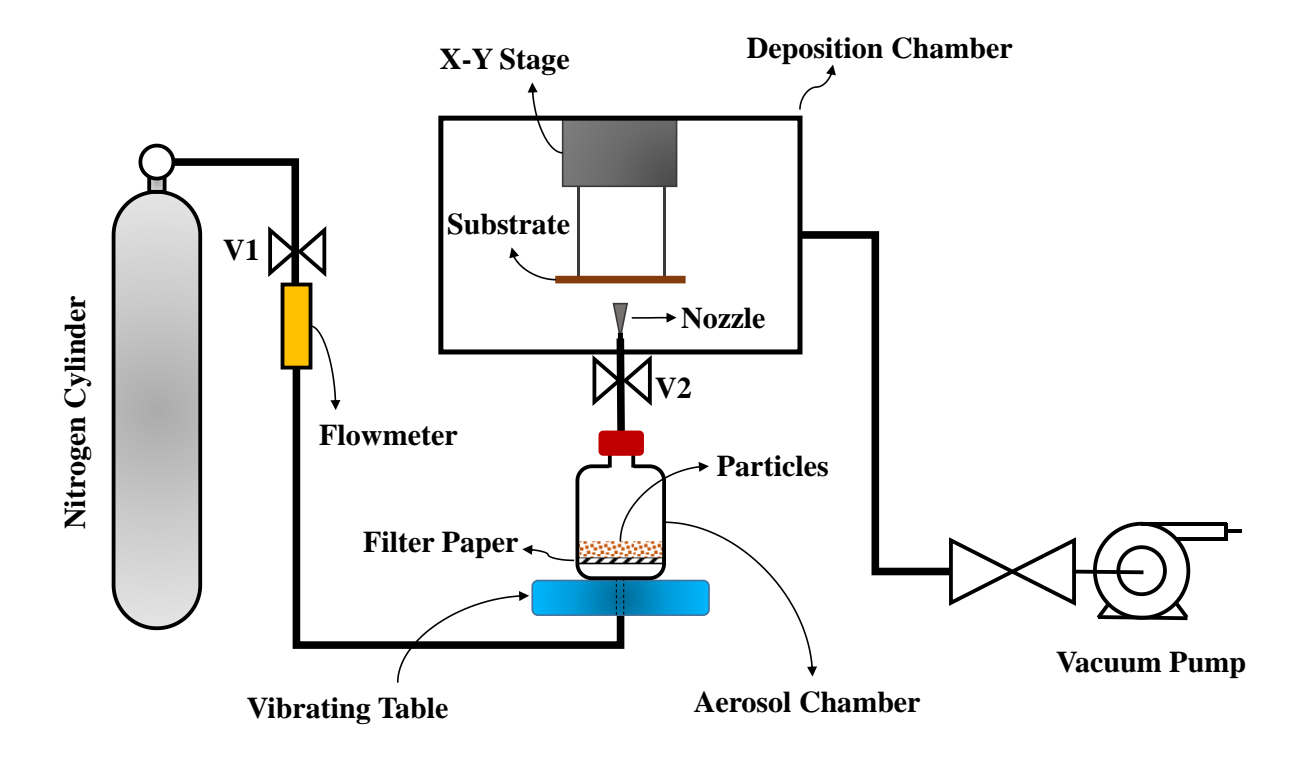


Figure 6-13 Schematic drawing of the AD rig.

For the experiments, fine (< 10 µm) copper particles (Goodfellow Cambridge Limited, Huntingdon, UK) are used for deposition on a polished SUS304 stainless steel substrate. An SEM image of the feed particles is shown in Figure 6-14 (a), taken by FEI Helios G4 CX DualBeam microscope at Leeds electron microscopy and spectroscopy centre, LEMAS (University of Leeds, UK). First, the deposition chamber is evacuated to 7.1 mbar using the vacuum pump. Subsequently, 2.5 g of the particles are placed on the filter paper inside the aerosol chamber and the vibrating plate is turned on. Valves V1 and V2 (Figure 6-13) are then simultaneously opened and the carrier gas is introduced into the system at an inlet pressure of 1.5 bar and a flow rate of 8.5 lit/min, aerosolising the particles and carrying them through the

nozzle to be deposited. After the test, a section of the substrate containing the deposited particles is cut for further analysis, as displayed in Figure 6-14 (b).

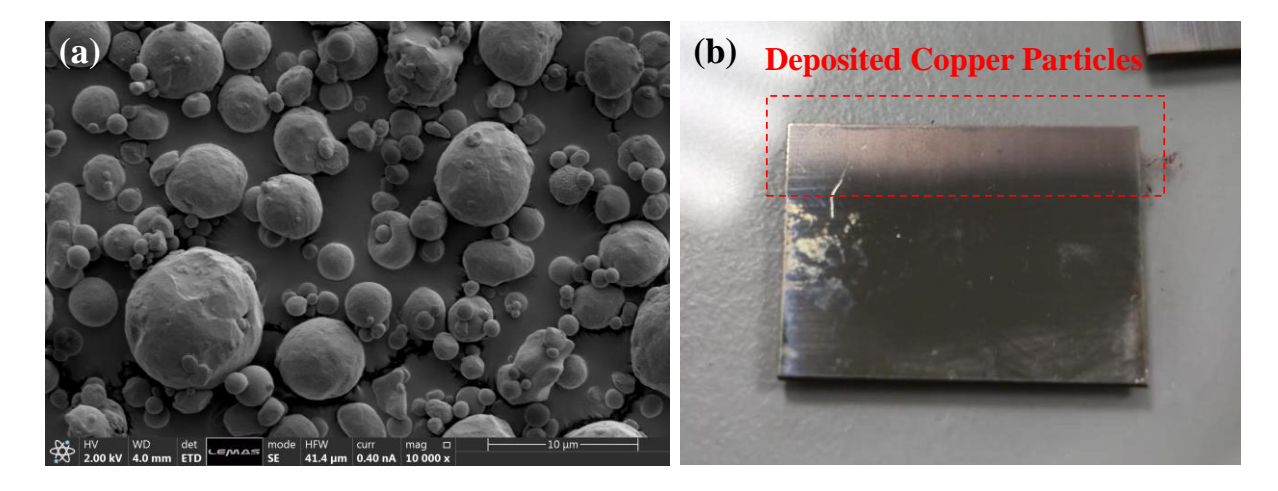


Figure 6-14 Impact tests in the AD rig: (a) SEM image of the feed copper particles and (b) a cut section of the substrate where the particles are deposited.

To measure the size and compression ratio of the deposited particles, the substrate is imaged in FEI Helios G4 CX DualBeam microscope at LEMAS (University of Leeds, UK). Figure 6-15 (a) presents a representative image of the deposited particles on the substrate. For comparison, an image of the particle-free surface of the substrate is displayed in Figure 6-15 (b). Subsequently, deposited particles with a more prominent bulge and symmetrical appearance are covered with a platinum protective film and cut in half using an electron beam, as shown in Figure 6-15 (c). The SEM sample holder is then tilted so the cross-section of the particle is available for viewing by the microscope. Figure 6-15 (d) displays an example of such images, which are analysed using Fiji ImageJ software [204] to measure the deformed height ( $H_d$ ) of the particle and estimate its diameter (D) using the measured area of the cross-section. This is done for five different particles, due to time restrictions.

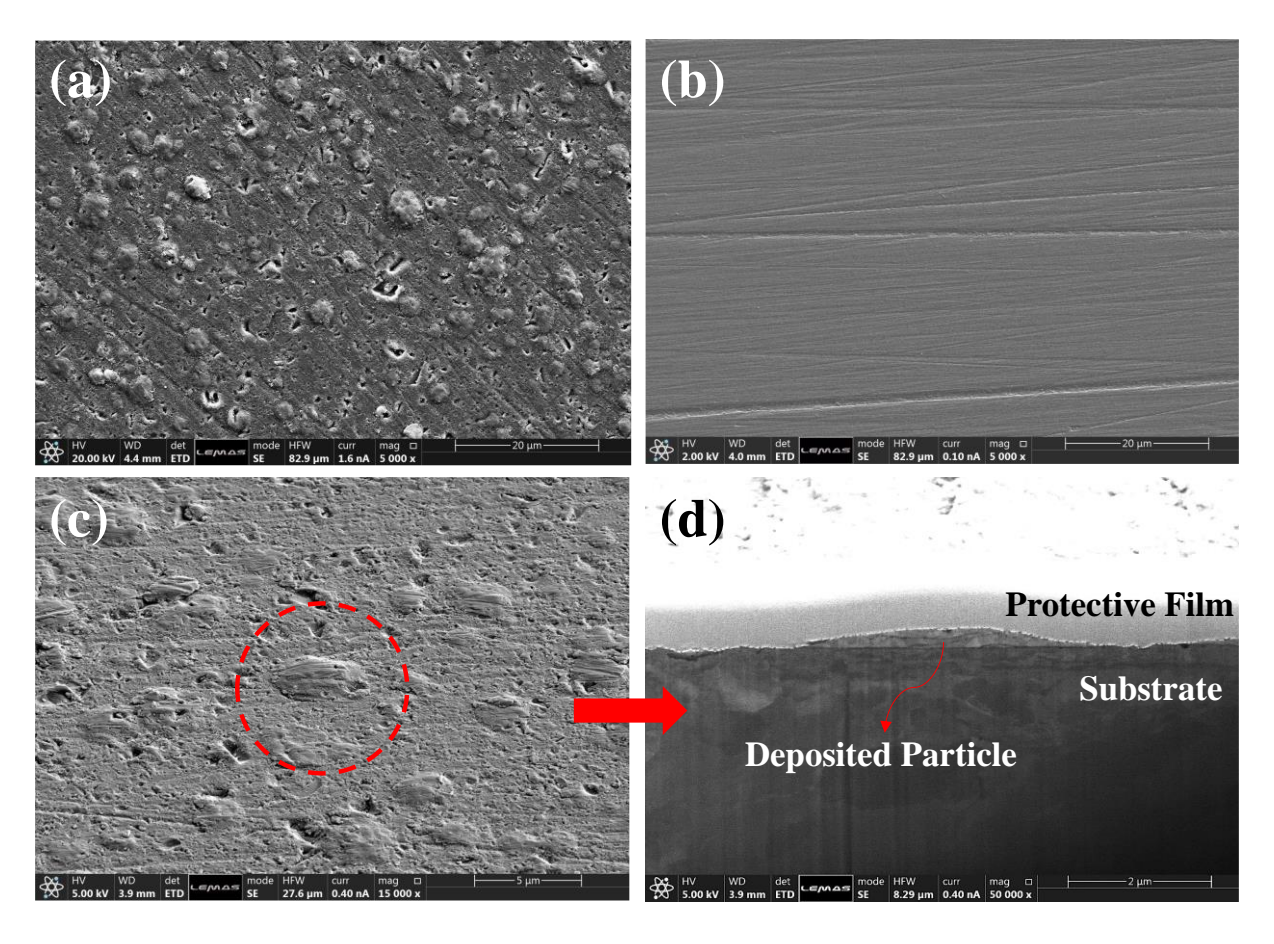


Figure 6-15 SEM images of (a) the top view of the copper particles deposited on the substrate, (b) particle-free surface of the substrate, (c) an example of the particles analysed (the view is slightly tilted) and (d) cross-section of the same particle cut in half using an electron beam.

Figure 6-16 shows the impact velocity of the particles based on the particle size, determined by Dr Fanchao Meng (The University of Manchester, UK) using his semi-analytical surrogate model [208], modified for the nozzle used in the current AD rig. The model has been developed based on Computational Fluid Dynamics (CFD) simulations, and takes into account the dimensions of the nozzle, particle properties, carrier gas properties and process parameters to predict the impact velocity of the particles. In the current analysis, for sizes smaller than those shown in Figure 6-16, the impact velocity is extrapolated assuming a linear relationship.

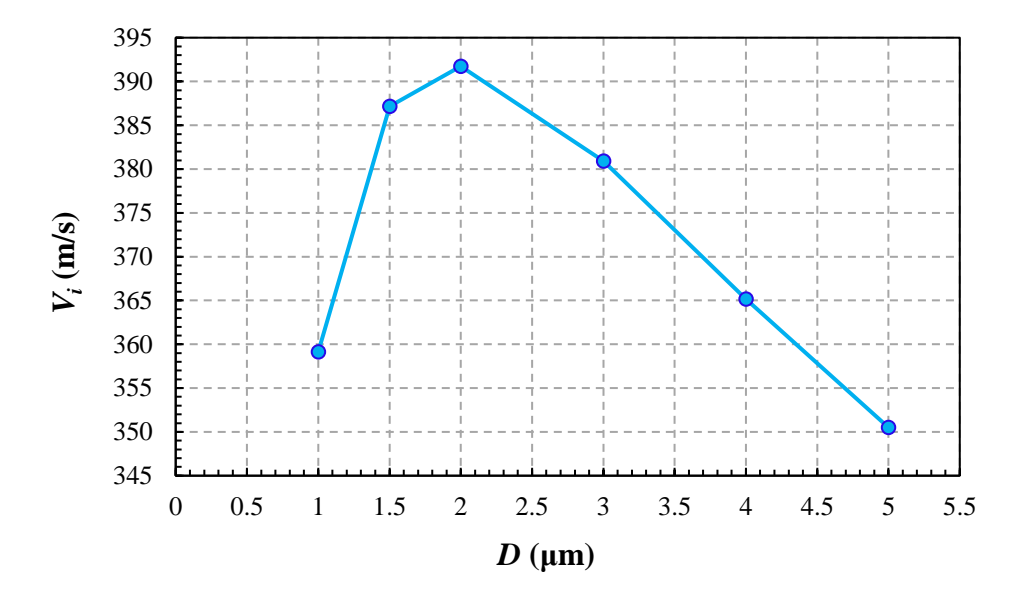


Figure 6-16 Particle impact velocity in the AD rig as a function of particle size, determined by Dr Fanchao Meng (The University of Manchester, UK) using his semi-analytical surrogate model [208], modified for the nozzle used in the current AD rig.

### 6.4.2. Compression Ratio

As mentioned before, to assess the applicability of Equation (5-5) for predicting the compression ratio of the particles in the AD rig, a representative value of the yield strength should be used. Originally, it was planned to measure the yield strength of the copper particles using high-temperature and displacement-controlled nano-indentation in the NanoTest device (Micro Materials Ltd., Wrexham, UK), to have representative values for different temperatures and strain rates. Unfortunately, this was not possible due to time restrictions. As reported by the supplier, the particles have the same properties as the copper samples used in Section 6.3.2.1 (refer to Table 6-10). Accordingly, the measured values of  $1-(H_d/D)$ , and those predicted by Equation (5-5) using the yield strength values in Table 6-10 are displayed in Table 6-12. The measured particle size and estimated impact velocities using Figure 6-16 are also included. It should be noted that yield strengths of 54 and 162 MPa cannot be considered as representative values, as they result in negative values for  $H_d/D$ .

Table 6-12 The measured values of the compression ratio,  $1-(H_d/D)$ , and those predicted by Equation (5-5) using the yield strength values of 270 and 446.6 MPa.

| <i>D</i> (μm) | $V_i$ (m/s) | $[1-(H_d/D)]$ experimental | $[1	ext{-}(H_d\ /D)]_{	ext{predicted-}Y=270\ MPa}$ | $[1	ext{-}(H_d/D)]$ predicted-Y=446.6 MPa |
|---------------|-------------|----------------------------|--|---|
| 0.5           | 331         | 0.63                       | 0.77   | 0.56                                      |
| 0.6           | 337         | 0.69                       | 0.79   | 0.57                                      |
| 0.7           | 342         | 0.57                       | 0.81   | 0.58                                      |
| 0.9           | 359         | 0.61                       | 0.86   | 0.62                                      |
| 1.5           | 387         | 0.57                       | 0.95   | 0.68                                      |

Considering Table 6-12, the trend of change in the measured values of the compression ratio with the estimated particle velocities is erratic. This can be attributed to the errors associated with the measurement of the deformed height and estimation of the impact velocity using extrapolation, emphasising the need for additional measurements to improve accuracy. Overall, a higher representative yield strength (446.6 MPa) provides better predictions of the compression ratio by Equation (5-5). Given that particle deformation at very high strain rates is governed by the interplay between thermal softening and work-hardening, this suggests that Equation (5-5) offers a better prediction when the selected representative yield strength mainly reflects the effect of work-hardening. One possible explanation is that thermal softening results in localised strain at the contact interface [2], primarily manifested as jetting in high-velocity impact, whereas the overall material deformation is predominantly controlled by strain rate hardening [126], as illustrated by Figure 6-17. Additionally, as the current analysis is conducted in an aerosol deposition rig where the carrier gas is not preheated, temperature rise upon impact is lower than that during cold spraying. As a result, changes in the particle height (and by extension, the compression ratio), are largely influenced by work-hardening, which explains the improved predictive capability of Equation (5-5) when using a higher representative yield strength.

Ultimately, further experimental work and simulations using a more appropriate material model, such as that of Johnson-Cook [119] or more advanced models, will be helpful to affirm the conclusions reached so far.

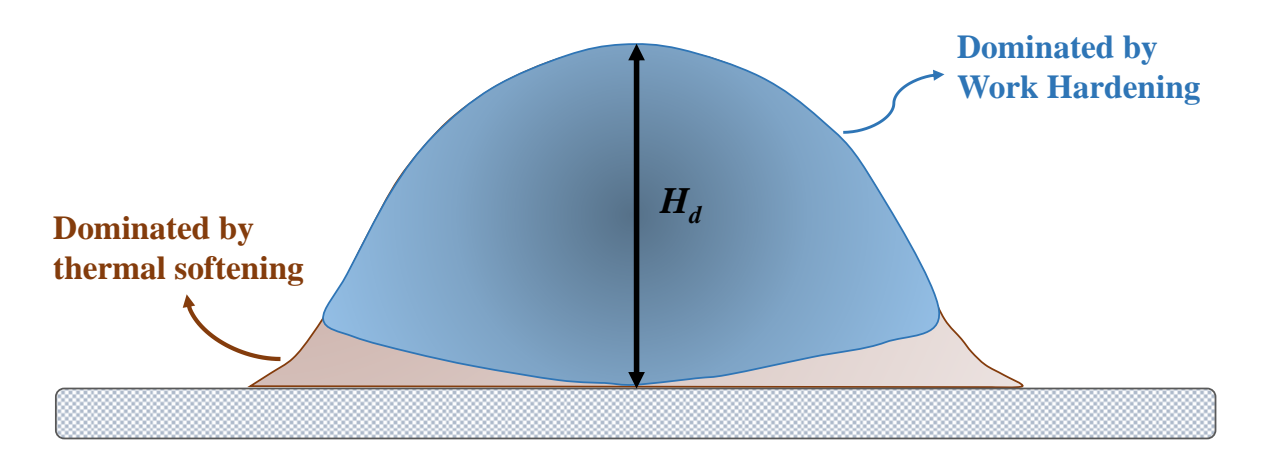


Figure 6-17 Schematic drawing of the regions of the particle affected by thermal softening and work hardening during high strain rate impact.

## **6.5.** Concluding Remarks

The results presented in this chapter demonstrate that the MPM simulations of impact for elastic balls can accurately capture the impact behaviour observed experimentally. Moreover, a good agreement is found between the experimental values of the compression ratio, and the predictions made by the previously developed empirical equation using the MPM data. The empirical equation for the coefficient of restitution underestimates the measured values. However, it still captures the trend in the data and the predictions are close to those of Johnson [27]. The chapter highlights the scope of the study, encompassing both advanced numerical modelling and carefully designed experimental validation.



# 7. Conclusions and Recommendations for Future Work

The aim of this work has been to investigate the relationship between the deformation behaviour of elastic-perfectly plastic particles during impact, and the material properties and impact velocity of the particles. To achieve this, MPM simulations are performed considering a wide range of material properties and impact velocities, followed by empirical modelling, AI-based analysis and experimental validation.

First, suitable criteria for selecting the optimal time step and discretisation settings for the simulations are established, ensuring accuracy, stability, and computational efficiency.

Subsequently, 3D TLMPM simulations are conducted to study the normal impact of an elastic-perfectly plastic particle with a rigid wall. The method scope and limitations regarding this problem are highlighted, showing that large deformation is conveniently accommodated, though the method produces inaccurate results for very small deformation. The plastic deformation and rebound behaviour of the particle are analysed, exhibiting a strong link to the material properties and impact velocity, expressed by the dimensionless groups E/Y and  $\rho V_i^2/Y$ . It is observed that the variables reflecting the plastic deformation of the particle, i.e. the equivalent plastic strain, compression ratio, and permanent displacement, are intuitively only influenced by the incident kinetic energy and yield strength of the material. On the other hand, the variables that are linked to the recovery from or resistance to deformation, i.e. the coefficient of restitution, the ratio of the plastic work to the incident kinetic energy, and the maximum displacement during loading, are additionally affected by the material's Young's modulus, specifically during small deformation. The importance of group  $\rho V_i^2/Y$  suggested by Johnson [27] for recognising the deformation patterns during impact is highlighted. Eventually, empirical equations are developed for predicting the compression ratio and coefficient of restitution.



To explore the use of artificial intelligence for trend recognition and refinement of the developed empirical equations, the simulation results are analysed using a hybrid AI framework. The framework successfully identifies meaningful relationships within well-structured input data, exhibiting its potential for equation discovery. However, there are limitations in the performance of the framework, including its inability to identify equations based on raw input data, its dependence on user-prepared dimensionless groups, and difficulty in capturing complex equations in the absence of DNNs. Suggestions are made to address this issue, i.e. improving the pre-processing procedure, expanding the equation library, and implementing more advanced AI techniques such as Physics-Informed Neural Networks (PINNs) [196] to incorporate physical laws directly into the learning process.

In the end, a series of impact experiments are conducted to evaluate the accuracy of the numerical approach and the empirical equations in predicting the deformation behaviour during impact. First, elastic impact is examined using elastic balls, and simulations are performed to compare measurable experimental parameters with their predicted values. Subsequently, elastic-plastic impact is investigated by subjecting metal particles to impact in an in-house device. The resulting compression ratio and, where possible, the coefficient of restitution are measured and compared against the predictions of the empirical equations. Finally, a methodology is examined to assess the applicability of the empirical equation for the compression ratio to very high-velocity impacts. This is achieved by depositing very fine copper particles using an aerosol deposition rig, allowing for an evaluation of the deformation extent under extreme strain rate conditions. The results of this analysis provide a preliminary assessment of whether the empirical equation can be extended to high strain rate impacts, offering insights into its potential applicability beyond the conditions initially considered in this study. Overall, the findings demonstrate that the TLMPM simulations accurately capture the elastic impact behaviour, and the empirical equation for the compression ratio provides



reasonable predictions for elastic-plastic impact at moderate strain rates. As for the coefficient of restitution, the empirical equation underestimates the experimental values, though it captures the trend in the experimental data. It is then found that incorporating a higher representative yield strength in the empirical equation for the compression ratio leads to better predictions at high strain rates. This is attributed to the overall deformation being primarily governed by work hardening, rather than the localised thermal softening effects. However, further experimental analysis and simulations using a more appropriate material model are needed to support these findings. This final component of the work highlights the scope of the study, demonstrating the synergy between numerical modelling and well-designed experimental validation.

While this research provides insights into the effect of material properties and impact velocity on the impact deformation behaviour of particles, several areas need further investigation. The contact force-displacement relationship can be studied more thoroughly in an attempt to develop a contact model based on the simulation results. This would involve extracting the precise force and displacement data from the MPM simulations across the full range of impact conditions. Advanced regression techniques as well as ML can be used to fit a new model to this data, which can then be implemented in methods like DEM. Moreover, including adhesion in the MPM framework can shed light on the bonding behaviour of the particle, which is particularly relevant for applications such as CS. A potential approach is to implement an "adhesion force" in the contact algorithm based on the surface energy of the contacting bodies and the contact area. MPM simulations can then be conducted to study the effect of material properties and impact conditions on the bonding behaviour of the particle, providing insight into coating formation and quality in CS. The findings of the current study are limited to elastic-perfectly plastic materials. So, it is beneficial to incorporate a more advanced material model to account for strain rate and temperature effects. Running MPM simulations with more realistic models would result in a more accurate assessment of the



deformation, temperature evolution at the interface, and residual stresses. This would allow for an assessment of whether the current findings extend to hyper-velocity impact processes like CS, and provide a much more realistic simulation of the process, leading to more reliable predictions. Furthermore, additional experiments should be conducted using a wider range of materials to determine whether the empirical equation for the compression ratio applies to CS. This empirical equation can be used to select optimal impact velocities for achieving desired levels of particle flattening in CS. Further experiments could also investigate how the compression ratio correlates with the mechanical strength of CS coatings. Experiments should be designed to produce coatings with varying levels of particle flattening. These coatings would then be subjected to mechanical testing to measure properties like tensile strength, hardness, and porosity.

This work highlights the strength of the Material Point Method as a robust tool for conveniently accommodating large deformation problems, making it well-suited for analysing the problem of high-velocity impact. The study lays the ground work for further research into the effects of material properties and impact velocity in high-velocity particle impact modelling, providing a foundation for improving the numerical simulations, refining empirical models, and broadening the understanding of particle deposition in industrial processes such as cold spraying.



## References

- [1] D. Hanft, J. Exner, M. Schubert, T. Stöcker, P. Fuierer, R. Moos, An overview of the Aerosol Deposition method: Process fundamentals and new trends in materials applications, J. Ceram. Sci. Technol. 6 (2015) 147–181. https://doi.org/10.4416/JCST2015-00018.
- [2] H. Assadi, H. Kreye, F. Gärtner, T. Klassen, Cold spraying A materials perspective, Acta Mater. 116 (2016) 382–407. https://doi.org/10.1016/j.actamat.2016.06.034.
- [3] T. Schmidt, F. Gärtner, H. Assadi, H. Kreye, Development of a generalized parameter window for cold spray deposition, Acta Mater. 54 (2006) 729–742. https://doi.org/10.1016/j.actamat.2005.10.005.
- [4] P.A. Cundall, O.D.L. Strack, A discrete numerical model for granular assemblies, Géotechnique. 29 (1979) 47–65. https://doi.org/10.1680/geot.1979.29.1.47.
- [5] O.C. Zienkiewicz, R.L. Taylor, J.Z. Zhu, The Finite Element Method: its Basis and Fundamentals, Elsevier, 2013. https://doi.org/10.1016/C2009-0-24909-9.
- [6] W.F. van Gunsteren, H.J.C. Berendsen, Computer Simulation of Molecular Dynamics: Methodology, Applications, and Perspectives in Chemistry, Angew. Chemie Int. Ed. English. 29 (1990) 992–1023. https://doi.org/10.1002/anie.199009921.
- [7] D. Sulsky, S.-J. Zhou, H.L. Schreyer, Application of a particle-in-cell method to solid mechanics, Comput. Phys. Commun. 87 (1995) 236–252. https://doi.org/10.1016/0010-4655(94)00170-7.
- [8] A. de Vaucorbeil, V.P. Nguyen, C.R. Hutchinson, A Total-Lagrangian Material Point Method for solid mechanics problems involving large deformations, Comput. Methods Appl. Mech. Eng. 360 (2020) 112783. https://doi.org/10.1016/j.cma.2019.112783.
- [9] R.C. Hibbeler, K.B. Yap, Mechanics of Materials in SI Units, 10th Edition, Pearson, 2018.
- [10] J.P.A. Tillett, A Study of the Impact of Spheres on Plates, Proc. Phys. Soc. Sect. B. 67 (1954) 677–688. https://doi.org/10.1088/0370-1301/67/9/304.
- [11] S.C. Hunter, Energy absorbed by elastic waves during impact, J. Mech. Phys. Solids. 5 (1957) 162–171. https://doi.org/10.1016/0022-5096(57)90002-9.
- [12] I.M. Hutchings, Energy absorbed by elastic waves during plastic impact, J. Phys. D. Appl. Phys. 12 (1979) 1819–1824. https://doi.org/10.1088/0022-3727/12/11/010.
- [13] J. Reed, Energy losses due to elastic wave propagation during an elastic impact, J. Phys. D. Appl. Phys. 18 (1985) 2329–2337. https://doi.org/10.1088/0022-3727/18/12/004.
- [14] C.-Y. Wu, L.-Y. Li, C. Thornton, Energy dissipation during normal impact of elastic and elastic–plastic spheres, Int. J. Impact Eng. 32 (2005) 593–604. https://doi.org/10.1016/j.ijimpeng.2005.08.007.
- [15] D. Tabor, A simple theory of static and dynamic hardness, Proc. R. Soc. London. Ser. A. Math. Phys. Sci. 192 (1948) 247–274. https://doi.org/10.1098/rspa.1948.0008.



- [16] W. Goldsmith, P.T. Lyman, The Penetration of Hard-Steel Spheres Into Plane Metal Surfaces, J. Appl. Mech. 27 (1960) 717–725. https://doi.org/10.1115/1.3644088.
- [17] A.B. Stevens, C.M. Hrenya, Comparison of soft-sphere models to measurements of collision properties during normal impacts, Powder Technol. 154 (2005) 99–109. https://doi.org/10.1016/j.powtec.2005.04.033.
- [18] H. King, R. White, I. Maxwell, N. Menon, Inelastic impact of a sphere on a massive plane: Nonmonotonic velocity-dependence of the restitution coefficient, EPL (Europhysics Lett. 93 (2011) 14002. https://doi.org/10.1209/0295-5075/93/14002.
- [19] M.C. Marinack, R.E. Musgrave, C.F. Higgs, Experimental Investigations on the Coefficient of Restitution of Single Particles, Tribol. Trans. 56 (2013) 572–580. https://doi.org/10.1080/10402004.2012.748233.
- [20] D. Patil, C. Fred Higgs, Experimental Investigations on the Coefficient of Restitution for Sphere–Thin Plate Elastoplastic Impact, J. Tribol. 140 (2018) 1–13. https://doi.org/10.1115/1.4037212.
- [21] F. Jebelisinaki, R. Boettcher, B. van Wachem, P. Mueller, Impact of dominant elastic to elastic-plastic millimeter-sized metal spheres with glass plates, Powder Technol. 356 (2019) 208–221. https://doi.org/10.1016/j.powtec.2019.07.105.
- [22] K.R.B. Melo, T.F. de Pádua, G.C. Lopes, A coefficient of restitution model for particle—surface collision of particles with a wide range of mechanical characteristics, Adv. Powder Technol. 32 (2021) 4723–4733. https://doi.org/10.1016/j.apt.2021.10.023.
- [23] B. Dahneke, Further measurements of the bouncing of small latex spheres, J. Colloid Interface Sci. 51 (1975) 58–65. https://doi.org/10.1016/0021-9797(75)90083-1.
- [24] L. Labous, A.D. Rosato, R.N. Dave, Measurements of collisional properties of spheres using high-speed video analysis, Phys. Rev. E. 56 (1997) 5717–5725. https://doi.org/10.1103/PhysRevE.56.5717.
- [25] A.H. Kharaz, D.A. Gorham, A.D. Salman, Accurate measurement of particle impact parameters, Meas. Sci. Technol. 10 (1999) 31–35. https://doi.org/10.1088/0957-0233/10/1/009.
- [26] G. Weir, S. Tallon, The coefficient of restitution for normal incident, low velocity particle impacts, Chem. Eng. Sci. 60 (2005) 3637–3647. https://doi.org/10.1016/j.ces.2005.01.040.
- [27] K.L. Johnson, Contact Mechanics, Cambridge University Press, 1985. https://doi.org/10.1017/CBO9781139171731.
- [28] C. Thornton, Coefficient of Restitution for Collinear Collisions of Elastic-Perfectly Plastic Spheres, J. Appl. Mech. 64 (1997) 383–386. https://doi.org/10.1115/1.2787319.
- [29] L.-Y. Li, C.-Y. Wu, C. Thornton, A theoretical model for the contact of elastoplastic bodies, Proc. Inst. Mech. Eng. Part C J. Mech. Eng. Sci. 216 (2001) 421–431. https://doi.org/10.1243/0954406021525214.
- [30] R.L. Jackson, I. Green, D.B. Marghitu, Predicting the coefficient of restitution of impacting elastic-perfectly plastic spheres, Nonlinear Dyn. 60 (2010) 217–229.



- https://doi.org/10.1007/s11071-009-9591-z.
- [31] S. Krijt, C. Güttler, D. Heißelmann, C. Dominik, A.G.G.M. Tielens, Energy dissipation in head-on collisions of spheres, J. Phys. D. Appl. Phys. 46 (2013) 435303. https://doi.org/10.1088/0022-3727/46/43/435303.
- [32] Y. Zhou, Modeling of softsphere normal collisions with characteristic of coefficient of restitution dependent on impact velocity, Theor. Appl. Mech. Lett. 3 (2013) 021003. https://doi.org/10.1063/2.1302103.
- [33] J. Xie, M. Dong, S. Li, Dynamic impact model of plastic deformation between microparticles and flat surfaces without adhesion, Aerosol Sci. Technol. 50 (2016) 321–330. https://doi.org/10.1080/02786826.2016.1150957.
- [34] I. Green, The prediction of the coefficient of restitution between impacting spheres and finite thickness plates undergoing elastoplastic deformations and wave propagation, Nonlinear Dyn. 109 (2022) 2443–2458. https://doi.org/10.1007/s11071-022-07522-3.
- [35] T. Schmidt, H. Assadi, F. Gärtner, H. Richter, T. Stoltenhoff, H. Kreye, T. Klassen, From Particle Acceleration to Impact and Bonding in Cold Spraying, J. Therm. Spray Technol. 18 (2009) 794. https://doi.org/10.1007/s11666-009-9357-7.
- [36] H. Assadi, T. Schmidt, H. Richter, J.-O. Kliemann, K. Binder, F. Gärtner, T. Klassen, H. Kreye, On Parameter Selection in Cold Spraying, J. Therm. Spray Technol. 20 (2011) 1161–1176. https://doi.org/10.1007/s11666-011-9662-9.
- [37] C.-J. Li, W.-Y. Li, H. Liao, Examination of the Critical Velocity for Deposition of Particles in Cold Spraying, J. Therm. Spray Technol. 15 (2006) 212–222. https://doi.org/10.1361/105996306X108093.
- [38] M. Grujicic, C.. Zhao, W.. DeRosset, D. Helfritch, Adiabatic shear instability based mechanism for particles/substrate bonding in the cold-gas dynamic-spray process, Mater. Des. 25 (2004) 681–688. https://doi.org/10.1016/j.matdes.2004.03.008.
- [39] H. Assadi, F. Gärtner, T. Stoltenhoff, H. Kreye, Bonding mechanism in cold gas spraying, Acta Mater. 51 (2003) 4379–4394. https://doi.org/10.1016/S1359-6454(03)00274-X.
- [40] H. Assadi, F. Gärtner, T. Klassen, H. Kreye, Comment on 'Adiabatic shear instability is not necessary for adhesion in cold spray,' Scr. Mater. 162 (2019) 512–514. https://doi.org/10.1016/j.scriptamat.2018.10.036.
- [41] G. Bae, S. Kumar, S. Yoon, K. Kang, H. Na, H.-J. Kim, C. Lee, Bonding features and associated mechanisms in kinetic sprayed titanium coatings, Acta Mater. 57 (2009) 5654–5666. https://doi.org/10.1016/j.actamat.2009.07.061.
- [42] W.B. Choi, L. Li, V. Luzin, R. Neiser, T. Gnäupel-Herold, H.J. Prask, S. Sampath, A. Gouldstone, Integrated characterization of cold sprayed aluminum coatings, Acta Mater. 55 (2007) 857–866. https://doi.org/10.1016/j.actamat.2006.09.006.
- [43] M.R. Rokni, S.R. Nutt, C.A. Widener, V.K. Champagne, R.H. Hrabe, Review of Relationship Between Particle Deformation, Coating Microstructure, and Properties in High-Pressure Cold Spray, J. Therm. Spray Technol. 26 (2017) 1308–1355. https://doi.org/10.1007/s11666-017-0575-0.



- [44] F.F. Lange, Powder Processing Science and Technology for Increased Reliability, J. Am. Ceram. Soc. 72 (1989) 3–15. https://doi.org/10.1111/j.1151-2916.1989.tb05945.x.
- [45] C.-J. Li, H.-T. Wang, Q. Zhang, G.-J. Yang, W.-Y. Li, H.L. Liao, Influence of Spray Materials and Their Surface Oxidation on the Critical Velocity in Cold Spraying, J. Therm. Spray Technol. 19 (2010) 95–101. https://doi.org/10.1007/s11666-009-9427-x.
- [46] K. Kang, S. Yoon, Y. Ji, C. Lee, Oxidation dependency of critical velocity for aluminum feedstock deposition in kinetic spraying process, Mater. Sci. Eng. A. 486 (2008) 300–307. https://doi.org/10.1016/j.msea.2007.09.010.
- [47] J. Villafuerte, Modern Cold Spray: Materials, Process, and Applications, Springer International Publishing, Cham, 2015. https://doi.org/10.1007/978-3-319-16772-5.
- [48] X. Suo, S. Yin, M.-P. Planche, T. Liu, H. Liao, Strong effect of carrier gas species on particle velocity during cold spray processes, Surf. Coatings Technol. 268 (2015) 90–93. https://doi.org/10.1016/j.surfcoat.2014.04.039.
- [49] S. Yin, M. Meyer, W. Li, H. Liao, R. Lupoi, Gas Flow, Particle Acceleration, and Heat Transfer in Cold Spray: A review, J. Therm. Spray Technol. 25 (2016) 874–896. https://doi.org/10.1007/s11666-016-0406-8.
- [50] M.A. Adaan-Nyiak, A.A. Tiamiyu, Recent advances on bonding mechanism in cold spray process: A review of single-particle impact methods, J. Mater. Res. 38 (2023) 69–95. https://doi.org/10.1557/s43578-022-00764-2.
- [51] O.C. Ozdemir, C.A. Widener, M.J. Carter, K.W. Johnson, Predicting the Effects of Powder Feeding Rates on Particle Impact Conditions and Cold Spray Deposited Coatings, J. Therm. Spray Technol. 26 (2017) 1598–1615. https://doi.org/10.1007/s11666-017-0611-0.
- [52] A. Sova, S. Grigoriev, A. Okunkova, I. Smurov, Potential of cold gas dynamic spray as additive manufacturing technology, Int. J. Adv. Manuf. Technol. 69 (2013) 2269–2278. https://doi.org/10.1007/s00170-013-5166-8.
- [53] S. Deng, H. Liang, Z. Cai, H. Liao, G. Montavon, Kinematic Optimization of Robot Trajectories for Thermal Spray Coating Application, J. Therm. Spray Technol. 23 (2014) 1382–1389. https://doi.org/10.1007/s11666-014-0137-7.
- [54] D. Kotoban, S. Grigoriev, A. Okunkova, A. Sova, Influence of a shape of single track on deposition efficiency of 316L stainless steel powder in cold spray, Surf. Coatings Technol. 309 (2017) 951–958. https://doi.org/10.1016/j.surfcoat.2016.10.052.
- [55] D. Fang, S. Deng, H. Liao, C. Coddet, The Effect of Robot Kinematics on the Coating Thickness Uniformity, J. Therm. Spray Technol. 19 (2010) 796–804. https://doi.org/10.1007/s11666-010-9470-7.
- [56] A. Moridi, S.M.H. Gangaraj, S. Vezzu, M. Guagliano, Number of Passes and Thickness Effect on Mechanical Characteristics of Cold Spray Coating, Procedia Eng. 74 (2014) 449–459. https://doi.org/10.1016/j.proeng.2014.06.296.
- [57] A.W.-Y. Tan, W. Sun, Y.P. Phang, M. Dai, I. Marinescu, Z. Dong, E. Liu, Effects of Traverse Scanning Speed of Spray Nozzle on the Microstructure and Mechanical Properties of Cold-Sprayed Ti6Al4V Coatings, J. Therm. Spray Technol. 26 (2017)



- 1484–1497. https://doi.org/10.1007/s11666-017-0619-5.
- [58] S. Yin, P. Cavaliere, B. Aldwell, R. Jenkins, H. Liao, W. Li, R. Lupoi, Cold spray additive manufacturing and repair: Fundamentals and applications, Addit. Manuf. 21 (2018) 628–650. https://doi.org/10.1016/j.addma.2018.04.017.
- [59] X.-T. Luo, Y.-J. Li, C.-X. Li, G.-J. Yang, C.-J. Li, Effect of spray conditions on deposition behavior and microstructure of cold sprayed Ni coatings sprayed with a porous electrolytic Ni powder, Surf. Coatings Technol. 289 (2016) 85–93. https://doi.org/10.1016/j.surfcoat.2016.01.058.
- [60] K. Binder, J. Gottschalk, M. Kollenda, F. Gärtner, T. Klassen, Influence of Impact Angle and Gas Temperature on Mechanical Properties of Titanium Cold Spray Deposits, J. Therm. Spray Technol. 20 (2011) 234–242. https://doi.org/10.1007/s11666-010-9557-1
- [61] A.A. Tiamiyu, Y. Sun, K.A. Nelson, C.A. Schuh, Site-specific study of jetting, bonding, and local deformation during high-velocity metallic microparticle impact, Acta Mater. 202 (2021) 159–169. https://doi.org/10.1016/j.actamat.2020.10.057.
- [62] A.A. Tiamiyu, C.A. Schuh, Particle flattening during cold spray: Mechanistic regimes revealed by single particle impact tests, Surf. Coatings Technol. 403 (2020) 126386. https://doi.org/10.1016/j.surfcoat.2020.126386.
- [63] C.E. Augarde, S.J. Lee, D. Loukidis, Numerical modelling of large deformation problems in geotechnical engineering: A state-of-the-art review, Soils Found. 61 (2021) 1718–1735. https://doi.org/10.1016/j.sandf.2021.08.007.
- [64] H. Hertz, Ueber die Berührung fester elastischer Körper, in: J. Für Die Reine Und Angew. Math. Band 92, De Gruyter, 1882: pp. 156–171. https://doi.org/10.1515/9783112342404-004.
- [65] A.P. Christoforou, A.S. Yigit, M. Majeed, Low-Velocity Impact Response of Structures With Local Plastic Deformation: Characterization and Scaling, J. Comput. Nonlinear Dyn. 8 (2013). https://doi.org/10.1115/1.4006532.
- [66] Y. Du, S. Wang, Energy Dissipation in Normal Elastoplastic Impact Between Two Spheres, J. Appl. Mech. 76 (2009). https://doi.org/10.1115/1.3130801.
- [67] R.L. Jackson, I. Green, A Finite Element Study of Elasto-Plastic Hemispherical Contact Against a Rigid Flat, J. Tribol. 127 (2005) 343–354. https://doi.org/10.1115/1.1866166.
- [68] L. Vu-Quoc, X. Zhang, An elastoplastic contact force—displacement model in the normal direction: displacement—driven version, Proc. R. Soc. London. Ser. A Math. Phys. Eng. Sci. 455 (1999) 4013–4044. https://doi.org/10.1098/rspa.1999.0488.
- [69] H. Ghaednia, D.B. Marghitu, R.L. Jackson, Predicting the Permanent Deformation After the Impact of a Rod With a Flat Surface, J. Tribol. 137 (2015). https://doi.org/10.1115/1.4028709.
- [70] L. Kogut, I. Etsion, Elastic-Plastic Contact Analysis of a Sphere and a Rigid Flat, J. Appl. Mech. 69 (2002) 657–662. https://doi.org/10.1115/1.1490373.
- [71] I. Etsion, Y. Kligerman, Y. Kadin, Unloading of an elastic-plastic loaded spherical

- contact, Int. J. Solids Struct. 42 (2005) 3716–3729. https://doi.org/10.1016/j.ijsolstr.2004.12.006.
- [72] A.S. Yigit, A.P. Christoforou, On the impact of a spherical indenter and an elastic-plastic transversely isotropic half-space, Compos. Eng. 4 (1994) 1143–1152. https://doi.org/10.1016/0961-9526(95)91288-R.
- [73] L. Kogut, K. Komvopoulos, Analysis of the spherical indentation cycle for elastic—perfectly plastic solids, J. Mater. Res. 19 (2004) 3641–3653. https://doi.org/10.1557/JMR.2004.0468.
- [74] D. Rathbone, M. Marigo, D. Dini, B. van Wachem, An accurate force—displacement law for the modelling of elastic—plastic contacts in discrete element simulations, Powder Technol. 282 (2015) 2–9. https://doi.org/10.1016/j.powtec.2014.12.055.
- [75] M.R.W. Brake, An analytical elastic plastic contact model with strain hardening and frictional effects for normal and oblique impacts, Int. J. Solids Struct. 62 (2015) 104–123. https://doi.org/10.1016/j.ijsolstr.2015.02.018.
- [76] R.K. Pal, A.P. Awasthi, P.H. Geubelle, Wave propagation in elasto-plastic granular systems, Granul. Matter. 15 (2013) 747–758. https://doi.org/10.1007/s10035-013-0449-1.
- [77] W.J. Stronge, Impact Mechanics, Cambridge University Press, Cambridge, 2000.
- [78] M.R. Brake, An analytical elastic-perfectly plastic contact model, Int. J. Solids Struct. 49 (2012) 3129–3141. https://doi.org/10.1016/j.ijsolstr.2012.06.013.
- [79] D. Ma, C. Liu, Contact Law and Coefficient of Restitution in Elastoplastic Spheres, J. Appl. Mech. 82 (2015). https://doi.org/10.1115/1.4031483.
- [80] A. Big-Alabo, P. Harrison, M.P. Cartmell, Elastoplastic half-space impact analysis using a novel contact model that accounts for post-yield effects, in: Proc. 9th Int. Conf. Struct. Dyn., 2014: pp. 3475–3482.
- [81] A. Big-Alabo, P. Harrison, M.P. Cartmell, Contact model for elastoplastic analysis of half-space indentation by a spherical impactor, Comput. Struct. 151 (2015) 20–29. https://doi.org/10.1016/j.compstruc.2015.01.005.
- [82] S.D. Mesarovic, N.A. Fleck, Frictionless indentation of dissimilar elastic–plastic spheres, Int. J. Solids Struct. 37 (2000) 7071–7091. https://doi.org/10.1016/S0020-7683(99)00328-5.
- [83] H. Ghaednia, X. Wang, S. Saha, Y. Xu, A. Sharma, R.L. Jackson, A Review of Elastic—Plastic Contact Mechanics, Appl. Mech. Rev. 69 (2017). https://doi.org/10.1115/1.4038187.
- [84] C. Thornton, Z. Ning, A theoretical model for the stick/bounce behaviour of adhesive, elastic-plastic spheres, Powder Technol. 99 (1998) 154–162. https://doi.org/10.1016/S0032-5910(98)00099-0.
- [85] J. Tomas, Adhesion of ultrafine particles—A micromechanical approach, Chem. Eng. Sci. 62 (2007) 1997–2010. https://doi.org/10.1016/j.ces.2006.12.055.



- [86] C.L. Martin, Unloading of powder compacts and their resulting tensile strength, Acta Mater. 51 (2003) 4589–4602. https://doi.org/10.1016/S1359-6454(03)00296-9.
- [87] S. Luding, Shear flow modeling of cohesive and frictional fine powder, Powder Technol. 158 (2005) 45–50. https://doi.org/10.1016/j.powtec.2005.04.018.
- [88] S. Luding, About contact force-laws for cohesive frictional materials in 2D and 3D, Behav. Granul. Media. (2006).
- [89] S. Luding, Cohesive, frictional powders: Contact models for tension, Granul. Matter. (2008). https://doi.org/10.1007/s10035-008-0099-x.
- [90] M. Pasha, S. Dogbe, C. Hare, A. Hassanpour, M. Ghadiri, A linear model of elastoplastic and adhesive contact deformation, Granul. Matter. 16 (2014) 151–162. https://doi.org/10.1007/s10035-013-0476-y.
- [91] H.P. Zhu, Z.Y. Zhou, R.Y. Yang, A.B. Yu, Discrete particle simulation of particulate systems: Theoretical developments, Chem. Eng. Sci. 62 (2007) 3378–3396. https://doi.org/10.1016/j.ces.2006.12.089.
- [92] B.. Mishra, A review of computer simulation of tumbling mills by the discrete element method: Part I—contact mechanics, Int. J. Miner. Process. 71 (2003) 73–93. https://doi.org/10.1016/S0301-7516(03)00032-2.
- [93] B.. Mishra, A review of computer simulation of tumbling mills by the discrete element method: Part II—Practical applications, Int. J. Miner. Process. 71 (2003) 95–112. https://doi.org/10.1016/S0301-7516(03)00031-0.
- [94] F. Bertrand, L.-A. Leclaire, G. Levecque, DEM-based models for the mixing of granular materials, Chem. Eng. Sci. 60 (2005) 2517–2531. https://doi.org/10.1016/j.ces.2004.11.048.
- [95] G. Beer, J.O. Watson, Infinite boundary elements, Int. J. Numer. Methods Eng. 28 (1989) 1233–1247. https://doi.org/10.1002/nme.1620280602.
- [96] A.H.-D. Cheng, D.T. Cheng, Heritage and early history of the boundary element method, Eng. Anal. Bound. Elem. 29 (2005) 268–302. https://doi.org/10.1016/j.enganabound.2004.12.001.
- [97] P.K. Kythe, An Introduction to Boundary Element Methods, CRC Press, 2020. https://doi.org/10.1201/9781003068693.
- [98] L.J. Lorig, B.H.G. Brady, P.A. Cundall, Hybrid distinct element-boundary element analysis of jointed rock, Int. J. Rock Mech. Min. Sci. Geomech. Abstr. 23 (1986) 303–312. https://doi.org/10.1016/0148-9062(86)90642-X.
- [99] A.-B. Huang, M.Y. Ma, J.S. Lee, A micromechanical study of penetration tests in granular material, Mech. Mater. 16 (1993) 133–139. https://doi.org/10.1016/0167-6636(93)90036-Q.
- [100] S. Nadimi, A. Ghanbarzadeh, A. Neville, M. Ghadiri, Effect of particle roughness on the bulk deformation using coupled boundary element and discrete element methods, Comput. Part. Mech. 7 (2020) 603–613. https://doi.org/10.1007/s40571-019-00288-3.



- [101] G. Barros, A. Pereira, J. Rojek, K. Thoeni, DEM-BEM coupling in time domain for one-dimensional wave propagation, Eng. Anal. Bound. Elem. 135 (2022) 26–37. https://doi.org/10.1016/j.enganabound.2021.10.017.
- [102] G. Barros, V. Sapucaia, P. Hartmann, A. Pereira, J. Rojek, K. Thoeni, A novel BEM-DEM coupling in the time domain for simulating dynamic problems in continuous and discontinuous media, Comput. Methods Appl. Mech. Eng. 410 (2023) 116040. https://doi.org/10.1016/j.cma.2023.116040.
- [103] K.K. Pradhan, S. Chakraverty, Finite Element Method, in: Comput. Struct. Mech., Elsevier, 2019: pp. 25–28. https://doi.org/10.1016/B978-0-12-815492-2.00010-1.
- [104] J.J. Quicksall, R.L. Jackson, I. Green, Elasto-plastic hemispherical contact models for various mechanical properties, Proc. Inst. Mech. Eng. Part J J. Eng. Tribol. 218 (2004) 313–322. https://doi.org/10.1243/1350650041762604.
- [105] L.P. Lin, J.F. Lin, A New Method for Elastic-Plastic Contact Analysis of a Deformable Sphere and a Rigid Flat, J. Tribol. 128 (2006) 221–229. https://doi.org/10.1115/1.2164469.
- [106] V. Brizmer, Y. Kligerman, I. Etsion, The effect of contact conditions and material properties on the elasticity terminus of a spherical contact, Int. J. Solids Struct. 43 (2006) 5736–5749. https://doi.org/10.1016/j.ijsolstr.2005.07.034.
- [107] S. Shankar, M.M. Mayuram, A Finite Element Based Study on the Elastic-Plastic Transition Behavior in a Hemisphere in Contact With a Rigid Flat, J. Tribol. 130 (2008). https://doi.org/10.1115/1.2958081.
- [108] P. Sahoo, B. Chatterjee, A Finite Element Study of Elastic-Plastic Hemispherical Contact Behavior against a Rigid Flat under Varying Modulus of Elasticity and Sphere Radius, Engineering. 02 (2010) 205–211. https://doi.org/10.4236/eng.2010.24030.
- [109] S. Mukhopadhyay, P.K. Das, N. Abani, A theoretical model to predict normal contact characteristics for elasto-plastic collisions, Granul. Matter. 25 (2023) 20. https://doi.org/10.1007/s10035-023-01307-0.
- [110] C. Wu, L. Li, C. Thornton, Rebound behaviour of spheres for plastic impacts, Int. J. Impact Eng. 28 (2003) 929–946. https://doi.org/10.1016/S0734-743X(03)00014-9.
- [111] K.L. Johnson, An Experimental Determination of the Contact Stresses Between Plastically Deformed Cylinders and Spheres, Eng. Plast. Cambridge Univ. Press. Cambridge. (1968) 341–361.
- [112] C. Hardy, C.N. Baronet, G. V. Tordion, The elasto-plastic indentation of a half-space by a rigid sphere, Int. J. Numer. Methods Eng. 3 (1971) 451–462. https://doi.org/10.1002/nme.1620030402.
- [113] G.B. Sinclair, P.S. Follansbee, K.L. Johnson, Quasi-static normal indentation of an elasto-plastic half-space by a rigid sphere—II. Results, Int. J. Solids Struct. 21 (1985) 865–888. https://doi.org/10.1016/0020-7683(85)90039-3.
- [114] E.R. Kral, K. Komvopoulos, D.B. Bogy, Elastic-Plastic Finite Element Analysis of Repeated Indentation of a Half-Space by a Rigid Sphere, J. Appl. Mech. 60 (1993) 829–841. https://doi.org/10.1115/1.2900991.



- [115] D. Tabor, The Hardness of Metals, Clarendon Press, Oxford, UK, 1951.
- [116] A. Fardan, C.C. Berndt, R. Ahmed, Numerical modelling of particle impact and residual stresses in cold sprayed coatings: A review, Surf. Coatings Technol. 409 (2021) 126835. https://doi.org/10.1016/j.surfcoat.2021.126835.
- [117] M.A. Meyers, Dynamic Behavior of Materials, Wiley, 1994. https://doi.org/10.1002/9780470172278.
- [118] Y. Liu, C. Xu, Investigating the cold spraying process with the material point method, Int. J. Mech. Mater. Des. 15 (2019) 361–378. https://doi.org/10.1007/s10999-018-9419-4.
- [119] G.R. Johnson, W.H. Cook, A Constitutive Model and Data for Metals Subjected to Large Strains, High Strain Rates and High Temperatures, in: 7th Int. Symp. Ballist., 1983: pp. 541–547.
- [120] G.R. Johnson, W.H. Cook, Fracture characteristics of three metals subjected to various strains, strain rates, temperatures and pressures, Eng. Fract. Mech. 21 (1985) 31–48. https://doi.org/10.1016/0013-7944(85)90052-9.
- [121] D.L. Preston, D.L. Tonks, D.C. Wallace, Model of plastic deformation for extreme loading conditions, J. Appl. Phys. 93 (2003) 211–220. https://doi.org/10.1063/1.1524706.
- [122] B. Banerjee, The Mechanical Threshold Stress model for various tempers of AISI 4340 steel, Int. J. Solids Struct. 44 (2007) 834–859. https://doi.org/10.1016/j.ijsolstr.2006.05.022.
- [123] F.J. Zerilli, R.W. Armstrong, Dislocation-mechanics-based constitutive relations for material dynamics calculations, J. Appl. Phys. 61 (1987) 1816–1825. https://doi.org/10.1063/1.338024.
- [124] F.H. Abed, G.Z. Voyiadjis, A consistent modified Zerilli-Armstrong flow stress model for BCC and FCC metals for elevated temperatures, Acta Mech. 175 (2005) 1–18. https://doi.org/10.1007/s00707-004-0203-1.
- [125] A.K. Gupta, V.K. Anirudh, S.K. Singh, Constitutive models to predict flow stress in Austenitic Stainless Steel 316 at elevated temperatures, Mater. Des. 43 (2013) 410–418. https://doi.org/10.1016/j.matdes.2012.07.008.
- [126] Q. Wang, N. Ma, M. Takahashi, X. Luo, C. Li, Development of a material model for predicting extreme deformation and grain refinement during cold spraying, Acta Mater. 199 (2020) 326–339. https://doi.org/10.1016/j.actamat.2020.08.052.
- [127] M.P. Allen, D.J. Tildesley, J.R. Banavar, Computer Simulation of Liquids, Phys. Today. 42 (1989) 105–106. https://doi.org/10.1063/1.2810937.
- [128] H. Ogawa, Molecular Dynamics Simulation on the Single Particle Impacts in the Aerosol Deposition Process, Mater. Trans. 46 (2005) 1235–1239. https://doi.org/10.2320/matertrans.46.1235.
- [129] H. Ogawa, Atomistic Simulation of the Aerosol Deposition Method with Zirconia Nanoparticles, Mater. Trans. 47 (2006) 1945–1948.



- https://doi.org/10.2320/matertrans.47.1945.
- [130] H. Ogawa, Molecular Dynamics Simulation on the Modification of Crystallographic Orientation in Fragmented Particles in the Aerosol-Deposition Process, Mater. Trans. 48 (2007) 2067–2071. https://doi.org/10.2320/matertrans.MA200712.
- [131] B. Daneshian, H. Assadi, Impact Behavior of Intrinsically Brittle Nanoparticles: A Molecular Dynamics Perspective, J. Therm. Spray Technol. 23 (2014) 541–550. https://doi.org/10.1007/s11666-013-0019-4.
- [132] H. Jami, A. Jabbarzadeh, Ultrafast thermomechanical effects in aerosol deposition of hydroxyapatite nanoparticles on a titanium substrate, Surf. Coatings Technol. 382 (2020) 125173. https://doi.org/10.1016/j.surfcoat.2019.125173.
- [133] B. Daneshian, F. Gaertner, H. Assadi, D. Hoeche, W. Weber, T. Klassen, Size Effects of Brittle Particles in Aerosol Deposition—Molecular Dynamics Simulation, J. Therm. Spray Technol. (2021). https://doi.org/10.1007/s11666-020-01149-9.
- [134] H. Gao, L. Zhao, D. Zeng, L. Gao, Molecular Dynamics Simulation of Au Cluster Depositing on Au Surface in Cold Gas Spray, in: First Int. Conf. Integr. Commer. Micro Nanosyst. Parts A B, ASMEDC, 2007: pp. 195–202. https://doi.org/10.1115/MNC2007-21609.
- [135] T. Malama, A. Hamweendo, I. Botef, Molecular Dynamics Simulation of Ti and Ni Particles on Ti Substrate in the Cold Gas Dynamic Spray (CGDS) Process, Mater. Sci. Forum. 828–829 (2015) 453–460. https://doi.org/10.4028/www.scientific.net/MSF.828-829.453.
- [136] A. Joshi, S. James, Molecular Dynamics Simulation Study on Effect of Process Parameters on Coatings during Cold Spray Process, Procedia Manuf. 26 (2018) 190–197. https://doi.org/10.1016/j.promfg.2018.07.026.
- [137] A. Joshi, S. James, Molecular dynamics simulation study of cold spray process, J. Manuf. Process. 33 (2018) 136–143. https://doi.org/10.1016/j.jmapro.2018.05.005.
- [138] S. Rahmati, A. Zúñiga, B. Jodoin, R.G.A. Veiga, Deformation of copper particles upon impact: A molecular dynamics study of cold spray, Comput. Mater. Sci. 171 (2020) 109219. https://doi.org/10.1016/j.commatsci.2019.109219.
- [139] S. Temitope Oyinbo, T.-C. Jen, Molecular Dynamics Simulation of Dislocation Plasticity Mechanism of Nanoscale Ductile Materials in the Cold Gas Dynamic Spray Process, Coatings. 10 (2020) 1079. https://doi.org/10.3390/coatings10111079.
- [140] S.T. Oyinbo, T.-C. Jen, Molecular dynamics investigation of temperature effect and surface configurations on multiple impacts plastic deformation in a palladium-copper composite metal membrane (CMM): A cold gas dynamic spray (CGDS) process, Comput. Mater. Sci. 185 (2020) 109968. https://doi.org/10.1016/j.commatsci.2020.109968.
- [141] D. Sulsky, Z. Chen, H.L. Schreyer, A particle method for history-dependent materials, Comput. Methods Appl. Mech. Eng. 118 (1994) 179–196. https://doi.org/10.1016/0045-7825(94)90112-0.
- [142] D. Sulsky, H.L. Schreyer, Axisymmetric form of the material point method with



- applications to upsetting and Taylor impact problems, Comput. Methods Appl. Mech. Eng. 139 (1996) 409–429. https://doi.org/10.1016/S0045-7825(96)01091-2.
- [143] A. de Vaucorbeil, V.P. Nguyen, S. Sinaie, J.Y. Wu, Material point method after 25 years: Theory, implementation, and applications, in: Adv. Appl. Mech., 2020: pp. 185–398. https://doi.org/10.1016/bs.aams.2019.11.001.
- [144] A. de Vaucorbeil, V.P. Nguyen, Modelling contacts with a total Lagrangian material point method, Comput. Methods Appl. Mech. Eng. 373 (2021) 113503. https://doi.org/10.1016/j.cma.2020.113503.
- [145] S. Nezamabadi, F. Radjai, Explicit total Lagrangian material point method with implicit frictional-contact model for soft granular materials, Granul. Matter. 26 (2024) 67. https://doi.org/10.1007/s10035-024-01438-y.
- [146] F. Li, J. Pan, C. Sinka, Contact laws between solid particles, J. Mech. Phys. Solids. 57 (2009) 1194–1208. https://doi.org/10.1016/j.jmps.2009.04.012.
- [147] P. Liu, Y. Liu, X. Zhang, Y. Guan, Investigation on high-velocity impact of micron particles using material point method, Int. J. Impact Eng. 75 (2015) 241–254. https://doi.org/10.1016/j.ijimpeng.2014.09.001.
- [148] G.I. Taylor, The use of flat-ended projectiles for determining dynamic yield stress I. Theoretical considerations, Proc. R. Soc. London. Ser. A. Math. Phys. Sci. 194 (1948) 289–299. https://doi.org/10.1098/rspa.1948.0081.
- [149] G.R. Johnson, T.J. Holmquist, Evaluation of cylinder-impact test data for constitutive model constants, J. Appl. Phys. 64 (1988) 3901–3910. https://doi.org/10.1063/1.341344.
- [150] T.J. Holmquist, G.R. Johnson, Determination of constants and comparison of results for various constitutive models, Le J. Phys. IV. 01 (1991) C3-853-C3-860. https://doi.org/10.1051/jp4:19913119.
- [151] R.M. Telikicherla, G. Moutsanidis, An assessment of the total Lagrangian material point method: Comparison to conventional MPM, higher order basis, and treatment of near-incompressibility, Comput. Methods Appl. Mech. Eng. 414 (2023) 116135. https://doi.org/10.1016/j.cma.2023.116135.
- [152] M.L. Wilkins, M.W. Guinan, Impact of cylinders on a rigid boundary, J. Appl. Phys. 44 (1973) 1200–1206. https://doi.org/10.1063/1.1662328.
- [153] L. Li, Y. Lian, M.-J. Li, R. Gao, Y. Gan, A contact method for B-spline material point method with application in impact and penetration problems, Comput. Mech. 73 (2024) 1351–1369. https://doi.org/10.1007/s00466-023-02414-8.
- [154] M.R. Hirmand, J. Tang, H. Jahed, A Particle-Based Numerical Model for Impact-Induced Bonding in Cold Spray, J. Therm. Spray Technol. 33 (2024) 1886–1913. https://doi.org/10.1007/s11666-024-01803-6.
- [155] W.-Y. Li, S. Yin, X.-F. Wang, Numerical investigations of the effect of oblique impact on particle deformation in cold spraying by the SPH method, Appl. Surf. Sci. 256 (2010) 3725–3734. https://doi.org/10.1016/j.apsusc.2010.01.014.
- [156] X. Zhang, K.Y. Sze, S. Ma, An explicit material point finite element method for hyper-



- velocity impact, Int. J. Numer. Methods Eng. 66 (2006) 689–706. https://doi.org/10.1002/nme.1579.
- [157] Y. Liu, H.-K. Wang, X. Zhang, A multiscale framework for high-velocity impact process with combined material point method and molecular dynamics, Int. J. Mech. Mater. Des. 9 (2013) 127–139. https://doi.org/10.1007/s10999-013-9213-2.
- [158] X. Zhang, Z. Chen, Y. Liu, The material point method: a continuum-based particle method for extreme loading cases, Academic Press, FL, United States, 2016.
- [159] O.T. Unke, S. Chmiela, H.E. Sauceda, M. Gastegger, I. Poltavsky, K.T. Schütt, A. Tkatchenko, K.-R. Müller, Machine Learning Force Fields, Chem. Rev. 121 (2021) 10142–10186. https://doi.org/10.1021/acs.chemrev.0c01111.
- [160] S. Nezamabadi, T.H. Nguyen, J.-Y. Delenne, F. Radjai, Modeling soft granular materials, Granul. Matter. 19 (2017) 8. https://doi.org/10.1007/s10035-016-0689-y.
- [161] S. Nezamabadi, F. Radjai, J. Averseng, J.-Y. Delenne, Implicit frictional-contact model for soft particle systems, J. Mech. Phys. Solids. 83 (2015) 72–87. https://doi.org/10.1016/j.jmps.2015.06.007.
- [162] S. Nezamabadi, X. Frank, J.-Y. Delenne, J. Averseng, F. Radjai, Parallel implicit contact algorithm for soft particle systems, Comput. Phys. Commun. 237 (2019) 17–25. https://doi.org/10.1016/j.cpc.2018.10.030.
- [163] S. Nezamabadi, M. Ghadiri, J.-Y. Delenne, F. Radjai, Modelling the compaction of plastic particle packings, Comput. Part. Mech. 9 (2022) 45–52. https://doi.org/10.1007/s40571-021-00391-4.
- [164] S. Saifoori, S. Nezamabadi, M. Ghadiri, Analysis of impact deformation of elastic-perfectly plastic particles, Comput. Part. Mech. (2024). https://doi.org/10.1007/s40571-024-00742-x.
- [165] J.J. Moreau, Evolution problem associated with a moving convex set in a Hilbert space, J. Differ. Equ. 26 (1977) 347–374. https://doi.org/10.1016/0022-0396(77)90085-7.
- [166] M. Jean, Unilateral contact and dry friction: time and space variables discretization, Arch. of Mech., Warszawa. 40 (1988) 677–691.
- [167] F. Radjai, V. Richefeu, Bond anisotropy and cohesion of wet granular materials, Philos. Trans. R. Soc. A Math. Phys. Eng. Sci. 367 (2009) 5123–5138. https://doi.org/10.1098/rsta.2009.0185.
- [168] S.G. Bardenhagen, J.E. Guilkey, K.M. Roessig, J.U. Brackbill, W.M. Witzel, J.C. Foster, An improved contact algorithm for the material point method and application to stress propagation in granular material, C. Comput. Model. Eng. Sci. 2 (2001) 509–522.
- [169] P. Huang, X. Zhang, S. Ma, X. Huang, Contact algorithms for the material point method in impact and penetration simulation, Int. J. Numer. Methods Eng. 85 (2011) 498–517. https://doi.org/10.1002/nme.2981.
- [170] M. Jean, Frictional contact in collections of rigid or deformable bodies: numerical simulation of geomaterial motions, in: 1995: pp. 463–486.

- https://doi.org/10.1016/S0922-5382(06)80022-X.
- [171] B. Brogliato, Nonsmooth Mechanics, Springer London, London, 1999. https://doi.org/10.1007/978-1-4471-0557-2.
- [172] H. Wang, X. Yin, H. Hao, W. Chen, B. Yu, The correlation of theoretical contact models for normal elastic-plastic impacts, Int. J. Solids Struct. 182–183 (2020) 15–33. https://doi.org/10.1016/j.ijsolstr.2019.07.018.
- [173] H. Deresiewicz, A note on Hertz's theory of impact, Acta Mech. 6 (1968) 110–112. https://doi.org/10.1007/BF01177810.
- [174] J. Ahrens, B. Geveci, C. Law, ParaView: An End-User Tool for Large-Data Visualization, in: Vis. Handb., Elsevier, 2005: pp. 717–731. https://doi.org/10.1016/B978-012387582-2/50038-1.
- [175] C.E. Anderson, An overview of the theory of hydrocodes, Int. J. Impact Eng. 5 (1987) 33–59. https://doi.org/10.1016/0734-743X(87)90029-7.
- [176] R. Hill, The Mathematical Theory of Plasticity, Clarendon Press, Oxford, 1950.
- [177] R.F. Bishop, R. Hill, N.F. Mott, The theory of indentation and hardness tests, Proc. Phys. Soc. 57 (1945) 147–159. https://doi.org/10.1088/0959-5309/57/3/301.
- [178] K.E. Puttick, Indentation fracture of oriented polymethylmethacrylate, J. Phys. D. Appl. Phys. 11 (1978) 595–604. https://doi.org/10.1088/0022-3727/11/4/004.
- [179] A. Hassanpour, M. Ghadiri, Distinct element analysis and experimental evaluation of the Heckel analysis of bulk powder compression, Powder Technol. 141 (2004) 251–261. https://doi.org/10.1016/j.powtec.2004.02.010.
- [180] W. Martienssen, WarlimontHans, Springer Handbook of Condensed Matter and Materials Data, 1st ed., Springer Berlin, Heidelberg, 2005. https://doi.org/10.1007/3-540-30437-1.
- [181] D.J. Benson, Computational methods in Lagrangian and Eulerian hydrocodes, Comput. Methods Appl. Mech. Eng. 99 (1992) 235–394. https://doi.org/10.1016/0045-7825(92)90042-I.
- [182] O.C. Zienkiewicz, R.L. Taylor, D. Fox, The Finite Element Method for Solid and Structural Mechanics, Elsevier, 2014. https://doi.org/10.1016/C2009-0-26332-X.
- [183] S. Saifoori, S. Hosseinhashemi, M. Alasossi, C. Schilde, S. Nezamabadi, M. Ghadiri, AI-Assisted Prediction of Particle Impact Deformation Simulated by Material Point Method "under review," Powder Technol. (2025).
- [184] D. Angelis, F. Sofos, T.E. Karakasidis, Artificial Intelligence in Physical Sciences: Symbolic Regression Trends and Perspectives, Arch. Comput. Methods Eng. 30 (2023) 3845–3865. https://doi.org/10.1007/s11831-023-09922-z.
- [185] I. Goodfellow, Y. Bengio, A. Courville, Deep Learning, The MIT Press, Cambridge, Massachusetts, 2016.
- [186] D.E. Goldberg, Genetic Algorithms in Search, Optimization, and Machine Learning,



- Addison-Wesley, 1989.
- [187] P. Veličković, G. Cucurull, A. Casanova, A. Romero, P. Liò, Y. Bengio, Graph Attention Networks, 6th Int. Conf. Learn. Represent. ICLR 2018 Conf. Track Proc. (2017) 39–41. https://doi.org/10.1007/978-3-031-01587-8\_7.
- [188] S. Hosseinhashemi, Y. Zhang, C. Thon, C. Schilde, Process insights with physics-inspired data-driven modeling- example of battery electrode processing, J. Energy Storage. 73 (2023) 109046. https://doi.org/10.1016/j.est.2023.109046.
- [189] S. Hosseinhashemi, Q. Liu, S. Saifoori, C. Thon, C. Schilde, Physics-Inspired Hybrid AI Framework for Mechanistic Process Model Development, (2025).
- [190] T. Stephens, gplearn's Documentation, (2016). https://gplearn.readthedocs.io/en/stable/(accessed September 24, 2024).
- [191] I. Guyon, J. Weston, S. Barnhill, V. VAPNIK, Gene Selection for Cancer Classification using Support Vector Machines, Mach. Learn. 46 (2002) 389–422. https://doi.org/https://doi.org/10.1023/A:1012487302797.
- [192] R. Artusi, P. Verderio, E. Marubini, Bravais-Pearson and Spearman Correlation Coefficients: Meaning, Test of Hypothesis and Confidence Interval, Int. J. Biol. Markers. 17 (2002) 148–151. https://doi.org/10.1177/172460080201700213.
- [193] S. Brody, U. Alon, E. Yahav, How Attentive are Graph Attention Networks?, ICLR 2022 10th Int. Conf. Learn. Represent. (2021) 1–26. http://arxiv.org/abs/2105.14491.
- [194] S. Zhang, H. Tong, J. Xu, R. Maciejewski, Graph convolutional networks: a comprehensive review, Comput. Soc. Networks. 6 (2019) 11. https://doi.org/10.1186/s40649-019-0069-y.
- [195] T.N. Kipf, M. Welling, Semi-Supervised Classification with Graph Convolutional Networks, 5th Int. Conf. Learn. Represent. ICLR 2017 Conf. Track Proc. (2016) 1–14. http://arxiv.org/abs/1609.02907.
- [196] A. Farea, O. Yli-Harja, F. Emmert-Streib, Understanding Physics-Informed Neural Networks: Techniques, Applications, Trends, and Challenges, AI. 5 (2024) 1534–1557. https://doi.org/10.3390/ai5030074.
- [197] T. Bonakdar, M. Ali, M. Ghadiri, Particle breakability assessment using an Aero S disperser, Int. J. Pharm. 597 (2021) 120365. https://doi.org/10.1016/j.ijpharm.2021.120365.
- [198] Z.N. Mao, X.H. An, X.Z. Liao, J.T. Wang, Opposite grain size dependence of strain rate sensitivity of copper at low vs high strain rates, Mater. Sci. Eng. A. 738 (2018) 430–438. https://doi.org/10.1016/j.msea.2018.09.018.
- [199] Y. Noh, M.-S. Lee, U.M. Chaudry, T.-S. Jun, Effect of strain rate on the deformation of 6061-T6 aluminum alloy at cryogenic temperature, Mater. Charact. 206 (2023) 113403. https://doi.org/10.1016/j.matchar.2023.113403.
- [200] N. Ma'at, M.K.M. Nor, C.S. Ho, N. Abdul Latif, A.E. Ismail, K.A. Kamarudin, S. Jamian, M.N. Ibrahim-Tamrin, M.K. Awang, Effects of temperatures and strain rate on the mechanical behaviour of commercial aluminium alloy AA6061, J. Adv. Res. Fluid

- Mech. Therm. Sci. 54 (2019) 185–190.
- [201] X. Long, J. Xu, S. Wang, W. Tang, C. Chang, Understanding the impact response of lead-free solder at high strain rates, Int. J. Mech. Sci. 172 (2020) 105416. https://doi.org/10.1016/j.ijmecsci.2020.105416.
- [202] X. Long, T. Su, C. Lu, S. Wang, J. Huang, C. Chang, An insight into dynamic properties of SAC305 lead-free solder under high strain rates and high temperatures, Int. J. Impact Eng. 175 (2023) 104542. https://doi.org/10.1016/j.ijimpeng.2023.104542.
- [203] P. Lall, D. Zhang, V. Yadav, D. Locker, High strain rate constitutive behavior of SAC105 and SAC305 leadfree solder during operation at high temperature, Microelectron. Reliab. 62 (2016) 4–17. https://doi.org/10.1016/j.microrel.2016.03.014.
- [204] J. Schindelin, I. Arganda-Carreras, E. Frise, V. Kaynig, M. Longair, T. Pietzsch, S. Preibisch, C. Rueden, S. Saalfeld, B. Schmid, J.-Y. Tinevez, D.J. White, V. Hartenstein, K. Eliceiri, P. Tomancak, A. Cardona, Fiji: an open-source platform for biological-image analysis, Nat. Methods. 9 (2012) 676–682. https://doi.org/10.1038/nmeth.2019.
- [205] C. Wu, Finite element analysis of particle impact problems, PhD Thesis, The University of Aston in Birmingham, 2001.
- [206] J. Akedo, Room Temperature Impact Consolidation (RTIC) of Fine Ceramic Powder by Aerosol Deposition Method and Applications to Microdevices, J. Therm. Spray Technol. 17 (2008) 181–198. https://doi.org/10.1007/s11666-008-9163-7.
- [207] A. Moridi, S.M. Hassani-Gangaraj, M. Guagliano, M. Dao, Cold spray coating: Review of material systems and future perspectives, Surf. Eng. 30 (2014) 369–395. https://doi.org/10.1179/1743294414Y.0000000270.
- [208] F. Meng, Modelling of Ceramic Particle Impact Behaviour in Aerosol Deposition, PhD Thesis, The University of Manchester, 2024.

## Appendix A

### Sensitivity Analysis: Effect of Material Points and Mesh Discretisation

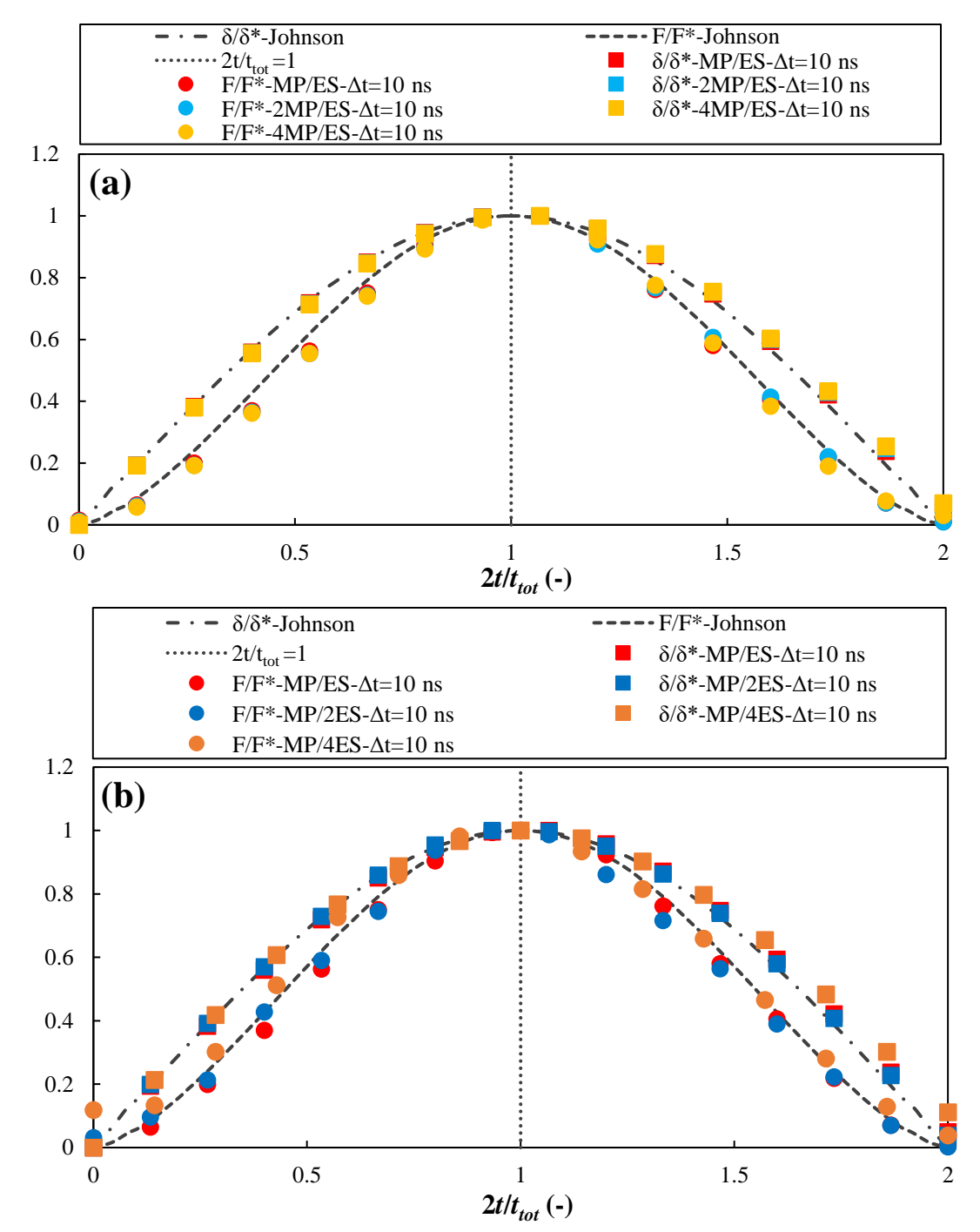


Figure A-1 Variation of the contact force and displacement with time for the impact of an elastic sphere undergoing small deformation, calculated using Johnson's [27] analytical approach (dashed lines) and MPM simulations (discrete symbols) considering a time step of 10 ns for (a) cases MP/ES, 2MP/ES and 4MP/ES, to highlight the effect of increasing the number of material points per element, and (b) cases MP/ES, MP/2ES and MP/4ES, to highlight the effect of increasing the element size.

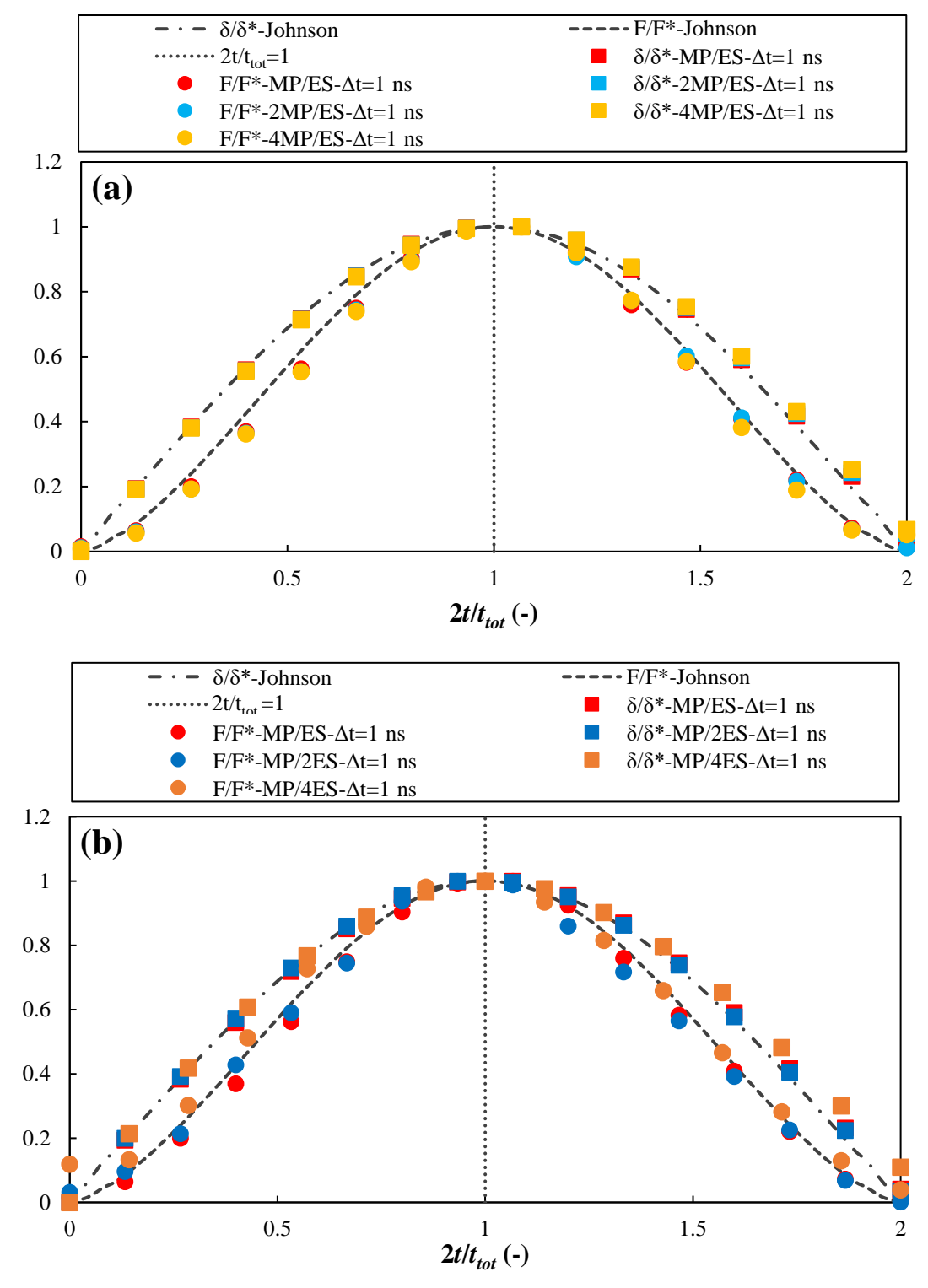


Figure A-2 Variation of the contact force and displacement with time for the impact of an elastic sphere undergoing small deformation, calculated using Johnson's [27] analytical approach (dashed lines) and MPM simulations (discrete symbols) considering a time step of 1 ns for (a) cases MP/ES, 2MP/ES and 4MP/ES, to highlight the effect of increasing the number of material points per element, and (b) cases MP/ES, MP/2ES and MP/4ES, to highlight the effect of increasing the element size.



#### **Sensitivity Analysis: Effect of Time Step**

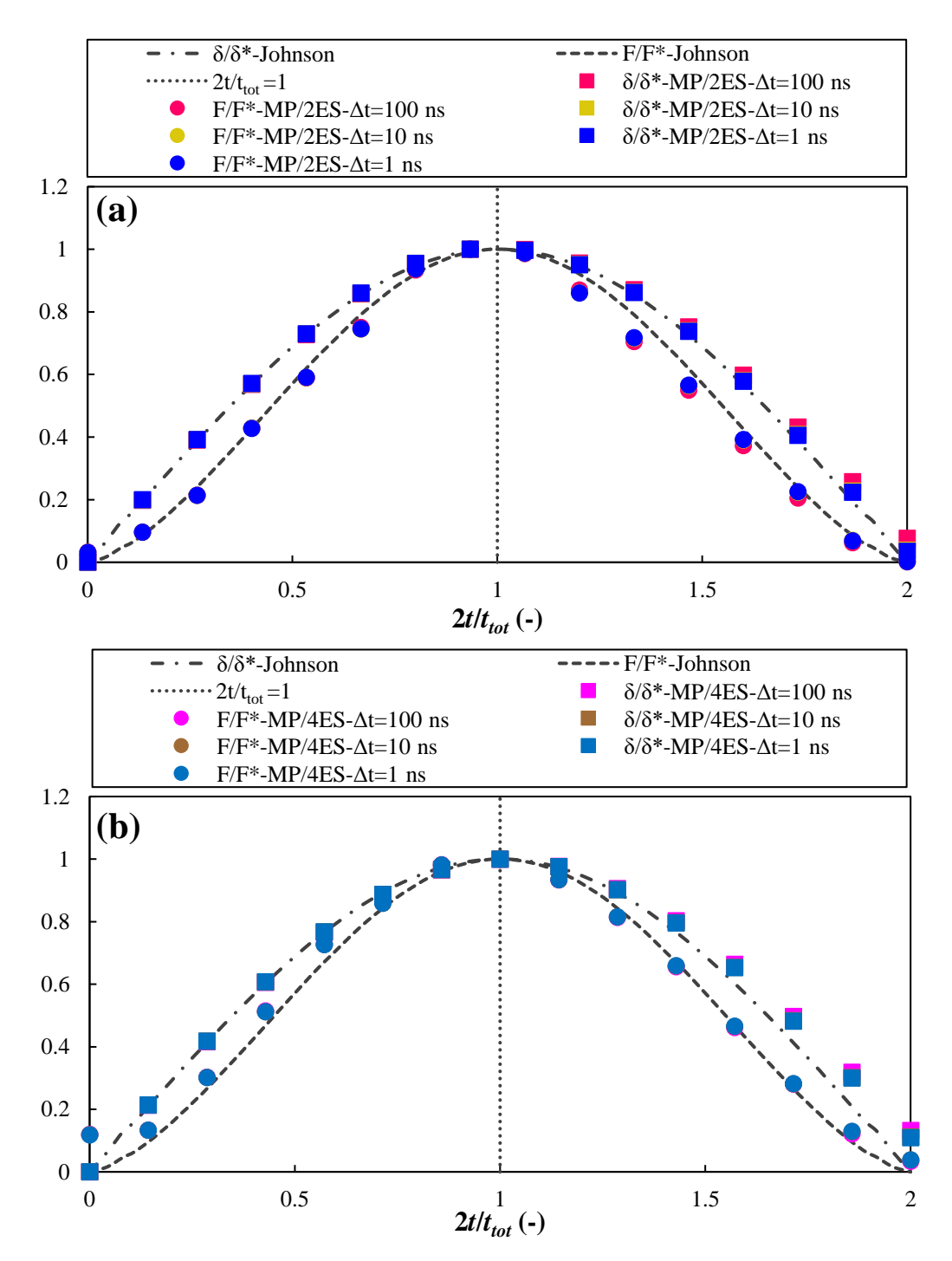


Figure A-3 Variation of the contact force and displacement with time for the impact of an elastic sphere undergoing small deformation, calculated using Johnson's [27] analytical approach (dashed lines) and MPM simulations (discrete symbols) considering time steps of 1, 10 and 100 ns for (a) case MP/2ES and (b) case MP/4ES of the sensitivity analysis.



## Appendix B

#### **Impact Deformation: Simulation Success of Case Studies**

Table B-1 Case studies for the impact of an elastic-perfectly plastic particle at 10 m/s, colour coded based on the simulation success: red signifies the cases for which no result is obtained, green represents the cases for which the simulation is successful and orange denotes the cases that do not undergo plastic deformation and therefore are dismissed from further analysis.

| $\rho  (\text{kg/m}^3)$ | 1000    |    |     | 2000 |    |     | 4000 |    |     | 8000 |    |     |
|-------------------------|---------|----|-----|------|----|-----|------|----|-----|------|----|-----|
|                         | E (GPa) |    |     |      |    |     |      |    |     |      |    |     |
| E/Y (-)                 | 1       | 10 | 100 | 1    | 10 | 100 | 1    | 10 | 100 | 1    | 10 | 100 |
| 20                      |         |    |     |      |    |     |      |    |     |      |    |     |
| 40                      |         |    |     |      |    |     |      |    |     |      |    |     |
| 80                      |         |    |     |      |    |     |      |    |     |      |    |     |
| 160                     |         |    |     |      |    |     |      |    |     |      |    |     |
| 320                     |         |    |     |      |    |     |      |    |     |      |    |     |
| 640                     |         |    |     |      |    |     |      |    |     |      |    |     |
| 1280                    |         |    |     |      |    |     |      |    |     |      |    |     |
| 2560                    |         |    |     |      |    |     |      |    |     |      |    |     |

Table B-2 Case studies for the impact of an elastic-perfectly plastic particle at 20 m/s, colour coded based on the simulation success: red signifies the cases for which no result is obtained, green represents the cases for which the simulation is successful and orange denotes the cases that do not undergo plastic deformation and therefore are dismissed from further analysis.

| $\rho$ (kg/m <sup>3</sup> ) | 1000    |    |     | 2000 |    |     | 4000 |    |     | 8000 |    |     |
|-----------------------------|---------|----|-----|------|----|-----|------|----|-----|------|----|-----|
|                             | E (GPa) |    |     |      |    |     |      |    |     |      |    |     |
| E/Y (-)                     | 1       | 10 | 100 | 1    | 10 | 100 | 1    | 10 | 100 | 1    | 10 | 100 |
| 20                          |         |    |     |      |    |     |      |    |     |      |    |     |
| 40                          |         |    |     |      |    |     |      |    |     |      |    |     |
| 80                          |         |    |     |      |    |     |      |    |     |      |    |     |
| 160                         |         |    |     |      |    |     |      |    |     |      |    |     |
| 320                         |         |    |     |      |    |     |      |    |     |      |    |     |
| 640                         |         |    |     |      |    |     |      |    |     |      |    |     |
| 1280                        |         |    |     |      |    |     |      |    |     |      |    |     |
| 2560                        |         |    |     |      |    |     |      |    |     |      |    |     |



Table B-3 Case studies for the impact of an elastic-perfectly plastic particle at 30 m/s, colour coded based on the simulation success: red signifies the cases for which no result is obtained, and green represents the cases for which the simulation is successful.

| $\rho  (\text{kg/m}^3)$ | 1000    |    |     | 2000 |    |     | 4000 |    |     | 8000 |    |     |
|-------------------------|---------|----|-----|------|----|-----|------|----|-----|------|----|-----|
|                         | E (GPa) |    |     |      |    |     |      |    |     |      |    |     |
| E/Y (-)                 | 1       | 10 | 100 | 1    | 10 | 100 | 1    | 10 | 100 | 1    | 10 | 100 |
| 20                      |         |    |     |      |    |     |      |    |     |      |    |     |
| 40                      |         |    |     |      |    |     |      |    |     |      |    |     |
| 80                      |         |    |     |      |    |     |      |    |     |      |    |     |
| 160                     |         |    |     |      |    |     |      |    |     |      |    |     |
| 320                     |         |    |     |      |    |     |      |    |     |      |    |     |
| 640                     |         |    |     |      |    |     |      |    |     |      |    |     |
| 1280                    |         |    |     |      |    |     |      |    |     |      |    |     |
| 2560                    |         |    |     |      |    |     |      |    |     |      |    |     |

Table B-4 Case studies for the impact of an elastic-perfectly plastic particle at 40 m/s, colour coded based on the simulation success: red signifies the cases for which no result is obtained, and green represents the cases for which the simulation is successful.

| $\rho$ (kg/m <sup>3</sup> ) | 1000    |    |     | 2000 |    |     | 4000 |    |     | 8000 |    |     |
|-----------------------------|---------|----|-----|------|----|-----|------|----|-----|------|----|-----|
|                             | E (GPa) |    |     |      |    |     |      |    |     |      |    |     |
| <i>E/Y</i> (-)              | 1       | 10 | 100 | 1    | 10 | 100 | 1    | 10 | 100 | 1    | 10 | 100 |
| 20                          |         |    |     |      |    |     |      |    |     |      |    |     |
| 40                          |         |    |     |      |    |     |      |    |     |      |    |     |
| 80                          |         |    |     |      |    |     |      |    |     |      |    |     |
| 160                         |         |    |     |      |    |     |      |    |     |      |    |     |
| 320                         |         |    |     |      |    |     |      |    |     |      |    |     |
| 640                         |         |    |     |      |    |     |      |    |     |      |    |     |
| 1280                        |         |    |     |      |    |     |      |    |     |      |    |     |
| 2560                        |         |    |     |      |    |     |      |    |     |      |    |     |



Table B-5 Case studies for the impact of an elastic-perfectly plastic particle at 50 m/s, colour coded based on the simulation success: red signifies the cases for which no result is obtained, and green represents the cases for which the simulation is successful.

| $\rho  (\text{kg/m}^3)$ | 1000    |    |     | 2000 |    |     | 4000 |    |     | 8000 |    |     |
|-------------------------|---------|----|-----|------|----|-----|------|----|-----|------|----|-----|
|                         | E (GPa) |    |     |      |    |     |      |    |     |      |    |     |
| E/Y (-)                 | 1       | 10 | 100 | 1    | 10 | 100 | 1    | 10 | 100 | 1    | 10 | 100 |
| 20                      |         |    |     |      |    |     |      |    |     |      |    |     |
| 40                      |         |    |     |      |    |     |      |    |     |      |    |     |
| 80                      |         |    |     |      |    |     |      |    |     |      |    |     |
| 160                     |         |    |     |      |    |     |      |    |     |      |    |     |
| 320                     |         |    |     |      |    |     |      |    |     |      |    |     |
| 640                     |         |    |     |      |    |     |      |    |     |      |    |     |
| 1280                    |         |    |     |      |    |     |      |    |     |      |    |     |
| 2560                    |         |    |     |      |    |     |      |    |     |      |    |     |



#### Impact Deformation: $\varepsilon_p$ as a function of E/Y

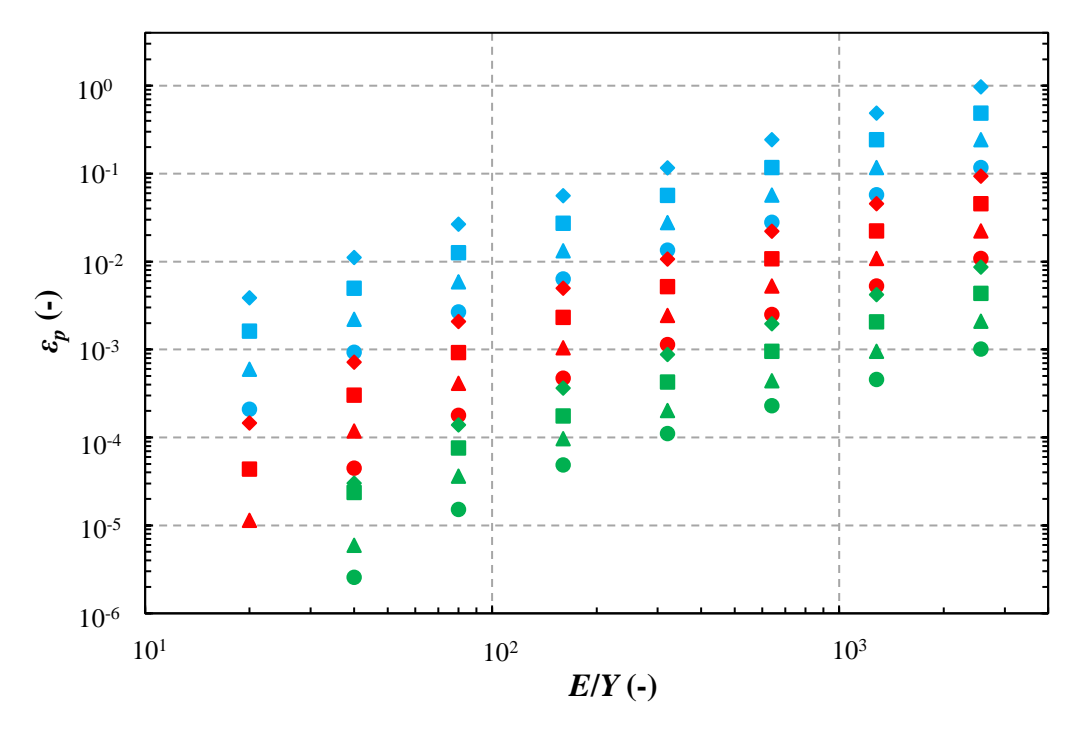


Figure B-1 The equivalent plastic strain,  $\varepsilon_p$ , as a function of the ratio of Young's modulus to yield strength, E/Y, for all the cases with an impact velocity of 10 m/s. For designation of the symbols, see Table 4-2.

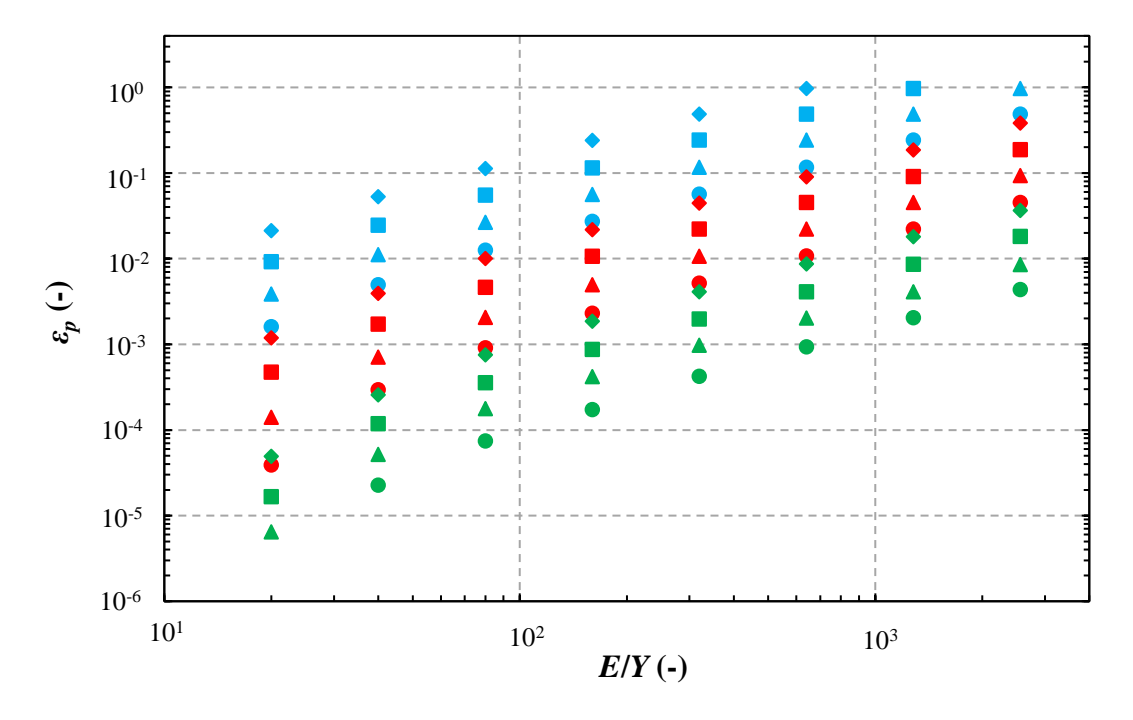


Figure B-2 The equivalent plastic strain,  $\varepsilon_p$ , as a function of the ratio of Young's modulus to yield strength, E/Y, for all the cases with an impact velocity of 20 m/s. For designation of the symbols, see Table 4-2.

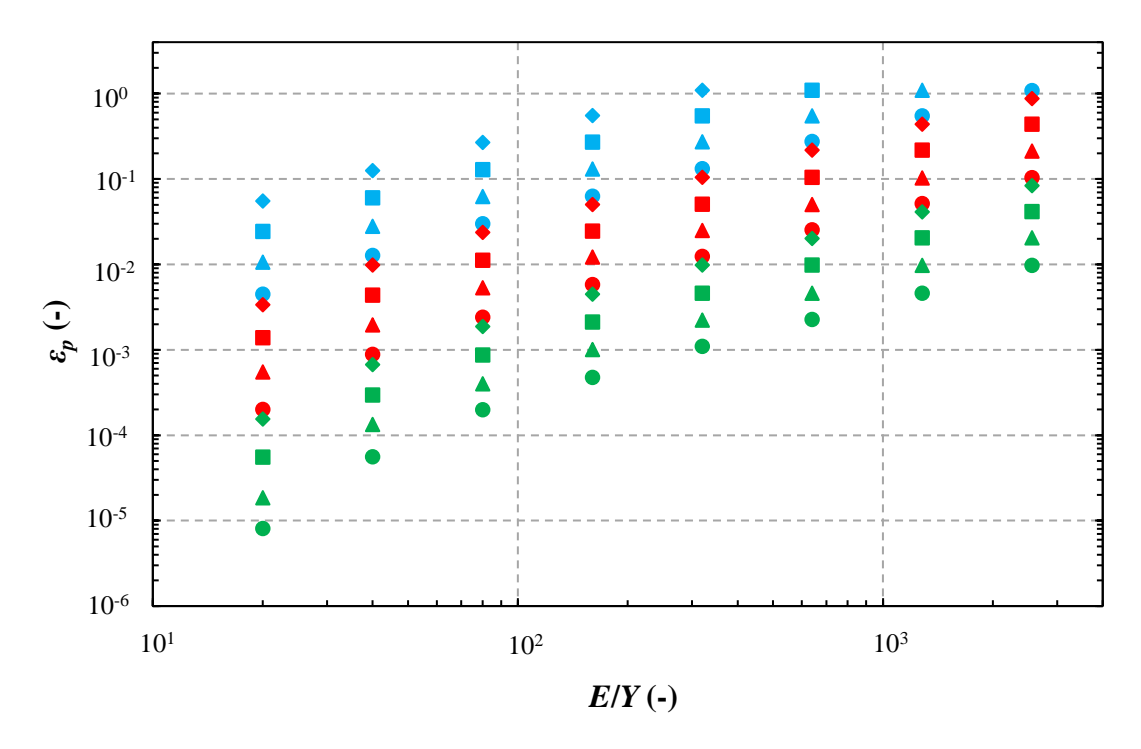


Figure B-3 The equivalent plastic strain,  $\varepsilon_p$ , as a function of the ratio of Young's modulus to yield strength, E/Y, for all the cases with an impact velocity of 30 m/s. For designation of the symbols, see Table 4-2.

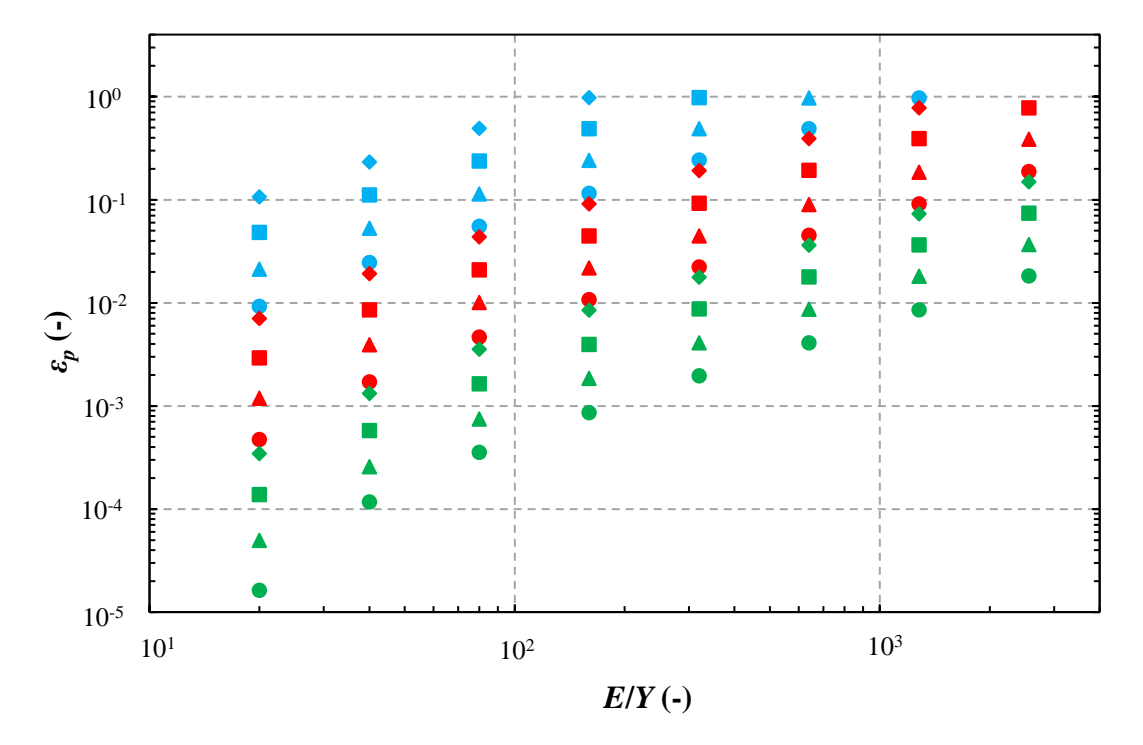


Figure B-4 The equivalent plastic strain,  $\varepsilon_p$ , as a function of the ratio of Young's modulus to yield strength, E/Y, for all the cases with an impact velocity of 40 m/s. For designation of the symbols, see Table 4-2.



### Impact Deformation: e as a function of $V_i/V_v$

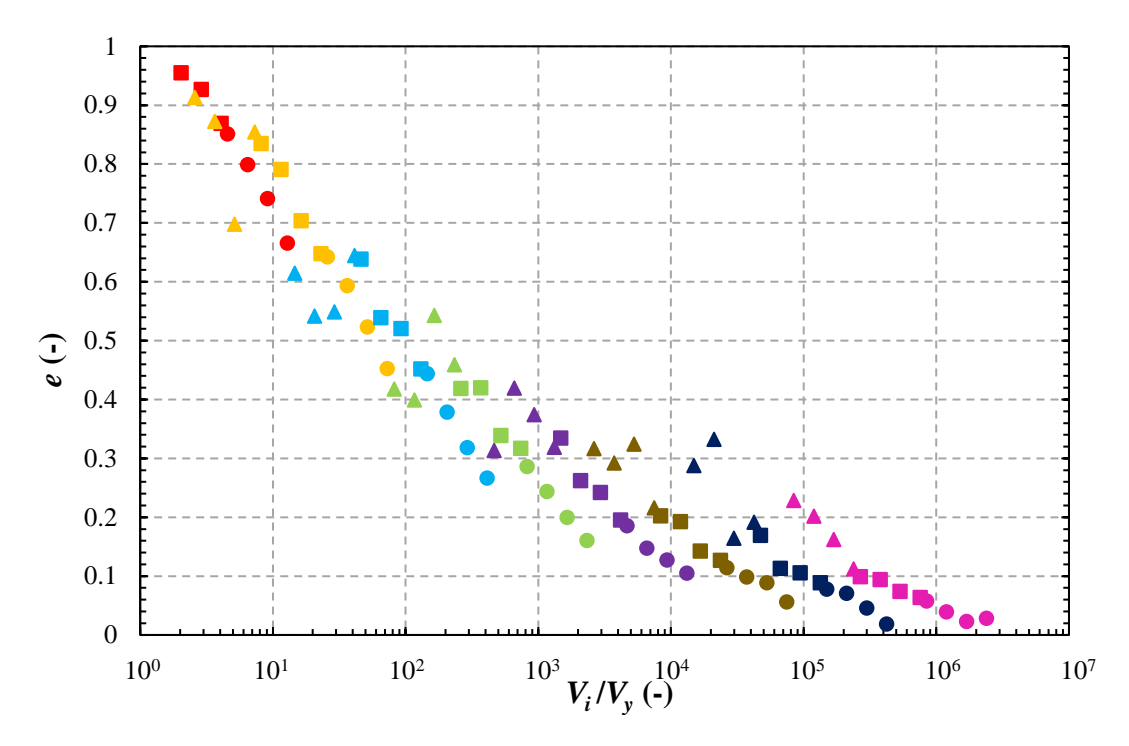


Figure B-5 The coefficient of restitution, e, as a function of  $V_i/V_y$ , for all the cases with an impact velocity of 10 m/s. For designation of the symbols, see Table 4-3. Note that the data points in each data set correspond to different densities.

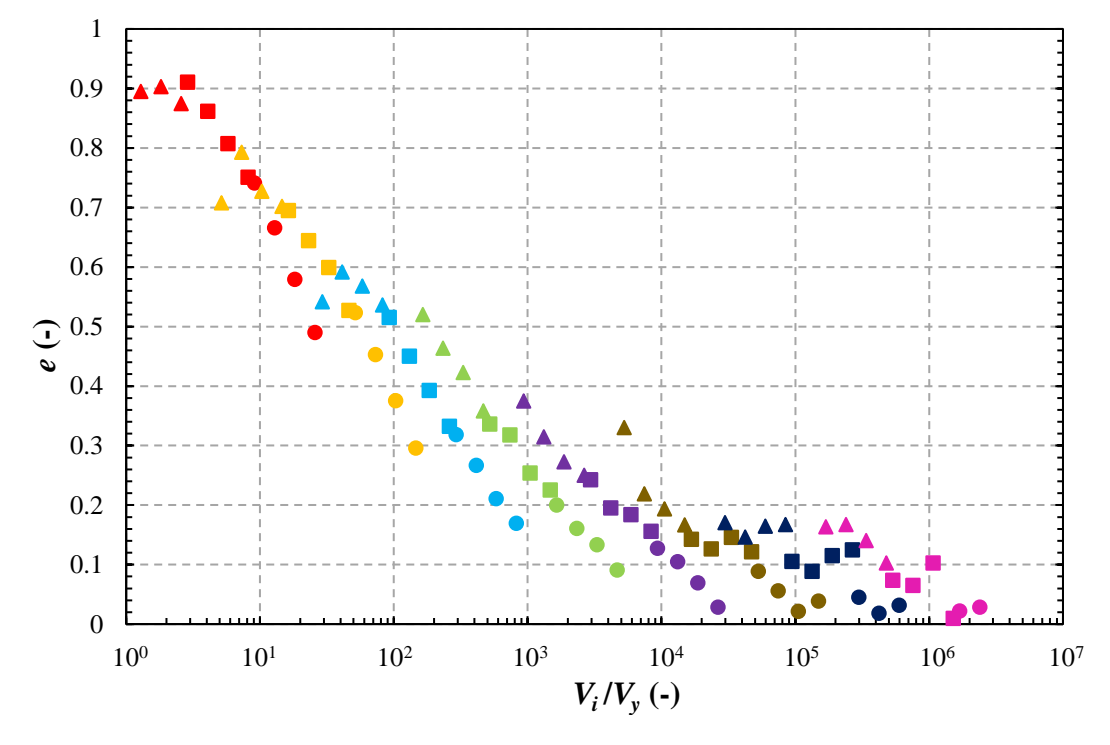


Figure B-6 The coefficient of restitution, e, as a function of  $V_i/V_y$ , for all the cases with an impact velocity of 20 m/s. For designation of the symbols, see Table 4-3. Note that the data points in each data set correspond to different densities.

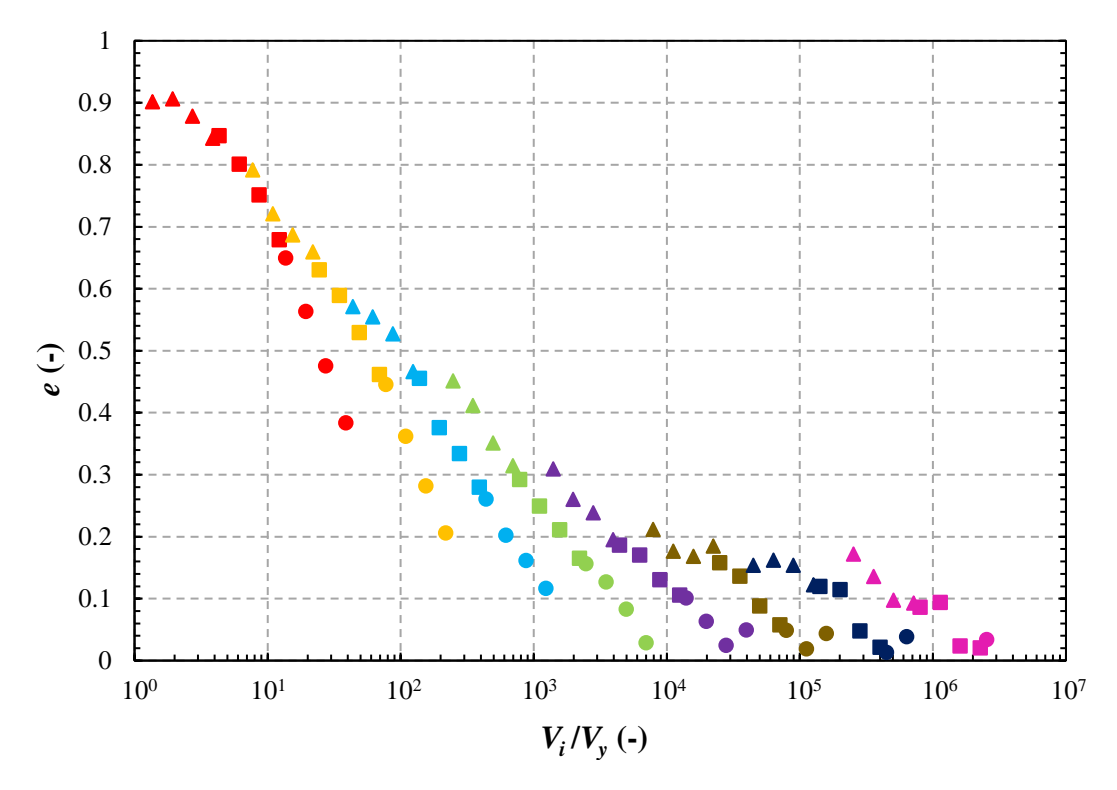


Figure B-7 The coefficient of restitution, e, as a function of  $V_i/V_y$ , for all the cases with an impact velocity of 30 m/s. For designation of the symbols, see Table 4-3. Note that the data points in each data set correspond to different densities.

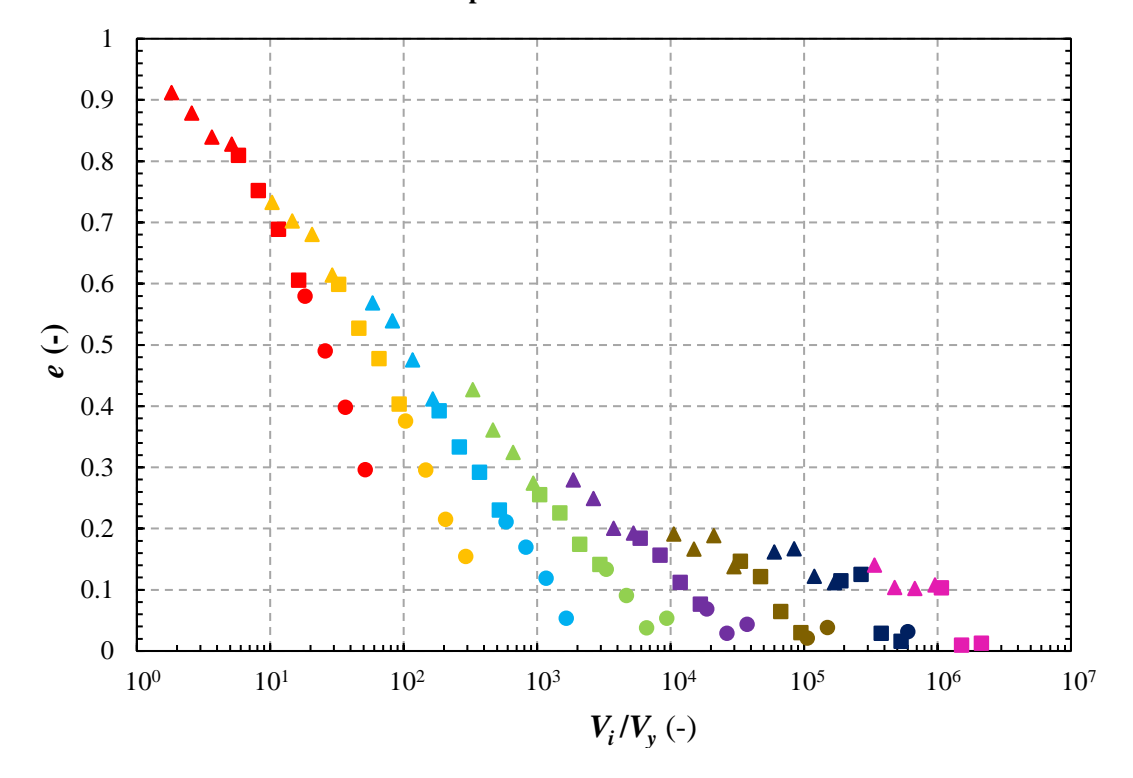
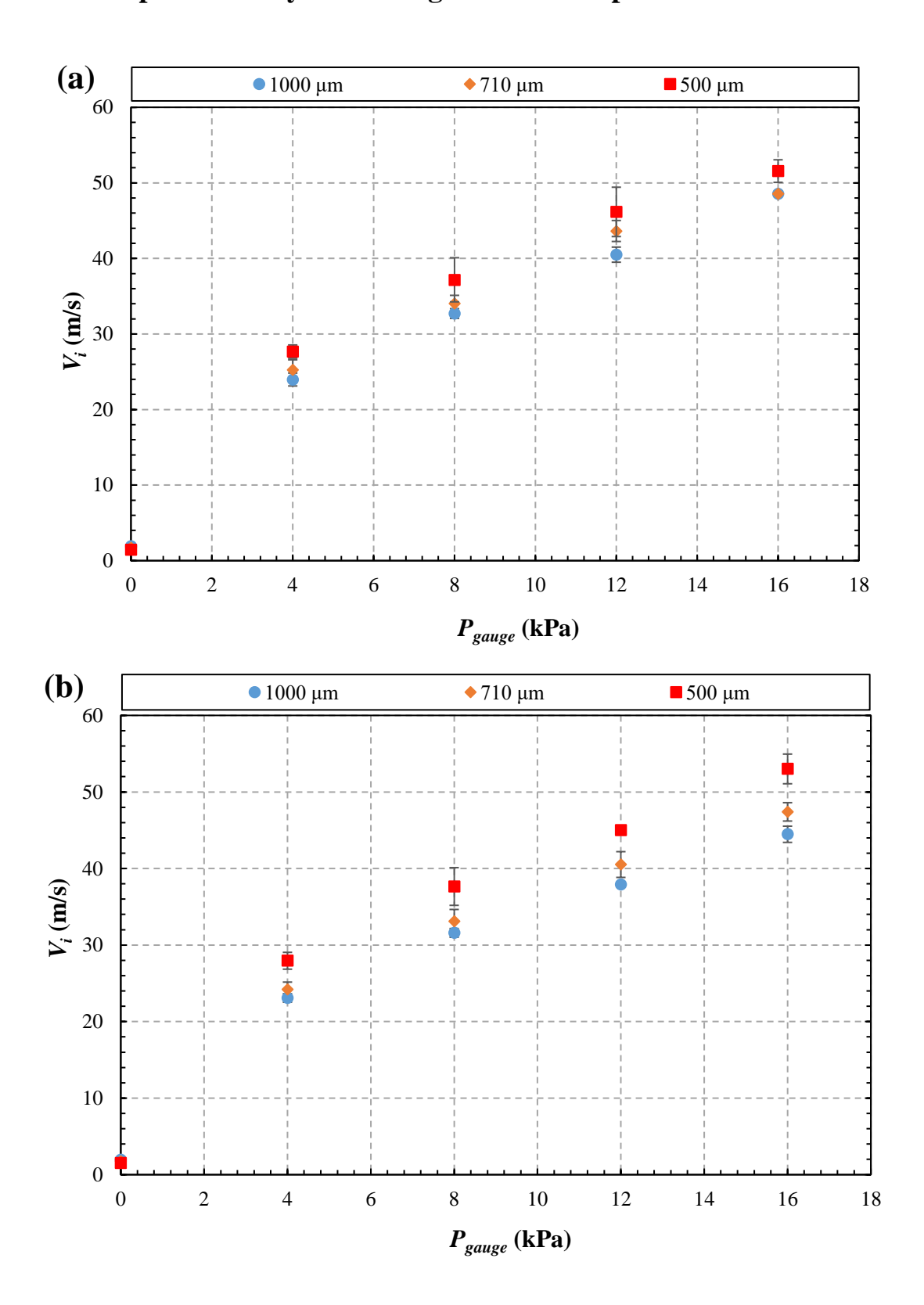


Figure B-8 The coefficient of restitution, e, as a function of  $V_i/V_y$ , for all the cases with an impact velocity of 40 m/s. For designation of the symbols, see Table 4-3. Note that the data points in each data set correspond to different densities.



# **Appendix C**

## **Particle Impact Velocity in the Single Particle Impact Tester**



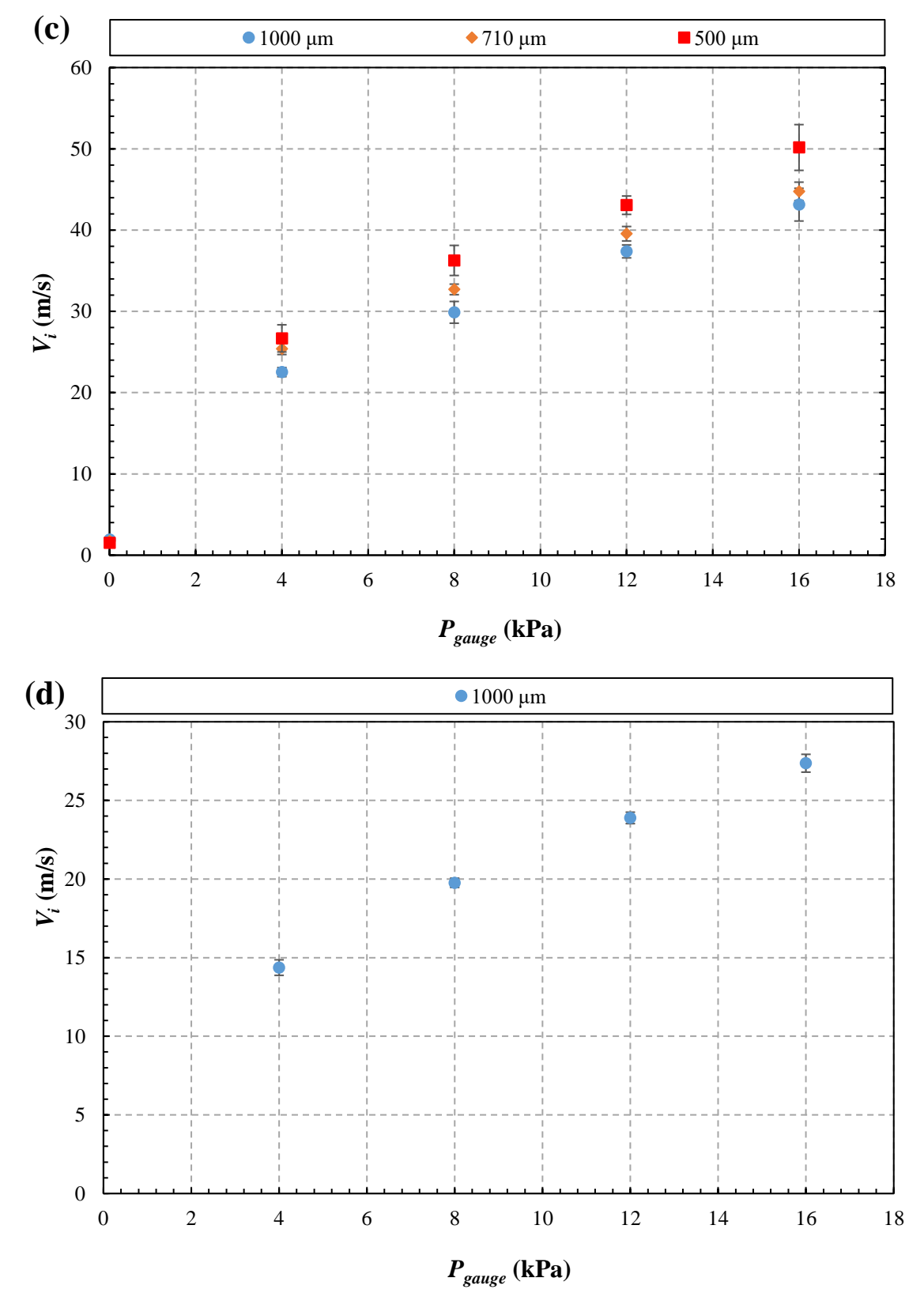
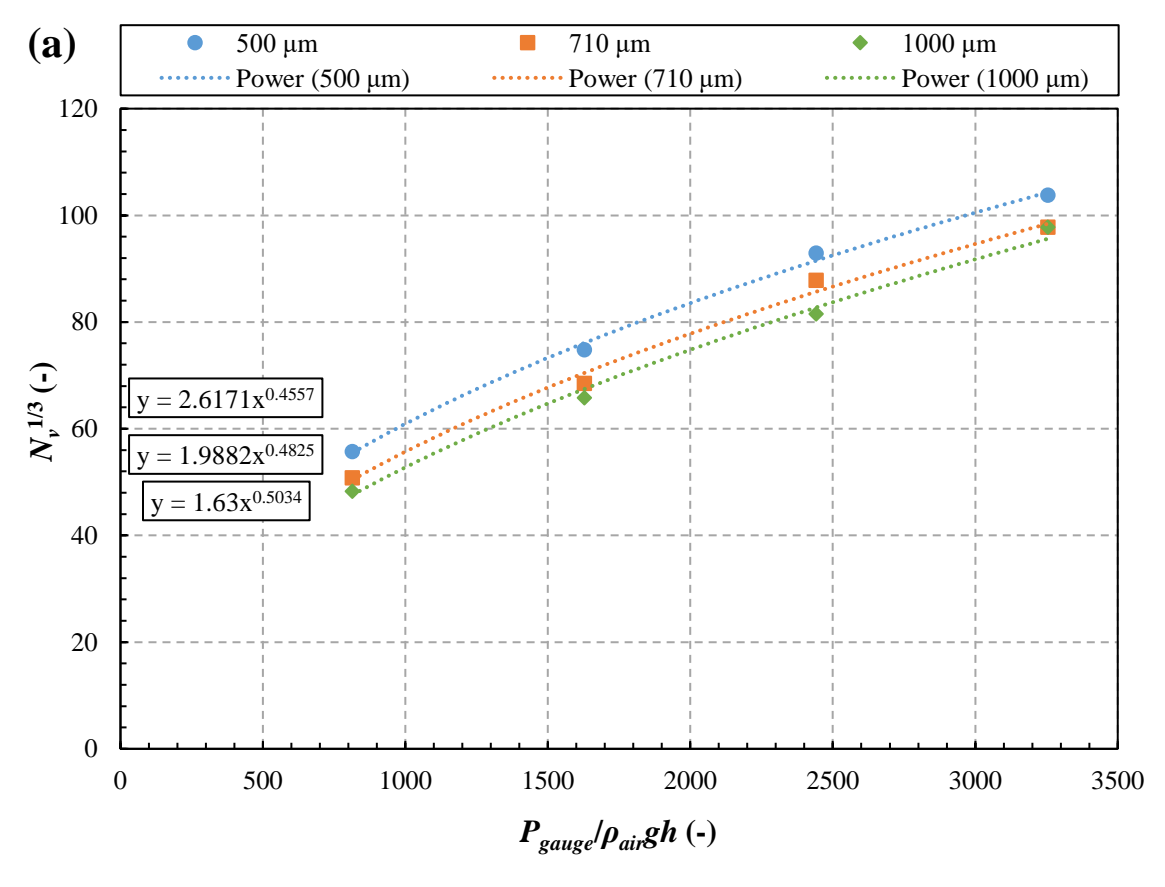
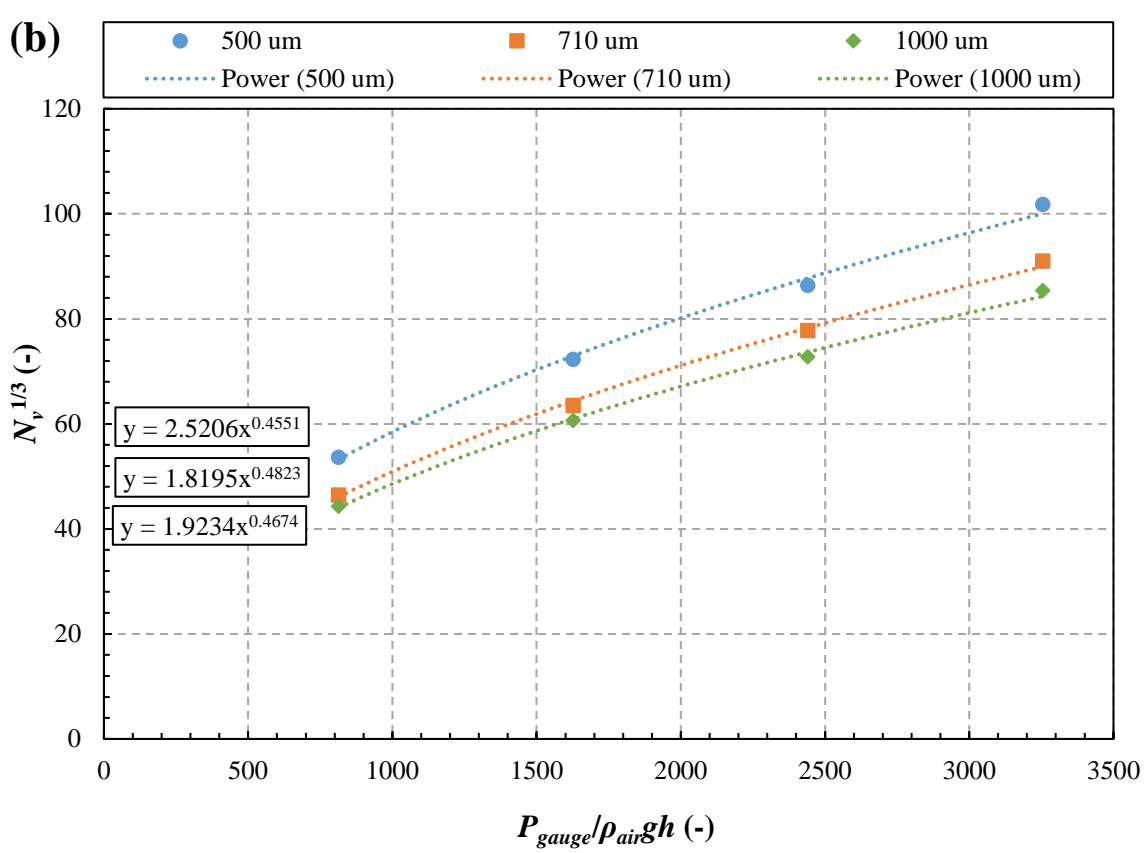


Figure C-1 The impact velocity,  $V_i$ , measured using high-speed imaging for different sizes of (a) HDPE, (b) PP Homo, (c) PP RaCo particles and (d) 1000  $\mu$ m glass beads, as a function of the vacuum gauge pressure,  $P_{gauge}$ , in the single particle impact tester.



#### Finding $C_1$ , $C_2$ , $C_3$ and $C_4$ for Equation (6-1)





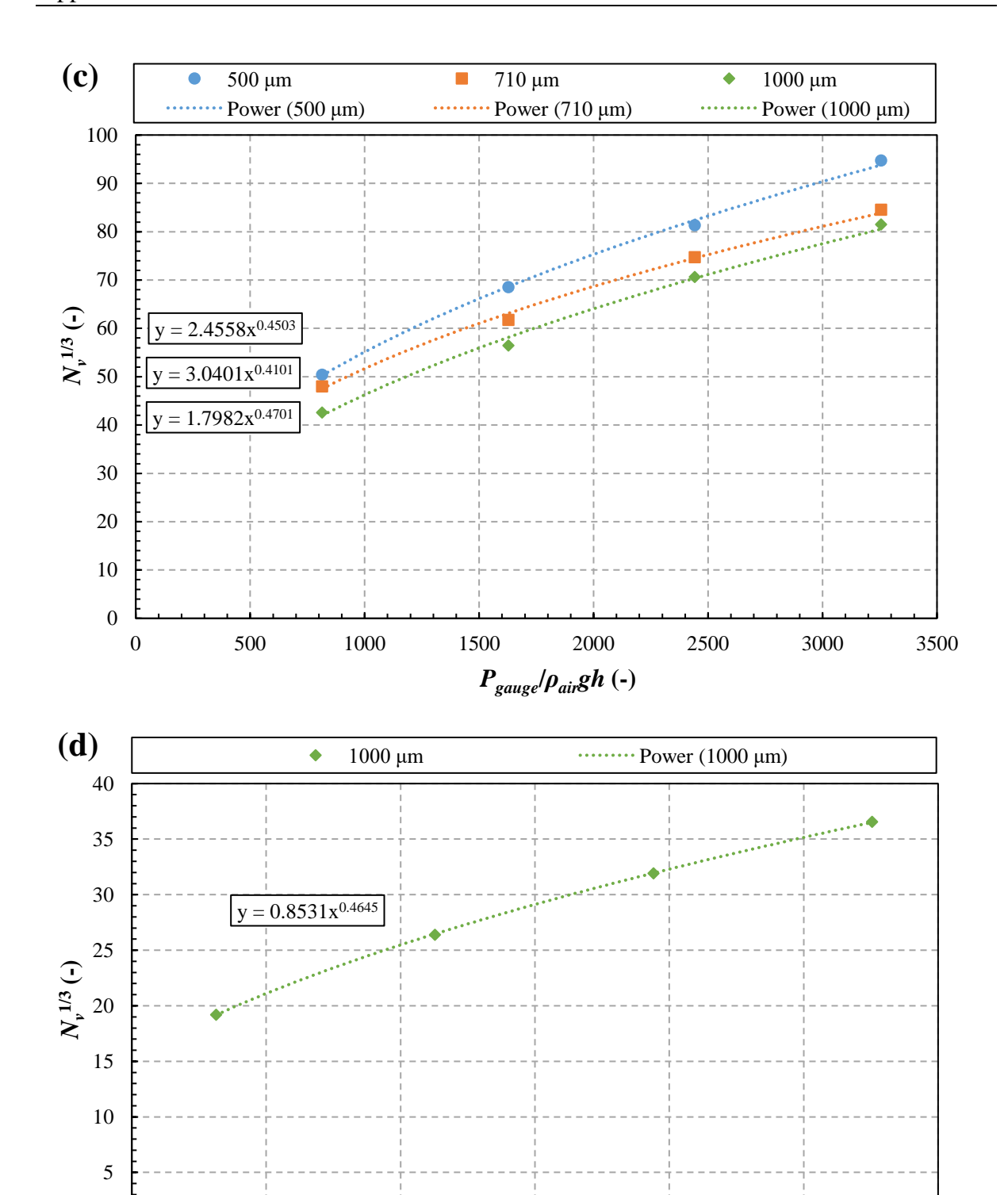
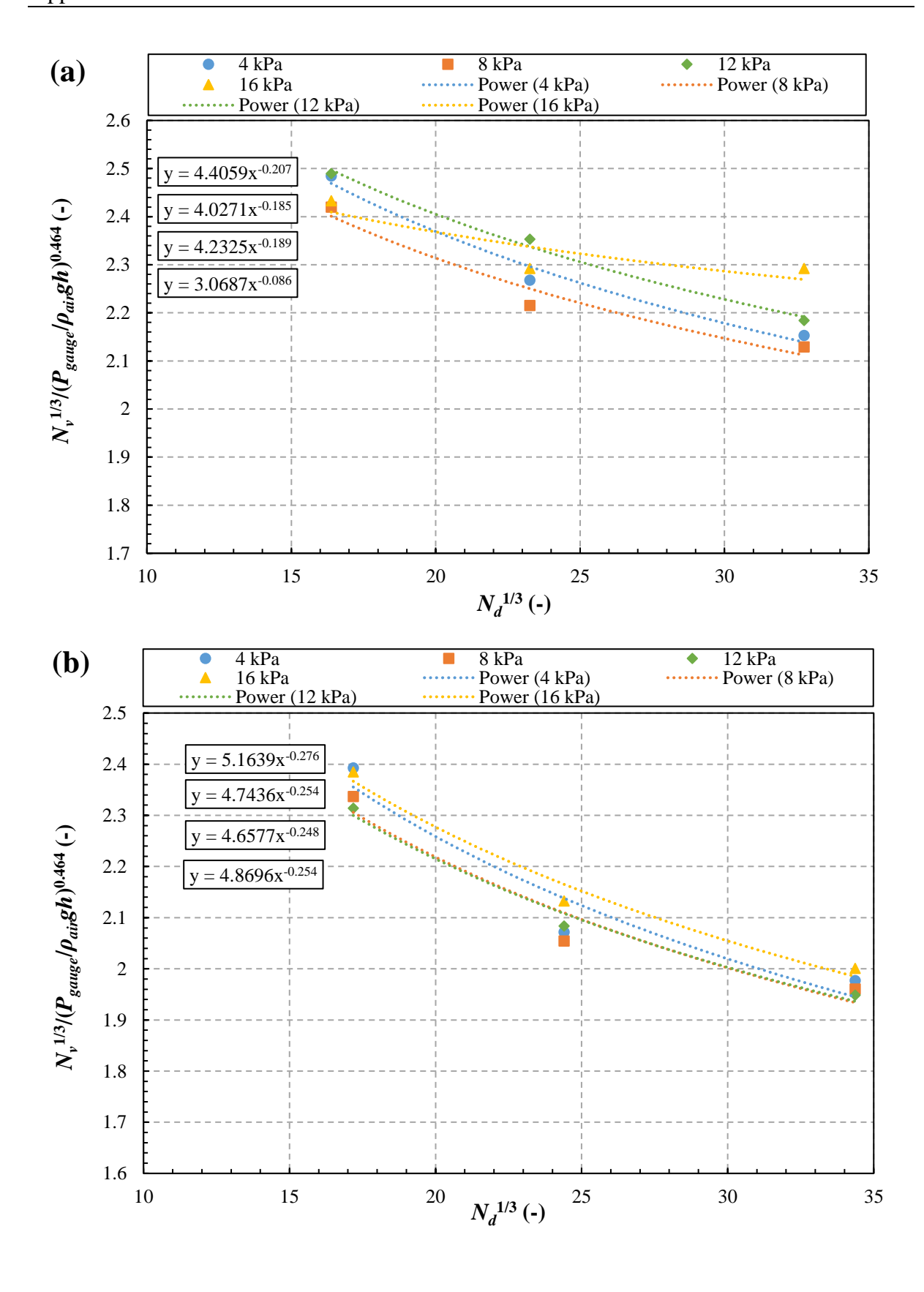


Figure C-2 The experimental value of the dimensionless velocity,  $N_v^{1/3}$ , as a function of  $P_{gauge}|p_{air}gh$  for (a) HDPE, (b) PP Homo, (c) PP RaCo particles for different particle sizes and (d) glass beads for 1000  $\mu$ m particles. The arithmetic mean value for the power indices of all the fitted lines is taken as the power index  $C_2$  of Equation (6-1).

 $P_{gauge}/\rho_{air}gh$  (-)



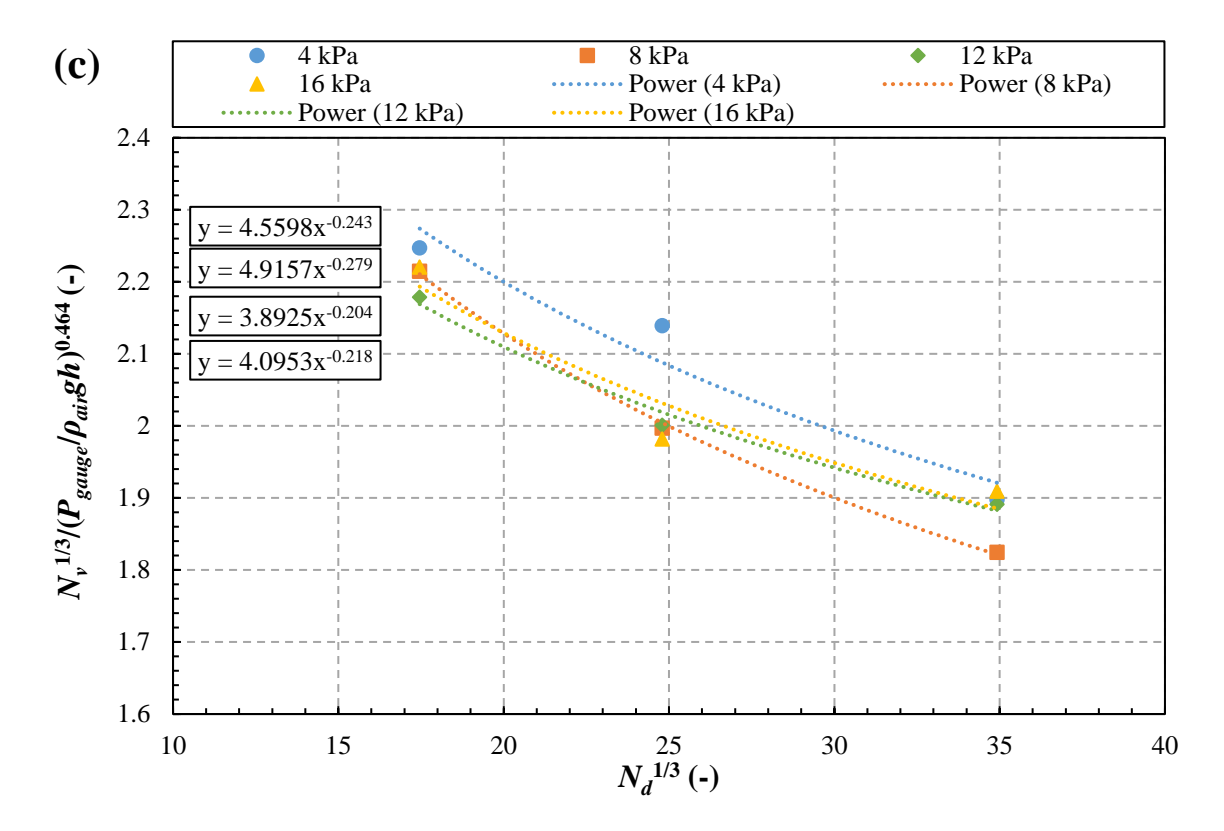


Figure C-3 Plot of  $N_v^{1/3}/(P_{gauge}/\rho_{air}gh)^{0.464}$  as a function of  $N_d^{1/3}$  for (a) HDPE, (b) PP Homo and (c) PP RaCo particles at different vacuum gauge pressures. The arithmetic mean of the absolute value for the power of all the fitted lines is taken as the power index  $C_4$  of Equation (6-1). Glass beads are not included in this analysis as the corresponding data are only available for one particle size.

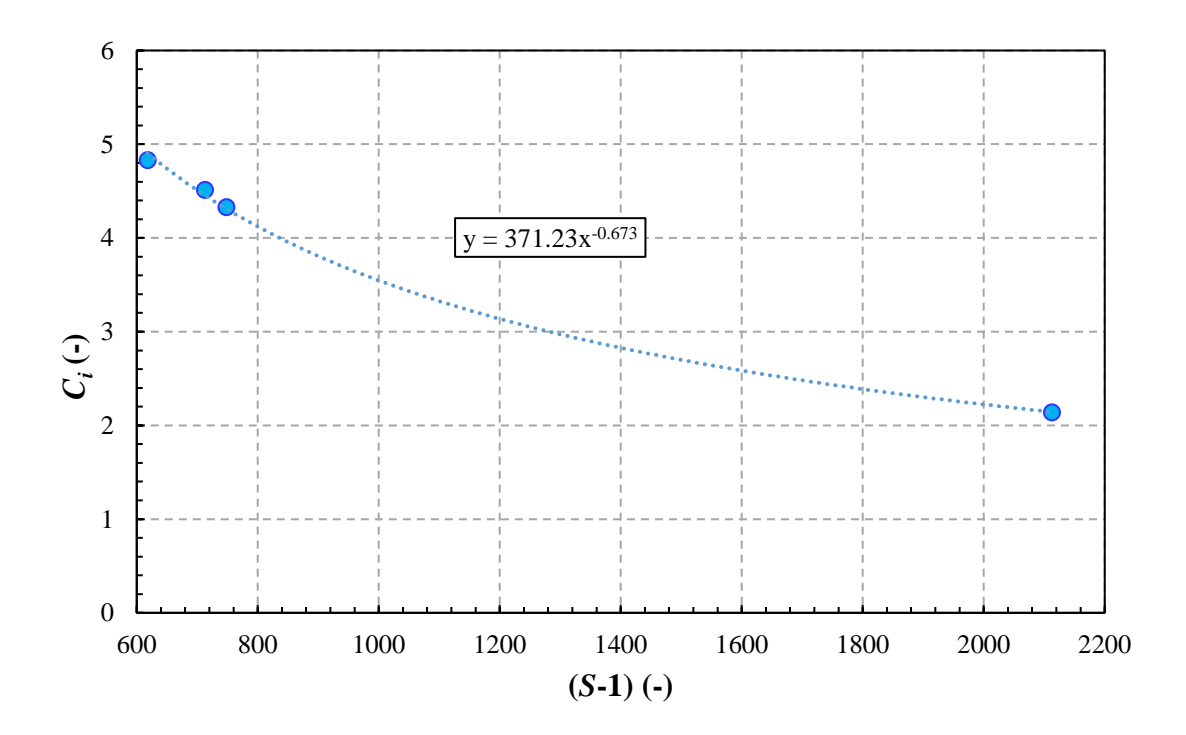
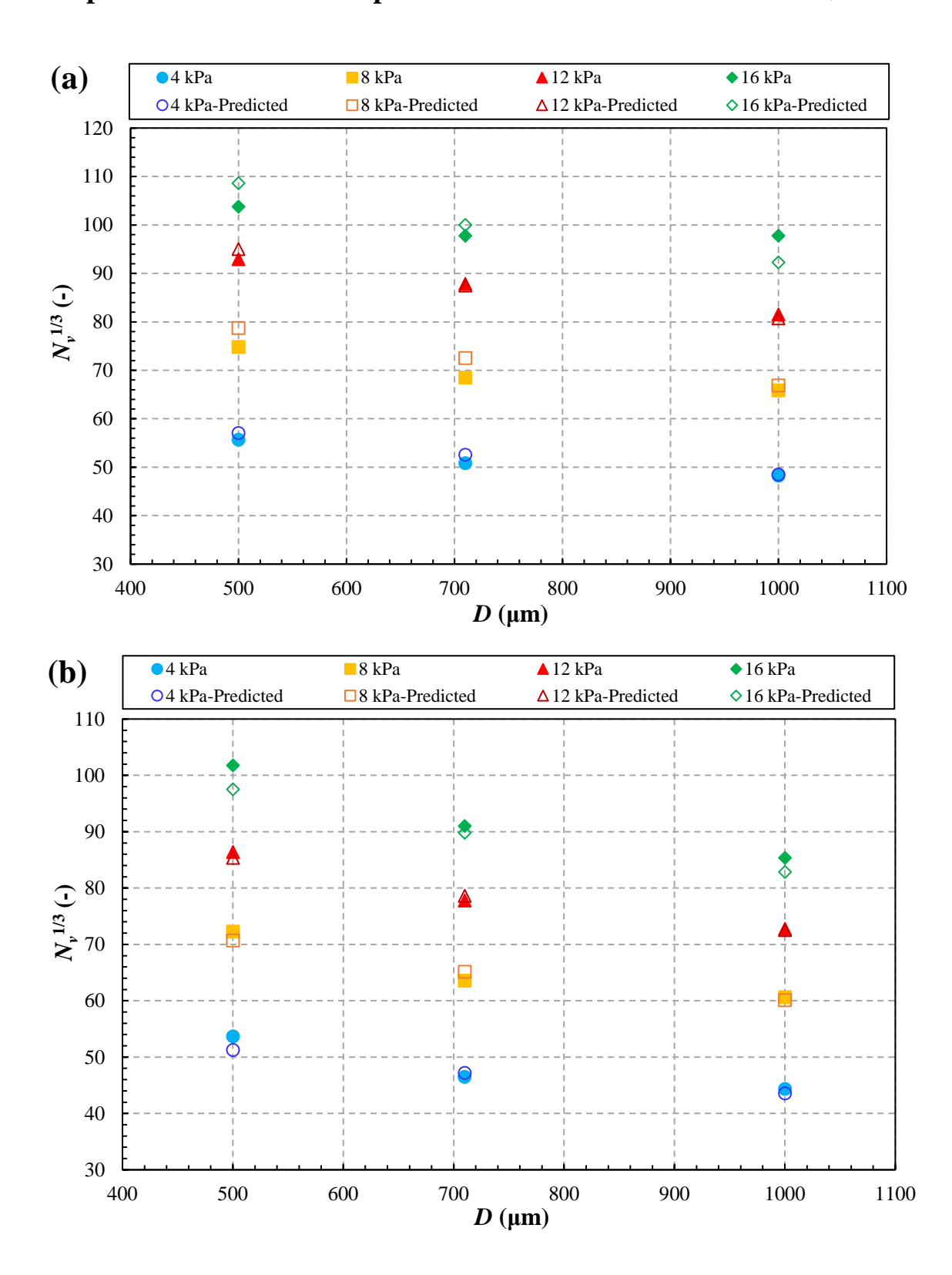


Figure C-4 Plot of  $C_i$  as a function of (S-1) for all the sample materials. The slope and absolute value of the power of the fitted line are taken as the empirical constant  $C_1$  and power index  $C_3$  of Equation (6-1), respectively.



## Comparison between the Experimental and Predicted values of $N_{\nu}^{1/3}$



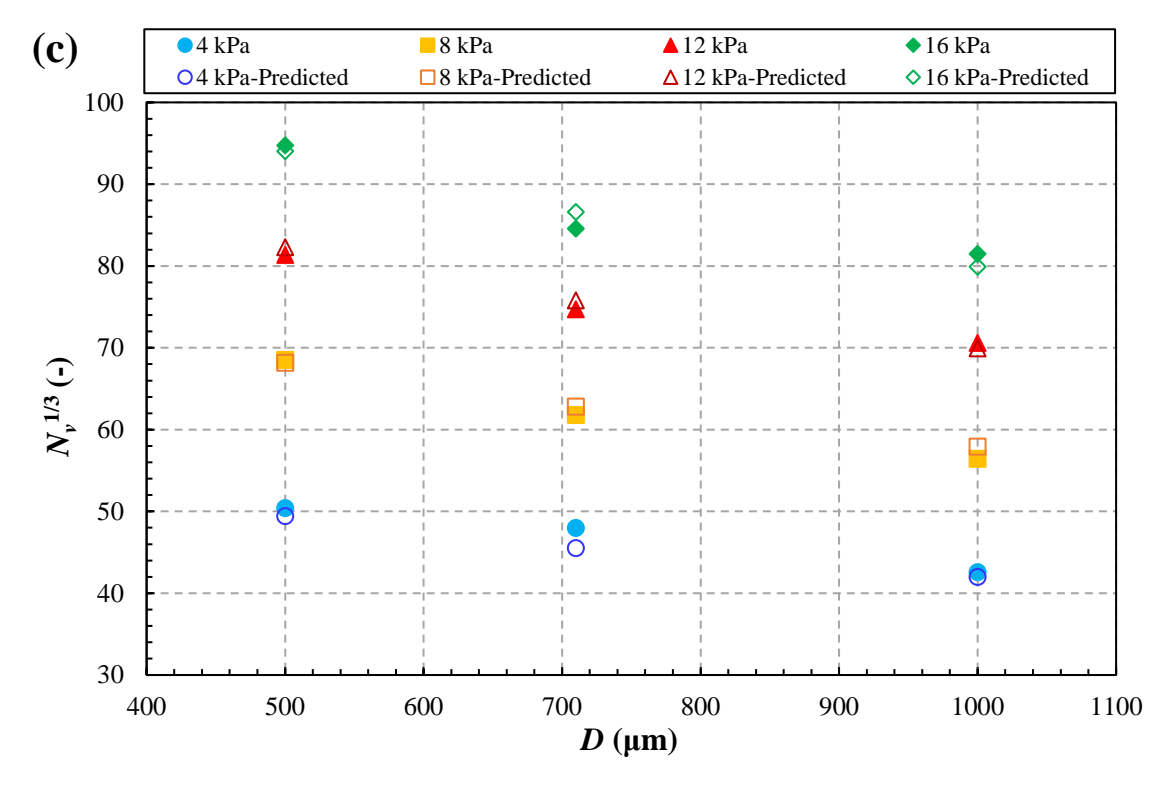


Figure C-5 Comparison between the experimental (solid symbols) and predicted (hollow symbols) values of the dimensionless impact velocity,  $N_{\nu}^{1/3}$ , at different vacuum gauge pressures for (a) HDPE, (b) PP Homo and (c) PP RaCo particles.

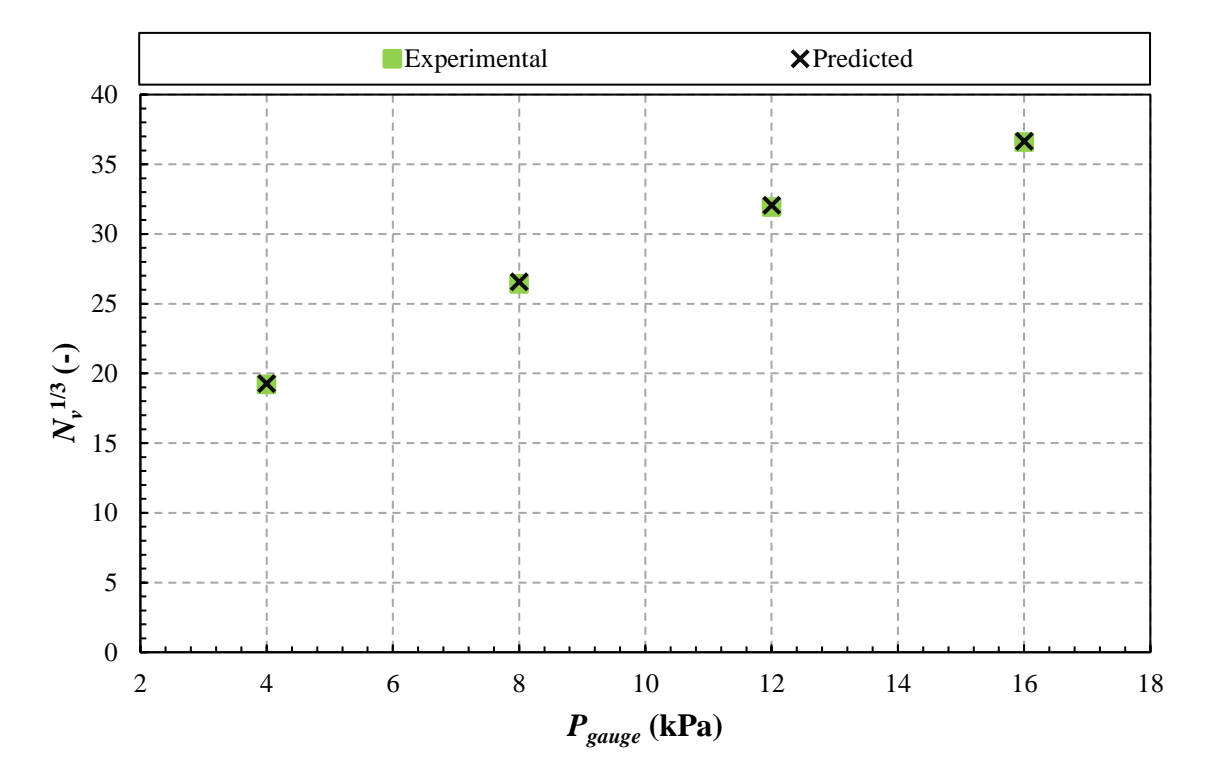


Figure C-6 Comparison between the experimental and predicted values of the dimensionless impact velocity,  $N_v^{1/3}$ , at different vacuum gauge pressures for 1000  $\mu$ m glass beads.



## The Measured/Estimated Impact Velocity for the Metal Particles

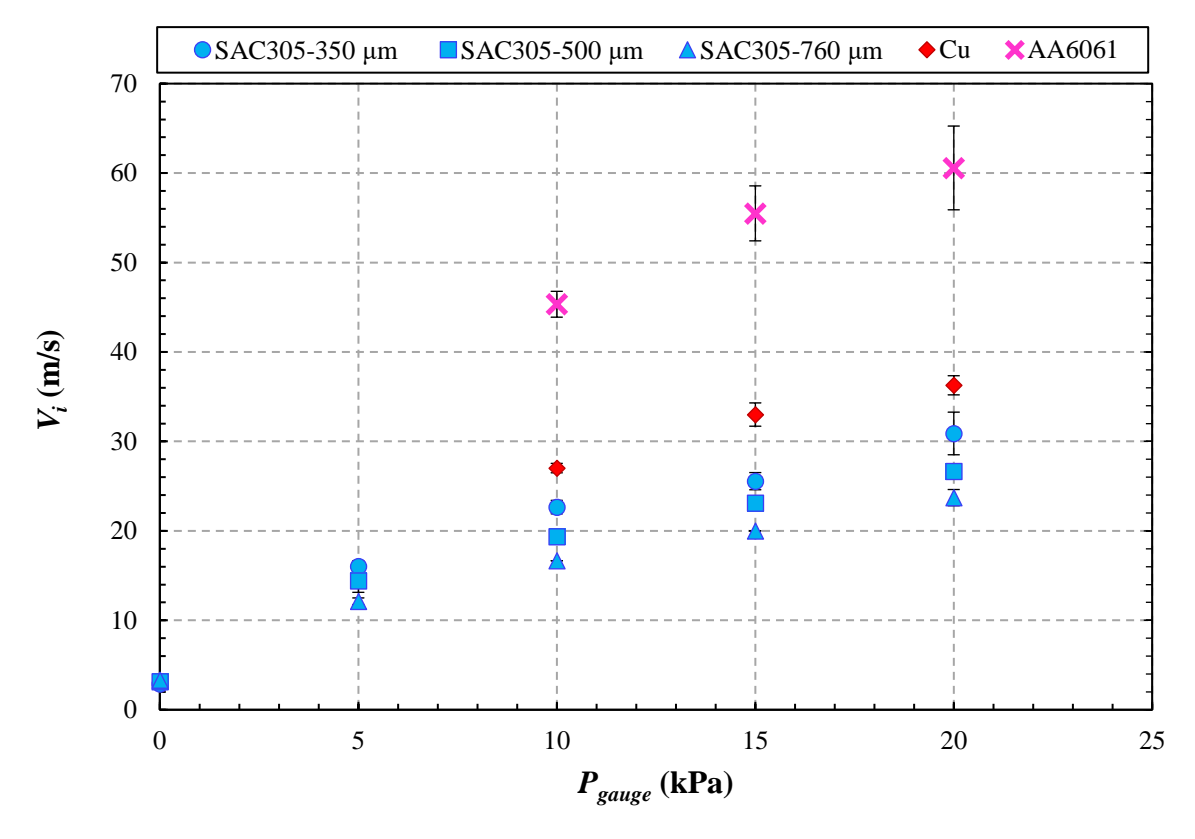


Figure C-7 The impact velocity,  $V_i$ , measured using high-speed imaging for different sizes of the solder balls (SAC305), and estimated using Equation (6-7) for copper (Cu) and aluminium alloy (AA6061) particles, as a function of the vacuum gauge pressure,  $P_{gauge}$ , in the single particle impact tester.